DESIGN, FABRICATION AND CHARACTERIZATION OF NOVEL PLANAR SOLID OXIDE FUEL CELLS

A Dissertation
Presented to
The Academic Faculty

by

Charles E. Compson

In Partial Fulfillment
of the Requirements for the Degree
Doctor of Philosophy in the
School of Materials Science & Engineering

Georgia Institute of Technology
May 2007

DESIGN, FABRICATION AND CHARACTERIZATION OF NOVEL PLANAR SOLID OXIDE FUEL CELLS

Approved by:

Dr. Meilin Liu, Advisor
School of Materials Science & Engineering
Georgia Institute of Technology

Dr. Paul Kohl
School of Chemical and Biochemical Engineering
Georgia Institute of Technology

Dr. Joe K. Cochran
School of Materials Science & Engineering
Georgia Institute of Technology

Dr. David Parekh
School of Mechanical Engineering
Georgia Institute of Technology

Dr. Robert Snyder
School of Materials Science & Engineering
Georgia Institute of Technology

Date Approved: February 20, 2007

To Ed, Linda, Melissa, Valerie and Chris:

Its family that got me here and family that helped me finish.

ACKNOWLEDGEMENTS

I would like to start by thanking my advisor, Dr. Meilin Liu, for his guidance throughout my time here. His patience and confidence has allowed me to design, fabricated and execute a project I can call my own. Dr. Cochran has also been very helpful source of information and encouragement throughout my research. His knowledge of ceramics has decreased my processing time considerably. I would also like to thank my other committee members, Dr. Paul Kohl, Dr. David Parekh and Dr. Robert Snyder, for their time commitment, useful discussions and advice throughout this process. I'd me remiss if I didn't add Dr. Bill Rauch to the list of advisors during my time here. His help and guidance has been crucial to my knowledge and many of my successes are as much his as mine. Without him, many ideas wouldn't have made it past the paper stage.

Many group members, present and past have contributed greatly to my research efforts. My officemates, Harry, Erik and Zhe have provided useful advice throughout many discussions. Other group members Robert, Songho, David and Dr. Yongman Choi are also thanked for the collaborations. I've also had the pleasure of becoming friends with Jeremy Walker, Kip Findley, Will Hughes, Brent Buchine, Chris Ma, Matt Trexler, Shubhra Bansal, Heather Graham and many other colleagues during my time here. Together we've enjoyed many weekends and won a few intramural T-shirts along the way.

Finally I'd like to thank my family. My parents, Ed and Linda, have been constant sources of encouragement and never-ending support. Some of their contributions just can't be put into words. My sister, Melissa, has always been a source

of joy. Her courage and commitment to helping others is contagious. My accomplishments here pale in comparison to her selfless efforts towards others. My second family, the Buttaccio's, should also be acknowledged. Jeff and Kathy have treated me like a son. Chris, you've given me more than I can repay. I've never understood why you've had so much confidence and faith in me, but it has brought me farther than I can tell you. You're as much the reason I'm here as anyone, and for that I can only say thank you. Lastly, I'd like to thank my wife, Valerie for her love and patience with me. She's a joy to come home to and reminds me of what's truly important in life.

This work was supported by the NASA URETI on UAPT program.

TABLE OF CONTENTS

LIST OF TABLES

LIST OF FIGURES

LIST OF SYMBOLS AND ABBREVIATIONS

ACAC	Acetylacetone
AFC	Alkaline Fuel Cell
AMU	Atomic Mass Unit
ANOVA	Analysis of Variance
APU	Auxiliary Power Unit
ARAES	Angle-Resolved Auger Electron Spectroscopy
ASR	Area-Specific Resistance
ATS	Applied Test Systems
CCD	Central Composite Design
CCVD	Combustion Chemical Vapor Deposition
CE	Counter Electrode
CTE	Coefficient of Thermal Expansion
CVD	Chemical Vapor Deposition
DC	Direct Current
DFT	Density Functional Theory
DLVO	Derjaguin Landau Verwey and Overbeek
DMFC	Direct Methanol Fuel Cell
EDS	Energy Dispersive X-Ray Spectroscopy
EIS	Electrochemical Impedance Spectroscopy
EMF	Electromotive Force
EPD	Electrophoretic Deposition
ESDIAD	Electron Stimulated Desorption in Ion Angular Distributions
EVD	Electrochemical Vapor Deposition

GDC	Gadolinia-Doped Ceria
GT-SOFC	Gas Turbine – Solid Oxide Fuel Cell
ISS	Ion Scattering Spectroscopy
LVDW	London van der Walls
MBE	Molecular Beam Epitaxy
MCFC	Molten Carbonate Fuel Cell
MEK	Methyl Ethyl Ketone
MFO	Menhaden Fish Oil
MS	Mass Spectrometry
NEB	Nudged Elastic Band
NEXAFS	Near-Edge X-Ray Adsorption Fine Structure
OCV	Open Circuit Potential
PAFC	Phosphoric Acid Fuel Cell
PAW	Projector Augmented Wave
PE	Phosphate Ester
PEI	Polyethyl Imine
PEM	Proton Exchange Membrane
PEMFC	Proton Exchange Membrane Fuel Cell
PNNL	Pacific Northwest National Laboratory
PRESS	Predicted Error Sum of Squares
PSZ	Partially-Stabilized Zirconia
PVB	Polyvinyl Butyral
PVD	Physical Vapor Deposition
RF	Radio Frequency
ScSZ	Scandia-Stabilized Zirconia

SDC	Samaria-Doped Ceria
SEM	Scanning Electron Microscopy
SOFC	Solid Oxide Fuel Cell
UHV	Ultra High Vacuum
VASP	Vienna *ab initio* Simulation Package
WE	Working Electrode
XRD	X-Ray Diffraction
YSZ	Yittria-Stabilized Zirconia

SUMMARY

Planar solid oxide fuel cells (SOFCs) were designed, fabricated and characterized in order to develop a (1) cost-effective method for fabrication of thin electrolyte layers, (2) hermetic sealing and (3) stable interconnects. Electrophoretic deposition (EPD) was discovered to be an excellent method for fabricating dense electrolyte layers of about 5μm thick on porous non-conducting substrates. The EPD process was thoroughly studied from proof-of-concept to statistical reproducibility, deposition mechanism, modeling and process optimization. Deposition on non-conducting substrates was found to follow many of the same fundamental trends as that on conductive substrates except for the voltage efficiency and detailed charge transfer mechanism. Eventually, the process was optimized such that an SOFC was fabricated that achieved 1.1W/cm^2 at 850ºC. Further, a novel sealless planar SOFC was designed that incorporates a hermetic interface between the electrolyte and interconnect similar to tubular and honeycomb designs. The hermetic interface successfully acted as a blocking electrode under DC polarization, indicating its potential to act as a sealant. Leakage rates across the interface were 0.027sccm at 750ºC, similar to polycrystalline mica seals. Through a process of tape casting and lamination, a two-cell stack without sealant was fabricated and achieved a power density of 75mW/cm^2 at 750ºC. Finally, the degradation rate of silver and silver-based interconnects was studied under static and dual-atmosphere conditions. Corrosion of silver grain boundaries along with sublimation losses results in the formation of large pores, resulting in up to 30μm of anode oxidation after 8hrs testing at 750ºC. Further stability studies indicated that silver-based interconnects would be better suited for applications at operating temperatures less than 650ºC.

I. INTRODUCTION

Energy independence is a goal that many nations are striving to achieve, and few have actually realized. To build an infrastructure that relies simply on ones own resources significantly improves the economic, political, and social strength of a nation. To base that infrastructure on renewable resources and alternative energies impacts not only the wellbeing of a nation, but also its people. Reliance on ones own renewable resources guarantees that energy related jobs would always remain available, which impacts job growth, unemployment and spending. When dependence on imported energy supplies such as oil, coal and natural gas is eliminated, so are the political pressures of dealing with foreign nations and the impact of costly imports on a countries trade balance/deficit. The byproducts of alternative energy systems are also much more environmentally friendly, which not only reduces emissions of global warming and pollutant gases, but also provides a healthier atmosphere for those living in that region.

The desire to develop alternative energy sources, along with the ever-diminishing fossil fuel supply has resulted in a present push for fuel cell technology. Fuel cells are direct chemical to electrical energy conversion devices that operate via an electrochemical reaction involving a fuel source (e.g. any hydrogen containing gas such as gasified coal and various hydrocarbons) and an oxygen source (e.g. air, pure oxygen or some intermediate).[1,2] Traditional energy technologies such as combustion engines, convert chemical energy to mechanical energy and then to electrical energy, during which there are large losses involved with fuel to heat conversion. Since energy conversions of the electrochemical type bypass the mechanical step, they yield both higher efficiency (~60%) and environmentally safer bi-products (only H_2O when pure hydrogen is used as fuel, CO_2 and H_2O when hydrocarbon fuels are used) compared to current combustion technologies.[1]

1.1 History of fuel cells

Sir William Robert Grove is credited with developing the first fuel cell, based on dilute sulfuric acid electrolyte, in 1839.[3] A patent lawyer by trade, Grove's interest in chemistry and understanding of electrolysis led him to the hypothesis that a reverse reaction must also be possible, which would react the two gases to produce electricity and water. A schematic of his first cell is given in Figure 1.

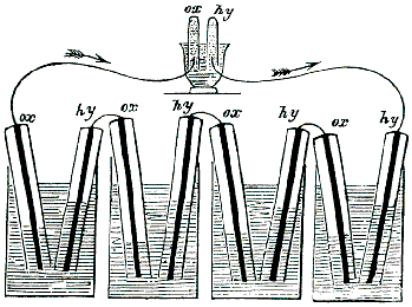

Figure 1. Schematic of Grove's 'gas voltaic battery'. Oxygen and Hydrogen in the tubes over the reservoirs react with the dilute sulfuric acid to form electricity and water.

While many scientists struggled to understand exactly how his fuel cell, or Grove cell as it was called, worked; Mond and Langer developed the first hydrogen-oxygen fuel cell. Using thin platinum electrodes and a quasi-solid electrolyte composed of an earthenware plate saturated with dilute sulfuric acid; the cell achieved 6 A/ft^2 at 0.73V in 1889.[4] Some scientists lobbied for 'Contact Theory' or that physical contact between multiple components allowed for current to flow, while others thought that 'Chemical Theory' or chemical reactions and gas diffusion was the cause of current flow. Freidrich Ostwald provided the theoretical understanding of how Grove's fuel cell operated, thus discerning the roles of each component with respect to electrodes, electrolytes, anions, cations and oxidizing and reducing agents. He showed that chemical reactions within a gas diffusion electrode took place in a contact area where the catalyst, reactant gas and electrolyte met.[5]

Nernst discovered an oxide electrolyte composition in 1899, 15-wt% Y_2O_3 doped into ZrO_2, which he used to replace carbon filaments as the glower in electric lamps.[6] Though the glower operated successfully, electrolysis was also observed. Later it was found that the same amount of oxygen generated at the anode was consumed at the cathode, indicating the electrolyte composition was conducting oxygen between the electrodes during current flow. Schottky proposed, in 1935, that Nernsts' electrolyte composition could be used as a solid oxygen ion conductor for fuel cells.[7] In 1937, Baur and Pries operated a fuel cell using that solid electrolyte composition, observing open circuit voltages from 1.1-1.2V at 1000-1050ºC, respectively.[8] Francis Thomas Bacon built a low-temperature pressurized fuel cell in 1939 using nickel gauze electrodes and an alkali electrolyte (potassium hydroxide). Bacon believed the cell, operated at pressures up to 3000psi, might prove useful in replacing storage batteries in British Royal Navy submarines.[9] Eventually, Bacon's 1950's fuel cell work lead to an alkaline fuel cell used by NASA in the 1968-1972 Apollo space shuttle missions.

Strong efforts to develop a ceramic fuel cell began in the 1960's, however the planar disk and segmented-cell-in-series designs involved thick electrolyte's that suffered from large ohmic losses during operation. Thin film electrolyte research lead to a successful segmented-cell-in-series design in the 1970's. The sealless tubular design was introduced in the 1980's by Westinghouse, improving many of the engineering issues related to the segmented-cell-in-series design.[10] Renewed interest in planar or flat-plate cells also occurred in the 1980's, mostly due to the drastic improvements in thin film ceramic processing techniques such as tape casting. Today, planar designs offer higher power densities than do the tubular designs due to shorter current paths and lower ohmic losses, however the tubular designs have fewer issues from a stack development standpoint, as sealing and manifolding are much easier.[2,11]

1.2 Types of Fuel Cells

There are five major types of fuel cells currently being investigated for direct energy conversion.[1] They are proton exchange membrane, alkaline, phosphoric acid, molten carbonate and solid oxide fuel cells. Alkaline fuel cells (AFCs) are best known for their role in the Apollo space program, most notably the cause of the Apollo 13 power supply issue. Phosphoric acid fuel cells (PAFCs) are probably the most commercially ready technology, followed by the molten carbonate fuel cells (MCFCs). Though these two technologies are the most advanced from an industrial standpoint, they contain highly corrosive electrolyte materials and aren't widely considered to be long-term alternative energy solutions. The two most promising technologies are proton-exchange membrane (PEM) and solid oxide fuel cells (SOFCs), due to the potential for much higher power and energy densities and their use of all solid components rather than liquid electrolytes. A schematic depicting various fuel cell technologies and their relative operating temperatures is shown in Figure 2.[12]

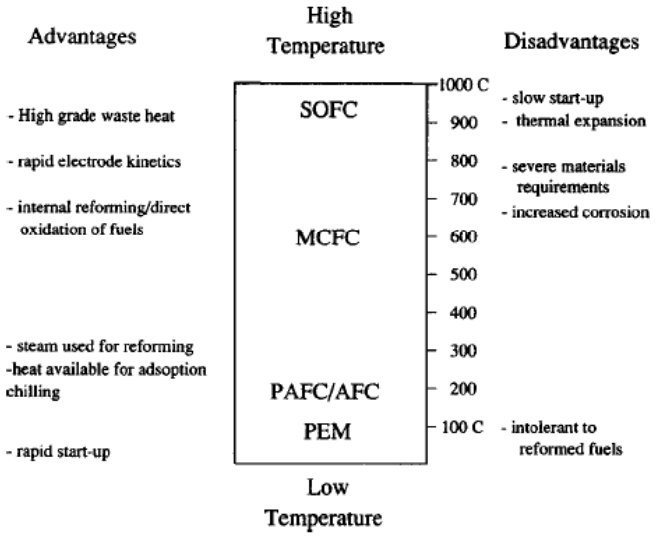

Figure 2. Various Types of Fuel Cells and their advantages and disadvantages with respect to operating temperature.[12]

1.2.1 Alkaline Fuel Cells

Alkaline fuel cells (AFCs) operate at 60-90ºC via the continuous diffusion of hydroxyl ions from the cathode to the anode and the subsequent counter-motion of water. Potassium hydroxide and sodium hydroxide are the main electrolyte materials, which are either circulated through the system or remain static, depending on the design. Pure hydrogen fuel and air oxidant are fed to the anode (typically porous nickel) and cathode (either platinum or a carbon matrix), respectively, resulting in the following electrochemical reactions.[13]

Reaction 1

$$2H_2 + 4OH^- \longrightarrow 4H_2O + 4e^- \quad (anode)$$

$$O_2 + 4e^- + 2H_2O \longrightarrow 4OH^- \quad (cathode)$$

$$2H_2 + O_2 \longrightarrow 2H_2O \quad (Overall)$$

Since oxygen reduction reactions occur more favorably in alkaline environments than in acid environments, the voltage drop or activation overpotential is quite low, leading to the highest voltage of any fuel cell system (E^o=1.23V) and efficiencies of 40-50%. The lack of a necessary noble metal catalyst and operability at room temperature, which leads to excellent cold-start capability, are also advantages over other fuel cell systems. The problem with alkaline fuel cells is that carbon dioxide in the air can cause the formation of potassium or sodium carbonate crystals, which can block electrolyte pathways and electrode pores.[14] An example carbonate producing reaction involving potassium is shown in Reaction 2.

Reaction 2

$$KOH + CO_2 \longrightarrow K_2CO_3 + H_2O$$

Another issue with AFCs is the necessity of using pure hydrogen fuel. Alternative fuels such as methanol have been tested, but the oxidation reaction produces carbon dioxide, as shown in Reaction 3, which diffuses into the electrolyte producing carbonate as in Reaction 2.[15]

Reaction 3

$$CH_3OH + 6OH^- \longrightarrow 5H_2O + CO_2 + 6e^-$$

Low operating temperatures and cost effective materials resulted in NASA using AFCs in the Apollo Space Program. Since air and carbon dioxide aren't readily available in space, many of the deficiencies of these fuel cells were eliminated.

1.2.2 Molten Carbonate Fuel Cells

Molten carbonate fuel cells (MCFCs) operate in the temperature range of 600-700ºC since they rely on molten carbonate ions to conduct from the cathode, through the electrolyte to the anode. Typically the electrolyte is composed of a mixture of Li_2CO_3 and K_2CO_3 (62:38 ratio) or Li_2CO_3 and Na_2CO_3 (50:50 ratio) in a $LiAlO_2$ ceramic matrix. Oxygen and carbon dioxide are reduced by a porous lithiated NiO cathode producing carbonate ions, which travel through the molten electrolyte and combine with hydrogen, which was oxidized by a NiCr or NiAl-based anode. The electrochemical half-cell and overall reactions are as shown in Reaction 4.

Reaction 4

$$2H_2 + 2CO3^{2-} \longrightarrow 2H_2O + 2CO_2 + 4e^- \quad (anode)$$

$$O_2 + 2CO_2 + 4e^- \longrightarrow 2CO_3^{2-} \quad (cathode)$$

$$2H_2 + O_2 + \longrightarrow 2H_2O \quad (overall)$$

The advantages of MCFCs are high temperature operation resulting in high value steam, the potential for use of methane or carbon dioxide fuels and the use of inexpensive catalyst materials compared to other high temperature fuel cells. When carbon dioxide or carbon monoxide fuels are used, the exhaust fuel can also be recycled to the cathode for use in the reduction reaction. Disadvantages of the MCFC system are carbon dioxide management, since it's a strong greenhouse gas, and corrosion of the cathode due to electrolyte creep. Nickel oxide is soluble in molten carbonate material, which leads to diffusion of nickel ions into the electrolyte and to the anode where it can precipitate out as nickel metal by Reaction 5.[15]

Reaction 5

$$NiO + CO_2 \longrightarrow Ni^{2+} + CO_3^{2-}$$

When enough nickel precipitates, shorting can occur between the two electrodes. To combat the issue of shorting, thicker electrolytes are used, however the thicker electrolytes lead to greater ohmic losses and reduced performance. Therefore, though MCFC stacks have been demonstrated from 250kW-2MW and some commercialization has taken place, corrosion and electrode leaching continue to plague the technology.[16]

1.2.3 Phosphoric Acid Fuel Cells

Phosphoric acid fuel cells (PAFCs) were the first commercially available fuel cells with an operating temperature in the range of 150-220ºC. Basic cell operation occurs as hydrogen is oxidized, by a composite carbon-Pt-PTFE anode, after which the protons are then conducted through the H_3PO_4 acid electrolyte (contained within the capillaries of a SiC matrix) to the cathode where they combine with oxygen ions. Oxygen ions are formed by reduction of oxygen from the air, by a carbon-Pt-PTFE composite cathode. The half-cell and overall electrochemical reactions are shown in Reaction 6.

Reaction 6

$$2H_2 \longrightarrow 4H^+ + 4e^- \quad (anode)$$

$$O_2 + 4H^+ + 4e^- \longrightarrow 2H_2O \quad (cathode)$$

$$2H_2 + O_2 \longrightarrow 2H_2O \quad (overall)$$

The high proton conductivity of the electrolyte results in very low ohmic losses during operation. Phosphoric acid does not react with carbon dioxide; therefore issues of carbonate formation, as in AFCs, aren't encountered. Due to the operating temperature, some useful waste heat is produced in the system, however the cell itself must be cooled using liquid (e.g. water) or gas (e.g. air), else the phosphoric acid will evaporate during operation. The coolant system increases the cost of PAFCs significantly as the water must be purified so as not to contaminate the cell. System costs increase even more if the cell is pressurized during operation because of the toxicity and corrosiveness of any

leaking acidic gases. PAFCs suffer from high costs due to the necessary expensive catalyst material for the electrodes and matrix material to hold the electrolyte. Also, phosphoric acid has a freezing point of 42ºC, therefore the cell must always remain above that temperature, or else the large volume expansion it undergoes during freezing may crack the SiC matrix.

1.2.4 Proton Exchange Membrane Fuel Cells

Proton exchange membrane fuel cells (PEMFCs) have great potential to be an affordable low cost fuel cell. With an operating temperature range from 50-140ºC, PEMFCs utilize pure hydrogen fuel and air oxidant.[16] A Pt/Ru anode oxidizes hydrogen and the proton is then conducted through a water solvated polymer membrane (e.g. Nafion) to the cathode where it combines with oxygen ions to form water. The operation is very similar to the previously mentioned PAFCs and the half-cell and overall cell reactions are the same as Reaction 6. The two electrodes, the anode and the cathode, are composed of Pt particles dispersed in a porous carbon/PTFE support in order to increase surface area and limit the amount of noble metal catalyst required. The main problem with PEM fuel cells is water management, since the conductivity of the electrolyte is highly dependent on humidity. Nafion membrane conductivity has been observed to change orders of magnitude 30% and 70% relative humidity environments. Another issue also exists with respect to too much water. Since the byproduct of the electrochemical reaction is liquid water (T<100ºC), electrolyte flooding can occur, which reduces surface area and dilutes proton transport. Therefore the water produced at the cathode must be accounted for so as to neither flood nor dry out the electrolyte. The last issue with respect to water is that its natural dipole is slightly positive, causing it to migrate towards the cathode during operation. This process is call electro-osmotic drag and can result in the removal of all water from the anode side of the cell under high-load conditions. PEM fuel cells also must operate on pure hydrogen and therefore require a

large balance-of-plant, involving a fuel reformer. Not all aspects of PEMs are negative though. There are many advantages including high power densities compared to other low temperature fuel cells, ease of cell stackability, lack of material interactions, small in size and reasonable cost. These are the reasons that many companies are pushing to commercialize PEM technology including Dupont and Ballard Power Systems.

1.2.5 Direct Methanol Fuel Cells

Direct methanol fuel cells (DMFCs) operate very similarly to PEMFCs except that a liquid fuel, methanol, is used instead of hydrogen. Liquid fuels have much higher energy densities than do their gas counterparts and are considerably easier to store and transport for mobile applications. Since methanol is used as the fuel, the half-cell and overall electrochemical reactions change from Reaction 6 to Reaction 7:

Reaction 7

$$CH_3OH + H_2O \longrightarrow CO_2 + 6H^+ + 6e^- \quad (anode)$$

$$1.5O_2 + 6H^+ + 6e^- \longrightarrow 3H_2O \quad (cathode)$$

$$CH_3OH + 1.5O_2 \longrightarrow CO_2 + 2H_2O \quad (overall)$$

The methanol oxidation does not always completely occur however, which is problematic to DMFC operation. First, an issue called methanol crossover occurs when un-oxidized methanol transports through the electrolyte to the cathode. When the fuel and oxidant mix without an electrochemical reaction, the cell exhibits a voltage loss. Eventually enough methanol may leak through the electrolyte so as to reduce the cell voltage to an unusable level. A second issue with methanol is that is adsorbs to and poisons the platinum catalyst through the following reaction(s).[17]

Reaction 8

$$CH_3OH + xPt \longrightarrow Pt_xCH_2OH + H^+ + e^-$$

$$CHOH + xPt \longrightarrow Pt_xCO + xPt + 2H^+ + e^-$$

Though the alloying of Pt with Ru, as is often done in PEM anodes, can prevent poisoning of the electrode, there is not current solution to the issue of crossover. Other

issues with DMFCs include slow electrode kinetics (particularly at the cathode), high costs associated with the noble metal electrodes and carbon monoxide poisoning at both electrodes. These issues have slowed commercialization and pushed companies to use hydrogen-based fuel cells, such as PEMFCs, for low temperature applications.[15]

1.2.6 Solid Oxide Fuel Cells

Solid oxide fuel cells are the topic of this thesis and will be discussed in detail in Chapter 2.

1.3 Principles of Fuel Cell Operation

The operating principles of fuel cells are similar to batteries in that electricity is produced from an electrochemical reaction. Unlike batteries, however fuel cells use a continuous flow of fuel and oxidant gases to generate electricity and therefore don't require charging. So long as a supply of fuel and oxidant are available, electricity will be produced. Electrochemical reactions are chemical reactions where electrons or electricity either take part in or are produced as a result of the reaction. Typically these reactions are termed 'redox reactions,' since they involve the oxidation of one chemical species and subsequent reduction of another. These reactions can be either spontaneous in their release of energy, as in galvanic cells, or driven to completion, as in electrolytic cells. Fuel cells are a form of galvanic cell, where the electrochemical reactions occur spontaneously resulting in the formation of a byproduct (in this case water) and electrical energy.[18] An example reaction that spontaneously proceeds from reactants to products is given in Reaction 9.

Reaction 9 $$aA + bB \longrightarrow cC + dD$$

According to Le Châtelier's Principle a reaction should reverse slightly to offset the increase in reaction product concentration. To determine the direction that the reaction

will proceed in order to reach equilibrium, we determine the reaction quotient, *Q*, which has the same form as the equilibrium constant, *K*.

Equation 1

$$K = Q = \frac{a_C^c a_D^d}{a_A^q a_B^b}$$

where a_j^i represents the activity of chemical *j* with a stoichiometry of *i*. Though they are governed by the same relation, the reaction quotient, *Q*, can be used at any point in the reaction or concentration level that exists even before equilibrium has been achieved, whereas the reaction constant, *K*, is only used when equilibrium has been reached, at which point $Q = K$. When $Q < K$, the reaction will always proceed towards the products to reach equilibrium and when $Q > K$, the reaction must reverse towards forming reactants in order to achieve equilibrium.[19] In an ideal gas system, such as fuel cells, the activity of a component, a_j^i, can be approximated by its mole fraction, X_j^i, which can be reduced to its concentration $[j]^i$.

Equation 2

$$K = Q = \frac{[C]^c [D]^d}{[A]^a [B]^b}$$

The thermodynamic balance between the enthalpy, *H*, and entropy, *S*, of the chemical reaction determines the equilibrium formation of products from reactants. Enthalpy is defined as the heat adsorbed or released by the reaction, with a negative value ($-\Delta H$) indicating an exothermic reaction. The entropy of the system describes the amount of its disorder or rather it's a property that monitors the proper or spontaneous direction of change for a given system and its surroundings.[20] An easy way to think about this is to consider phase changes. A gas is always more disordered than a liquid and a liquid is more disordered than a solid. Therefore the gas has the highest entropy and the solid has the lowest entropy. By convention, the entropy of a system that spontaneously moves from products to reactants always has a positive value ($+\Delta S$) and is associated with consumption of the available capacity for spontaneous change when a process occurs.[20]

In general, thermodynamics only tells us whether a given reaction under a given set of conditions *can* happen, not whether it *will* happen; that is governed by kinetics. To determine if a reaction can happen, we must calculate the change in Gibbs Energy of the reaction. The Gibbs Energy is defined as the energy available to do work, neglecting any work done by changes in pressure or volume. [16,21] In equation form, the Gibbs energy represents the balance between the enthalpy and entropy of the system.

Equation 3 $$\Delta G = \Delta H - T\Delta S$$

By convention, a given reaction can proceed spontaneously if the change in Gibbs Energy is negative *(-ΔG)*, which indicates that the products of the reaction have a lower energy state or rather are more stable state than the reactants. A given reaction is favored to occur (negative Gibbs Energy) when heat is released (negative enthalpy) and disorder is increased (positive entropy).

The Gibbs energy for the chemical reaction given in Reaction 9 is

Equation 4 $$\Delta G = \Delta G^{o} + RT \ln K$$

where ΔG^{o} is the Gibbs energy of the reaction at standard temperature and pressure. The natural log dependence of the equilibrium constant comes about through integration of the partial molal Gibbs Energy of component *j*, also termed the chemical potential, $\Delta\mu_j$, from an initial pressure to a final pressure while also evaluating the partial molal volume.

Equation 5 $$\Delta G_j = \Delta\mu_j = \int_{P_i}^{P_f} V_j dP = \int_{P_i}^{P_f} \frac{RT}{P} dP = RT \ln \frac{P_i}{P_f}$$

Dalton's law of partial pressures states that the diatomic gases, such as H_2 and O_2 used in fuel cells, are Henrian in behavior and therefore the partial pressure of each gas component is equal to its mole fraction multiplied by the total pressure of the gas system.

Equation 6 $$P_j = X_j P$$

Rearranging Equation 6, solving for each component in the system and substituting Equation 2 and Equation 6 into Equation 5 results in an expanded version of Equation 4, which can be used to calculate the Gibbs Energy of the entire chemical reaction.

Equation 7
$$\Delta G = \Delta G^o + RT \ln \frac{P_C^c P_D^d}{P_A^a P_B^b}$$

The energy of a chemical system drives charges to move in a specific direction; the driving force for charge movement gives rise to an electrical or cell potential. Nernst first developed an equation relating the chemical energy and electrical potential of a galvanic or electrolytic cell.[6] The Gibbs Energy of a system has also been defined as the negative value of the maximum available work, *W*. In a redox reaction, the energy released results in a potential difference; the maximum potential difference is termed the electromotive force (EMF). Maximum work is the product of the electromotive force (ΔE) and the charge.

Equation 8
$$W = -\Delta G = q\Delta E = nF\Delta E$$

Where q is the charge in coulombs and F is Faraday's constant (96485 C/equiv). Substituting Equation 8 into Equation 7 results in

Equation 9
$$-nF\Delta E = -nF\Delta E^o + RT \ln \frac{P_C^c P_D^d}{P_A^a P_B^b}$$

Equation 9 can be reduced to the form of the Nernst Equation that we are most familiar with

Equation 10
$$\Delta E = \Delta E^o - \frac{RT}{nF} \ln \frac{P_C^c P_D^d}{P_A^a P_B^b}$$

For a fuel cell operating on hydrogen as the fuel and oxygen as the oxidant, the overall electrochemical reaction is

Reaction 10
$$2H_2 + O_2 \longrightarrow 2H_2O$$

The Nernst equation, rearranged into its conventional form, is therefore

Equation 11

$$\Delta E = \Delta E^{o} + \frac{RT}{nF} \ln \frac{P_{H_2}^2 P_{O_2}}{P_{H_2O}^2}$$

The efficiency of fuel cells is much higher than those of combustion engines because they aren't governed by the Carnot Cycle.[1,20,21] Instead, fuel cell efficiency, ε, is directly related to the thermodynamics of the system.

Equation 12

$$\varepsilon = \frac{\Delta G}{\Delta H} = 1 - \frac{T\Delta S}{\Delta H}$$

For common fuels such as hydrogen, carbon monoxide and other hydrocarbons, $\varepsilon < 1$, because they have both negative enthalpy and entropy values. Fuels with positive entropy values however could theoretically result in efficiencies ≥ 1.[1]

II. SOLID OXIDE FUEL CELLS

Solid oxide fuel cells (SOFCs) are solid-state electrochemical devices that convert chemical energy directly to electrical energy. For the most part, SOFCs are entirely ceramic-based systems, which operate in the temperature range of 450-1000ºC.[1,1722] SOFC operation is based on oxygen reduction at the cathode, followed by the vacancy transport of oxygen ions through a solid electrolyte to the anode, where the oxygen ions combine with the protons of oxidized hydrogen to form water and electricity.[23] An SOFC schematic is given in Figure 3.

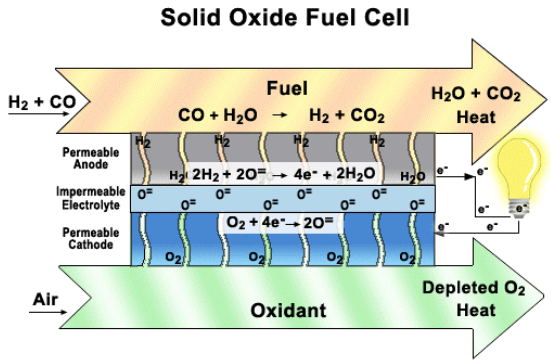

Figure 3. Schematic of SOFC including half-cell and overall electrochemical reactions.[24]

The high operating temperature of SOFCs holds some advantages compared to other fuel cell technologies such as fuel versatility, internal fuel reforming (T>650ºC), no need for water or thermal management, and the highest power density of any system. Unlike any other fuel cell system, SOFCs can operate on hydrocarbons (e.g. propane, butane, heptane, decane, dodecane..etc), logistic fuels (e.g. JP-3, JP-8), commercial fuels (e.g. octane, diesel, biodiesel) and syngas as well as pure hydrogen.[25,26,27,28,29,30,31] There are some materials related issues with operating on many of these fuels, for instance coking or the deposition of carbonaceous material at the anode and sulphur poisoning also at the

anode. These involve the high temperature reactions between Ni-based oxidation catalysts and corrosive impurities present in the fuel. Much research is being conducted to develop novel anode materials that don't suffer from performance degradation in 'dirty' fuels as well as to understand the mechanism of catalyst degradation and its long-term effects on performance.[32,33,34,35]

Water management isn't an issue because water exists only in the vapor phase and has no effect on the conductivity of any component of the cell. Water is used to humidify the fuel stream of SOFCs because it's well known that dry hydrogen oxidizes with a large overpotential, whereas humidified hydrogen oxidizes at significantly less overpotential.[36,37] Water vapor is also useful when hydrocarbon fuels are present for steam reforming, completion of the water-gas shift reaction and steam cleaning of carbonaceous deposits from the anode surface.[38,39,40] The steam reforming and water gas shift reactions are given in Reaction 11 and Reaction 12, respectively.

Reaction 11 $CH_4 + H_2O \longrightarrow CO + 3H_2$

Reaction 12 $CO + H_2O \longrightarrow CO_2 + H_2$

Materials stability and thermal mismatch between components are two of the biggest issues plaguing SOFCs. The materials issues begin with the interconnect material, which is either a doped lanthanum chromate ceramic (T>750ºC) or a stainless steel (T<750ºC).[41,42,43] Both the ceramic and metallic interconnect compositions contain chromium, which is present for oxidation resistance, but also changes its valence state, sublimates, diffuses to the cathode and forms a resistive contaminant layer.[44,45] Metallic interconnect compositions also corrode when fuel gases other than pure hydrogen are used. Carburisation is the most common contaminant on the anode side of the interconnect, as hydrocarbon fuels flow through the chamber and aren't completely utilized.[46,47] The ions from sealant materials such as glass and metallic compositions have been found to react with both the interconnect and electrolyte causing secondary

phase formation, cracking and/or delamination.[48,49,50,51] Delamination occurs due to thermal expansion mismatch between SOFC components, especially between the ceramic layers and metallic interconnects. Though there are some metallic compositions with an equivalent high temperature thermal expansion coefficient (CTE), there aren't any compositions with room temperature to operating temperature CTE profile matching the ceramic components of the cell.[52]

2.1 SOFC Components

Solid oxide fuel cells consist of four basic active components: electrolyte, anode, cathode, and interconnect. The electrolyte conducts a gas phase ionic species, either oxygen ions or protons, between the anode and cathode to produce water and complete the electrochemical reaction. Currently, 8-mole % yittria-stabilized zirconia, $8Y_2O_3$-$92ZrO_2$ (YSZ) is the most common SOFC electrolyte due to its low cost and sufficient conductivity, however other doped-zirconia and ceria compounds (e.g. Sc_2O_3-ZrO_2, Gd_2O_3-CeO_2, Sm_2O_3-CeO_2) have been studied. Oxygen ions are created through the electrochemical reduction of oxygen (typically from air) at the cathode and protons are created by the oxidation of hydrogen (typically pure hydrogen or from hydrocarbons) at the anode. Cathode materials currently used with YSZ are strontium doped lanthanum-based perovskites, where the B-site cation is either manganese or cobalt (e.g. $La_{0.85}Sr_{0.15}MnO_3$, $La_{0.6}Sr_{0.4}CoO_3$, $La_{0.6}Sr_{0.4}Co_{0.8}Fe_{0.2}O_3$). The anode is a composite electrode made up of the electrolyte material (YSZ) and a catalytically active metal such as nickel. Usually termed a 'cermet' electrode, for ceramic-metallic electrode, the anode also must contain a good deal of porosity.

2.1.1 Electrolyte

The main purpose of an electrolyte in any type of fuel cell is to conduct a specific ion between two electrodes in order to complete the overall electrochemical reaction and

form byproduct water. Without conduction of that specific ion, no appreciable current would be able to flow through the fuel cell and only potential would exist. In the case of SOFCs, the electrolyte conducts oxygen ions (O^{2-}) produced at the cathode through oxygen reduction, to the anode where it combines with protons (H^{+}) to form water, as shown in Figure 3. Ionic conduction isn't the only requirement that electrolyte materials must follow, electrolyte materials also must be electrically insulating, gas impermeable, microstructurally dense and inert to simultaneous highly oxidizing and reducing atmospheres. This set of criteria leaves only extremely stable, oxygen ion or proton conducting ceramics (please note that this author lumps glass materials, which at the time this was written were being researched for low-temperature electrolytes, into the ceramic family.) as viable electrolyte materials.

The vast majority of SOFCs operate with oxygen ion conducting ceramics, however some recent SOFCs have also used proton-conducting ceramics derived from the family of barium cerate materials.[53] The problem with using proton-conducting ceramics is the formation of water at the cathode, which leads to many materials related issues. In that light, a suitable cathode material has yet to be developed. Traditional oxide ceramics, such as ZrO_2, are chemically stable in oxidizing and reducing environments (down to ~10^{-26}atm oxygen partial pressure). Zirconia, however undergoes a series of phase transformations from room temperature to 2400ºC and therefore must be stabilized so as not to significantly change its molar volume, physical and chemical properties during SOFC start-up and operation. The room temperature phase of ZrO_2 is monoclinic, which changes to tetragonal at 1170ºC and undergoes 3 to 5 volume % shrinkage. The tetragonal phase is stable up to 2370ºC, at which point it transforms to the cubic phase and remains stable up to the melting point of 2680ºC.[1] A summary of the zirconia polymorphs from room temperature to the melting point is given in Reaction 13.[54]

Reaction 13 $$Monoclinic \xrightarrow{1170} Tetragonal \xrightarrow{2370} Cubic \xrightarrow{2680} Liquid$$

A visual unit cell reaction summary is also given in Figure 4.[55,56]

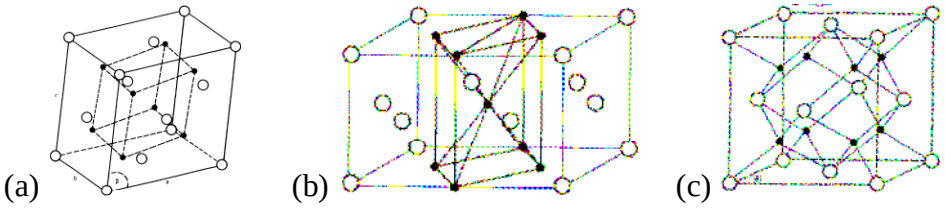

Figure 4. (a) Monoclinic unit cell of ZrO_2, which transforms at 1170ºC to (b) Tetragonal unit cell of ZrO_2. At 2370ºC, the tetragonal structure transforms to (c) the cubic fluorite phase of zirconia, which is stable up to the 2680ºC melting point. (○) Oxygen (●) Zirconium.

The associated lattice constants, unit cell volumes and angles of the zirconia polymorphs shown in Reaction 13 and Figure 4 are given in
Table 1.

Table 1. Lattice parameters, unit cell volumes, and unit cell angles associated with zirconia polymorphs.[57,58]

Phase	Stable Temperature Range (ºC)	Lattice Parameter (nm) a	b	c	B	Unit Cell Volume (nm^3)	Reference
Monoclinic	R.T - 1170C	0.5147	0.5206	0.5135	80.77	$1.358*10^2$	57
Tetragonal	1170C-2370C	0.5082	-	0.5185	-	$1.3391*10^2$	57
Cubic	2370C-2680C	0.5113	-	-	-	$1.3367*10^2$	58

Aliovalent doping can stabilize any one of the phases from room temperature to the melting point, making doped-zirconia a very useful and stable high temperature ceramic.[1,23] Common oxide dopants include CaO, MgO, Y_2O_3, and Sc_2O_3, which easily form solid solutions with ZrO_2 at levels from roughly 0-20 mole %. Zirconia doped with 3-mole % Y_2O_3 leads to what is termed 'partial stabilization' (PSZ) or rather the stabilization of the tetragonal phase. Increased Y_2O_3 doping to levels from 8-15 mole % stabilizes the cubic phase down to room temperature and is termed 'fully stabilized' zirconia. The ZrO_2-$Y2O_3$ phase diagram is given in Figure 5.[59]

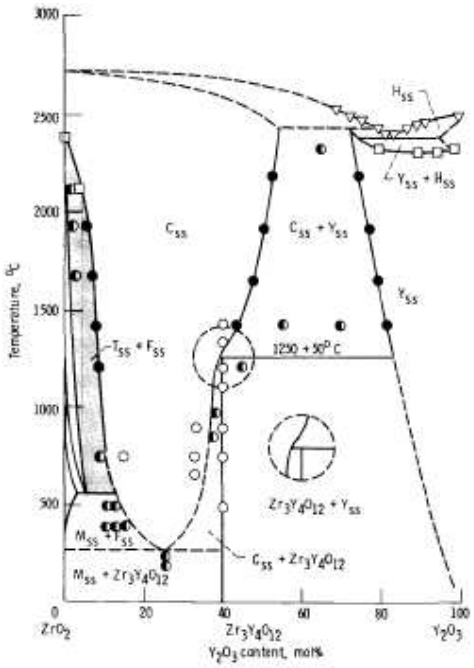

Figure 5. ZrO_2-Y_2O_3 phase diagram.[59]

The addition of dopants also brings about an associated defect structure, forming the basis for oxygen ion conduction. Oxygen ions are conducted through oxygen vacancies, which form through divalent and trivalent metal oxide doping on the zirconium site. An example of oxygen vacancy formation in ZrO_2 due to Y_2O_3 addition is given in Reaction 14, using Kroger-Vink notation.[60]

Reaction 14 $$Y_2O_3 \xrightarrow{ZrO_2} 2Y_{Zr}^{'} + V_O^{\bullet\bullet} + 3O_O^x$$

The Kroger-Vink notation denotes the effective charge associated with defects formed by addition of one compound, which is soluble in another. Reaction 14 can be read as: addition of one mole yittria to one mole zirconia results in yttrium taking the place of zirconium with an associated negative charge (since yttrium has a 3^+ oxidation state and zirconium a 4^+ oxidation state, replacing a zirconium with a yttrium effectively gives that site a negative charge). To compensate for the negative charge due to cation substitution, oxygen vacancies form on the anion site or rather oxygen is given up from the lattice

resulting in a vacant site with an effective double positive charge. As in all substitutionary reactions, the charge, site and mass balance rules of electroneutrality must be followed. Therefore every mole of yittria added to zirconia forms two moles of cation substitution and one mole of oxygen vacancy. When vacancy-substitution pair defects form in a crystal, the point defect is termed a 'Schottky' defect, as opposed to 'Frenkel' defects, which are vacancy-interstitial pair defects.

The oxygen deficiency of the stabilized cubic fluorite structure leads to an associated conductivity of oxygen vacancies. Increased metal oxide addition will increase the resultant bulk conductivity of YSZ, as seen in Figure 6.

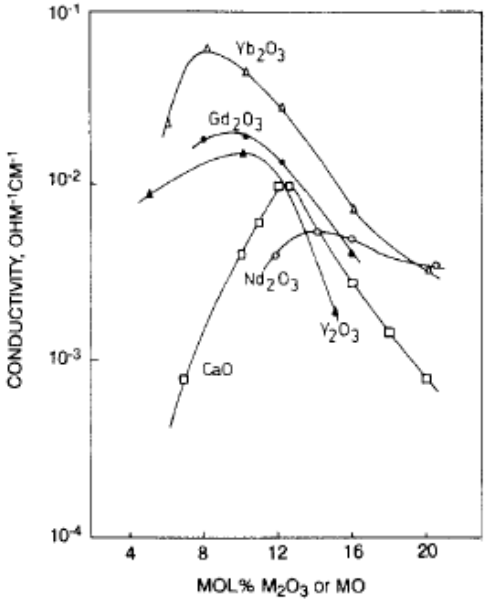

Figure 6. Change in conductivity ZrO_2 as a function of metal oxide addition.[2]

YSZ is not the only electrolyte material being investigated for SOFCs. Other materials such as rare earth oxide doped-ceria's and lanthanum gallate's have higher ionic conductivities than YSZ, however are also of higher cost and have experienced some reactionary and phase stability issues. A comparison of the conductivities of some candidate electrolyte materials is given in Figure 7.

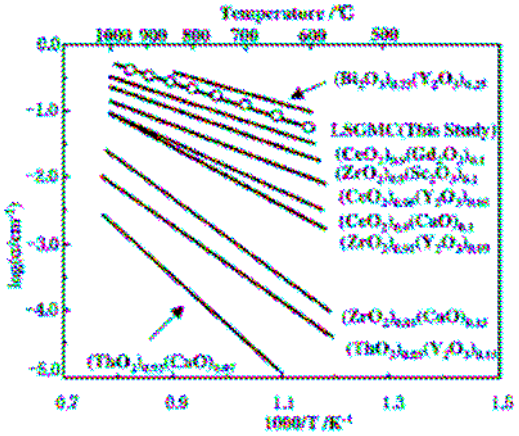

Figure 7. Conductivity of candidate SOFC electrolyte materials.[61]

Thermal expansion of these electrolyte materials is also very important. Table 2 lists the average thermal expansion coefficient (CTE) for candidate SOFC electrolyte materials from 25-800ºC and 25-1000ºC. Since the CTE of the electrolyte material is harder to change without also altering its physical properties, most other SOFC components are chosen and/or designed to match the expansion of the electrolyte.

Table 2. Thermal expansion coefficients for candidate SOFC electrolyte materials.[62,63,64,65,66,67]

Material	$\alpha*10^{-6}\ K^{-1}$ (25-800ºC)	$\alpha*10^{-6}\ K^{-1}$ (25-1000ºC)	Reference
$Y_{0.15}Zr_{0.85}O_{1.93}$	10.5	10.9	62,63
$Y_{0.18}Zr_{0.82}O_{1.91}$	10.6	11	63
$Sc_{0.15}Zr_{0.85}O_{1.93}$	10.3	10.4	64
$Sc_{0.18}Al_{0.02}Zr_{0.8}O_{1.9}$	10.5	10.9	63
$Gd_{0.2}Ce_{0.8}O_{1.9}$	12.5	12.7	63
$Sr_{0.1}Ce_{0.9}O_{1.9}$	12.8	13.1	63
$La_{0.8}Sr_{0.2}Ga_{0.9}Mg_{0.1}O_{3-x}$	10.4	10.8	65
$La_{0.8}Sr_{0.2}Ga_{0.8}Mg_{0.2}O_{3-x}$	10.5	11.3	66
$La_{0.9}Sr_{0.1}Ga_{0.75}Mg_{0.2}Co_{0.05}O_{3-x}$	10.9	11.4	65
$La_{0.9}Sr_{0.1}Ga_{0.8}Mg_{0.2}O_{3-x}$	12.3	13	67

2.1.2 Anode

The function of an SOFC anode is to electrochemically oxidize hydrogen contained within the fuel. The protons formed during oxidation also combine with oxygen ions, conducted through the electrolyte from the cathode, to form byproduct water vapor in the anode chamber as shown in Reaction 15.

Reaction 15 $$2H_2 + 2O^{2-} \longrightarrow 2H_2O + 4e^-$$

The requirements for SOFC anodes are stability in reducing atmospheres, catalytic activity to hydrogen oxidation, high electronic and ionic conductivity, and chemical and physical compatibility with surrounding components. Stability and compatibility of the anode applies to both chemical and dimensional/phase changes, which could occur due to interactions with other SOFC components, the highly reducing atmosphere, the byproduct water vapor and/or the 450-1000ºC operating temperatures.[1,2]

In order to perform its proper electrochemical functions, the anode must be able to transport oxygen ions to the active oxidation sites as well as product electrons away from the active sites. Since there are no adequate mixed-conducting materials available to perform both functions, ceramic-metallic or 'cermet' composites of electronic and ionic conducting materials are used. Typically the electronic conducting phase is a catalytically active metal such as nickel and the ionic conducting phase is the same material as the electrolyte. Usage of the electrolyte material in the anode also ensures that the thermal expansion coefficient of the composite electrode is close to that of the electrolyte. Figure 8 shows the CTE of a Ni-YSZ composite anode as a function of Ni content.

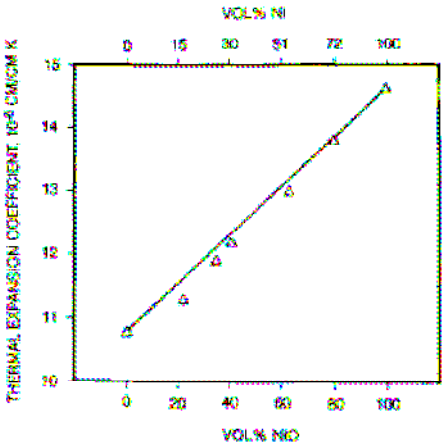

Figure 8. Thermal expansion coefficient of NiO-YSZ cermet anodes as a function of Ni or NiO addition.[2]

Due to processing and sintering difficulties associated with fabricating Ni and YSZ together, the metallic phase is usually added as an oxide (i.e. NiO) and then reduced *in situ*. Porosity is engineered into the structure through addition of pore forming agents to the ceramic-metallic composite as well as the increased volume associated with the reduction of NiO to Ni. The function of the porous phase in the anode is to allow for fuel flow, increased oxidation and elimination of mass transport overpotential. The amount of porosity formed due to reduction of NiO to Ni is shown in Figure 9.

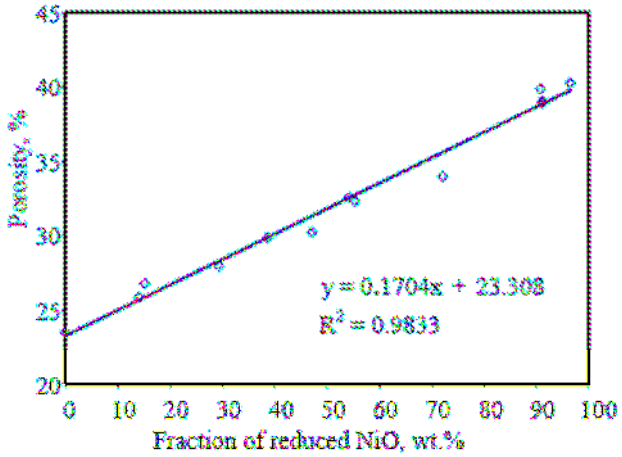

Figure 9. Overall porosity of reduced NiO-YSZ cermet as a function of the fraction NiO reduced.[68]

Percolation theory relates the volume fraction of each component within a composite to the connectivity of those phases. As a rough estimate, for three phases to achieve connectivity within a composite, each should be 33 volume %. The content of anode cermets is traditionally aimed at achieving percolation between the metallic, ionic and porous phases, thus each phase should account for about 33% of the anode structure. Figure 10 shows the physical result of percolation theory as it applies to the conductivity of anode cermets.

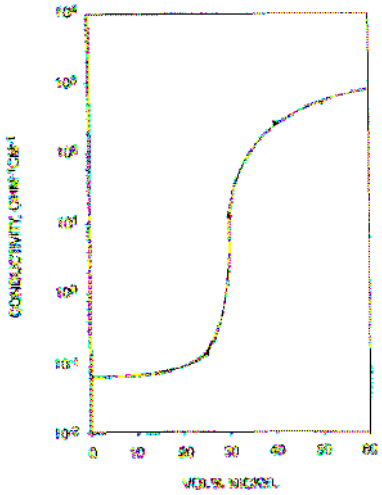

Figure 10. Conductivity of Ni-YSZ anode cermet at 1000°C as a function of Ni content.[2]

Anode cermets are made out of more materials than just Ni and YSZ. Alternative electrolyte materials such as doped-ceria and lanthanum gallate compounds can be substituted as the ionic conducting phase.[69,70,71] Metallic phases such as Co, Ru, Cu and alloys of these metals with each other and with Ni have been studied and modeled in order to improve anode performance when hydrocarbon and sulfur-containing fuels are used.[32,35,72,73,74,75] Stability and performance in hydrocarbon and especially sulfur-containing fuels is the single biggest challenge facing anode development.[76,77] There have been considerable efforts to understand the mechanism of anode poisoning and to improve the design of anodes, such that SOFC performance doesn't significantly degrade

when carbon and sulfur are present within the fuel stream.[78,79,80] The reaction of carbon with SOFC anodes is similar to that given in Reaction 11, which can be accounted for through the addition of steam as in Reaction 12. A proposed mechanism of sulfur poisoning is given in Reaction 16.

Reaction 16 $$xNi + yH_2S \longrightarrow Ni_xS_y + 2H^+$$

Until a suitable material exists that can effectively oxidize hydrogen from carbon and sulfur-containing fuels without long-term degradation, pure hydrogen or low molecular weight hydrocarbons (i.e. methane to propane) will have to be used.

2.1.3 Cathode

The cathode in SOFCs is responsible for the electrochemical reduction of oxygen from O_2 to O^{2-} as shown in Reaction 17.

Reaction 17 $$O_2 + 4e^- \longrightarrow 2O^{2-}$$

The oxygen ions formed by reduction then are incorporated into the electrolyte, through oxygen vacancies, and conducted to the anode. In order to function properly, SOFC cathode materials must be catalytically active to oxygen reduction, chemically and physically stable, compatible with the electrolyte, possess sufficient electronic conductivity and contain some porosity. Cathode compatibility refers to preventing high temperature reactionary phases to form at the cathode-electrolyte and cathode-interconnect interfaces, ensuring thermal expansion matching over the entire SOFC operating range as well as the rapid incorporation of oxygen ions into vacancies within the electrolyte. In addition to being an electronic conductor, performance and activation overpotential can be significantly improved if the cathode is also an ionic conductor.[81,82,83]

Since the cathode is constantly in an oxidizing atmosphere, the electrode materials are mostly oxide-based, which typically aren't known for high electronic conductivities. $LaMnO_3$ has intrinsic p-type conductivity due to cation vacancy formation at high

temperatures in oxidizing atmospheres. The electrical conductivity can be increased by doping $LaMnO_3$ with lower valency cations such as strontium and calcium, which increases the content of Mn^{4+} in place of Mn^{3+} according to Reaction 18.[2]

Reaction 18 $$SrO \xrightarrow{LaMnO_3} La_{1-x}Sr_xMn^{3+}_{1-x}Mn^{4+}_xO_3$$

Therefore the most common cathode materials for oxygen reduction are perovskite-based doped transition metal oxides (e.g. $La_xSr_{1-x}MnO_{3+\delta}$, $La_xSr_{1-x}CoO_{3+\delta}$).[84] The total conductivity as a function of strontium dopant level is shown in Figure 11.

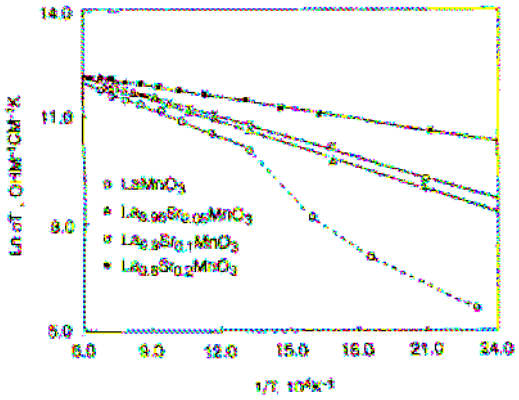

Figure 11. Total conductivity of $La_{1-x}Sr_xMnO_3$ cathode as a function of Sr content.[2]

The average thermal expansion coefficient of $LaMnO_3$ is $11.2*10^{-6}$ $^oC^{-1}$ from room temperature to 1100^{o}C and increases with Sr content.[2,85] A summary of thermal expansion coefficients of common perovskites-based oxide cathodes is given in Table 3.

Table 3. Thermal expansion coefficients for some common SOFC cathode materials.[86,87,88,89,67,90,91,92,93]

Material	α*10^{-6} K^{-1} (25-800ºC)	α*10^{-6} K^{-1} (25-1000ºC)	Reference
$La_{0.8}Sr_{0.2}MnO_{3-x}$	13.1	-	86
$La_{0.79}Sr_{0.2}MnO_{3-x}$	10.8	11.1	87
$La_{0.79}Sr_{0.2}MnO_{3-x}$	-	12.4	88
$La_{0.69}Sr_{0.3}MnO_{3-x}$	11.7	12	87
$La_{0.69}Sr_{0.3}MnO_{3-x}$	-	12.8	88
$La_{0.65}Sr_{0.3}MnO_{3-x}$	12	12.3	67
$La_{0.8}Sr_{0.2}Mn_{0.8}Co_{0.2}0_{3-x}$	14.1	-	86
$La_{0.65}Sr_{0.3}Mn_{0.8}Co_{0.2}0_{3-x}$	11.6	11.7	67
$Pr_{0.8}Sr_{0.2}MnO_{3-x}$	9.5	10.1	89
$Pr_{0.7}Sr_{0.3}MnO_{3-x}$	11.1	-	90
$Pr_{0.65}Sr_{0.3}MnO_{3-x}$	11	11.6	67
$Pr_{0.8}Sr_{0.2}Mn_{0.8}Co_{0.2}0_{3-x}$	9.6	10.3	89
$Pr_{0.8}Sr_{0.2}Mn_{0.8}Co_{0.2}0_{3-x}$	10.2	10.9	67
$Pr_{0.7}Sr_{0.3}Mn_{0.8}Co_{0.2}0_{3-x}$	10.5	11.1	67
$Nd_{0.7}Sr_{0.3}MnO_{3-x}$	10.8	-	91
$Nd_{0.65}Sr_{0.3}MnO_{3-x}$	9.3	9.7	67
$Nd_{0.65}Sr_{0.3}Mn_{0.8}Co_{0.2}0_{3-x}$	10.4	10.8	67
$Gd_{0.8}Sr_{0.2}MnO_{3-x}$	2.3	3.8	92
$Gd_{0.8}Sr_{0.2}Mn_{0.8}Co_{0.2}0_{3-x}$	8.2	10.2	92
$Gd_{0.65}Sr_{0.3}MnO_{3-x}$	9.7	9.9	67
$Gd_{0.65}Sr_{0.3}Mn_{0.8}Co_{0.2}0_{3-x}$	10.4	10.6	67
$La_{0.7}Sr_{0.3}CoO_{3-x}$	17.5	19.2	65
$Pr_{0.7}Sr_{0.3}CoO_{3-x}$	18.8	-	93

An analytical expression correlating cathode ionic conductivity with the thermal expansion coefficient was determined by Ullmann et al. and is given in Equation 13.

Equation 13 $$Log\sigma_o = -7.08 + 2.9 * 10^5 CTE$$

Figure 12 shows the relation between the CTE of common SOFC cathode materials and their oxygen ion conductivity.

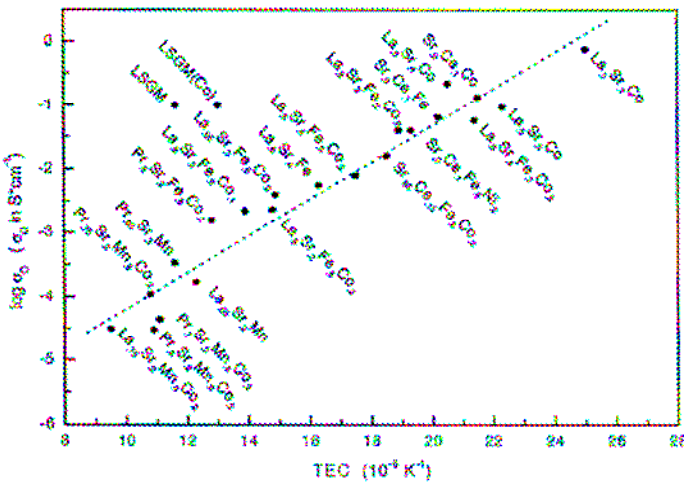

Figure 12. Relation between the CTE and oxygen ion conductivity of common SOFC cathode materials.

2.1.4 Interconnect

SOFC interconnect materials act as current collectors and carriers between the anode and cathode of adjacent cells in a stack.[41,42,43] They also act as a gas separation membrane between two adjacent cells, ensuring that oxidant and fuel mixing does not occur. Similar to SOFC electrolytes, interconnect materials must remain chemically and dimensionally stable in a dual oxidizing-reducing environment. Where SOFC electrolytes must remain ionically conductive and electronically insulating during operation, the interconnect must possess the opposite properties. Interconnect materials must remain electronically conductive and ionically inert during SOFC operation. SOFC stack engineering, materials and fabrication costs are still significant hindrances to production of these devices. Though SOFCs operating at temperatures above 750°C are currently performing better, they also cost almost 8x more than those operating below that temperature. Currently the reason for this is the cost of ceramic interconnects that can withstand those operating temperatures. At over $200 per kW, ceramic interconnect materials alone account for 90% of the total material costs for high temperature SOFCs.

Lowering the operating temperature into a range where metallic interconnects can be used reduces the interconnect materials cost by 200% to $10 per kW. Table 4 shows a comparison of the relative cost per kW for SOFCs using metallic or ceramic interconnect materials.

Table 4. Relative cost per kW of SOFC materials in a stack with metallic-based interconnects and with ceramic-based interconnects.[1]

SOFC Component	Material cost for ceramic-based SOFC ($/kW)	Percent of Total Cost (%)	Material cost for Metallic-based SOFC ($/kW)	Percent of Total Cost (%)
Electrode Stack	22.6	9.875	22.6	69.325
Interconnects	206.25	90.125	10	30.675
Total	228.85		32.6	

The interconnect composition used for SOFCs is dependent on the application and temperature range. The composition determines the physical properties of the alloy and further the temperature range at which the thermal properties mirror those of the electrolyte. Ferritic-based alloys involving nickel and often chromium have the ability to serve as SOFC interconnects at intermediate operating temperatures. Potential stainless steel compositions are shown in the phase diagram in Figure 13.

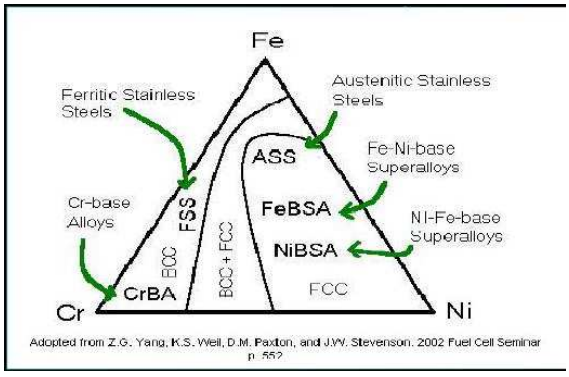

Figure 13. Fe-Ni-Cr phase diagram.

Though these materials have high conductivity and mechanical strength, their operating temperature range is limited by many factors such as oxidation, phase transitions, creep and curie temperatures.[47] Optimal compositions of iron, nickel and chrome have been determined, but vary greatly depending on the operating temperature range, thermal cycling frequency, and electrolyte material used.[97] Since no single alloy has thermal expansion characteristics identical to YSZ from room temperature to SOFC operating temperatures, an alloy has to be picked specially for the application.[98] Therefore a different alloy would be used for a long-term continuous stationary application than would be used for an auxiliary power unit (APU) that cycles as needed. Longetivity for stationary applications has been predicted to be from 40,000-80,000 hrs and therefore degradation and aging mechanisms must be reduced considerably.[94]

Doping of the interconnect material with rare earth oxides has shown to increase lifetime by drastically reducing the oxidation rate, while having a negligible effect on the thermal properties.[97] In order to improve the oxidation resistance a multitude of rare-earth ions such as Y, Zr, La, Ce, Sm, Ta, and W have been doped into the alloy compositions.[41,42]

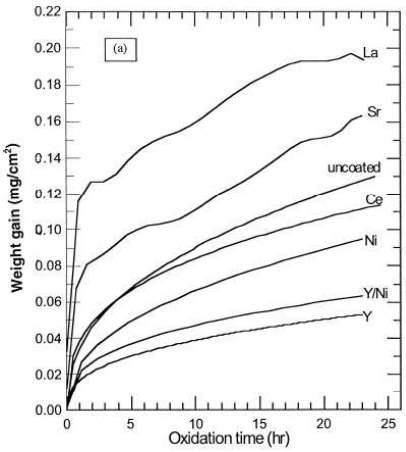

Figure 14. Weight gain of various doped interconnect alloys showing that addition of Y_2O_3 results in increased oxidation resistance.[95]

Chromia scale as well as other oxide formations due to these dopant ions has also been determined, mostly under oxidizing conditions. However this is only relevant at the cathode, where the interconnect material is exposed to oxidizing atmosphere. The chromia scale formed between the interconnect and cathode also leads to chromia poisoning due to vapor phase transport as given by Reaction 19.[96]

Reaction 19 $$Cr_2O_3 + 1.5O_2 + 2H_2O \longrightarrow 2CrO_2(OH)_2$$

At the anode side of the SOFC, the interconnect could encounter any number of different reducing gases from syngas to heavy sulfur-containing fuels. Therefore the interface would also be influenced by any reactions due to deposition and subsequent degradation at the anode side.[46,47,48] Deposition, particularly of sulfur and carbon, is incredibly suffocating to the anode stream of the SOFC. New phases, such as sulfur dioxide, resulting from interactions of the metallic alloy and sulfur or carbon containing fuels could potentially have drastically different physical properties than those of the parent metal and ruin the interface.[33,34] Typically the interconnect material is placed in a single atmosphere, whether it be oxidizing or reducing, and characterized.

Ferritic-based alloys involving nickel and often chromium have the ability to serve as SOFC interconnects at intermediate operating temperatures. Though these materials have high conductivity and mechanical strength, their operating temperature range is limited by many factors such as oxidation, phase transitions, creep and curie temperatures.[47] Optimal compositions of iron, nickel and chrome have been determined, but vary greatly depending on the operating temperature range, thermal cycling frequency, and electrolyte material used.[52,97] Since no single alloy has thermal expansion characteristics identical to YSZ from room temperature to SOFC operating temperatures, an alloy has to be picked specifically for the application, as shown in Table 5.[98]

Table 5. Thermal Expansion Coefficients of some SOFC interconnect materials.

Material	$\alpha*10^{-6} K^{-1}$ (25-800ºC)	$A*10^{-6} K^{-1}$ (25-1000ºC)	Reference
$Cr Fe_5 Y_2 0_3$	-	11.3	83
$Cr Fe_5 Y_2 0_3$	11.3	12	65
X 10 CrAl 18 (1.4742)	12.9	13.9	65
$La_{0.9}Sr_{0.1}CrO_3$	-	10.7	2
$La_{0.79}Sr_{0.2}CrO_3$	-	11.1	88
$La_{0.7}Ca_{0.3}Cr_{0.5}Ti_{0.5}0_3$	9.6	10.1	67
$La_{0.7}Sr_{0.3}Cr_{0.8}Ti_{0.2}0_3$	10.4	10.7	67

2.1.5 Sealant

One of the major problems facing the advancement of SOFC technology is sealing between cells in a stack.[99,100] Typical glass and ceramic seals can form reactive phases, leak and/or degrade over time, decreasing SOFC performance.[101,102,103] Recent work addressing the issue of SOFC sealant materials has improved, but not solved the problems facing them.[99,100] Hard seals such as those achieved using glass sealant materials are rigid and readily prevent gas mixing, but degrade over time due to atmospheric conditions.[103,104,105] The seal itself is manifested from chemical bonding of the sealant material with the individual cells forming a single structure. Degradation can be due to ionic diffusion leading to secondary phase formation as the glass reacts with the SOFC materials or can be due to reactions with the oxidizing and reducing atmospheres causing leaks.[101-104] Glass seals also have difficulty relaxing to the thermal stresses of cycling and often crack the materials in which they are in contact. Soft or compressive sealant materials such as various mica compositions and ceramic fiber seals have also been examined. Compliant sealing such as with mica or metallic gaskets requires the use of external pressure to facilitate the seal. These materials leak more than the rigid glass materials, but show better thermal cycling characteristics. In fact soft seals aren't

actually seals, but rather permeation resistors aimed to reduce leakage rates rather than eliminate them.

Soft seal is the name given to seals made which do not chemically bond to either the ceramic or metallic plate, but instead rely on an externally applied compressive force to deform a soft, compliant material to create a gas tight seal. Most research in this area involves a metallic gasket formed within or welded to the metallic interconnect. This metallic gasket consists of one or more thin deformable contours that will under pressure mate hermetically to the ceramic plate. The advantage to these seals is that since they do not bond the layers, they are free to expand differentially without building up stress during thermal cycling. Another advantage to these soft sealing systems is their ability to be readily disassembled.

Another type of soft seal based on ceramic materials is the application of mica as a gasket material.[106] Mica, a mineral composed of layers of thin plates, is suitable for high temperatures and has the ability to deform and compress due to the natural gaps between the plates. In both the case of mica and with the metallic compression seals, many problems have been encountered. In each case, the quality of the seal is a reflection on the flatness and smoothness of the surfaces to be mated. Minor defects in the ceramic fuel cell or the interconnect can eliminate the possibility of ever attaining a complete seal. It is also interesting to note, that those researchers working in this field discuss the actual permeation rate through the seals indicating that they are seeking a low number that would be acceptable and not able to consider zero permeation as an answer.

Furthermore, gasket type soft seals require external pressure to produce the seal. This requires that the stack be placed in a high strength frame capable of evenly applying pressure through thermal cycling.[106] The pressure on any unit length of seal will dictate its ability to be gas tight. As cell sizes and number of cells in the stack increase, the required pressure also increases, often beyond reasonable levels, and whereas duplicate and wider gaskets will produce seals with lower leaks and higher reliability, this similarly

increases the required pressure. Many leaks for these cells can also be blamed on the added rigidity induced near the corners of the gaskets where the change in geometry adds stiffness and diminishes the seals' ability to conform.

One other method of producing a soft seal is to use a glass or metal material, which will not react with either the cell or interconnect and flow to fill the space at the operating temperature of the fuel cell. These seals are typically short lived given that they continue to flow for the life of the cell and cannot be used in the case of pressurized systems. These systems can be based on either a load frame to encourage material filling or simply by the design of suitable wetting in the materials to allow surface tension to drive the sealing process. The overall prospects for soft sealing systems appear that it will be limited to laboratory scale systems for the meantime.[107]

Hard seals are produced either through glass, glass-ceramics or metallic brazing.[108,109,110] These systems were initially developed as sealing techniques for single cells to produce gas tight fittings in laboratories or for cells sealed to a ceramic interconnect as in previous higher temperature fuel cells. With the hard seals, a bonding material is heated to the point at which it will flow and react with the adjacent materials to form a chemical bond. This process is similar to the seal at the base of a standard incandescent light bulb. During the process, the bond phase goes beyond the glass transition temperature to flow and fill gaps and irregularities. Some shrinkage will occur during this process.

Once up to process temperature, the glass material will react to some degree with the metallic and ceramic plates. In this case, the reaction zone will create a transitional bonding region where the chemistry may be modified by the reaction products. Most of the reactive glass bonding materials are actually pyro-ceramics, which are essentially recrystallizing glass compositions. These compositions flow like glass initially to fill voids and when held at an appropriate temperature for a suitable period of time will

precipitate a ceramic crystalline phase within the glass matrix adding substantial rigidity to the system.

The bond formed by the glass-ceramic is a rigid bond and will transfer stress throughout the cell stack. For this reason, thermal expansion match of the ceramic cell, interconnect and bonding layer must be extremely well matched.[111] Stress concentrations due to thermal mismatch may be particularly concentrated within the bonding layer. Under-reactivity or over-reactivity with either the electrolyte ceramic or interconnect will create a weak bond destined to failure. Depending on the glass composition and heating schedule, the crystallization process can occur over relatively fast or extremely long periods of time. As the crystallization occurs, the properties of the seal change dramatically, especially the thermal expansion. In some cases, the thermal expansion of the glass-ceramic can change by 30 % over subsequent heating and cooling cycles. In spite of their difficulties, hard seals are generally seen as a more viable route to commercialization.

Overall, the matching the thermal expansion of materials is one of the major keys to the success of bonding the planar stack components. Well match components may lead to limited stress and an attainable strength threshold within the bond layer, but the bond layer itself is prone to difficulties. Ceramics and metals are by nature difficult to bond and the requirements for this bond are extreme. The difference in bond type between ceramics and metals makes them inherently incompatible, only achieving bond through the formation of interlayers or reaction zones. Paradoxically, in some cases, these reaction zones develop new compositional ranges, which may poison cell components or be a source of porosity and leakage.[101] Glass, by its nature more readily bonds to oxide ceramics than to metals. Bonding to metals is achieved through a surface oxidation on the metal to form a mechanical bonding layer to the glass. The oxidation process on the metallic surface is like any oxide scale; if it grows too thick, it will flake away from the metal surface.

Though presently there is no universal sealing method, research to improve stack sealing has centered on glass, ceramic and glass-ceramic hybrid materials. Hybrid sealant materials developed at Pacific Northwest National Labs (PNNL) are the state of the art and have shown leakage rates as low as 0.01sccm/cm at 800°C for polycrystalline muscovite and phlogopite mica layers under $6.89*10^5$-$2.76*10^6$ Pa (100-400psi) compressive stresses.[112] Hybrid sealants using single crystal muscovite mica show leakage rates two orders of magnitude lower at compressive stresses of $1.72*10^5$-$6.89*10^5$ Pa (25-100psi).[112,113,114,115]

2.2 SOFC Fabrication Methods

SOFCs are typically fabricated by bulk ceramic processing methods such as tape casting, tape calendaring and screen-printing in conjunction with spray pyrolysis an/or magnetron sputtering, which are used to fabricate porous electrodes.[116] A list of major companies performing research on SOFCs and their preferred fabrication methods for both electrolyte- and anode-supported cells is given in Figure 16(a-b).

Company	Country	Component	Material	Production Process	Thickness (um)
Sulzer Hexis	CH	Electrolyte	YSZ	Tape Casting	NA
		Cathode	LSM	Screen Printing	NA
		Anode	NiYSZ	Screen Printing	NA
ECN/inDec	NL	Electrolyte	YSZ	Tape Casting	NA
		Cathode	LSM	Screen Printing	50
		Anode	NiYSZ	Screen Printing	NA
Fraunhofer Ges., IKTS	D	Electrolyte	YSZ	Tape Casting	150
		Cathode	LSM	Screen Printing	NA
		Anode	NiYSZ	Screen Printing	NA
CFCL	AUS	Electrolyte	8-, 3- YSZ	Tape Casting	100
		Cathode	LSM	Screen Printing	50-60
		Anode	NiYSZ	Screen Printing	50
SOFCo	USA	Electrolyte	YSZ, $(Ce,Sm)O_2$	Pressing	180, 300
		Cathode	LSC	Screen Printing	NA
		Anode	NiYSZ	Screen Printing	NA
Tokyo Gas	JP	Electrolyte	3YSZ	Tape Casting	50-100
		Cathode	LSM	Screen Printing	150
		Anode	NiYSZ, (Ce,Y)SZ	Screen Printing	30
Mitsui Eng. & Shipbuilding	JP	Electrolyte	8YSZ	Tape Casting	300
		Cathode	$(La,Sr)(Mn,Cr)O_3$	Painting	150
		Anode	NiYSZ	Painting	150

(a)

Figure 15. List of major SOFC companies performing research on (a) electrolyte-supported SOFCs and (b) anode-supported SOFCs along with their preferred materials, fabrication methods and component thicknesses.[116]

(b)

Company	Country	Component	Material	Production Process	Thickness (um)
Sulzer Hexis	CH	Anode	NiYSZ	Tape Casting	250-500
		Electrolyte	YSZ, (Ce,Y)O2	Reactive Magnetron Sputte	1, 5
		Cathode	LSCF	Screen Printing	NA
ECN/inDec	NL	Anode Substra	NiYSZ	Tape Casting	500-800
		Anode	NiYSZ	Screen Printing	3-7
		Electrolyte	YSZ	Screen Printing	7-10
		Cathode	LSM+YSZ	Screen Printing	NA
FZJ	D	Anode Substra	NiYSZ	Tape Casting	200-500
		Anode Substra	NiYSZ	Warm Pressing	1500
		Anode	NiYSZ	Vacuum Slip Casting	5-15
		Electrolyte	YSZ	Vacuum Slip Casting	5-30
		Electrolyte	YSZ	Reactive Magnetron Sputte	2-10
		Cathode	LSM+YSZ	Wet Powder Spraying	50
CFCL	AUS	Anode Substra	NiYSZ	Tape Casting	500-700
		Electrolyte	YSZ	Lamination and Sintering	10-30
		Electrolyte	YSZ	Reactive Magnetron Sputte	<16
		Cathode	LSM	Screen Printing	NA
Allied Signal	USA	Anode	NiYSZ	Tape Casting/Calendering	100
		Electrolyte	YSZ	Tape Calendering	5-10
		Cathode	Doped LM	Tape Calendering	NA
Riso	DK	Anode	NiYSZ	Tape Casting	200-300
		Electrolyte	YSZ	Wet Powder Spraying	10-25
		Cathode	LSM+YSZ	Screen Printing	50
Mitsui Eng. & Shipbuildi	JP	Anode	NiYSZ	NA	1000
		Electrolyte	8YSZ	NA	30
		Cathode	(La,Sr)(Mn,Cr)O3	NA	150
Global Thermoelectric	CAN	Anode	NiYSZ	Tape Casting	1000
		Electrolyte	YSZ	Vacuum Slip Casting	10
		Electrolyte	YSZ	Screen Printing	NA
		Cathode	LSM	Screen Printing	40

Figure 16 Continued. List of major SOFC companies performing research on (a) electrolyte-supported SOFCs and (b) anode-supported SOFCs along with their preferred materials, fabrication methods and component thicknesses.[116]

2.2.1 Tape Casting

Tape casting is a ceramic processing method used to fabricate bulk thick films.[117,118] The scalability and long standing success of the tape casting process makes it a legitimate technique for low cost manufacturing of many SOFC components such as electrolyte membranes, anode materials, interconnect layers and laminates thereof.[1,2,17,22] The process of tape casting involves the dispersion of powder in a solvent using a dispersant-binder-plasticizer combination to form a slurry, which is milled together to lower the viscosity. The slurry is then added to a hopper and pulled on a carrier film under a doctor blade of a given height in order to prepare the bulk thick film. The film is then dried in a chamber using flowing air (sometimes heated), where the solvent evaporates at a controlled rate until it's finally spooled up at the end. Schematics of the doctor blade assembly and tape casting process are shown in Figure 17(a-b).

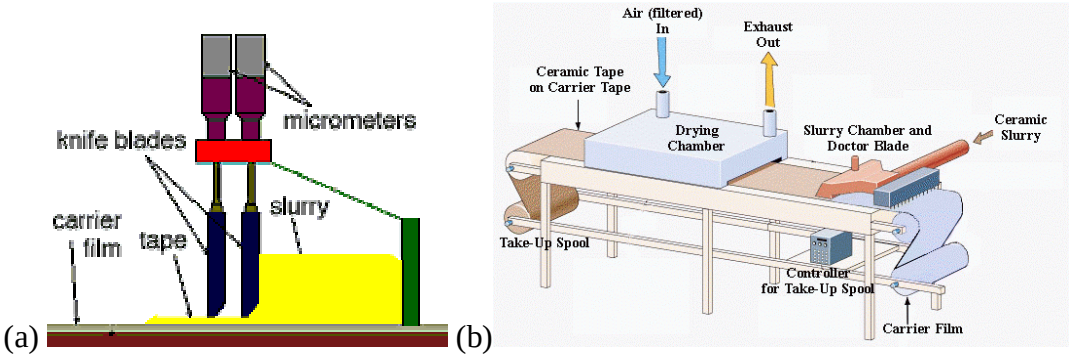

Figure 17. Schematic of (a) the casting process where the slurry is pulled under the doctor blade and (b) the entire tape caster including the drying chamber and carrier film take-up roll.

Glenn Howatt invented the process known today as tape casting while, during WWII, he had to find a replacement for mica as a capacitor material.[119] He then founded the first tape casting company, Glenco Corp. in Metuchen, NJ, to fabricate capacitors. Five years later, in 1952, he received the first patent on tape casting.[120] J.L. Park of American Lava Corp of Chattanooga, TN developed a continuous casting process to fabricate bulk thin sheets of ceramic and filed a patent, which was issued seven years later in 1961.[121] Research at RCA lead to the development of multilayer ceramics based on lamination of ceramics fabricated by tape casting, which also lead to co-sintering of ceramics and metals.[122,123] The capability to laminate thin sheets of ceramic layers revolutionized the circuits and packaging industries, as RCA, IBM and Western Electric Co. were interested in computer applications.[124,125] R.E. Mistler, D.J. Shanefield and R.B. Runk then wrote the first definitive publication on the tape casting process, after learning from H. Stetson, in 1978, after which the tape casting process became extremely popular both in research and industrial sectors.[126] Since then, two excellent books have been written describing the fundamentals of the tape casting process: one by R.E. Mistler and E.R. Twiname, which describes the process from a ceramics perspective and one by D.J. Shanefield, which describes ceramic processing from a chemistry perspective.[117,118]

There are five basic ingredients necessary to prepare a slurry for tape casting: powder, solvent, dispersant, plasticizer and binder. The powder characteristics, which will later form the ceramic body, are the most important parameters in determining how much of each component to add in order to prepare a stable/usable slurry. Of the overall powder characteristics, knowledge of the exact surface area is critical. Particle density and surface moisture content are secondary, but still important factors in slurry preparation. The particle surface area determines how large a solids loading can be added to the solvent and how much organic (dispersant, plasticizer and binder) can be added. In general, higher surface area particles can't be loaded as highly into slurries because more organic additives are necessary to disperse and bind the particles stably. The most common surface area powders used for tape casting are between 5-10 m^2/g or sometimes a bit higher and contain a narrow particle size distribution.[117]

The solvent is the vehicle or liquid within which the powder is dispersed homogeneously such that a uniform tape can be fabricated. There are two major solvent categories used for tape casting: aqueous (polar) and organic (non-polar). Aqueous solvent, such as water, is called the 'universal solvent' because it serves a number of purposes in the suspension. Organic-based solvents (e.g. MEK, ethanol, isopropanol, xylenes) are usually used as binary mixtures in order to take advantage of the properties of both solvents. The solvent of choice mostly depends on what organic additives are chosen, as the solvent must be able to dissolve the dispersant, plasticizer and binder of choice, such that they can effectively adsorb on the particle surface and disperse the suspension. The advantages of organic solvents are faster drying rates, faster production and some reports of improved properties as compared to aqueous solvents. Aqueous solvents, however are much more environmentally friendly and don't present a serious health hazard to those working with it.

A dispersant is a form of surfactant (literally surface active agent) that alters the surface properties of the powder particle such that it can be stably suspended (through

steric repulsion). A dispersant or deflocculant provides an adsorbed layer on the particle surface that serves to separate individual particles from each other so that the solids loading can be sufficiently increased at a reasonable viscosity (~7000 centipoise and 700-1000 s^{-1} shear rate) while using as little solvent as possible.[117,118] A stable suspension or slip, is one that is deflocculated or rather has a continuous fluid phase surrounding each individual particle. In aqueous suspensions, dispersants usually serve to adjust the pH and thus the surface charge of the particle leading to ionic repulsion. Organic-based suspensions typically are dispersed using polymer additives (e.g. Menhaden fish oil, phosphate ester, polyethylene glycol, stearic acid) that adsorb on the particle surface and separate each particle by steric hindrance.

Binders are used to hold the particles together in ceramic systems. In tape casting, the binders encase the particle in order to both hold the particles together and provide mechanical integrity to the system once in the green state. The binder is therefore the only continuous phase in the green tape and probably the most important ingredient. The binder will ultimately determine the green tape's mechanical strength, flexibility, plasticity, laminatability, durability, toughness, printability (if it's to be screen-printed over) and smoothness.[117] The binder material must be soluble in the solvent, able to achieve a reasonable low viscosity in the system, have a decent green strength, low T_g or the ability to be modified such that it has a low T_g and able to be burned out without leaving any residue behind. Typical binders used in tape casting are polyvinyl butyral, polyvinyl alcohol, methyl cellulose, polyacrylate ester and polytetrafluoroethylene.

The plasticizer is used to enhance binder performance in ceramic systems and is added to make green tapes more plastic or bendable. Two types of plasticizers exist: Type I and Type II. Type I plasticizers are added to soften the binder chains between particles or rather to lower the T_g of the binder such that the chains holding particles together become more flexible. These types of plasticizers are sometimes referred to as

binder solvents. Type II plasticizers act as lubricants in the slurry in order to allow the green tape to bend with less effort by lowering yield stress and increasing strain to failure. The dual purpose of the Type II plasticizer causes it be termed the 'body plasticizer' or sometimes the 'lamination aid.'

In SOFC systems, tape casting is most aptly used for fabrication of porous anode materials and dense electrolyte and interconnect materials. Tape casting is best suited for homogeneous microstructures and therefore cathode materials typically aren't fabricated using this technique. Since tapes can be cut and laminated together without difficulty, co-sintered bi-layers of anode and electrolyte are easily fabricated. This fabrication method significantly reduces cost and time as bulk quantities of fuel cells can be produced simultaneously and virtually continuously. The introduction of the tape casting method into fabrication of SOFCs has pushed the limiting step in the fabrication process from component fabrication step the to the sintering phase. SOFCs fabricated by co-firing of tape cast layers have achieved an open circuit voltage over 1.1V and a power density of almost 1.8W/cm^2 at 1000ºC.[127,128] Long-term performance results have shown little change in terminal voltage under galvanostatic control.[129]

2.2.2 Screen-Printing

Screen-printing is probably the second most used (after tape casting) ceramic processing fabrication technique for SOFCs. Similar to tape casting, a slurry is prepared using powder, solvent and a dispersant/binder organic. The slurry is typically of a different, higher viscosity and thus termed an 'ink.' First powder and solvent are mixed together along with the addition of some organic that serves both as a dispersant and binder. A patterned screen called a 'mask' is then placed over the substrate, the prepared ink placed on an edge of the pattern and a squeegee pulled over the mask. A schematic of the screen-printing process is shown in Figure 18.

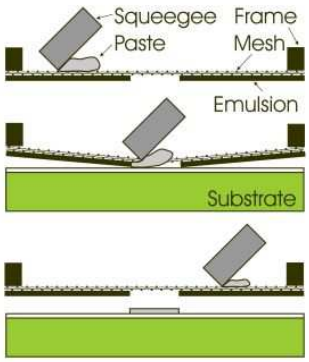

Figure 18. Schematic of the screen-printing process.

Candidate components for the solvent and dispersant/binder are similar to those discussed in the above section on tape casting. The solvent must be able to dissolve the dispersant/binder system such that the molecules can adsorb on and cover the particle surface, have a low viscosity at high solids loading (~40,000 centipoise and 400-1000s^{-1} shear rate), have a low tendency to form bubbles and have a decently fast evaporation rate.[118] Solvents for preparation of inks include water, ethanol, isopropanol, toluene, diethyl ether and heptane. The binder/dispersant system has to both hold the particles together and apart in a uniform, homogeneous system. Some organics/polymers used for dispersants are fish oil, oleic acid, glycerin, and polyvinyl butyral and for binders are polyvinyl alcohol, polyethylene glycol, ethyl cellulose, and polyvinyl butyral.

Interest in the use of screen-printing for SOFCs started for the application of uniform cathode layers on top of electrolyte-supported cells. A single print resulted in roughly a 30μm thick layer after firing, which is a desired thickness for SOFC cathodes.[130] After research on the application of cathodes for electrolyte-supported SOFCs slowed down, screen-printing was looked at for the application of thin layers of dense electrolyte on anode-supported SOFCs.[131,132] Dollen and Barnett achieved power densities of about 1.5W/cm^2 at 800ºC using a 30μm screen-printed electrolyte fabricated using a 35-vol% solids loading ink.[131]

2.2.3 Electrophoretic Deposition

Electrophoretic deposition (EPD) involves the charging, migration and subsequent deposition of charged particles onto a substrate material in response to an applied electric field.[133,134] The phenomenon was first discovered by De Bozes during a liquid siphon experiment and later put into application by Reuss, who noticed the electric field induced migration of clay particles suspended in water.[135,136] The EPD process has since been believed to involve the following steps: (1) the formation of charged particles due to the creation of a lyosphere, (2) the migration of particles towards the deposition electrode in response to an applied electric field, and (3) the deposition of these particles on the desired substrate.[137] Mechanistic studies have led to many different theories as to how particles deposit, including gravitational accumulation, DLVO, minimum field strength, hydroxyl induced polymerization, charge neutralization, and a combination of hydroxyl-induced polymerization with charge neutralization.[133,134,138,139,140,141,142,143,144] Sarker and Nicholson prepared a thorough review of these previous deposition mechanisms and also added some of their own theories including thinning of the lyosphere, ahead of the particle, to a thickness less than the sphere of closest approach, resulting in van der Waals attraction.[145] Later Van der Biest also added a review of previous literature, noting the role of the potential drop during the deposition process.[146] In addition, there have been many other theories, such as the role of ionic depletion at the depositing electrode causing a local change in pH, the role of dissociative salts and hydroxide formation, and the origin and role of the potential drop at the deposit and effects due to suspension concentration.[147,148,149,150,151,152]

Electrophoretic deposition (EPD), a cost effective fabrication method, offers many advantages such as simple apparatus, short deposition time, little restriction in the shape of deposition substrate, suitability for mass production, suitability for deposition of laminates and no requirement for binder burnout because the green coating contains little or no organics. The EPD technique has been used successfully for many applications, including biomedical materials,[153,154] luminescent materials,[155,156,157] gas diffusion electrodes,[158] oxidation resistant coatings,[159] multi-layer composites,[160] oxide nano-rods,[161] carbon nanotube film, [162] functionally graded ceramics,[163,164] layered ceramics,[165] superconductors,[166] piezoelectric materials,[167] thick film of silica,[168] and nano-size zeolite membrane.[169] The ability to form thin and dense deposits is of particular interest for solid oxide fuel cells (SOFCs).[171,172] SOFCs are solid-state energy conversion devices, which may be well suited for many stationary and mobile applications.[1] Typically, the metallic phase of anode cermets (most commonly nickel) is left in its oxide phase throughout the fabrication of anode- and electrolyte-supported SOFCs, due to problems associated with the re-oxidizing and re-reducing of the cermet.[170] The oxide phase (e.g. NiO) gets reduced to its metallic form (e.g. Ni) *in situ* during the fuel cell testing which is conducted under reducing atmosphere. It is impractical to use anode materials in its metallic/ reduced state before application of the cathode layer because the cathode must be fired in air, which leads to re-oxidation of the metallic anode. Since EPD is previously known to occur only on conductive substrates, the initial efforts to fabricate SOFCs by EPD focused on deposition of YSZ onto conductive cathode membranes such as $La_{0.8}Sr_{0.2}MnO_3$ (LSM).[152,171,172,173,174,175] Cathode-supported SOFCs, however are not as mechanically robust as anode and electrolyte-supported structures and therefore are

considered somewhat inferior. To that end, researchers then moved to fabrication of thin film electrolyte layers on Ni-YSZ anode supports and sintering of the deposit either in air, which re-oxidizes the anode, or in a hydrogen-containing atmosphere, which necessitates sintering of the cathode *in situ*.[176,177,178] In order to prevent redox of the metallic phase of the anode, some researchers placed a conductive backing such as carbon or platinum on porous oxide substrates.[179,180,181,182] EPD was still observed on these non-conductive substrates, though purportedly only because of the conductive backing placed on the substrate.

Contrary to the general assumption that EPD was limited to conductive substrates, we have recently observed the deposition of yittria-stabilized zirconia (YSZ) particles on porous, non-conductive NiO-YSZ substrates, given that those substrates are of sufficient porosity to allow the conducting solvent, within the lyosphere, a path to the working electrode.[183] Though the authors didn't make any claims to the fact, there have been a few reports in the literature that seem to show evidence that deposition can occur on a non-conductive surface. Sarkar et al. found that when a dialysis membrane was placed anywhere between two EPD electrodes, a dense deposit formed even though it was not connected to the circuit.[184] They also observed that the current continued to pass despite blockage of the particles. In a similar study, Zhang and Lee also placed a non-conductive polymer sheet between the two EPD electrodes and observed the current to be much lower when the sheet was perpendicular to the electric field in comparison to the case when it was parallel.[185] Ishihara et al. performed a series of depositions, each followed by a firing step, in order to fabricate a dense fuel cell electrolyte.[180,182] It is evident from their experiments that after the first deposit was sintered, subsequent deposits were being formed on a non-conductive layer.

2.3 SOFC Designs

SOFC cell designs must factor in the potential restrictions of the materials used and the desired properties for each component. Cell designs must also take into account the physical, chemical, electrical, electrochemical and mechanical requirements of the stack at operating temperatures. Another consideration to factor into designs of SOFCs is how to manifold them in order to ensure proper and safe gas transport to the electrodes. There are three basic SOFC designs: segmented-cell-in-series, tubular and planar. Figure 19(a-d) shows schematics of all three designs.

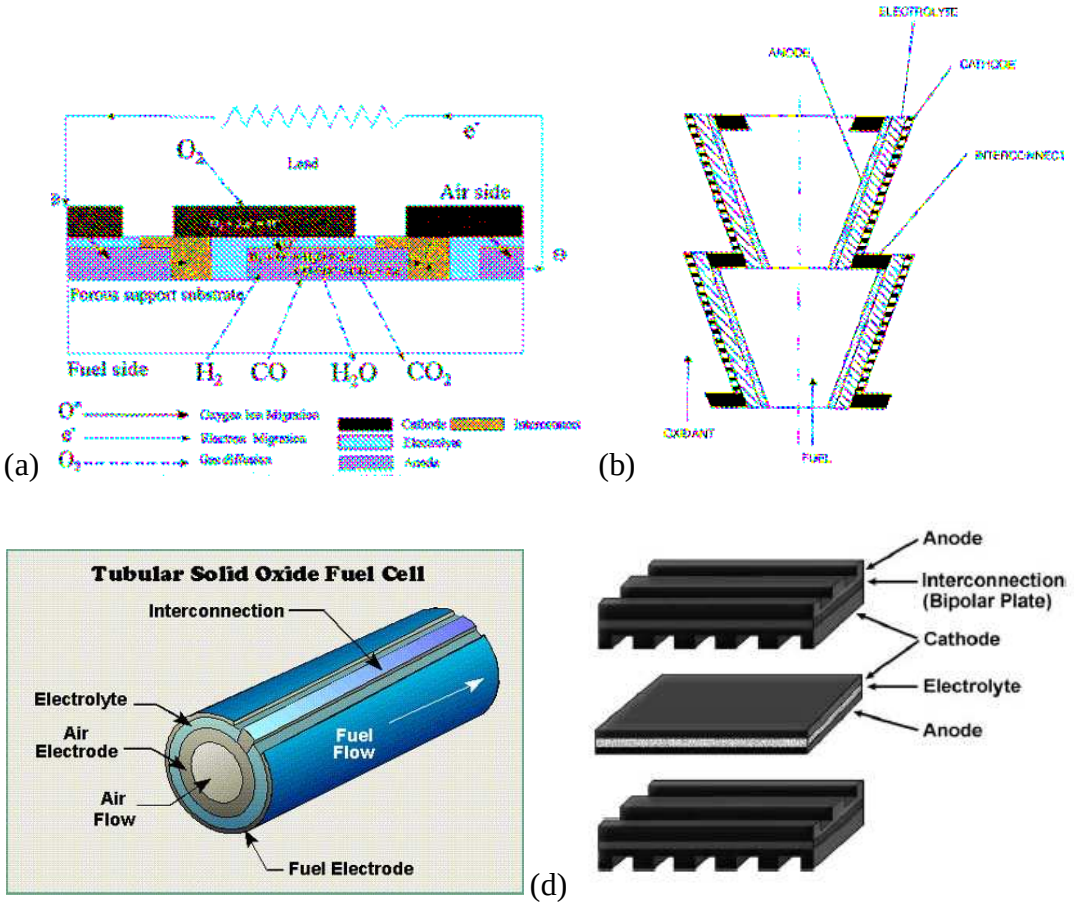

Figure 19. Schematics of SOFC designs. (a) Segmented-cell-in-series design (banded configuration) used by Rolls Royce.[186] (b) Segmented-cell-in-series design (bell-and-spigot configuration). (c) Tubular design developed by Westinghouse.[187] (d) Planar design most used today.

Segmented-cell-in-series design was the first SOFC design having been proposed in the 1960s. There are two configurations of this design: the banded and the bell-and-spigot. The banded configuration is shown in Figure 19(a) and consists of components placed as thin 'bands' on a porous support with interconnects bracketed between the anode and cathode providing both sealing and electrical connection. The bands are built and stacked as rings with the fuel flowing inside the porous support and the oxidant flowing outside the ring. While gas manifolding is easier in the banded segmented-cell-in-series design than in others, the problems are that the current path is quite long, leading to greater losses and lower performance than in other cell designs and fabrication can be expensive due because vapor deposition methods such as EVD are used. The bell-and-spigot configuration is similar to a tubular design, as show in Figure 19(b). Though its advantages and disadvantages mirror those of the banded configuration, the general power output is considerably less due to thicker electrolyte layers. An SOFC of the banded configuration containing 12 cells produced about 35W of power, whereas an SOFC of the bell-and-spigot configuration containing 10 cells only produced about 20W.[1,2]

The Tubular design was proposed in 1980 and is sometimes referred to as the Westinghouse design, as the research done at Westinghouse turned this design from a proposal to a working stack. The single biggest advantage of the tubular design, show in Figure 19(c), is that it is sealless. Since its sealless, electrical connections and current collection can be made it the anode chamber rather than the cathode chamber and can be done with cheaper metals. The SOFC tubes are bundled in pairs and electrical connections are made in series to each parallel bundle. Fabrication of these cells is fairly inexpensive with extrusion and colloidal spray techniques being used for the majority of the components. The interconnect is sometimes made using EVD, which increases costs, but not nearly as much as the segmented-cell-in-series design. Gas manifolding is similar to the segmented-cell-in-series banded configuration except that the oxidant flows in the

middle of the tube and the fuel is passed over the outside of the tube. Disadvantages of this design include a long current path leading to greater losses, gas diffusion through the length of the tube causing mass-transport limitations and lower power density.

Planar or flat-plate designs offer the highest power density because the current path from cell to interconnect is the shortest resulting in less ohmic losses. These designs, sometimes called monolithic designs if a corrugated structure is used, consist of individual cells stacked on top of each other, as shown in Figure 19(d). Fabrication of these cells is perhaps the simplest of any design as all the layers can be made by inexpensive ceramic processing methods such as tape casting and screen-printing. Many of the components are also fabricated together as bi-layers and sintered as one unit, thus lowering costs, time and increasing integrity of the cell. Gas manifolding becomes easier in this design when cross-flow is used. Cross-flow is the perpendicular flow of oxidant and fuel. Cell geometries are also very flexible in the planar design as squares, rectangles, hexagons and other shapes can simply be cut from the tapes and laminated together. Disadvantages of the planar design include the formation of high temperature seals and the oxidation of metallic interconnects.

SOFC efficiency, regardless of design, can also be increased to upwards of 85% when the byproduct heat is converted to energy using a thermoelectric system.[188] Recently, increased efficiencies have been shown using gas turbine-SOFC hybrids (GT-SOFC) where exhaust fuel and heat from the SOFC anode is used to drive the compressor of the gas turbine, which in turn provides pressurized air back to the cathode of the SOFC.[189] A schematic of the GT-SOFC hybrid is given in Figure 20:

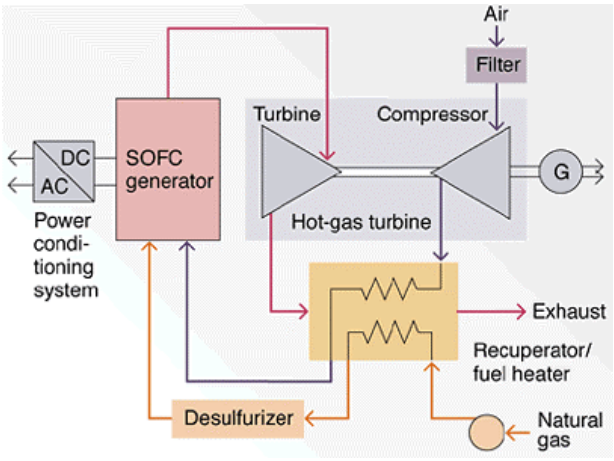

Figure 20. Schematic of solid oxide fuel cell - gas turbine (GT-SOFC) hybrid system for stationary power generation.[189]

III. PROPOSED WORK

The purpose of this work was to address certain engineering-related problems associated with low-cost fabrication of thin electrolytes and stacking of planar SOFCs. Ceramic processing techniques such as tape casting and screen-printing are low cost fabrication methods, however there is a limit to how thin of layers can be fabricated. Another ceramic processing technique, electrophoretic deposition, is used for fabrication of thin ceramic layers and coatings. Ideally, fabrication of anode-supported SOFCs starts with a porous anode substrate upon which a thin electrolyte is deposited. Due to the fundamental requirement of a conductive substrate for deposition by EPD, fabrication by this method was time consuming, often involving a series of deposition and firing sequences. We developed a method to deposit thin film electrolyte layers on porous non-conducting anode substrates in a single step. Not only have we shown that EPD can occur on non-conductive substrates, but we've reduced the number of processing steps from more than five to only one.

Two of the biggest issues from an engineering perspective are with regard to seals and interconnects. Tubular SOFC designs are sealless and their interconnect layers aren't as subject to oxidation as those in planar designs. Tubular designs are also easier to bundle together to form a stack. Since planar designs have shorter current paths, their power densities are higher making this them more desirable than tubular cells. If the planar design could be modified such it could become sealless as well, issues with reliability, lifetime and thermal cycling effects related to external seals would be eliminated. We have developed a hermetic planar SOFC design that eliminates the necessity of external seals. The new design incorporates a hybrid or composite region between the electrolyte and interconnect, similar to the seals formed in segmented-cell-in-series and tubular designs.

Interconnect materials for SOFCs include doped lanthanum chromate ceramics and Ferritic stainless steels. The conductivity of ceramic interconnects is too low to use below 800ºC and therefore are only used in high temperature fuel cell applications. Ferritic stainless steels have sufficient conductivity for fuel cell applications, however their oxidation resistance at temperatures above 700ºC isn't adequate for long-term use. Since the interconnect doesn't need to be a thick layer, we've investigated the use of noble metals such as silver for use as an SOFC interconnect. Noble metals have a unique thermodynamic advantage over other metals in that their metallic phase is stable at higher temperatures and their oxide phase is stable at low temperatures. Therefore we've studied the properties of polycrystalline silver in single and dual atmospheres under SOFC operating conditions to determine silver's ability to act as an SOFC interconnect.

3.1 Electrophoretic Deposition on Non-conducting Substrates

EPD is a well-known thin film coating technique used in ceramic and metallurgy applications. Some of the fundamental requirements for EPD are stably suspended particles in a high quality solvent and a conductive deposition substrate. The necessity of a conductive substrate, however, comes into question when discussing the mechanism of charge transport and particle deposition. Some researchers argue that charge is carried by the particles themselves (possibly by physic-adsorbed ions on the particle surface) and not the solvent.[185] Other experts believe that the charge is carried within the solvent vehicle (all lyosphere counter-ions transport charge) and not by the particle.[145,148] If the charge is carried by the particle and not by the solvent, and the mechanism of particle deposition involves charge transfer (which is likely to be the case), then a conductive substrate is necessary for deposition to occur. A conductive substrate would not be necessary, however, if charge is carried by the solvent because then particles could be deposited on a substrate that's not conductive or connected to the electrical path while charge is still transferred.

It's this conundrum of charge transport and deposition mechanism, along with a single body of work by Sarkar and Nicholson[184] that triggered an idea, which became the most complete body of work presented in this thesis. The idea was that a conductive substrate is not necessary for deposition to occur, so long as charge can still be transferred at the deposition electrode. The foundation for this idea was knowledge that a stable particle is surrounded by a lyosphere of counter-ions, and its those counter-ions along with the ions adsorbed to the particle surface, that allow for particle movement, deposition and charge transfer. Therefore as long as solvent ions have an unobstructed path to the deposition electrode, charge transfer can be completed and particles can be deposited anywhere between the two EPD electrodes. This theory isn't without merit or supporting information as colloidal or particle stability is generated by the formation of a charged lyosphere. That lyosphere is most often the direct result of added counter-ions to the system, not due to solvent-particle interaction. Therefore the formation of a charged lyosphere around a particle is the direct result of externally added counter-ions, meaning that it's those ions that give charge to the system. Current is the rate of charge movement thus charge transfer must be due to the counter-ions in the lyosphere, not from the particle. This reasoning prompted the idea of performing EPD on porous non-conductive substrates. The hypothesis was that particles could be deposited on a non-conductive substrate placed between the EPD electrodes given that the substrate contained sufficient open porosity such that charge could be transferred between the EPD electrodes, just as it was in the dialysis membrane experiment.[184]

The importance of being able to deposit particles on non-conducting substrates lies not only in its novelty, but also in its potential to revolutionize the fabrication of SOFCs by EPD. As was outlined in *section 2.2.3,* EPD has been used to deposit thin-film electrolytes for cathode- and anode-supported planar SOFCs. Though Ishihara, Yamaji and Matsuda have all fabricated high-performance SOFCs using EPD, their fabrication route or number processing steps is are too numerous to any realistic scaling and

reproducibility. Ishihara obtained a power density if 1.87W/cm^2 at 1000ºC, however their process required five repetitions of particle deposition followed by sintering at 1400ºC. In two other works by Ishihara, 6 and 12 repetitions were required to obtain a reasonable open circuit voltage and power density.[172] Given that a single firing step to 1400ºC can take up to 24hrs, a process such as theirs could take well over a week before the SOFC was suitable for testing. Though long fabrication times are fine for research purposes, they aren't suited for industry and mass production. Will,[176] Yamaji[179] Matsuda[181] and Hosomi[190] all fabricated anode-supported SOFCs by EPD, using conductive Ni-YSZ substrates. Each of their processes only required a single deposition and firing step, however the Ni within the deposition substrate had to undergo multiple redox cycles. After these researchers fabricated the anode substrate in the oxide (NiO-YSZ) state and then reduced (Ni-YSZ) to form a conductive substrate, it was re-oxidized during cathode sintering. The anode must be re-oxidized because cathode materials must be sintered in an oxygen-containing atmosphere. Redox cycling of the anode substrate is problematic because of the associated volume expansion and contraction, which causes cracking and/or delamination from adjacent layers.[170,191,192]

From this review of SOFC fabrication by EPD, it's obvious that the ideal situation would be to eliminate the necessity of a conductive substrate while also fabricating an electrolyte layer in a single step. Therefore we proposed to deposit thin film YSZ electrolyte layers on non-conductive NiO-YSZ substrates. As was outlined previously, our theory is that sufficient porosity within the NiO-YSZ substrate will allow for counter-ions in the lyosphere to be transported through the substrate and complete the charge transfer at the deposition electrode while the particles are deposited on the substrate. In this manner the substrate won't have to be redox cycled, eliminating volume expansion issues, and an electrolyte layer can be deposited and sintered in a single step.

3.2 Hermetic SOFC without Sealant

SOFC technology is hindered by the number of interfaces within a single cell and the number of extra interfaces needed to stack cells together. Interfaces are the number one cause of all performance, material and reactionary problems encountered. The cathode-electrolyte interfacial resistance limits performance when H_2 is used as the fuel.[193] Seals are failing due to phase instability at the interface with SOFC components such as the interconnect.[48-51] Interconnect materials form reactionary phases both at interfaces with the electrodes and with the atmosphere.[45-47,50] Electrodes, particularly the cathode, become poisoned by chromium species diffusing from the interconnect.[45] Current research has tried to improve these interfaces by incorporating intermediary phases aimed to decrease resistance, ion mobility or phase reactivity. Adding new materials to SOFCs only increases their complexity and the potential for more reactions to occur. For every new material added to a SOFC, up to two new interfaces are developed. Eventually, if further intermediary phases are added, the interfaces will control the material properties more than the bulk materials themselves. This renders SOFC material choice useless. Further the interfaces formed will need new materials to compensate for their reactionary tendencies. This cycle will continue until the complexity of SOFCs is decreased and building the cell out of only the necessary components for electrochemical operation can only do that. Hermetically sealing SOFCs without the use of sealant will eliminate the need for unnecessary material addition and interface compensation.

Rather than aiming to minimize the problem, the aim of this research will be to eliminate what we believe to be potentially extraneous components within SOFCs. Earlier the complexity of the SOFC system was attributed to its many components and subsequent numerous interfaces. To reduce the complexity, the number of layers and differing materials in contact should be minimized. In the case of interconnects and sealants, bonds and interfaces created between components can lead to the possibility of

CTE mismatch, chemical incompatibility, ion diffusion and new phase formations. Using a combination of ceramic processing techniques, metal and ceramic layers will be fabricated in a novel design to form the basis for hermetic SOFCs without sealant. Eliminating the need for sealant materials through the use of an inherent SOFC interface will drastically reduce the number of problems SOFC materials and fabrication is currently facing. A simple SOFC design has been developed, which is shown in Figure 21, that only depends on the four independent materials necessary for the electrochemical reaction to take place: interconnect, cathode, electrolyte and anode.[194]

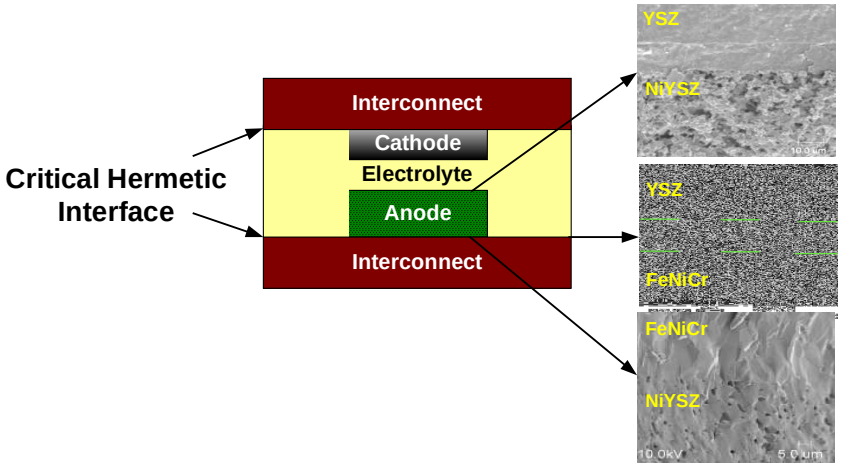

Figure 21. Proposed hermetic SOFC without sealant.

This hermetic seal is based on the formation of a blocking interface, which prohibits oxygen ion transport out of the cell. The electrolyte itself is used to prevent hydrogen leakage. This novel SOFC design eliminates unnecessary interface formation and material addition, thus greatly simplifying what is becoming a very complex system.

The main goal of the proposed work is to fabricate and characterize the hermetically sealed SOFC using low cost ceramic processing techniques. More specifically, the technical objectives are: (1) to effectively design a hermetic SOFC without the use of an external sealant, (2) to develop a cost effective technique through

novel combinations of ceramic processing and cathode deposition methods to produce the hermetic SOFC without sealant and (3) to characterize the transport properties of the each cell component and the interfaces between them, particularly the novel interconnect-electrolyte interface, under well-controlled conditions. A range of possible interconnect materials for both stationary and cycling applications will be examined as well as the effects of cell geometry and fabrication method on reliability and bond strength.
A fundamental understanding of the critical interface, the interconnect-electrolyte, will lead to novel SOFC architecture and stack designs. The hermeticity or sealing ability of this interface will depend on the nature of the ceramic-metal interface to effectively block oxygen transport. These SOFC designs will prove critical in forming a new generation of planar SOFC stacks and architecture.

3.3 Silver-based Interconnect Materials

Lanthanum chromite and ferritic stainless steel are currently the two major interconnect materials used for current collection and transport from a stack. Lanthanum-based chromates and chromites are highly conductive ceramic interconnects used in high temperature SOFCs (T>800°C), however their conductivity and therefore current collection efficiency decreases significantly in the intermediate temperature range.[41,43] Metallic interconnect materials such as those based on the Fe-Ni-Cr phase diagram are much less expensive than the ceramic interconnects and operate at temperatures below 750°C.[195] Chromium containing alloy interconnects suffer from material instability, however, when exposed to a wide variety of fuels, as oxidation and chromium poisoning can readily occur at the cathode while carburization and sulfur poisoning can cause degradation at the anode.[42,46,47] Therefore it is necessary to develop an interconnect material that can withstand operating temperatures around 750°C and remain stable in oxidizing, reducing and contaminating environments.

Silver is a noble metal most often used in current collection and electrode applications due to its stability in oxidizing atmospheres, as shown by the Ellingham diagram.[21] Some researchers have shown interest in applying the inert properties of silver to SOFC interconnects. Past literature has also documented silver to be a selective conductor of oxygen and therefore its use as an interconnect could cause oxygen to permeate into the anode chamber, resulting in gas mixing, oxidation of the nickel metal, lower fuel utilization, and reduced Nernst potential. Many studies have been conducted on the permeation rate of oxygen through silver membranes starting with Dushman,[196] Whetten and Young,[197] Coles,[198] Burroughs,[199] Beavis[200] and Outlaw.[201] Their primary focus was the use of silver membranes to admit high purity oxygen gas into vacuum systems, separate O_2 from CO_2 for space applications and to understand the catalytic behavior in the epoxidation of ethylene and partial oxidation of methanol to formaldehyde.[202,203,204] Van Herle and McEvoy measured the diffusivity of oxygen through silver using impedance spectroscopy.[205] They deposited a dense silver cathode by PVD followed by electroplating as well as a porous silver cathode by brush painting. Based on the angle of the impedance curve measured as a function of oxygen partial pressure, they proposed bulk diffusion of oxygen to be rate limiting. Kontoulis and Steele found impedance spectroscopy unable to measure the oxygen diffusivity, though DC polarization techniques proved to return consistent results.[206] Their inability to resolve oxygen diffusivity could have been due to the fact that their frequency sweep was only down to 5Hz, whereas Van Herle and McEvoy swept to 100mHz.

The main focus of this work is to evaluate the use of silver in SOFC applications. More specifically, we intend to study the use of silver as a conduction path through any surface oxide of the interconnect in order to connect to reduced metal maintained at locations with lower oxygen activity in proximity with the fuel side of the interconnect. Due to previous reports that silver selectively conducts both oxygen and hydrogen, we intend to first study the oxygen permeation and diffusion rate through polycrystalline

silver in single and dual atmosphere environments. Oxygen permeation through silver would result in gas mixing on the anode side, oxidation of the anode catalyst, decreased fuel utilization and decreased Nernst potential. Once the temperature dependence of oxygen permeability through silver is known, the leaking current density can be calculated, which will give a realistic view of silver's effectiveness as an SOFC interconnect. A low leaking current density would indicate that little performance loss would be seen if silver were used as an interconnect. The second objective of this study will be to measure the degradation rate of silver in single and dual atmosphere environments. Single atmosphere studies simulate the use of silver as a catalytic material to enhance SOFC cathode performance. The dual atmosphere environment emulates real interconnect conditions, where oxygen and hydrogen can mix in the lattice and form water. Since SOFCs are considered to be stationary power sources, their expected lifetime needs to be on the order of 10+ years, therefore the silver interconnect can't degrade much within that timeframe.

IV. ELECTROPHORETIC DEPOSITION ON NON-CONDUCTING SUBSTRATES

4.1 Literature Review

Numerous different techniques have been employed for deposition of thin and dense electrolyte films on anode supports,[207] including physical vapor deposition (PVD) such as sputtering, pulsed laser deposition and molecular beam epitaxy (MBE),[208] chemical vapor deposition (CVD) or electrochemical vapor deposition methods (EVD),[209,210] combustion chemical vapor deposition (CCVD)[211] and plasma technologies.[212] However, the PVD and CVD deposition methods ordinarily require sophisticated and expensive equipment, making them either undesirable or impracticable for implementation in manufacturing processes. These deposition methods are also plagued by high processing temperatures and limitations on the materials with which the support anode is made.

Recently, there have also been many attempts to use electrophoretic deposition for SOFC fabrication.[171-177,180-182] To date however, these studies used electrically conducting substrates for deposition of YSZ films by EPD. Ishihara et al. was the first to report fabrication of an SOFC by EPD. [180] YSZ, suspended in acetylacetone with 0.6g/L I_2 was deposited on a thick LSM cathode at 5V for 3min and sintered at 1400ºC. The process required at least 5 repetitions of deposition and sintering before an open circuit voltage of 1.03V was achieved, resulting in a power density of 1.87W/cm^2 at 1000ºC. Figure 22 shows the surface and cross-sectional images of the cathode-supported SOFC. [180]

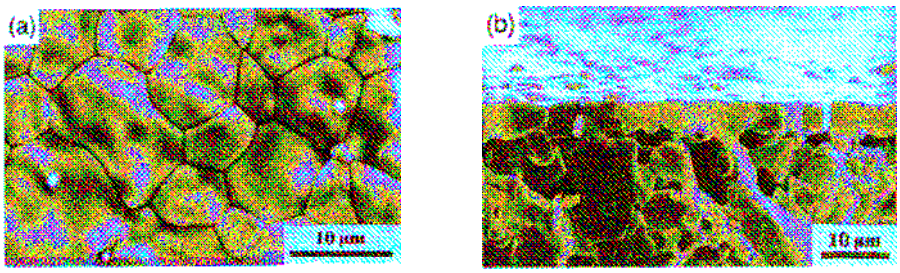

Figure 22. (a) Surface and (b) cross-sectional images of SOFC fabricated by Ishihara et al.

Later, Ishihara et al. deposited YSZ on a NiO-CaSZ anode, which was coated with platinum to make it conductive.[182] The anode-supported cell required 6 repetitions of deposition at 10V for 3min followed by sintering at 1375ºC. The anode was then reduced at 1000ºC for 1hr in H_2 prior to cell operation. The evolution of the open circuit voltage and power density with each repeated deposition is shown in Figure 23.

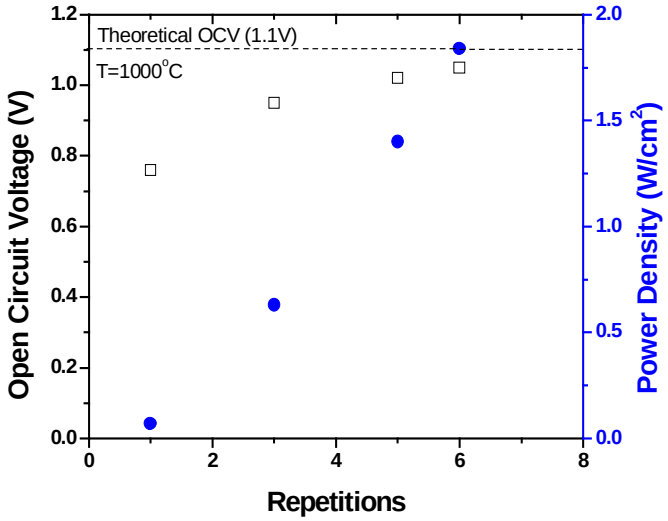

Figure 23. Evolution of OCV (□) and power density (●) with increased repetitions. [182]

In 2000, Ishihara et al. again deposited YSZ on LSM, only this time they determined that 12 repetitions were necessary to achieve a working SOFC. The cell operated at less then 1.5W/cm^2 and had an OCV of about 1.1V.[172] Yamaji et al., in 2004, prepared a pressed pellet of NiO-ScSZ containing graphite and deposited YSZ due the conductive graphite filler.[179] Matsuda et al., then coated the front of a NiO-YSZ substrate, deposited YSZ at

400V for 30 sec, and burned away the graphite during sintering.[181] Their cell achieved an OCV of 1.09V and power density of 1.02W/cm^2 at 800ºC. Hosomi and Matsuda again repeated their process a year later in 2006 and reported an OCV of 1.15V and a power density exceeding 2W/cm^2 at 800ºC.[213]

In this work we report our findings unique method for electrophoretic deposition of thin and dense YSZ films on a non-conducting NiO-YSZ substrate for SOFC applications. Contrary to the general assumption that EPD was limited to conductive substrates,[214,215] we have recently observed the deposition of yittria-stabilized zirconia (YSZ) particles on porous, non-conductive NiO-YSZ substrates, given that those substrates are of sufficient porosity to allow the conducting solvent, within the lyosphere, a path to the working electrode.[216,217] The novelty of the process lies in the fact that it does not necessitate the need for any heat treatment under reducing atmosphere or use of a conductive substrate/coating. The deposition has been made possible simply through the use of adequately porous substrates to ensure presence of a conducting solvent path during EPD. The process of EPD on non-conducting substrates will be discussed from proof-of-concept experiments to fundamentals of the deposition process[218] including statistics of process reproducibility,[219] optimization, empirical and physical modeling.

4.2 Proof of Concept

Porous NiO-YSZ substrates used for electrophoretic deposition were formed via tape casting. Commercial NiO powder (Alfa Aesar, USA) containing a maximum particle size of 10μm was too large to stably disperse in a slurry for tape casting and therefore was milled with 6mm diameter YSZ balls as the milling media in ethanol for 96hrs. Milling yielded much smaller particle sizes than the as-received powders as shown in Figure 24.

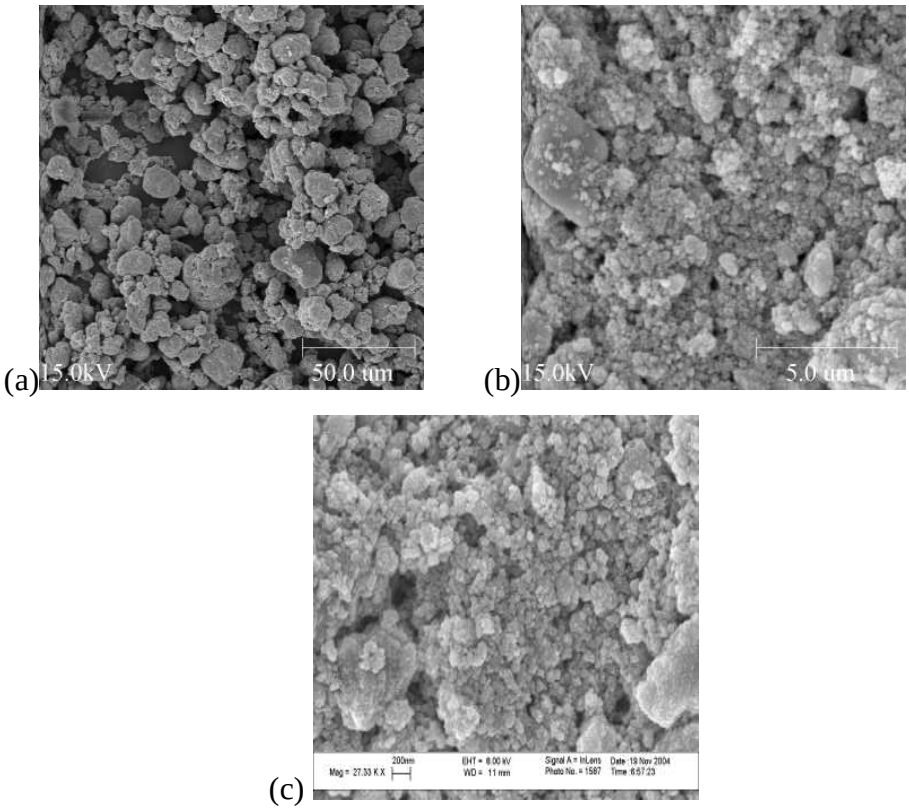

Figure 24. SEM images showing particle size of NiO powder (a) as received, (b) milled for 96 hrs, and (c) milled for 240 hrs.

The milled NiO powder was then dried, ground to separate agglomerates and mixed with YSZ powder. The YSZ powder (Daiichi Corporation, 8 mol %) with a median particle size of 0.26μm was dried at 120°C for 48hrs prior to use to ensure removal of constituent hydroxyl groups from the surface. Mixing of NiO and YSZ powders was made in a stoichiometric ratio that would produce a 1:1 volume ratio of Ni to YSZ after reduction. The slurry for tape casting was prepared in a two-stage ball milling process. The mixed powder was first dispersed in a 50:50 mixture of ethanol and xylenes using Menhaden Fish oil and then milled for four hours with 6mm diameter YSZ balls as grinding media to prepare a slurry of 17.3 vol % (or 65 wt %) solids loading. After four hours, polyvinyl butyral (PVB) was added as binder and two plasticizers namely- Polyalkylene glycol (to

reduce the binder T_g and control plasticity) and Butyl benzyl phthalate (as lubricant and to control plasticity) were added to the slurry and milling resumed for 24 hrs.

After de-airing in a vacuum oven at -5mm Hg for 15 minutes, to eliminate air entrapped in the suspension during milling, the slurry was cast using a stationary blade six-foot tabletop caster (Richard E. Mistler Inc.). The tabletop caster was equipped with a DC motor, variable speed control, heated five-foot casting bed, one-foot square granite casting block, and counter directional mass-controlled airflow. Casting was performed at a blade height of 150μm and a rate of 20cm/min. The casting chamber atmosphere was controlled using flowing air at a rate of 30mL/min and a heated casting bed set at 26°C. The temperature and humidity were monitored throughout the duration of casting. After casting was complete, the tape was dried overnight, cut into 13mm discs and fired in air at different temperatures to obtain NiO-YSZ substrates of varying porosity. A typical schedule for firing the sample at 1400°C is presented in Table 6.

Table 6. Typical schedule for sintering the tape-cast NiO-YSZ discs at 1400 °C.

Temperature Range (°C)	Ramp Rate (°C/min)	Dwell Time (min)
25 - 200	4	0
200 - 450	1	0
450 - 1100	4	0
1100 - 1400	1	300
1400 - 1100	2	0
1100 - 25	4	0

All NiO-YSZ samples fired from 1100°C-1400°C were held for 5hrs at the peak sintering temperature. The fired samples were weighed and their diameters and thickness measured using calipers to estimate density/porosity as presented in Table 7.

Table 7. Relative density and/or porosity of NiO-YSZ substrates obtained by tape-casting and firing at different temperatures.

Temperature (°C)	Relative Density (%)	Relative Porosity (%)
1100	47.5	52.6
1200	56.4	43.6
1300	67.4	32.6
1400	77.5	22.5

The surface of NiO-YSZ substrate obtained by tape casting was very smooth and of uniform thickness. The density and/or porosity values reported in this paper are an average of five samples with a repetition of five measurements per sample and are confirmed by volume fraction stereology measurements. This ensured in minimizing the density/porosity data presented in Table 7. The resulting microstructures were analyzed using SEM and are given in Figure 25.

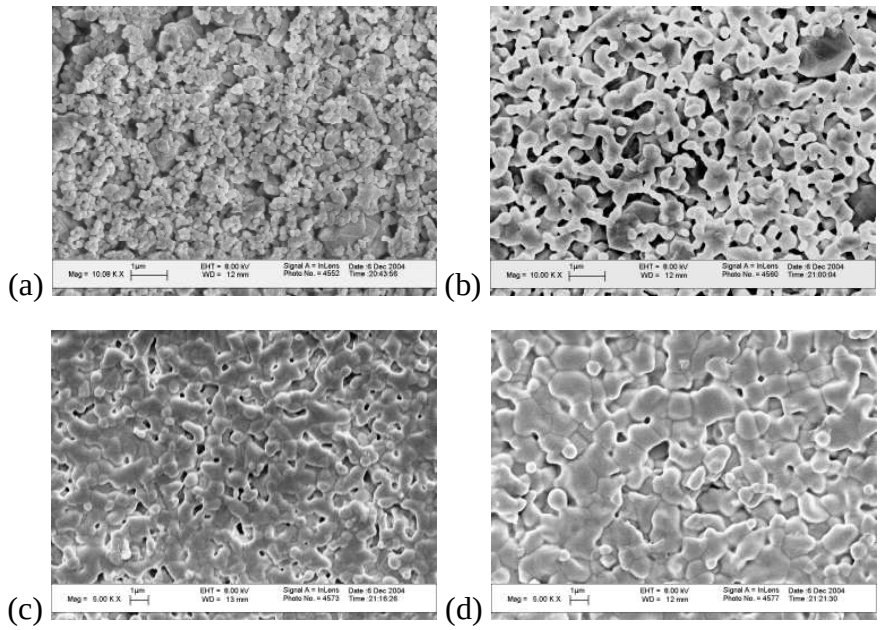

Figure 25. SEM pictures showing microstructures of NiO-YSZ substrates obtained by tape-casting followed by sintering in air for 5hrs at different temperatures: (a) 1100°C, (b) 1200°C, (c) 1300°C, and (d) 1400°C.

Suspensions of YSZ powder were prepared by dispersing YSZ powder (TZ-8YS, Tosoh, Japan) in acetylacetone (Acac) under a high intensity ultrasonic bath in order to break up agglomerates and form a homogeneous and stable colloidal suspension. The median particle size, D_{50}, was 0.54μm as measured by a Horiba CAPB-700 particle size analyzer resulting in a specific surface area of 2.2m^2/g. The particle size distribution is shown in Table 8.

Table 8. Particle size distribution for Tosoh YSZ powder, as measured by Horiba CAPB-700.

Particle size, micron	Distribution, vol %		Cummulative vol %	
	Measurement-1	Measurement-2	Measurement-1	Measurement-2
10	0.0	0.0	0.0	0.0
10.0-9.0	0.0	0.0	0.0	0.0
9.0-8.0	0.0	0.0	0.0	0.0
8.0-7.0	0.0	0.0	0.0	0.0
7.0-6.0	0.0	0.0	0.0	0.0
6.0-5.0	1.2	0.0	1.2	0.0
5.0-4.0	0.0	0.0	1.2	0.0
4.0-3.0	0.2	0.0	1.4	0.0
3.0-2.0	7.4	5.1	8.8	5.1
2.0-1.0	15.1	12.1	23.9	17.2
1.0-0.90	2.4	1.8	26.3	19.0
0.90-0.80	2.0	2.9	28.3	22.1
0.80-0.70	5.3	6.4	33.6	28.5
0.70-0.60	9.3	8.6	42.9	37.1
0.60-0.50	12.4	8.9	55.3	46.0
0.50-0.40	15.4	16.7	70.7	62.7
0.40-0.30	10.5	23.4	81.2	86.1
0.30-0.20	15.0	9.5	96.2	95.6
0.20-0.10	3.1	3.8	99.3	99.4
0.10-0.00	0.7	0.6	100.0	100.0
Median, μ	0.54	0.49		
SD	0.89	0.69		
Sv, m^2/g	2.184	2.314		

It was equilibrated for 24hrs and sonicated again for 5min before electrophoretic deposition. The zeta potential of the YSZ-acetylacetone system was measured to be about 8.5mV without the addition of any charging agents. After addition of 0.2, 0.4 and 0.6g/L

of iodine to the system, the zeta potential increased to 41, 46 and 49mV, respectively, as shown in and similar to that reported by Ishihara and Chen.[175,180]

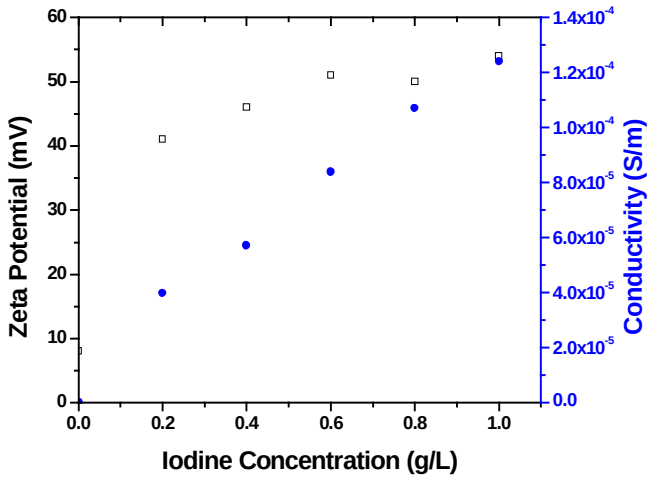

Figure 26. Influence of I_2 on the zeta-potential and conductivity of YSZ particles suspended in acetylacetone.

After addition of more than 0.5g/L of iodine, deposition ceased to occur in the system and some residual deposit was seen at the counter electrode, following the suspected proton formation charging mechanism.[182] The conductivity and dielectric constant of the suspensions, as measured using impedance spectroscopy, are summarized in Table 9.

Table 9. Zeta potential, conductivity and dielectric constant data for the YSZ-acetylacetone suspensions as a function of particle and I_2 concentration.

Solvent	YSZ Concentration	I_2 Concentration	Zeta Potential	Conductivity (S/m)	Dielectric Constant
Acetylacetone	0	0	0	$3.46*10^{-8}$	25.9
Acetylacetone	1	0	8	$2.06*10^{-7}$	23.4
Acetylacetone	10	0	8	$2.44*10^{-7}$	21.9
Acetylacetone	100	0	8	$1.19*10^{-6}$	21.4
Acetylacetone	10	0.2	41	$3.98*10^{-5}$	21.7
Acetylacetone	10	0.4	46	$5.72*10^{-5}$	21.9
Acetylacetone	10	0.6	49	$8.40*10^{-5}$	21.6

In contrast to many EPD processes, where suspension stability requires the addition of additives like binders, dispersants and charging agents,[180,220] merely addition of the powder to the solvent followed by ultrasonication was sufficient for deposition to occur. The dispersion of YSZ in acetylacetone solvent was adequate for development of positive surface charge on the YSZ particle surface, which facilitated migration of the particles to the oppositely charged cathode and deposition during EPD. Most organic solvents, like the acetylacetone solvent used in the present investigation, are not completely anhydrous. Invariably some amount of residual water is present in these organic solvents. The development of surface charge, in the absence of I_2, is possibly due to the presence of this residual water, which is responsible for charging in a manner similar to that in an aqueous medium.[221] Based on the Debye-Huckel equation

Equation 14
$$\psi = \psi_o \exp(-\kappa x)$$

and knowledge of the surface electrostatic potential,

Equation 15
$$\psi_o = \frac{q}{\kappa \varepsilon_D}$$

the Debye length, or double layer thickness can be approximated.

Equation 16
$$x = \frac{1}{\kappa} = \left(\frac{\varepsilon_o \varepsilon_r kT}{\sum (z_i e)^2 c_o} \right)^{1/2}$$

Based on the aforementioned values, the double layer thickness is about 10nm, which is reasonable for a colloidal system such as this. The double layer thickness is the distance from the particle surface to the edge of the shear plane, as shown in Figure 27.

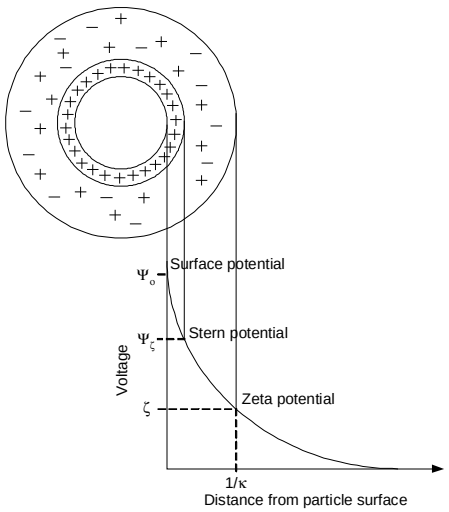

Figure 27. Relationship between the lyosphere, double layer thickness, surface charge density and zeta-potential.

Charging agents for colloidal systems include acids (HNO_3), metal-chlorides ($MgCl_2$, $AlCl_3$) and organics (polyethyl imine).[222] For fuel cells applications, metal chlorides aren't desired because they could leave behind contaminants. Acids also aren't desired due to their corrosive behavior towards the electrodes and potentially the particles in suspension. Organics could be used, except that they'd have to be burned out and could result in porosity. Iodine is another well-known charging agent for particles in a ketone-based solvent system, due to the keto-enol reaction that takes place.[223]

Reaction 20

$$CH_3COCH_3 \xleftarrow{H_2O,I_2} CH_3C(OH)CH_2$$
$$CH_3C(OH)CH_2 \longrightarrow CH_3COCH_2I + H^+ + I^-$$

Halogen ions are used because they are able to push the keto-enol reaction towards the enol using general base catalysis. When 0.2g/L I_2 was present in the system, which forms $1.8*10^{-5}$ mol/L H^+, the theoretical surface charge density is 0.0796C/m^2 and was measured to be 0.076C/m^2. Stable colloidal systems should have surface charge densities between 0.01 and 0.1 C/m^2.

The deposition experiments were conducted using an electrophoretic deposition setup shown schematically in Figure 28.

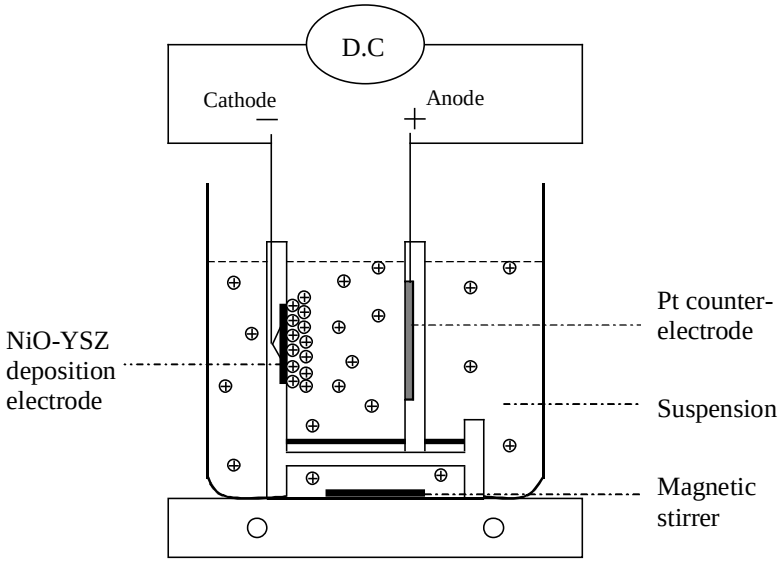

Figure 28. A schematic diagram of the electrophoretic deposition apparatus.

The deposition apparatus consists of two electrode holders made of Teflon, as the principal components. One electrode holder is fixed and the other is movable and can slide along two parallel rods at the bottom so that the distance between the electrodes can be adjusted to a desirable position. Each of the electrode holders has a circular window facing each other to allow the electrodes to be fixed on it. NiO-YSZ substrates were mounted on the fixed holder with a spring contact at the back and served as cathode whereas a platinum disc served as the counter-electrode on the movable holder. The spring contact was made from a 0.5mm diameter platinum wire, the other end of which was directly connected to the negative terminal of the DC power supply unit. The silver and platinum were stable in the acetylacetone solvent and did not undergo any reaction in it. Unless otherwise mentioned, an electrode spacing of 1cm was maintained in all of our EPD experiments. The holders along with the electrodes were immersed in the reservoir containing the suspension of YSZ. Sedimentation of YSZ particles was prevented by agitation using a magnetic stir bar. Electrophoretic deposition experiments were carried out at constant voltages varied in the range from 50V to 300V, using a high voltage DC power supply unit (Model PS 310, Stanford Research Systems, USA) with a deposition

time from 1 to 5 minutes. During deposition, the YSZ particles were attracted and migrated towards the negative electrode (cathode) where they eventually get deposited. Similar cathodic electrophoretic deposition of YSZ from acetylacetone has been reported by several other researchers.[175,180,182] This indicates that the YSZ particles were positively charged in acetylacetone solvent. The bi-layer consisting of the NiO-YSZ substrate and the deposited YSZ were then sintered in air at 1400°C for 5hrs. After sintering, an obvious thickness gradient was observed between the deposit at the center of the substrate and the deposit at the edge. Figure 29 shows the discrepancy between the thickness at the center and the thickness at the edge as a function of deposition time.

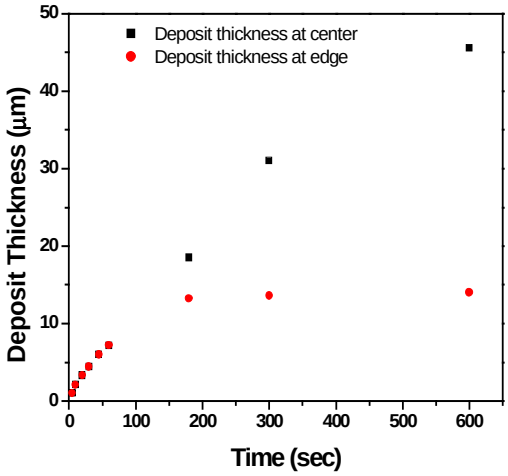

Figure 29. Plot comparing the deposit thickness at the center of the substrate to the deposit thickness at the edge of the substrate for different deposition times. Note that NiO-YSZ substrates pre-fired at 1100°C and a deposition voltage of 50V was used in all experiments.

The reason that the deposit thickness at the edge of the substrate flattened out after 130sec time was that the area of the cathode electrode was less than that of the substrate. Since the cathode attracts the counter-ions of the lyosphere for charge transfer, particles are going to be steered to the center of the deposit and not to the edge. Therefore in order to obtain a deposit of uniform thickness, the cathode area must be equal to or larger than

that of the substrate. A schematic, showing the effect of cathode area on particle deposition is shown in Figure 30.

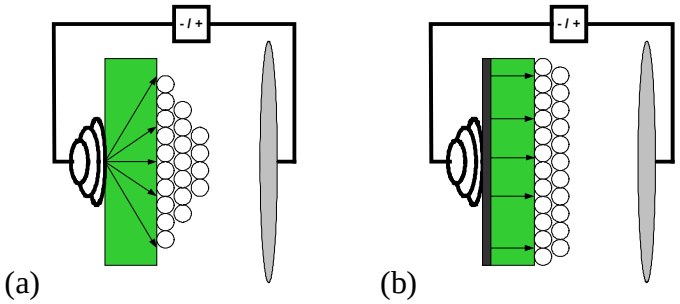

Figure 30. Schematic of particle deposition when the cathode area is (a) less than that of the substrate leading to concentrated deposition at the center and limited deposition at the edge and (b) when the cathode are is equal to that of the substrate such that uniform deposition occurs.

In Figure 30, note that the dark arrows represent the least resistive path for charge transfer to occur or rather the distance the counter-ions need to travel to achieve charge transfer. Charged species always try to move along the least resistive path, which is why the particles concentrate in the center of the substrate as indicated in Figure 30(a). When the cathode area is equal to or greater than that of the substrate, as in Figure 30(b), the path length for charge transfer is equivalent for deposition at the center or the edge, which leads to a uniform deposit thickness.

Once uniform deposit thickness was achieved, a single fuel cell was constructed on the sintered bi-layer by brush painting a layer of mixed cathode consisting of a 50:50 ratio of commercial $La_{0.8}Sr_{0.2}MnO_3$ (LSM, Rhodia) and YSZ on the electrolyte followed by sintering at 1200^{o}C for 2hrs. The fuel cell was fixed and sealed to an alumina tube using silver paste (Heraeus, C8710) and the silver wires were bonded to the electrodes as leads. The seals were cured at 550^{o}C for 1hr before the fuel cell was cooled and a second layer of sealant applied. The cell-tube apparatus was then placed in a clam-shell (ATS Systems) furnace and brought to the testing temperature with continuous flow of H_2 gas

as fuel and air the oxidant. Fuel cell performance and electrochemical impedance were measured using a Solartron Electrochemical Interface (Model SI 1287) combined with a Solartron Frequency Response analyzer (Model SI 1255) interfaced with a computer running Corrware version 2.4a software for potentiometry measurements and Zplot version 2.4a software for impedance measurements. The impedance was measured in the frequency range from 100kHz to 0.1Hz with 10mV amplitude. Figure 31 shows the surface and cross-sectional view of a sintered YSZ film obtained by a single deposition step.

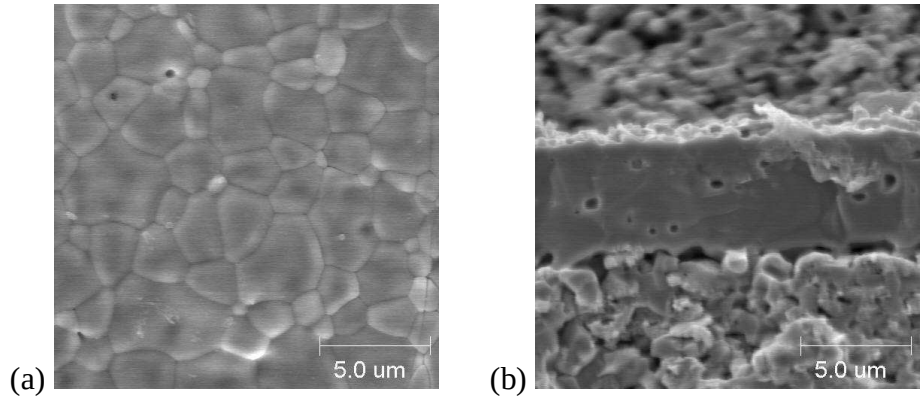

Figure 31. Typical SEM pictures showing (a) surface and (b) cross-sectional image of YSZ film on NiO-YSZ substrate (pre-sintered at 1100ºC for 2hrs), obtained by constant voltage EPD at 50V for 1min. The deposits were sintered at 1400ºC for 4hrs. The cross-sectional image was taken after SOFC testing with an LSM-YSZ composite cathode layer painted on it.

The surface view Figure 31(a) clearly reveals a YSZ film with no cracks. There appears to be some intra-granular holes on the surface of YSZ film, but a close examination of the cross section Figure 31(b) reveal that they are isolated and are not continuous in nature. This ensures that the YSZ film is sufficiently dense to prevent gas permeation and would serve as a good electrolyte for SOFC. The thickness of the YSZ film was about 5μm. There is good adherence of the electrolyte to the porous NiO-YSZ substrate. There indeed appear strong interconnections between the YSZ grains of the film and the

substrate, which is helpful to transport of oxygen ions from the electrolyte to the anode during SOFC operation. X-ray diffraction of the sintered film shows the presence of polycrystalline YSZ grains and also polycrystalline NiO grains, as shown in Figure 32.

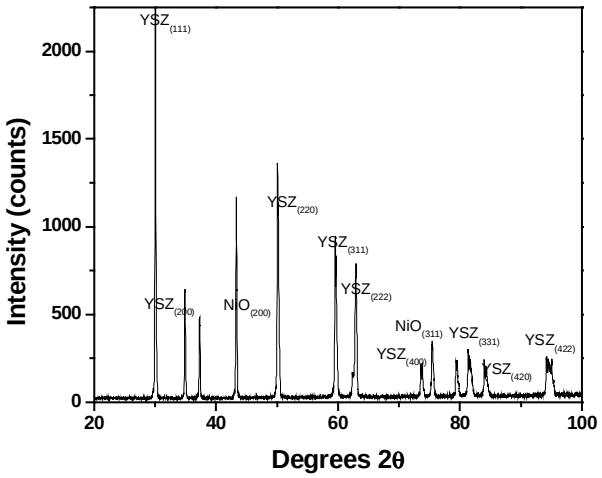

Figure 32. XRD pattern of YSZ film deposited by EPD.

Figure 33 shows the performance of a SOFC constructed on sintered bi-layers, tested in H_2 at varying temperatures.

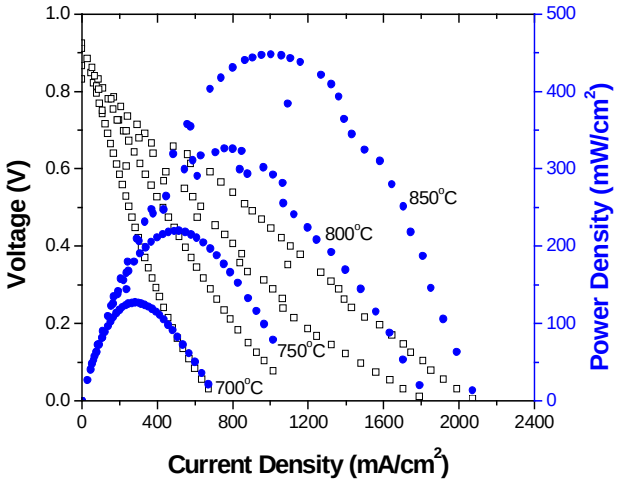

Figure 33. Performance characteristics of SOFC with configuration of NiO-YSZ/YSZ/LSM-YSZ as a function of operating current density, tested with H_2 as fuel at different temperatures. Power density represented by ● and voltage represented by □.

An open circuit voltage (OCV) of 0.91V was obtained at 850°C, suggesting that the YSZ layer was fairly dense, but that some gas leakage occurred. A peak power density of 611mW/cm^2 with a corresponding cell voltage of 0.41V was obtained at 850°C. The cell also exhibited a reasonably good performance at 750°C, with a power density of 384mW/cm^2. Such improved performance at intermediate temperature range is significant since this will help reduce the degradation of cell components, increase flexibility in cell design, and lower manufacturing costs by broadening materials choices, especially the use of cheap and readily available ferritic steel interconnectors.[41,42] The performance curves are in concurrence with the impedance data shown in Figure 34, as measured under open circuit condition from 650 to 850°C using a two-electrode configuration.

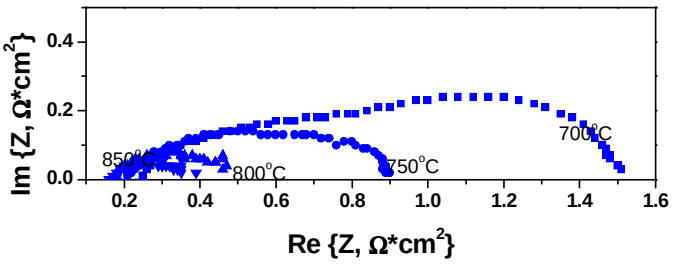

Figure 34. Typical impedance spectra of a SOFC with configuration of NiO-YSZ /YSZ/LSM-YSZ under open circuit condition using a two electrode configuration, tested using H_2 as fuel.

Decreasing the total interfacial impedance of an SOFC is an important objective for improving the performance of SOFCs. The total interfacial impedance determined from Figure 34 is presented in Table 10.

Table 10. Total interfacial resistance of SOFC at different operating temperatures.

Temperature (^oC)	Electrolyte resistance (ohm.cm$^{2)}$	Total interfacial resistance (ohm.cm$^{2)}$
650	0.256	0.56
700	0.227	0.39
750	0.188	0.32
800	0.154	0.3
850	0.145	0.22

4.3 Statistical Modeling & Reproducibility

Statistical design of experiments can be used for optimization of linear and non-linear systems.[224] Factorial designs allow the effects of several different factors to be analyzed and combined into a response model. To create a 2^k factorial design, all combinations of k-factors set at two different levels with respect to a central point are evaluated and the response must be assumed to be relatively linear over the range of factor levels. Though typically used for screening experiments rather than surface response modeling, 2^k factorial designs are easily augmented and/or modified to form robust designs.[224] Augmentation with centerpoint replicates allows for an estimate of pure experimental error and detection of curvature from second-order effects. Improved models for non-linear effects are achieved through augmentation into central composite designs.[225]

4.3.1 Factorial Design

Before fabricating the treatment combinations, some brief screening experiments were conducted to determine reasonable factor levels and the centerpoint placement. Depositions of YSZ were performed on porous NiO-YSZ pellets using varying voltages (25 to 500 V) and times (30 seconds to 5 minutes). The resulting green deposit was observed for substrate coverage, consistency and uniformity. After the preliminary

depositions were completed, high and low levels were chosen for each factor. The levels for factor A (substrate firing temperature) were chosen based on characterization of the substrate porosity and ranged from 1100°C-1300°C. Factor B (deposition voltage) and Factor C (deposition time) were chosen to range from 50-300V and 1-5min, respectively. SOFC performance and impedance spectroscopy characterization were measured using a Solartron 1287 electrochemical interface and Solartron 1255 frequency response analyzer running Corrware and Zplot software, respectively. The characterization range was from 550°C to 850°C with humidified hydrogen (3 vol% H_2O) as the fuel and air as the oxidant. Though the samples were characterized over a range of temperatures, statistical models were only prepared for the highest operating temperature, in this case 850°C.

A 2^3 factorial design with the addition of three centerpoint experiments was employed to determine both main and interaction effects on particle deposition, as shown in Figure 35 and Table 11.

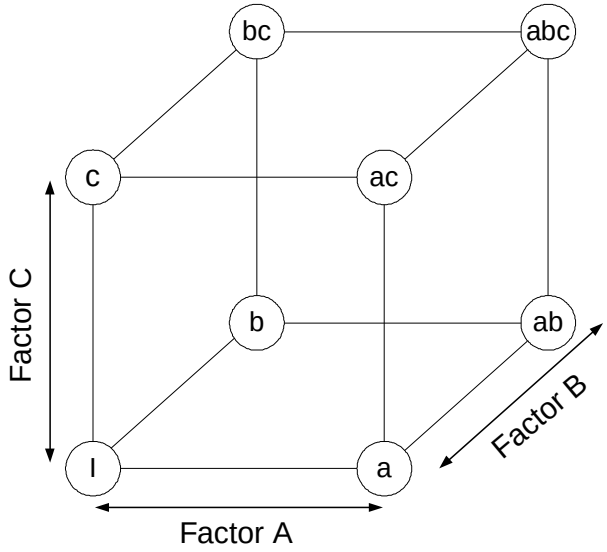

Figure 35. Schematic of the design matrix for 2^3 full factorial.

Table 11. Randomized experimental runs for 2^3 full factorial design with three repetitions of centerpoint.

Experiment Order	Run Order	Firing Temperature (°C)	Deposition Voltage (V)	Deposition Time (min)	Treatment Combination
1	9	1200	175	3	Center
2	10	1200	175	3	Center
3	8	1300	300	5	*abc*
4	7	1100	300	5	*bc*
5	3	1100	300	1	*b*
6	1	1100	50	1	-1
7	5	1100	50	5	*c*
8	11	1200	175	3	Center
9	2	1300	50	1	*a*
10	4	1300	300	1	*ab*
11	6	1300	50	5	*ac*

Design Expert v.7 statistical software (Stat-Ease, Inc.) was used to determine the geometric notation and coded notation as well as randomize the treatment combinations, resulting in a standard and experimental order. After all experiments were conducted, the desired responses of power density, area-specific interfacial resistance and deposition layer thickness were input into the factorial matrix, diagnosed and modeled using the software. Factor effects with a significance level of 0.05 or lower (p-value ≤ 0.05; 95% confidence level) were included in the regression models.

A 2^3 factorial design was chosen to model particle deposition because it provided the minimum number of experiments for which linear effects and interactions of all factors could be investigated. Each factor was run at two levels and the intermediate response was assumed to be linear, which is necessary for 2^k designs. The assumption of linearity is considered valid for such responses as open circuit voltage and substrate density, but may not be valid for deposition thickness and power density. There are methods to account for potential non-linearity within the design space, mainly through the introduction of centerpoints and model augmentation. Centerpoints are essentially used to test for evidence of pure second-order or quadratic effects in the response region of exploration, represented by the regression coefficient β_{jj}. Therefore, three repetitions of the centerpoint were added to the 2^3 factorial design. Centerpoint placement within the

experimental order can be random or non-random depending on a number of considerations. Randomizing the centerpoint runs allows the determination of linearity within the design matrix. Addition of centerpoints to the design matrix allows for determination of unusual occurrences throughout the experiments. In a well-known process, the centerpoint is often the normal operating condition and periodic placement (non-randomly) ensures negligible deviation from operating standards.[224] Plotting the periodic centerpoint responses in order can reveal abnormal baseline trends and experimental stability. When a new process is being used, the centerpoint experiments can be front-loaded in the run order to determine the magnitude and reasonableness of the variability. Since the EPD process was well known, but deposition on non-conducting substrates unknown, two centerpoint experiments were conducted at the beginning of the run order while a third was inserted randomly.

After completion of all factorial experiments and centerpoint runs, the treatment responses were used to determine the degree of main and interaction effects within a regression model. Analysis of variance was completed and models were generated for the responses of deposition thickness, power density and interfacial resistance, with each model indicating that all factors and interactions were significant. Table 12 shows the initial analysis of variance results for deposition thickness.

Table 12. Analysis of Variance of 2^3 full factorial model shown in Table 1. Note that the F-values listed are at the largest value allowed by the software and were driven to infinity as a result of insufficient degrees of freedom necessary to calculate the mean square error.

Source	Sum of Squares	Degrees Of Freedom	Mean Square	F Value	p-value Prob > F
Model	1541.671	7	220.239	63660000	< 0.0001
Firing Temperature	787.847	1	787.847	63660000	< 0.0001
Voltage	317.394	1	317.394	63660000	< 0.0001
Time	16.217	1	16.217	63660000	< 0.0001
*Firing Temperature*Voltage*	165.529	1	165.529	63660000	< 0.0001
*Firing Temperature*Time*	37.802	1	37.802	63660000	< 0.0001
*Voltage*Time*	158.509	1	158.509	63660000	< 0.0001
*Firing Temperature*Voltage*Time*	58.374	1	58.374	63660000	< 0.0001
Curvature	13.924	1	13.924	63660000	< 0.0001
Pure Error	0	2	0		
Cor Total	1555.595	10			

The regression model was only significant if all of the linear, interaction, and curvature terms were simultaneously included. However, there were insufficient degrees of freedom remaining to calculate the mean square error, which is the value representing the total model error. With a model error value of zero, unrealistically large F-values and R^2 and adjusted-R^2 values of unity resulted. F-values are calculated by dividing the mean square value for a factor by the mean square error for the entire model; therefore, the F-values would be driven to infinity with a mean square error of zero. The maximum F-values that could be output by the statistics software are displayed. Required mutual inclusion between the factors and interactions indicates that not enough information was present to form an accurate response model. Similar results were obtained for the analysis of variance of the power density and area-specific interfacial resistance responses.

4.3.2 Augmented Central Composite Design

The factorial model was therefore augmented with 6 axial runs and two additional centerpoints, forming a central composite design (CCD). In addition, the original 2^k

factorial experiments were repeated in order to validate the initial findings and potentially reduce model prediction error. The choice of central composite design (spherical or cuboidal) depends mainly on whether the resulting design matrix needs to be rotatable and whether the design region encompasses non-allowable conditions. Rotatable designs have equivalent prediction error for all design points, which is desired for optimization within an unknown system, yet necessitates more design runs and may not result in a significant reduction in prediction error compared to cuboidal or non-rotatable CCDs.[224,225,226] Since two faces of the factorial matrix were near the extremes of allowable operation, an inscribed CCD was chosen. Inscribed CCD's are rotatable and allow the experimenter to utilize data points at or near non-allowable operating conditions. Six inscribed design points were added randomly at coded factor levels of $\alpha = \pm 0.7$, along with two additional centerpoints. The inscribed CCD matrix and augmented treatment combinations are shown in Figure 36 and Table 13, respectively.

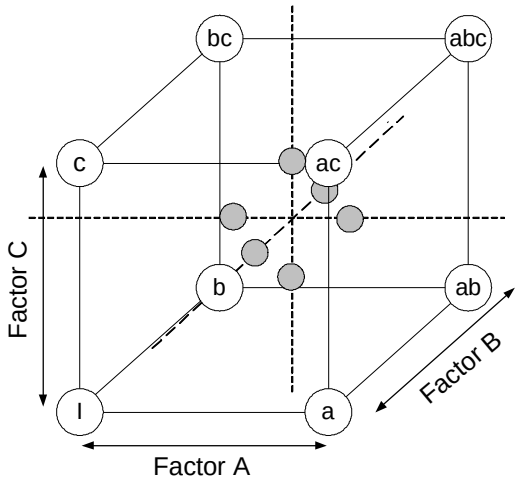

Figure 36. Inscribed CCD matrix resulting from augmentation of the 2^3 factorial design.

Table 13. Augmented design in actual terms. *Model validation experiment.

Standard Order	Experimental Run	Firing Temperature (^oC)	Deposition Voltage (V)	Deposition Time (min)	Power Density ($mW*cm^{-2}$)	Area-specific Resistance ($ohm*cm^2$)	Thickness (um)
17	1	1200	175	3	447	0.19	20
19	2	1200	175	3	442	0.191	20.2
8	3	1300	300	5	10	6.7	6.3
7	4	1100	300	5	406	0.47	38
3	5	1100	300	1	45.5	0.46	40.5
1	6	1100	50	1	611	0.215	5.3
5	7	1100	50	5	232	0.75	25
11	8	1200	175	3	442	0.191	20.2
2	9	1300	50	1	6.2	5.4	24
4	10	1300	300	1	0.7	5.9	11
6	11	1300	50	5	3	5.9	5.5
10	12	1100	50	5	224	0.72	27.5
8	13	1300	300	1	3.1	7.1	12
16	14	1300	300	5	5.2	6.1	7
12	15	1300	50	5	7	4.3	7
1	16	1100	50	1	628	0.21	6
18	17	1200	175	3	452	0.187	19.6
13	18	1100	300	5	404.7	0.44	38
5	19	1100	300	1	38	0.46	42
23	20	1200	262.5	3	35	2.9	23
26	21	1200	175	3	449	0.192	19.9
27	22	1200	175	3	431	0.189	20
24	23	1200	175	1.6	210	0.32	19
22	24	1200	87.5	3	100	1.2	14.6
25	25	1200	175	4.4	160	0.86	21
21	26	1270	175	3	80	2.7	13
20	27	1130	175	3	450	0.3	26
28*	28*	1174	216	3	616	0.192	25.9

4.3.3 Model for Deposit Thickness

Deposit thickness has a linear relation with deposition time and the amount of charge passed.[137,176] The statistical analysis in the present study also identified significant two-factor interactions. Figure 37(a-c) shows the surface response and interaction plots for the regression model for deposition thickness.

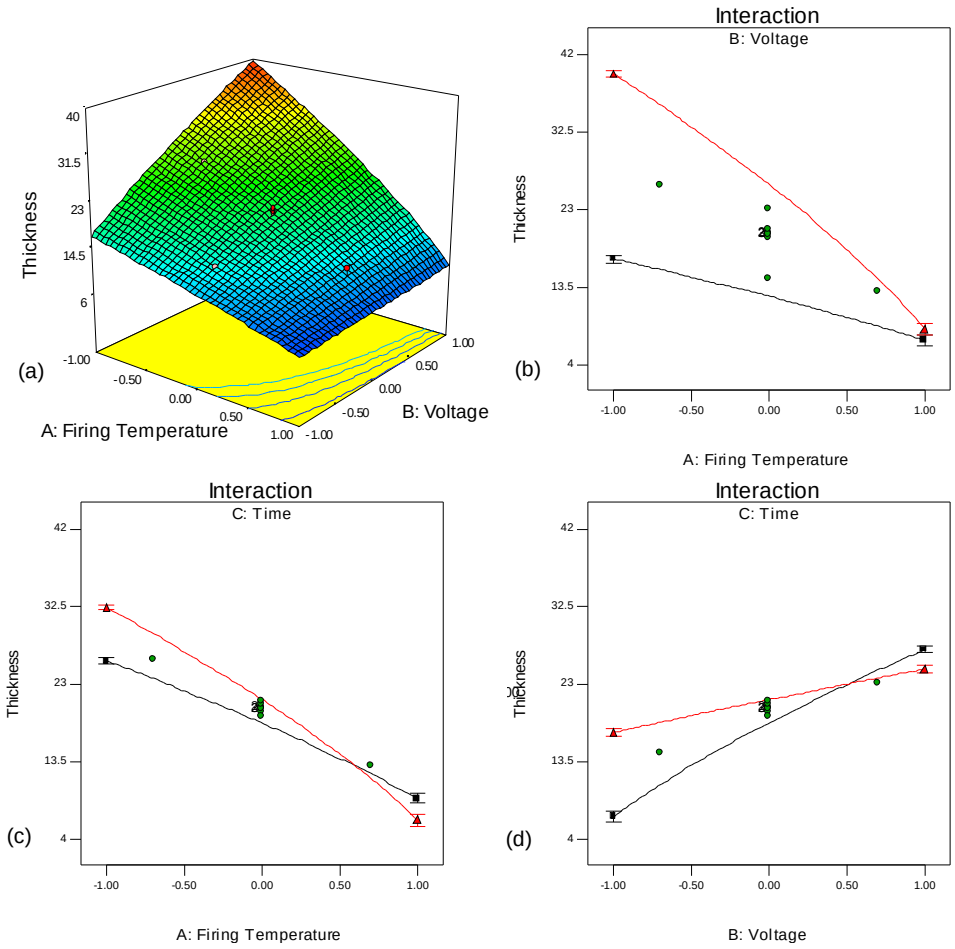

Figure 37. (a) Surface response plot for thickness model along with the (b) single factor and (c) interaction plots. Note that for single factor and interaction plots ▲ represents the high factor level and ■ represents the low factor level.

Interaction plots were generated from model predictions by holding the factor not included in the plot at its intermediate level. Based on trends observed in the diagnostic residual and Box-Cox plots, as shown in Figure 38, no transform of the raw data was necessary.

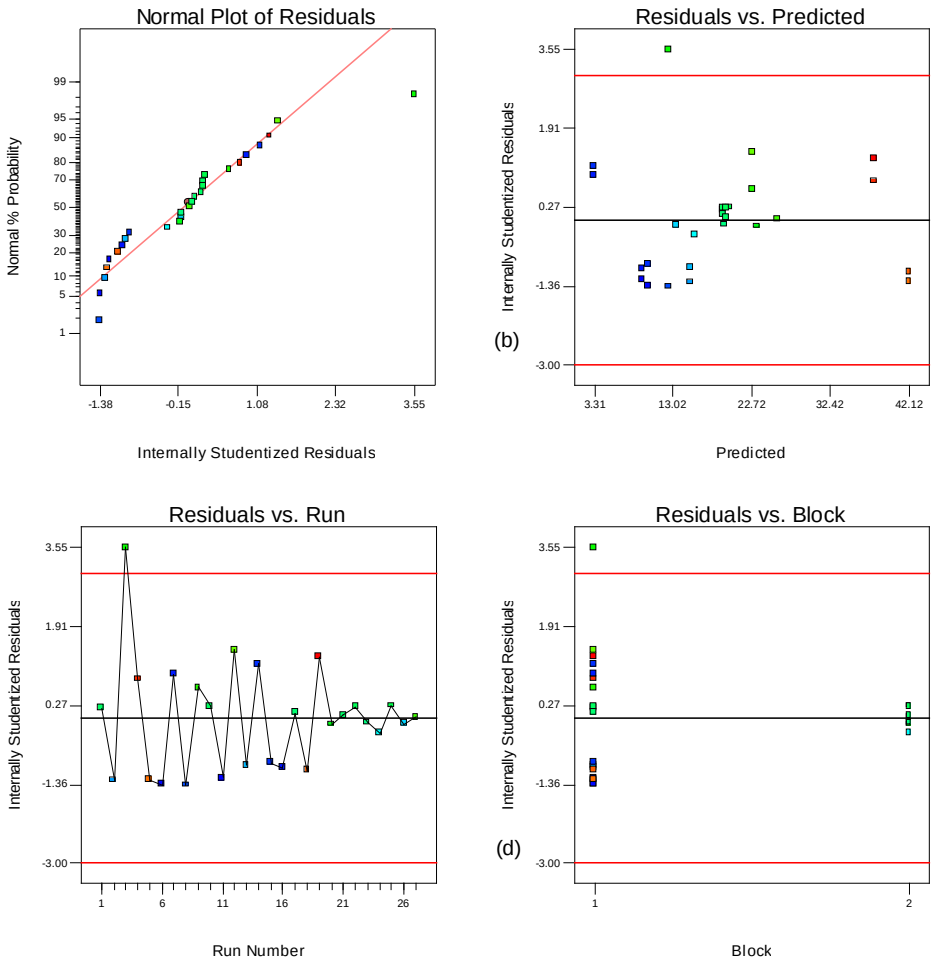

Figure 38. Residual plots of thickness model after power transform. (a) Normal probability plot of residuals (b) residuals versus predicted (c) residuals versus run number and (d) residuals versus block. Note the outlier (experimental run #3) on the right of the normal probability plot and also at the top of the residual plots.

The diagnostic plots therefore had a normal distribution with the exception of experimental run #3, which will be discussed later. The regression equation for deposition thickness is:

Equation 17

$$Thickness = 19.40 - 8.87(FiringTemperature) + 5.45(DepositionVoltage) + 0.41(Time) - 6.5(FiringTemperature * DepositionVoltage) - 4.06(FiringTemperature * DepositionTime) - 2.3(DepositionVoltage * DepositionTime)$$

Since all of the linear effects and two-factor interactions were significant (the linear *Time* term remains in the model due to hierarchy) in the analysis of variance, as shown in Table 14, the full and reduced models are identical.

Table 14. Analysis of Variance of reduced thickness interaction model.

Source	Sum of Squares	Degrees Of Freedom	Mean Square	F Value	p-value Prob > F
Block	1.295	1	1.295		
Model	2868.757	6	478.126	25.58	< 0.0001
Firing Temperature	1337.485	1	1337.485	71.55	< 0.0001
Voltage	503.684	1	503.684	26.94	< 0.0001
Time	2.886	1	2.886	0.15	0.6988
*Firing Temperature*Voltage*	676.000	1	676.000	36.16	< 0.0001
*Firing Temperature*Time*	264.063	1	264.063	14.13	0.0013
*Voltage*Time*	84.640	1	84.640	4.53	0.0467
Residual	355.188	19	18.694		
Lack of Fit	212.087	8	26.511	2.04	0.1359
Pure Error	143.102	11	13.009		
Cor Total	3225.240	26			

Quadratic terms were not significant and only increased the error if forced into the model. The fact that no quadratic terms were significant shows that the model follows a fairly linear trend between thickness and such variables as time and voltage, as mentioned previously. The linearity between thickness and time and indirectly between thickness and the amount of charge passed is demonstrated around the centerpoint, as shown in Figure 39(a-b).

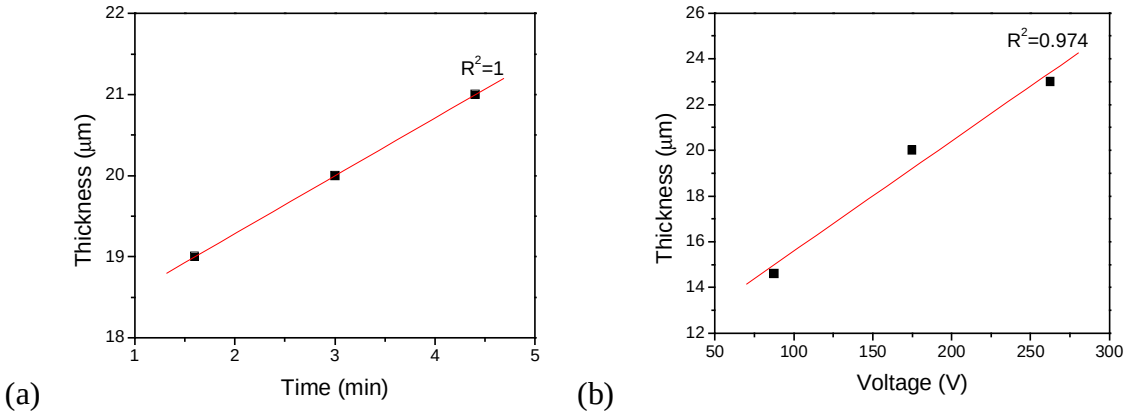

Figure 39. Linear relationship between deposition thickness and (a) time and (b) voltage around the centerpoint experiments.

The presence of interaction terms in the model gives rise to some curvature at the extreme factor levels, which is why slight non-linearity is observed at the high and low levels of substrate firing temperature. The regression coefficients and their corresponding *t*-values are listed in Table 15.

Table 15. Thickness model regression coefficients and their corresponding *t*-values.

Variable	Coefficient	*t*-value
Intercept	19.398	
Firing Temperature	-8.875	-8.458
Voltage	5.446	5.191
Time	0.412	0.393
*Firing Temperature*Voltage*	-6.500	-6.013
*Firing Temperature*Time*	-4.063	-3.758
*Voltage*Time*	-2.300	-2.128

Values of |t|>2.0 indicate at least 90% significance
Regression model R^2=0.890, Adj R^2=0.855
Standard error of design (Sy.x) = 4.32

The reduced model statistics of standard error (4.32), R^2 (0.890), adjusted-R^2 (0.855), and the signal to noise ratio (16.5) show that the model can account for nearly all the variability in the response data. The externally studentized residuals and Cook's

Distance plots did reveal one outlier point, experimental run #3 from Table 13, however the leverage plot didn't indicate the outlier influenced the response model more than any other data points as shown in Figure 40.

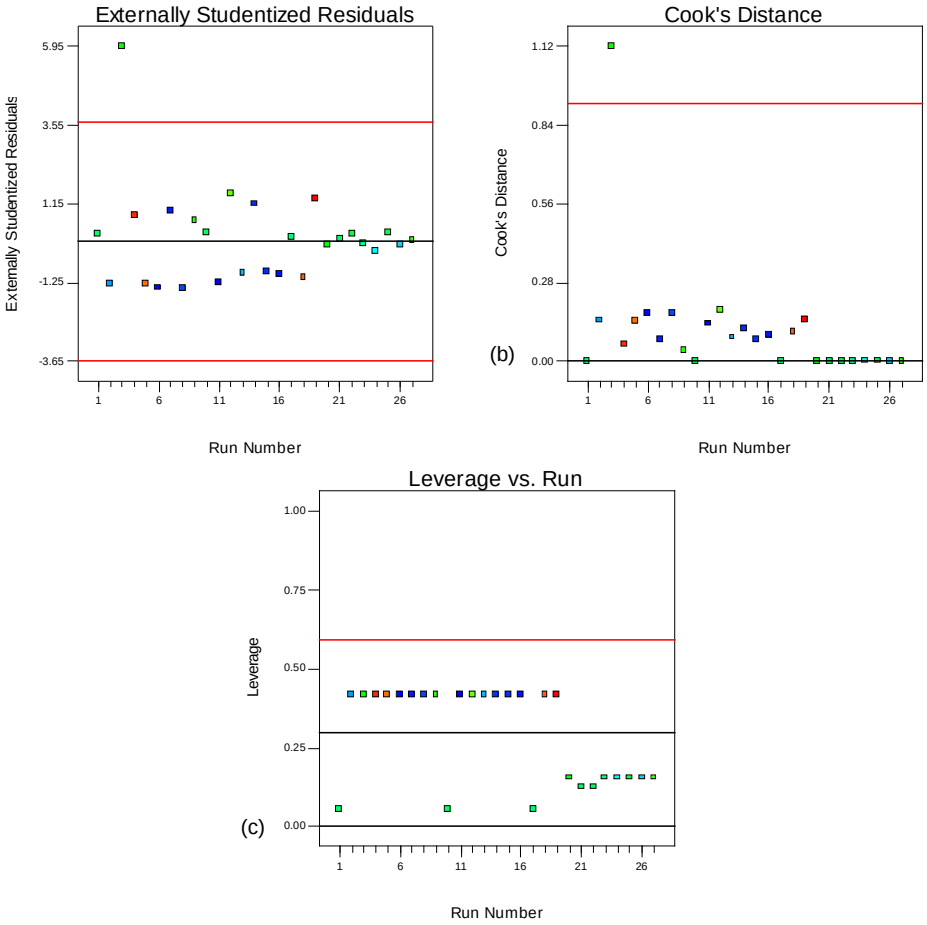

Figure 40. Plots showing the influence of individual responses on the thickness model. (a) Externally studentized residuals (b) Cook's Distance and (c) leverage plot. Note that the outlier (experimental run #3) point is present at the top of the studentized residual and Cooks distance plots, but doesn't have a greater leverage on the response than the other data points.

The outlier data point (experimental run #3) was replicated in experimental run #8, which resulted in a thickness value that appeared more suitable for the deposition parameters. Experimental run #8 is therefore considered a truer value for that treatment combination

and we speculate that the high thickness value observed for the outlier run was the result of a greater than normal porosity in the substrate.

An increase in the substrate firing temperature inhibits deposition thickness as seen in the regression equation and Figure 37(a). The reasoning for this is that as the substrate is fired at higher temperatures, the substrate porosity decreases. Since the substrate firing temperature has such a large significance compared to the other factors listed in Table 15, porosity is believed to be the most influential factor on YSZ deposition. The effect of porosity hasn't been completely quantified, however, because potential contributing effects of particle curvature can't be separated from the firing temperature factor. Though probably negligible compared to the porosity, the effects of firing temperature on particle curvature can't be ignored.

Except at the highest firing temperature tested, voltage has a positive effect on deposition thickness, as increasing voltage will increase the particle transport and deposition rates.[137,140,144] Reports have indicated that thickness varies linearly with voltage over a certain voltage range.[175,180] The surface response in Figure 37(a) shows that the positive voltage effect lessens with increasing firing temperature and is negligible at the highest temperature. Conversely, the temperature effect is also reduced as the voltage is lowered. The changing effects correspond to the interaction term.

Deposition time has been reported previously to have a positive effect on thickness.[145] Most reports indicate that there is a linear relation between thickness and time under constant current and constant concentration conditions. The conditions used in these experiments were constant concentration, but not constant current and therefore a complete comparison couldn't be made. The relationship between the thickness and time appears to depend on the substrate firing temperature, as indicated by the significant interaction. For all substrates fired at the lowest level (1100°C), the deposition thickness varies linearly with deposition time. This is not the case however as the substrate firing temperature is increased. At higher levels of firing temperature the deposition thickness

appears concave, leveling off just as seen in other reports. [145,181] Concavity within the deposition profile is probably due to the non-linear relation between the substrate firing temperature and the resulting substrate porosity.

All two-factor interactions were found to effect deposition thickness. The interactions of deposition voltage and time with firing temperature are significant because as the firing temperature increases there is less porosity and therefore less ability for the conducting electrolyte to move through the substrate.[216] Subsequently, as firing temperature increases more voltage and time are necessary to build up a film deposit. Due to the decrease in substrate porosity however, the deposit thickness necessary to reduce the deposition rate is lessened. The deposition voltage - deposition time interaction results in a reduced layer thickness, which isn't intuitive for the EPD process. The regression coefficient is the combination of the voltage-time interactions at each level of firing temperature. Since the deposit thickness relates linearly with firing temperature only at the lowest level studied, voltage and time effects only increase the thickness linearly at the lowest level of firing temperature. When the voltage-time interaction is studied at higher levels of firing temperature, the results are mixed. Lower values of the voltage-time interaction and higher levels of firing temperature typically lead to less particle velocity and deposition. The negative sign of this interaction coefficient therefore indicates the strong necessity of porosity for deposition, regardless of the voltage and time. High voltage and longer deposition time will still result in thin deposits even if the porosity is too low. This implies that there must be a critical porosity above which the voltage-time interaction has a positive affect and below which the voltage-time interaction has a negative affect. The response data indicates that the critical porosity level is achieved at temperatures near 1100°C.

4.3.4 Model for Power Density

A regression model based on the main, interaction and quadratic effects was developed from the observed power density responses. Analysis of variance of the full model revealed trends in the residual plots, suggesting a variance stabilizing transformation of the power density values should be performed before a regression model is developed. A Box-Cox plot indicated a logarithmic transform would be the most appropriate, which proved to negate any trends in the residual plots and normalize the data set. The regression equation in actual terms is given below and the surface response plot is shown in Figure 41(a-c):

Equation 18

$$Log_{10}(PowerDensity) = 2.52251 - 0.86651*Temperature - 0.15462*Voltage + 0.14949*Time + 0.25586*Voltage*Time - 1.20266*Voltage^2$$

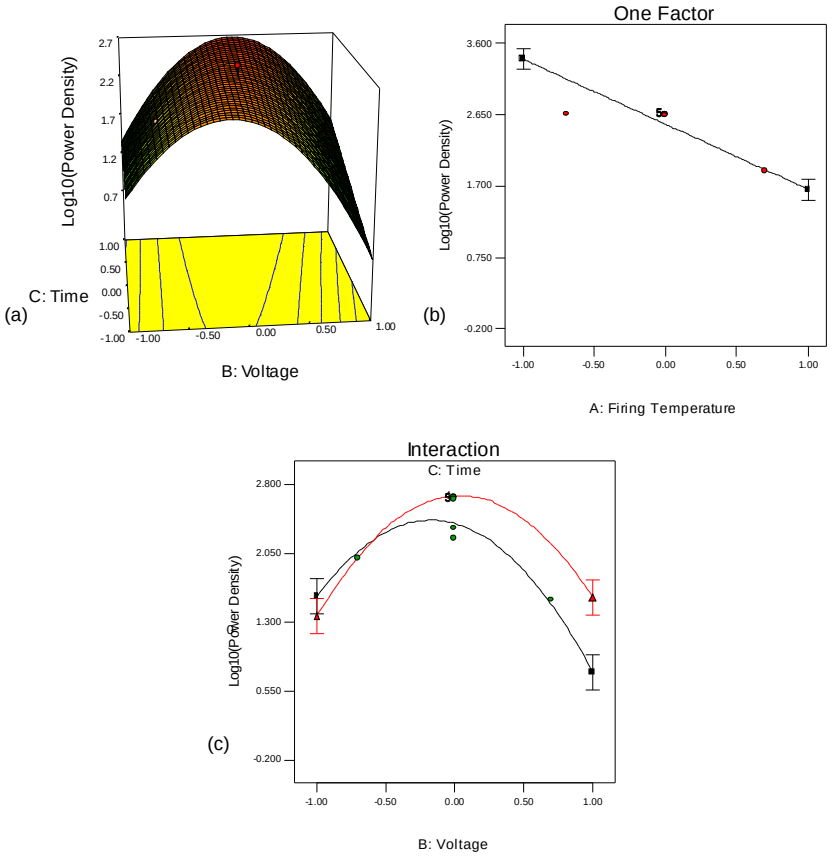

Figure 41. (a) Surface response plot for power density model along with the (b) single factor Firing Temperature and (c) Deposition Voltage-Deposition Time interaction plots. Note that for single factor and interaction plots ▲ represents the high factor level and ■ represents the low factor level.

Although the model contains a quadratic term and the R^2 values are very high, there is no evidence of "overfitting," which would be the case if the model error were significantly lower than the measured experimental error. The model error (Sy.x=0.232) is not lower than the experimental error (S_{test}=0.190) estimated by the pooled standard deviation of repeat experiments. The experimental error variance term (S_{test}^2), is also reported as the mean square pure error in the ANOVA, shown in Table 16.

Table 16. Analysis of Variance (ANOVA) of reduced power density quadratic model.

Source	Sum of Squares	Degrees of Freedom	Mean Square	F Value	p-value Prob > F
Block	1.983	1	1.983		
Model	18.757	5	3.751	69.703	< 0.0001
Firing Temperature	12.749	1	12.749	236.886	< 0.0001
Voltage	0.406	1	0.406	7.543	0.0124
Time	0.379	1	0.379	7.051	0.0152
*Voltage*Time*	1.047	1	1.047	19.462	0.0003
Voltage^2	4.175	1	4.175	77.574	< 0.0001
Residual	1.076	20	0.054		
Lack of Fit	0.678	9	0.075	2.082	0.1254
Pure Error	0.398	11	0.036		
Cor Total	21.816	26			

The regression coefficients determined at a 95% confidence interval and their corresponding *t*-values are listed in Table 17.

Table 17. Power density model regression coefficients and their corresponding *t*-values.

Variable	Coefficient	*t*-value
Intercept	2.523	
Firing Temperature (^oC)	-0.867	-15.39
Voltage (V)	-0.155	-2.75
Time (min)	0.149	2.66
*Voltage*Time (V*min)*	0.256	4.41
Voltage^2 (V^2)	-1.203	-8.81

Values of |t|>2.1 indicate at least 95% confidence level

Regression model R^2=0.946, Adj R^2=0.932

Standard error of model (Sy.x) = 0.232

Model reduction lead to little change in the amount of variability explained by the model. Reducing the model slightly decreased the R^2 statistic from 0.953 to 0.946, but the standard error was favorably lowered from 0.242 to 0.232. The adjusted-R^2 statistic was 0.932 after reduction, correlating very well with the reduced model R^2 statistic. Other model statistics such as the predicted error sum of squares (PRESS) and predicted-R^2, and their correlation with the R^2 and adjusted R^2 statistics, indicated that the reduced model is a good predictor and that reduction increased the model's ability to explain variability in new data. Diagnostic plots of the reduced model with a logarithmic transform of the density values showed an as expected normal probability plot of residuals as well as structureless residual plots, as shown in Figure 42.

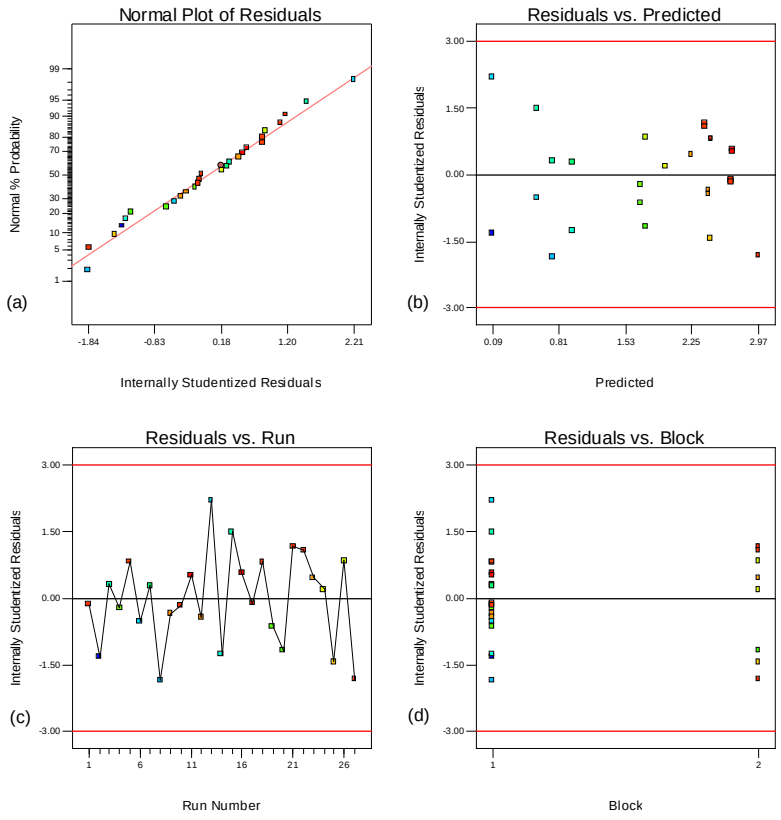

Figure 42. Residual plots of power density model after logarithmic transform. (a) Normal probability plot of residuals (b) residuals versus predicted (c) residuals versus run number and (d) residuals versus block.

Though two data points appeared separate from the other responses in the leverage plots, as shown in Figure 43, they were not outliers and the overall model lack of fit is insignificant.

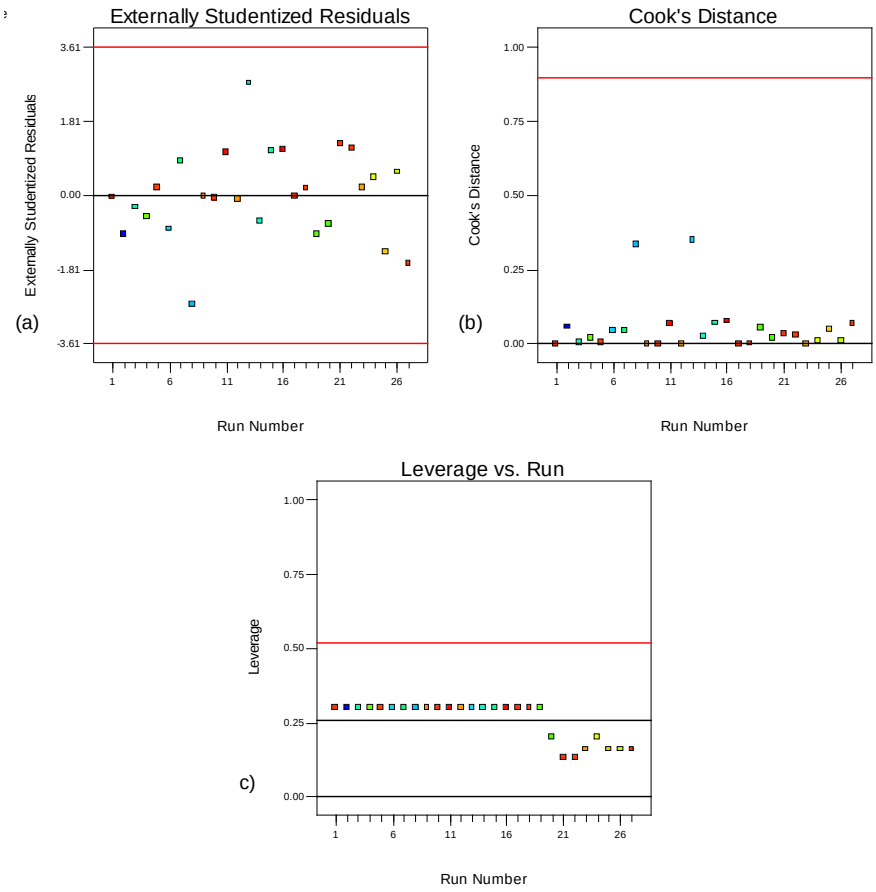

Figure 43. Plots showing the influence of individual responses on the power density model. (a) Externally studentized residuals (b) Cook's Distance and (c) leverage plot.

As seen in the regression Equation 18 for the reduced model, all main effects were significant as well as the voltage-time interaction and the voltage quadratic term. Insignificant factors were the substrate firing temperature interaction effects and the quadratic factors for the substrate firing temperature and deposition time. Overall the power density increases as the substrate firing temperature is decreased. A decrease in

the firing temperature leads to increased porosity and therefore increased mobility of the conducting species within the substrate, which results in a more uniform and densely packed deposit. This correlates well with our proposed deposition mechanism on porous non-conducting substrates, which states that adequate porosity will allow deposition to occur even in the absence of substrate conductivity.[216] The highest and lowest power densities were observed at the lowest and highest levels of substrate firing temperature, respectively, which explains why it has the largest *t*-value of all significant effects. Further decreases in substrate firing temperatures could potentially increase power density, however experimentally these samples weren't mechanically able to withstand the spring forces in the EPD apparatus and also lacked the microstructural phase connectivity necessary for percolation in the anode. [216]

Deposition voltage has a non-linear effect on power density, with a strong voltage-time interaction. Although the single highest power density observed during the experiments was at the lowest voltage, model predictions shown in Figure 41(a) indicate the lowest voltage level may not be optimal. Voltage only relates to the deposit through its influence on the electric field. Since the electrode spacing remained constant throughout all experiments, the effect of the electric field is proportional to the applied voltage. The voltage and further the electric field present in the suspension effectively influence the mobility of the particles and how fast they deposit. Higher deposition voltages lead to higher mobility's, but don't necessarily allow the particles time to pack together.[133,137,145,149,177] Typically, lower voltages lead to increased deposit density due to increased particle packing.[172, 176-182,216] Deposition time itself will lead to a sufficiently thick layer of material, however the density of that layer is linked to the deposition rate of the particles and therefore the electric field and the deposition voltage. [177,181] Insufficient deposition time will result in non-uniformity, pinholes and small pores in the deposit, which will lead to lower power density.[172,176,178-182] This explains why the deposition voltage - deposition time interaction was significant in the power density model.

4.3.5 Model for Area-Specific Resistance

A quadratic regression model was developed for area-specific interfacial resistance (ASR) between the electrolyte and the two electrodes. After model reduction, the significant effects were firing temperature, voltage, the firing temperature-voltage interaction and a quadratic voltage term, as shown in Table 18.

Table 18. Analysis of Variance (ANOVA) of reduced area-specific resistance quadratic model.

Source	Sum of Squares	Degrees of Freedom	Mean Square	F Value	p-value Prob > F
Block	14.816	1	14.816		
Model	147.715	4	36.929	120.667	< 0.0001
Firing Temperature	119.550	1	119.550	390.636	< 0.0001
Voltage	1.863	1	1.863	6.089	0.0223
*Firing Temperature*Voltage*	1.302	1	1.302	4.256	0.0517
Voltage^2	24.999	1	24.999	81.687	< 0.0001
Residual	6.427	21	0.306		
Lack of Fit	4.201	10	0.420	2.076	0.1233
Pure Error	2.226	11	0.202		
Cor Total	168.958	26			

The regression equation is given and regression coefficients with their corresponding *t*-values listed in Table 19.

Equation 19

$$ASR = 0.47437 + 2.65342 * FiringTemperature + 0.33127 * Voltage + 0.28531 * FiringTemperature * Voltage + 2.94295 * Voltage^2$$

Table 19. Area-specific resistance model regression coefficients and their corresponding t-values.

Variable	Coefficient	*t*-value
Intercept	0.474	
Firing Temperature	2.653	19.765
Voltage	0.331	2.468
*Firing Temperature*Voltage*	0.285	2.063
Voltage^2	2.943	9.038

Values of |t|>2.0 indicate at least 90% significance
Regression model R^2=0.958, Adj R^2=0.950
Standard error of design (Sy.x) = 0.559

Figure 44(a-c) shows the ASR surface response and interaction plots.

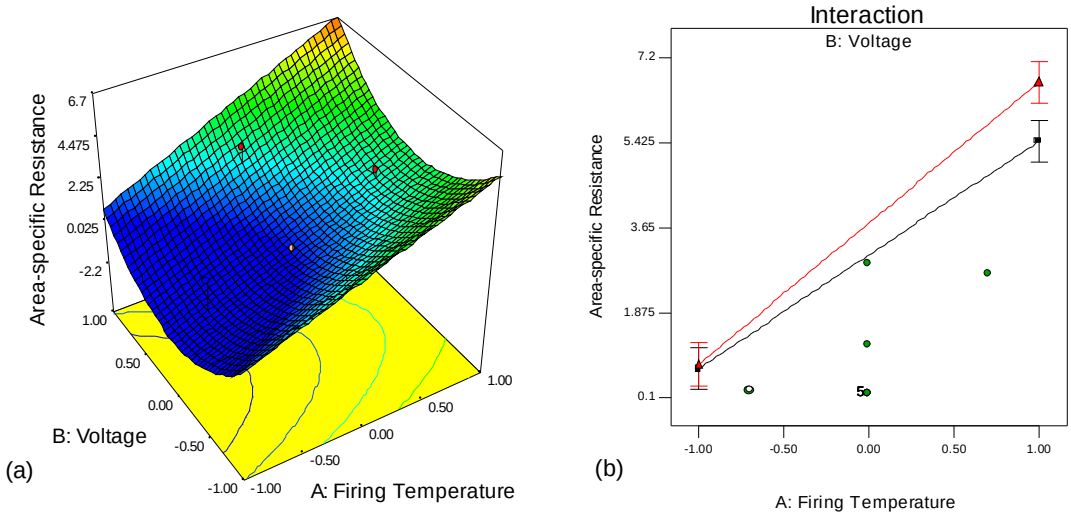

Figure 44. (a) Surface response plot for area-specific resistance model along with the (b) single factor Firing Temperature and (c) Deposition Voltage-Deposition Time interaction plots. Note that for single factor and interaction plots ▲ represents the high factor level and ■ represents the low factor level.

No single factor plots are shown because all factors are also present in interactions. Although the R^2 values are high and the model contains a quadratic term, there is no evidence of "overfitting," as the model error (Sy.x = 0.553) is higher than the experimental error (S_{test}=0.449). Though there are no apparent trends in the diagnostic plots, as shown in Figure 45, the Box-Cox plot did recommend a square root transform, which had a negligible affect on the model statistics and in the end wasn't used.

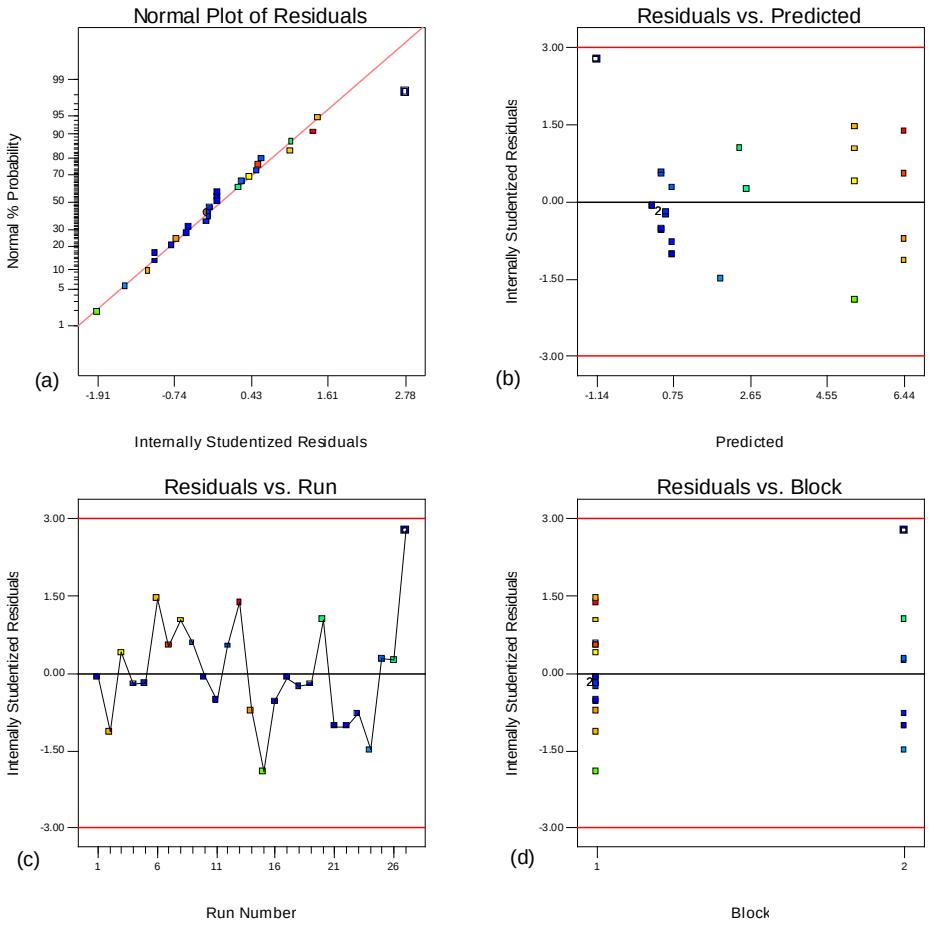

Figure 45. Residual plots of area-specific resistance model after logarithmic transform. (a) Normal probability plot of residuals (b) residuals versus predicted (c) residuals versus run number and (d) residuals versus block.

Experimental run #27 was found to be close to the outlier threshold according to the externally studentized residual plot, however its Cook's Distance and leverage were comparable to all other samples, as shown in Figure 46.

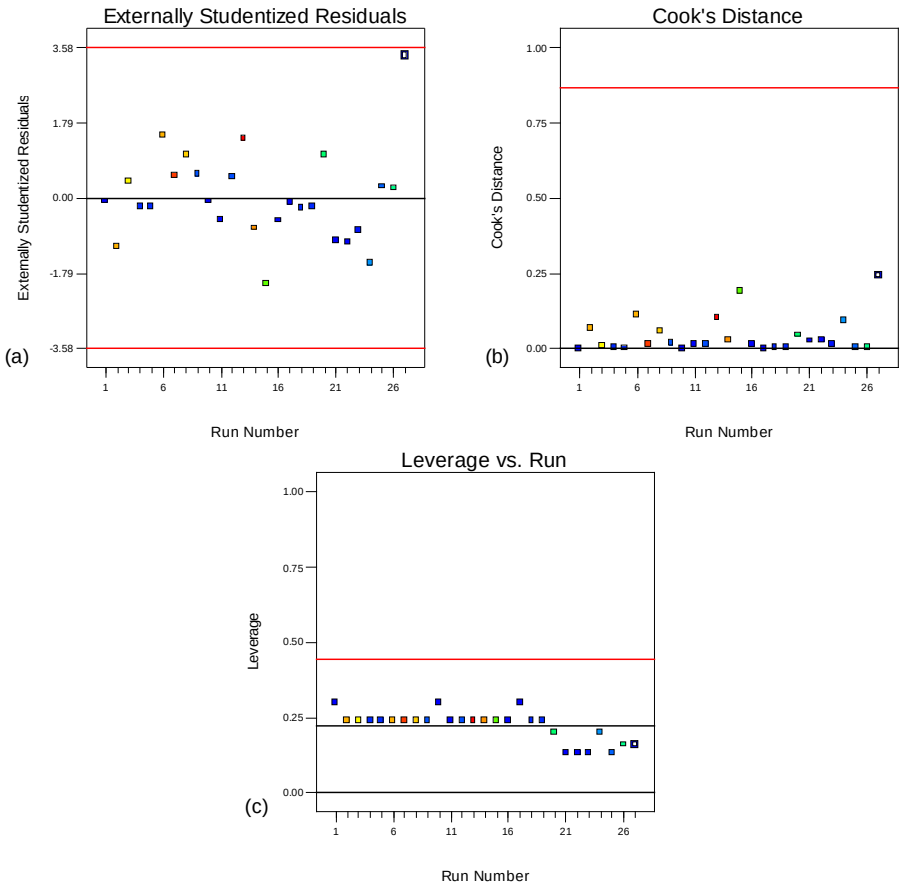

Figure 46. Plots showing the influence of individual responses on the area-specific resistance model. (a) Externally studentized residuals (b) Cook's Distance and (c) leverage plot.

This point was not deleted when establishing the model. Model reduction resulted in only a small decrease in the amount of total variability explained by the model. In fact, the reduced model is able to explain a greater amount of variability (adjusted-R^2 remained constant at 0.95) and is a better predictor of experimental data (predicted-R^2 increased from 0.897 to 0.935) than the unreduced model.

Substrate firing temperature increases the area specific interfacial resistance between the electrolyte and the electrodes, as seen in the regression Equation 19 and Figure 44(a). The major contributor to increasing area-specific resistance with firing temperature is loss in substrate porosity. Porosity is believed to be fundamental to the

deposition process on non-conducting substrates, since dense non-conducting substrates do not exhibit any deposit. Therefore any decrease in porosity should hinder the deposition process and lead to increased area-specific resistance. Another possible contributor to ASR increase is the reduced curvature of the particle surface due to the higher firing temperature. It's conceivable that reducing the particle curvature could affect the deposition process if there is in fact a charge transfer step. A fundamental study to separate the contributions of porosity and degree of particle coarsening was not performed, however it'll be a necessary part of any future study to determine the deposition mechanism.

Voltage has the largest overall effect on ASR. The non-linear relationship shown in Figure 44(a) indicates the highest ASR values occur at the highest voltage levels. Deposit porosity and uniformity is directly linked to applied voltage and area-specific resistance is highly dependent on surface area contact/coverage. Increasing the voltage should lead to a more porous deposit layer and higher ASR due to less contact area. The regression equation also includes a relatively weak firing temperature-voltage interaction. Therefore, to minimize ASR, the firing temperature should be low to ensure sufficient porosity and the voltage should also be relatively small in order to obtain a dense deposit of high contact area.

4.3.6 Model Validation

After all the experiments and appropriate response models were completed, a final validation and optimization experiment was performed. The numerical optimization feature of Design Expert v.7 (Stat-Ease, Inc.) allowed the preparation of an experiment based on a set of input criteria. The independent factors were all set to be in the range of the experimental matrix and the responses were set at desired levels: deposition thickness was set to be in the range of the experimental matrix, power density was set to be maximized and area-specific interfacial resistance was set to be minimized. The solution

with the highest level of desirability for achieving the optimum conditions was predicted to be experimental run #28, as listed in Table 13. Table 20 lists the predicted results based on the numerical solution and the actual experimental results for the validation experiment.

Table 20. Predicted versus experimental values for the model validation experiment.

	Predicted Values	Experimental Values	Error (%)
Power Density (mW/cm^2)	628	616	1.91
Area-specific Resistance ($ohm*cm^2$)	0.187	0.192	2.67
Deposition Thickness (um)	25.7	25.9	0.78

There is good correlation between the predicted and experimental results as seen with the low error, suggesting that the model can predict data accurately. Figure 47 shows the current-voltage characteristics of the cell fabricated for the validation experiment.

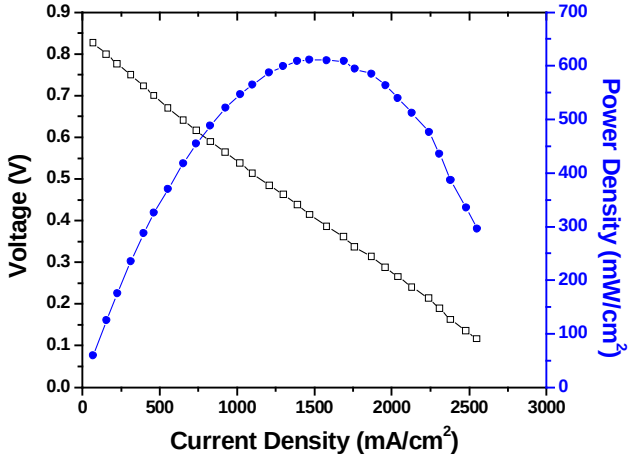

Figure 47. Current-voltage characteristics for validation experiment.

4.4 Fundamentals of Deposition

Suspensions for EPD were prepared at a fixed concentration of 10g/L by adding 1.75g of YSZ powder (0.3µm, Tosoh) into 175mL of acetylacetone solvent (>99%,

Aldrich Chemical Co.). Each suspension was ultrasonicated for at least 20 minutes prior to the initial deposition, 5 minutes between depositions, and was replenished after every 5 depositions. The zeta potential of each suspension was determined after ultrasonication, using a Delsa 440SX. The suspension conductivity and dielectric constant were also measured after ultrasonication using a Solartron 1296 dielectric interface and Solartron 1255 frequency response analyzer operating under SmaRT v2.20 software.

All depositions were performed under constant stirring in a 250mL beaker and the entire EPD setup was described elsewhere.[216] The EPD cell the same as used previously, as shown in Figure 28. The counter electrode was a 2cm diameter Pt disk and the working electrode was a 1.3cm carbon disk backed by a 0.5mm Pt wire, which was coiled up to act as a spring against the deposition substrate. A high voltage DC power supply unit (Model PS 310, Stanford Research Systems, USA) was used to provide a constant voltage of 25V to 300V for the EPD experiments.

The non-conductive deposition substrates were all prepared by tape casting, as reported elsewhere.[216,219] Commercial NiO powder (<10μm, Alfa Aesar) was milled, with 6mm YSZ media, in ethanol for 96 hours to reduce the particle size. The powder was then dried and mixed with YSZ powder (D_{50}=0.26μm, Daiichi Kogenso Corp.) in a 65:35 (NiO:YSZ) ratio. The powder was added to a 1:1 solvent mixture of ethanol and xylenes containing 3-wt% Menhaden fish oil dispersant (Richard E. Mistler, Inc.). After 12 hours of ball-milling, polyalkylene glycol and butyl benzyl phthalate (plasticizers) and polyvinyl butyral (binder) were added in amounts of 3, 1.54 and 3 wt%, respectively. The slurry was milled for another 24 hours, degassed and then cast at a rate of 8.5cm/min and a blade height of 150μm. The slurry formulation for the NiO-YSZ tape is shown in Table 21.

Table 21. Slurry formulation for NiO-YSZ tape.

Component	Purpose	Weight (%)	Weight (g)	Volume (%)	Volume (cm^3)
YSZ	powder		17.505	7.7	2.918
NiO	powder	65	32.495	9.6	3.651
Ethanol	solvent	12	9.23	30.23	11.5
Xylenes	solvent	12	9.23	30.23	11.5
Menhanden Fish Oil	dispersant	3	2.307	6.06	2.307
Polyalkylene Glycol	plasticizer (type I)	3	2.307	6.06	2.307
Butyl Benzyl Phthalate	plasticizer (type II)	2	1.54	4.04	1.54
Polyvinyl Butyral	binder	3	2.307	6.06	2.307

Pore formers (SnO_2, carbon black or starch) were added to subsequent NiO-YSZ tapes in amounts ranging from 5-25 wt % in order to systematically increase porosity. All tapes were then punched into 13mm disks, pressed into pellets from 100μm-1mm and sintered in air at temperatures ranging from 1000°C-1400°C for 2hrs. The density, open and impervious porosity of each sample, as determined using the Archimedes method, are listed in Table 22.[227]

Table 22. Archimedes measurements on all substrates used for EPD.

Substrate	Sintering Temperature (°C)	Substrate Thickness (μm)	Bulk Density (g/cm^3)	Total Porosity (%)	Open Porosity (%)
Pt Electrode[a]	N/A	500	21.4	0	0
Carbon Cloth[a]	N/A	200	0.48	80	80
NiO-YSZ	1100	100	3.05	52.55	32.14
NiO-YSZ	1100	200	3.05	52.55	32.14
NiO-YSZ	1000	300	2.38	63.11	31.74
NiO-YSZ	1100	300	3.05	52.55	32.14
NiO-YSZ	1200	300	3.63	43.57	30.5
NiO-YSZ	1300	300	3.43	32.6	25.1
NiO-YSZ	1400	300	4.99	22.47	18.87
NiO-YSZ	1100	500	3.05	52.55	32.14
NiO-YSZ	1100	700	3.05	52.55	32.14
NiO-YSZ	1100	1000	3.05	52.55	32.14
NiO-YSZ+10wt% Carbon	1100	100	2.33	63.77	59.95
NiO-YSZ+10wt% Carbon	1100	300	2.33	63.77	59.95
NiO-YSZ+15wt% Carbon	1100	300	2.31	66.38	64.11
NiO-YSZ+15wt% Carbon	1200	300	2.31	49.66	47.97
Ni-YSZ	1100	300	2.55	62.8	38.41
Ni-YSZ+10wt% Carbon	1100	300	1.95	76.21	71.64
NiO-YSZ+5wt% SnO_2	1100	300	2.98	53.71	24.96
NiO-YSZ+10wt% SnO_2	1100	300	1.64	74.54	27.42
NiO-YSZ+15wt% SnO_2	1100	300	1.45	77.46	30.04
NiO-YSZ+20wt% SnO_2	1100	300	1.88	70.78	48.21
NiO-YSZ+25wt% SnO_2	1100	300	1.58	75.45	57.67
YSZ+21.5wt% Carbon	1100	300	1.66	74.15	33.27

[a] Based on Manufacturers Report, not measured by Archimedes Method

Various experiments were conducted to determine the effects of each parameter on the area-specific deposit mass deposit thickness and deposit density including substrate porosity, substrate thickness, applied voltage, deposition time, electrode spacing and charge passed. The current transient across the cell was measured throughout all experiments and during certain experiments, reference electrodes were placed within the suspension in order to measure voltage drop across a particular part of the deposition cell.

We attempted to make direct correlations between the weight deposited on the non-conducting substrates and the applied voltage (or the applied electric field), total charge passed, deposition time, substrate porosity (porosity was partitioned into open and impervious pores), and substrate firing temperature. The resultant findings were compared to those from similar experiments on conducting substrates performed under similar conditions. The trends in these results allow for inferences to be made about the similarities and differences in deposition on conducting and non-conducting substrates. The most obvious and perhaps most significant difference between deposition on conducting and non-conducting substrates appears to be the voltage drop across the deposition cell, as schematically shown in Figure 48.

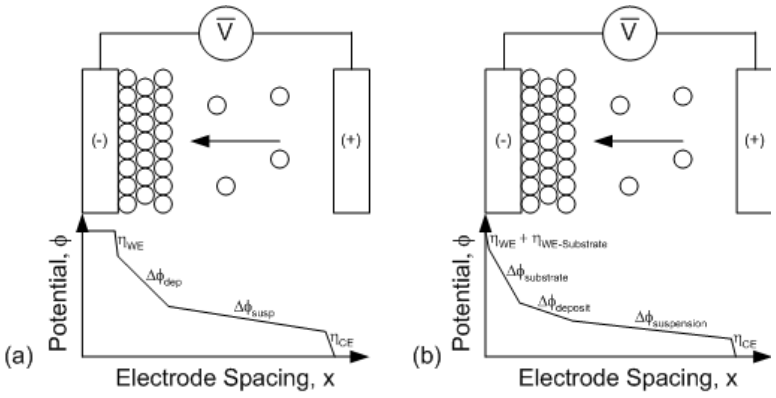

Figure 48. Schematic of the evolution of the voltage drop across an EPD cell when a (a) conductive substrate is used and (b) when a non-conductive substrate is used. This schematic represents the case of a positively charge particle, depositing at the working electrode under constant voltage conditions. Schematic is not to scale and does not show evolution of the voltage drop with time.

Van der Biest,[146] Negishi,[152] and Anné[150] all either measured or calculated the amount of voltage drop across components of the deposition cell and correlated these drops to the decreased rate of deposition with time for constant voltage EPD. Van der Biest[146] and Negishi[152] each gave a schematic of the voltage drop between the EPD electrodes, which indicated a constant voltage at the surface of the deposition substrate. Though this is likely the case when a conductive substrate is used, the potential distribution in a cell with a non-conductive substrate appears to be different. Adding an insulating layer such as a non-conductive deposition substrate over the surface of the working electrode significantly decreases the surface voltage of that substrate and also decreases the intensity of the electrical field lines as compared to the case when a conductive substrate is used. Figure 48 schematically shows the potential variation across an EPD cell when conductive and non-conductive substrates are used.

Since the velocity of the particles is proportional to the electric field (or voltage gradient) across the suspension, the effective electric field decreases as charged particles deposit, which in turn causes a decrease in the velocity of the particles and hence a decrease in the deposit rate. In order for the electrical field through the suspension to be near that of the initial applied field, there has to be negligible polarization losses across the electrodes and that the specific resistance of the deposit should be close to that of the suspension. For conducting substrates, Van der Biest described the voltage drop across an EPD cell with two equal surface area electrodes as follows: [146]

Equation 20 $$V_a = \Delta\phi_{WE} + \Delta\phi_{deposit} + \Delta\phi_{suspension} + \Delta\phi_{CE}$$

where V_a is the applied voltage and each $\Delta\phi$ represent the voltage drop across the corresponding constituent (as subscripted) of the cell due to ohmic losses. Essentially, two new terms must be introduced into this equation in order to adequately describe the voltage drop across an EPD cell when a non-conductive substrate is used.

Equation 21 $$V_a = \eta_{WE} + \eta_{WE-substrate} + \Delta\phi_{substreate} + \Delta\phi_{deposit} + \Delta\phi_{suspension} + \eta_{CE}$$

where η_{WE} is the activation polarization at the working electrode, $\eta_{WE-substrate}$ is the polarization resistance between the working electrode and the non-conductive substrate, and η_{CE} represents potential polarization at the counter electrode due to depletion of the suspension. Therefore facile deposition occurs when the voltage drop across the suspension dominates. Negishi and Van der Biest both showed that though the voltage drop across the suspension decreases as a function of time, the suspension resistance remains virtually constant. We performed similar experiments to determine the evolution of the voltage drop across different constituents of our EPD cell, and the results are shown in Figure 49(a-b).

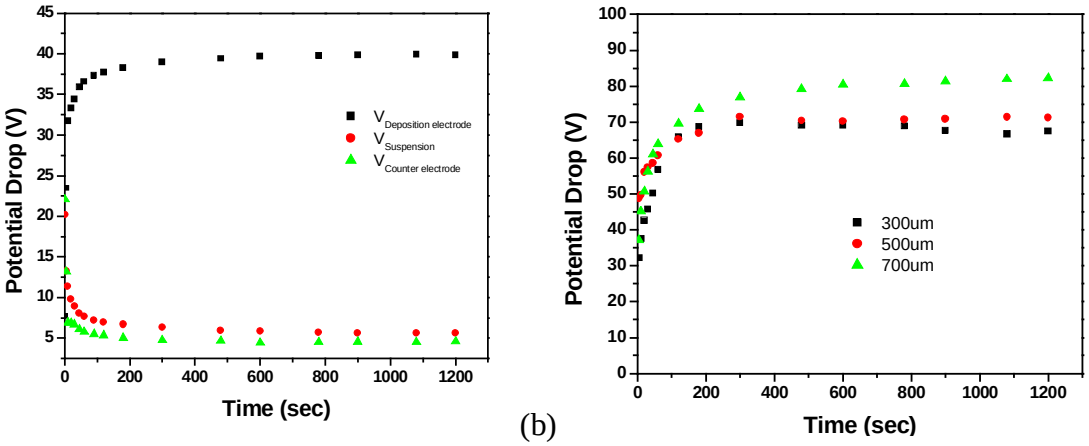

Figure 49. (a) Evolution of the voltage drop across different constituents of the EPD cell. Note that the applied voltage was 50V, the electrode spacing was 1cm, and the substrate thickness was 300μm. (b) The voltage drop due to ohmic losses within the substrate and interfacial polarization at the working electrode as a function of substrate thickness.

When a conductive substrate is used, the polarization resistance between the working electrode and the depositing substrate is minimal and the ohmic drop across the substrate is negligible resulting in the majority of the potential drop occurring between the electrodes within the suspension. When a non-conductive substrate is used, however, the opposite is true as the majority of the voltage drop occurs at the working

electrode/substrate interface and across the non-conducting substrate. The trends we observed for the voltage drop across the deposition electrode and the suspension are similar to those of Van der Biest.[146] However, the trends we observed at the counter electrode are opposite to his. Van der Biest claimed that the increased voltage drop at the counter electrode, as a function of time, was the result of concentration polarization, which is reasonable. The voltage drop at the counter electrode decreased with time in our experiment, indicating that concentration polarization was insignificant. Since at time zero our system acts as two dielectrics sandwiched between two parallel-plate electrodes, the high ohmic drop and interfacial resistance at the working electrode limits the particle velocity and thus a substantial particle concentration gradient can't be established. Based on the voltage drop analysis, deposit formation can be limited by either the ohmic drop across the substrate or the polarization resistance between the substrate and the working electrode. The ohmic drop across the substrate is expected to be limiting, which would result in a steadily decreased amount of deposit with increased substrate thickness. Since the samples are held against a spring-loaded working electrode, thin samples may not contact the working electrode firmly, resulting in a case where interfacial resistance dominates. When interfacial resistance dominates, it's difficult to obtain reproducible results as the polarization resistance changes for each substrate. Therefore it's imperative to control the quality of this contact/interface in order to attain reliable deposition rates and deposit quality. It's also important to note that when interfacial resistance dominates, the quality (density, uniformity, roughness…etc) of the deposit was inferior to deposits formed in the absence of the interfacial resistance.

Initial experiments focused on determining the effects of electrode spacing, applied voltage, and charge passed on the mass deposited and resultant thickness. As was reported earlier,[216,219] the deposit weight increases linearly with the applied voltage at time scales less than 1 minute. At times longer than 1 minute, the deposition rate began to decrease. Figure 50 shows the simultaneous effect of electrode spacing and substrate

thickness on mass deposited after 3 minutes deposition time using a constant applied field of 50V/cm.

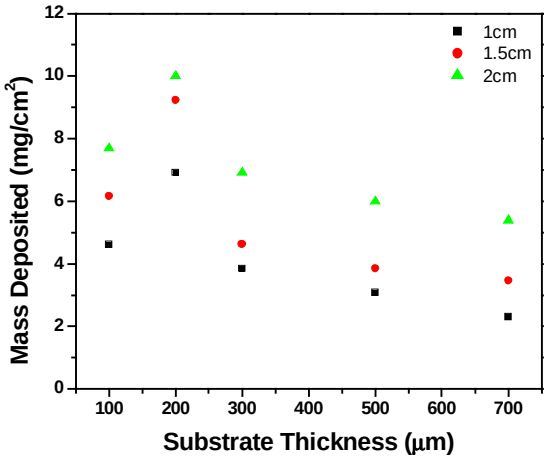

Figure 50. The effect of electrode spacing on weight deposited for different substrate thicknesses. All depositions were performed at a constant applied field of 50V/cm.

The general trend for weight deposited as a function of substrate thickness is similar for each electrode spacing. When the electrode spacing is held constant, the amount of deposit decreases with increased substrate thickness. This is intuitive as the only change in the system is an increase in the ohmic drop across the substrate, which should lead to a decreased current and reduced deposit weight. All the substrates greater than 200μm could be loaded identically and therefore followed a similar trend. The 100μm substrate thickness doesn't follow this trend, however, as the weight deposited actually increases as the substrate thickness goes from 100 to 200μm. The reason is because the mechanical integrity of the 100μm substrates was so low that solid contact between the substrate and the spring backed WE broke the substrate. Therefore the spring couldn't be loaded as firmly against the substrate, resulting in increased polarization resistance and reduced deposit weight. When the substrate thickness was held constant, the amount of deposit increased with electrode spacing for a constant applied field of 50V/cm. As electrode

spacing increases, the overall applied voltage increases, however the overall cell resistance does not scale with the voltage. This is because some components of the cell, such as the ohmic drop across the non-conductive substrate, remain independent of the applied voltage. Therefore if the applied voltage doubles, the cell resistance will be less than double, resulting in a greater current across the cell and thus more weight deposited. Figure 51 shows the effect of electrode spacing on weight deposited for a constant 300µm substrate thickness and a variable applied field from 50-300V/cm.

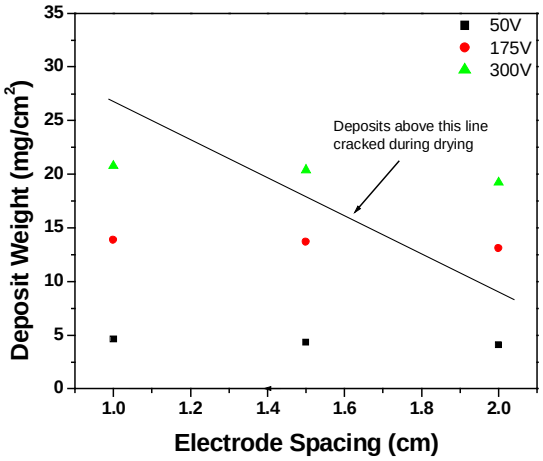

Figure 51. The effect of electrode spacing on deposit weight for different applied fields. Note that all substrates were 300µm thick.

As would be expected, for a given applied voltage, the overall deposit weight remained either linear or slightly decreased as a function of electrode spacing. Based on the results, a 1cm working distance results in a usable deposit at all applied voltages, whereas increased working distances result in some deposits that cracked during drying. In general, the threshold electrode spacing where a deposit begins to crack can be shifted by changing the thickness of the substrate. All else equal, a deposit is more likely to crack during drying on a thicker substrate than on a thinner substrate, which indicates a higher deposit porosity and weaker adherence on thick substrates. Additives such as polyvinyl

butyral (PVB)[177] and polyethelimine (PEI)[145,177,222] have been shown to improve deposit adherence and reduce cracking during shrinkage, but we chose not to use them in order to study solely the fundamental aspects of particle deposition on non-conducting substrates.

Figure 52 shows the amount of YSZ deposited on porous NiO-YSZ substrates, sintered at temperatures from 1100-1300^{o}C, as a function of deposition time.

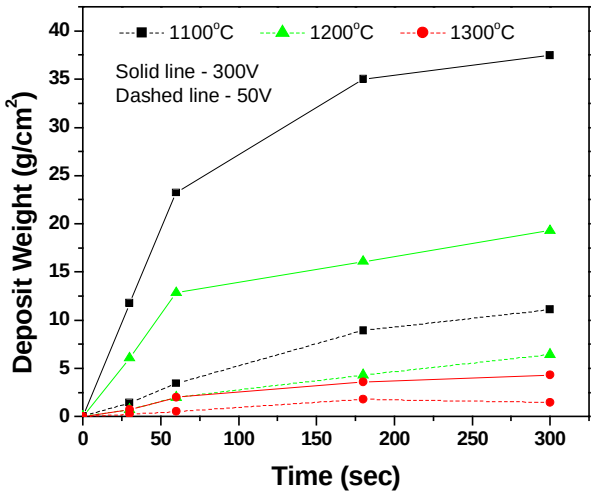

Figure 52. Deposition characteristics of YSZ on porous NiO-YSZ as a function of deposition time for a constant applied voltage of 300V (solid lines) and 50V (dashed lines) and 1cm electrode spacing.

It invariably shows rapid deposition rates in the initial period followed by a decrease with increase in time of deposition. During the initial period of EPD, there is generally a linear relationship between deposition mass and time. In a constant voltage EPD, these trends are expected because while the potential difference between the electrodes is maintained constant, the electric field influencing electrophoresis decreases with deposition time because of the formation of an insulating layer of ceramic particles on the surface of the deposition electrode. It also shows that for a given applied voltage, the density of the deposited layer on substrates of higher porosity (sintered at lower temperatures) is higher than on those of lower porosity (sintered at higher temperatures). In other words, the deposition density increases with substrate porosity. Also, the amount deposited is always

proportional to the applied voltage at a given deposition time. This is evident from Figure 53, which presents the weight of YSZ deposited with increasing applied voltages for a deposition time of 1min.

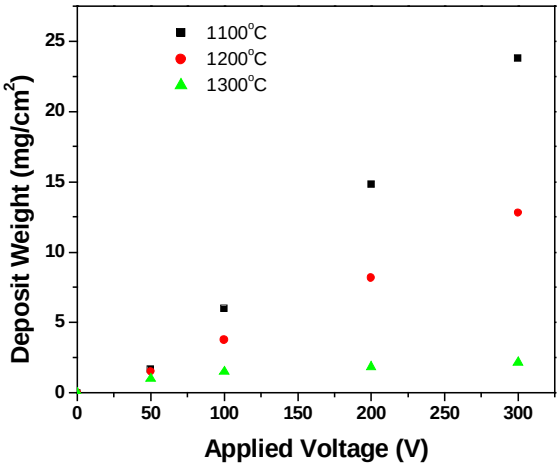

Figure 53. Amount of YSZ deposited after 1min as a function of applied potential on NiO-YSZ substrates sintered at different temperatures.

For each of the three substrates, there is a linear increase in YSZ deposition with increasing potential. The nature of the curves obtained for other deposition times were also similar in the range of applied potentials studied in this investigation.

When a dense substrate (pre-fired at 1400°C) was used instead of the porous substrates, no electrophoretic deposition occurred at any applied voltage and/or time of deposition. Similar observations were also reported by Matsuda.[181] This result clearly suggests that the substrate porosity is a key factor in electrophoretic deposition of YSZ films on a non-conductive substrate. In fact, we did show that for a given applied potential, EPD occurs only when the substrate porosity exceeded a certain threshold value.[228] The threshold porosity decreases with the amplitude of the applied voltage. The deposit weight increases with increasing substrate porosity. The rate of particle

deposition increases more rapidly in the region of lower porosity and tends to plateau above a certain porosity value.

The overall relation between substrate thickness, the amount of weight deposited and the applied voltage is shown in Figure 54.

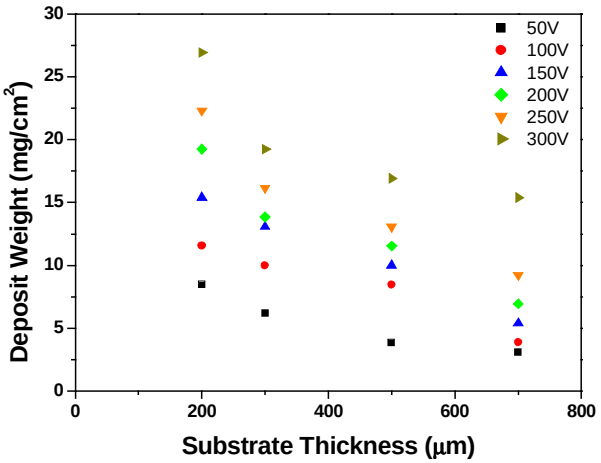

Figure 54. Relation between the substrate thickness, amount of weight deposited and applied voltage. Note that all depositions were performed for 3 minutes at an electrode spacing of 1cm using a 10g/L suspension concentration.

During the experiments, when substrates of different thickness were used, the current transient was also monitored. Figure 55(a-b) shows the current transients as a function of applied voltage and substrate thickness. For comparison, the current in the absence of any particles was a constant 0.04mA.

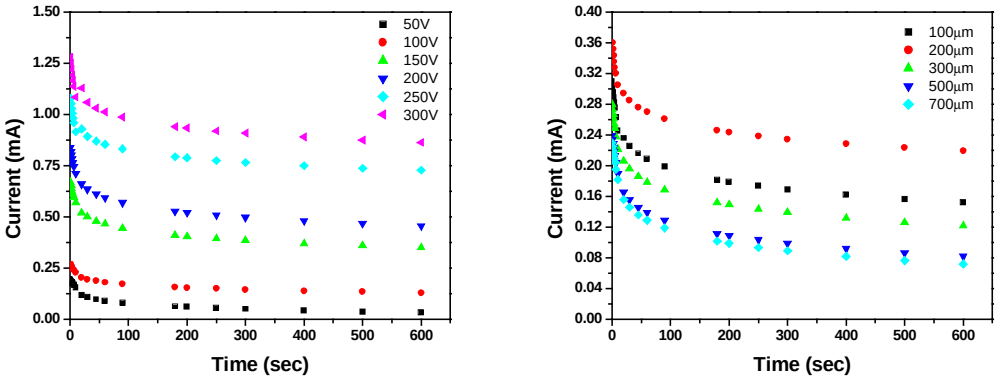

(a) (b)

Figure 55. The current transients for deposition as a function of (a) applied voltage on a 300µm substrate and (b) substrate thickness at constant applied voltage of 50V.

Based on the current transients, the deposit weight can be plotted against the amount of charge passed. Previous reports have shown that this should result in a linear trend as the charge passed is in direct correlation with the deposition rate. Figure 56 shows the deposit weight and thickness as a function of charge passed for a 300µm non-conductive substrate.

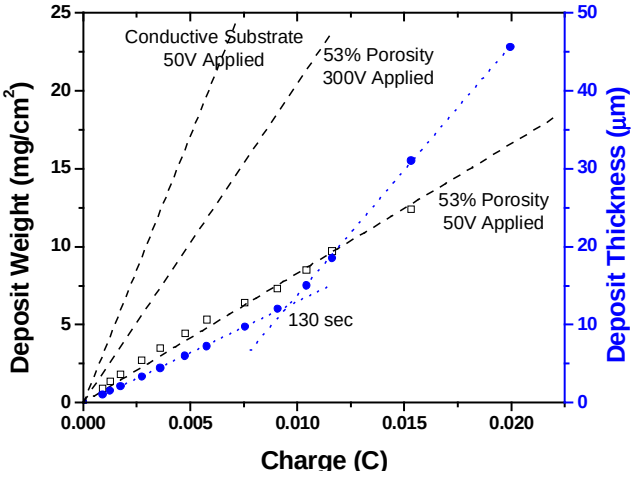

Figure 56. Relation between deposit weight (○) and thickness (●) as a function of the charge passed for a 300µm non-conductive substrate. The trend line was added to show the linearity between deposit weight and charge passed.

While the deposit weight holds a linear relation with charge passed, the deposit thickness appears to separate into two linear regions. The change in slope occurs after about 3 minutes of deposition time and reveals that the deposit becomes more porous. Therefore any deposition longer than about 3 minutes in time will have a denser layer near the substrate and a more porous layer farther away. The change in the slope of the thickness curve occurs at about 3 minutes, which coincides with the saturation point of the voltage curve in Figure 49(a). At the time when the voltage drop across the substrate reaches steady state, the voltage drop across the suspension also levels off, indicating a decreased driving force for deposition. This in turn causes a reduced deposit adherence and a more porous layer to form. Paramount to deposition on non-conductive substrates is the presence of porosity within the substrate. We believe that open porosity within the substrate allows for conduction of the solvent to the working electrode and facilitates particle deposition as was discussed previously.[216,219] A recent review of EPD shows the effect of a substrate's total porosity on the amount of mass deposited.[229] The total porosity is a good indicator of how much mass will deposit, however partitioning the porosity into open and impervious pores would be more quantitative. Figure 57 shows the deposit weight versus open porosity for NiO-YSZ substrates sintered at 1100ºC. For comparison, data from Besra and Liu[229] for deposit weight versus total porosity have also been superimposed.

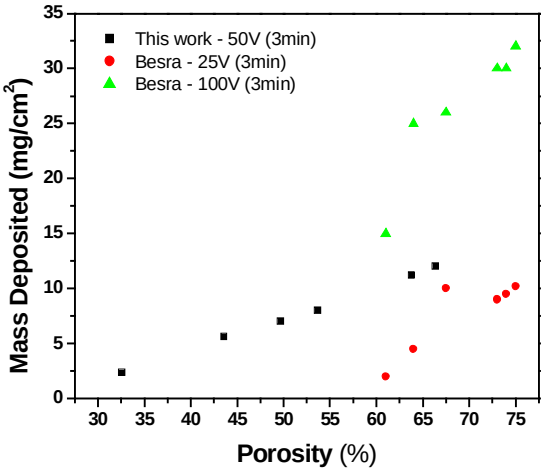

Figure 57. Relation between the amount of open porosity in the substrate and the mass deposited (■). All depositions performed for 3 minutes on 300µm NiO-YSZ substrates. Besra's data (●, ▲) for amount of mass deposited versus total porosity is shown for comparison.

Electrophoretic deposition of particles on non-conducting substrates depends strongly on the amount of open porosity within the substrate. When deposition occurs, the actual mechanism is believed to be similar to that on a conducting substrate, except that the driving force (potential drop across the suspension) is much less.

4.5 Mechanism of Deposition

Electrophoretic deposition on conducting substrates has been applied successfully for many applications. Although the exact mechanisms that allow a deposit to be formed are still not entirely clear,[146] several mechanisms have been suggested. Fukada et al.[230] gives a comprehensive account of the mechanism of deposit formation by EPD. Bouyer and Foissy[149] suggest that EPD is a two-step process. Under the application of an electric field, the particles in the suspension first migrate to one of the electrodes, depending on the particle charge, where they eventually deposit. The migration step depends on the bulk properties of the colloidal dispersion (bath conductivity, viscosity, particle concentration, size distribution, and surface charge density) and the actual field strength in the bath. Sarkar and Nicholson[164] inserted a dialysis membrane between the EPD

electrodes in an Al_2O_3 suspension. The membrane is permeable to ions but a dense deposit formed thereon and current passed via ionic discharge at the cathode. They concluded that the majority of charge is carried by ions and current passage results there from. The deposition step proceeds by a complex superposition of electrochemical and aggregation phenomena. Some of the suggested mechanisms are: (i) flocculation by particle accumulation,[133] (ii) particle charge neutralization mechanism,[143] (iii) electrochemical particle coagulation mechanism,[139] and (iv) the electrical double layer distortion and thinning mechanism.[145] Until recently, the electrical double layer distortion and thinning mechanism is most widely accepted for electrophoretic deposition on conducting substrates. According to this mechanism offered by Sarkar and Nicholson, [145] when the particle lyosphere system (the counter ions from liquid around the charged particle forms what is called diffuse double layer or lyosphere) moves, fluid dynamics and applied electric field will distort the double layer envelope in a way such that it becomes thinner at the front and wider behind the particle. The cations in the liquid also move to the cathode along with the positively charged particle. The counter ions in the extended 'tail' will tend to react with these accompanying cations in high concentration around them. As a result of such reaction, the double layer around the 'tail' of the particle will also become thin so that the next incoming particle (which has a thin leading double layer) can approach close enough for London Van der Waals (LVDW) attractive force to dominate and induce coagulation/deposition. The distortion of the double layer leading to coagulation is plausible considering the high concentration of particles near the electrode (or high collision efficiency). Secondly, this mechanism works for incoming particles with thin double layer heads, coagulating with particles already in the deposit.

When it comes to electrophoretic deposition on non-conducting substrates, however as in the present case, the mechanisms suggested for conducting substrates does not appear to hold true. The principal concern is how a non-conducting substrate ensures the existence of a uniformly distributed electric field in front of it. The presence of an

electrically non-conducting substrate will normally tend to block the conducting path from the electrical contact to the particles in suspension. Since electrophoretic deposition is based on mobility of the particles upon application of an electric field, deposition would not occur on a non-conducting substrate. In the present case, however deposition of YSZ on a porous non-conducting NiO-YSZ substrate is indeed possible. We believe that some sort of electrical contact is being developed between the substrate and the particles in the solvent. Two possibilities can be presumed: (i) when a DC voltage is applied, the current moves along the surface of the wetted substrate rather than through it, and (ii) the porous substrates, when saturated with the solvent, allows for development of a "conductive path" between the electrical contact and the particles in suspension. This is shown schematically in Figure 58.

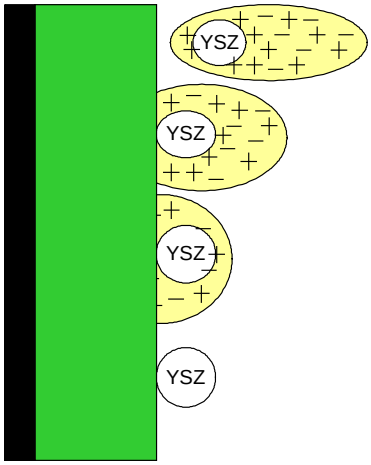

Figure 58. Proposed deposition mechanism of particles on porous non-conducting substrates. Note that as the particle approaches the substrate, under force of an applied field, the lyosphere is distorted with a thin leading edge. As the particle encounters the substrate, the lyosphere penetrates the porous substrate until finally the counter-ions in the lyosphere complete the charge transfer at the cathode, while the particle is deposited on the surface of the substrate.

If the former possibility were valid, then deposition would have occurred on any type (dense or porous) of substrate. But, since no deposition occurred on dense substrates at

any of the studied applied voltage, the former possibility may not be valid. The second possibility of establishment of a conducting path through the porous substrate is a more likely mechanism of deposition. Similar mechanism may also be valid for the previous work by Matsuda et al.,[181] since they also reported no deposition on dense substrates, but did not elaborate on the involved mechanism. It must be noted that the conductive path mechanism depicted in Figure 58 is an oversimplified illustration showing the manner of particle deposition and lyosphere motion during electrophoretic deposition. In reality, the incoming YSZ particles deposit not only on the surface of porous NiO-YSZ substrate, but they also penetrate the pores leading to continuous closure of the pores with increasing deposition time. Under such scenario, the electrical resistance of the substrate and YSZ film combined together will tend to increase rapidly leading to a decrease in the rate of deposition. However, it can be expected that deposition, however small, still occurs as long as a conductive path of solvent exist through the combined layer of substrate and deposit.

However, we also foresee that this mechanism of a "conductive path" through a porous substrate by saturation with solvent will be applicable only when the substrate has interconnected porosity. Presence of only closed pores in the substrate will tend to block the "conductive path" preventing any electrophoretic deposition. Although Matsuda et al.[181] also reported deposition of YSZ on NiO-YSZ substrate by EPD, it can be viewed as deposition on a conductive graphite substrate with increased electrical resistance due to NiO-YSZ layer. For this reason a relatively high deposition voltage of 400-900V was necessary for EPD. Our method is unique in that we did not coat any graphite or other conducting layer on the substrate, but rather only a spring connected to the DC power supply made contact with substrate. Secondly, our method required relatively low applied voltage of 50V to obtain dense YSZ films of 5μm thickness. Unlike multiple deposition and sintering steps adopted by other investigators,[172,182] our approach enabled obtaining dense and gas-tight films in a single deposition and sintering step. The difference in

requirement of applied voltage in this work and that reported by Matsuda et al.[44] may result from a number of other differences in the experimental conditions adopted. For example, the thickness of NiO-YSZ substrate used by Matsuda et al.[181] was 700µm, whereas we used substrates of 300µm thickness. The higher thickness of substrate is expected to offer higher electrical resistance. In a similar analogy, such increase in resistance can also be expected with increasing thickness of the YSZ deposit with time, for which a decrease in deposition rates will happen at loner deposition time. This is clearly evident from our result presented in Figure 52. Another possible parameter contributing to voltage requirement during EPD may be the solvent conductivity. A more conductive solvent is expected to require less voltage to transport the YSZ particles, although in the present case, where we are using organic solvent like acetylacetone, it is believed that such influences will be secondary compared to the effect from substrate thickness and zeta potential development in the solvent.

The proposed mechanism[216,218] of solvent (or counter-ions) moving through the porous non-conducting substrate, under the influence of an applied electric field, is able to transport charge from the particles to the working electrode to complete the current flow through the system, as shown in Figure 59.

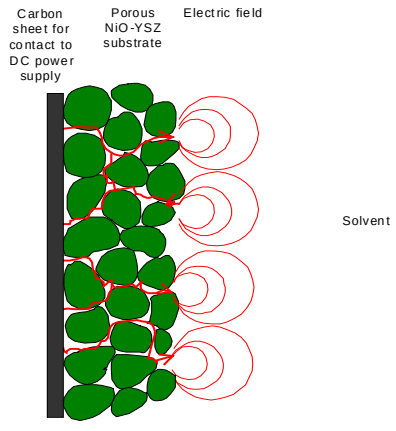

Figure 59. Conceptual representation of EPD mechanism on non-conducting substrates where the solvent can traverse the open porosity of the substrate to complete the charge transfer reaction.

Thus, charge transfer must occur between the particle/solvent lyosphere and the liquid electrode interface. Otherwise the deposition of charged particles will quickly stop when the applied electric field is cancelled by the electric field setup by the charged particles accumulated at the non-conducting substrate. In order for the charge to transfer from the particle to the electrode, it must leave the particle at the deposition surface and travel through the solvent within the porous substrate. This mechanism accounts for our observation that deposition does not occur in absence of sufficient porosity. It would also account for the observations of Sarkar and Nicholson[145] when they observed deposition on the dialysis membrane, Brown and Salt[140] when they observed deposition on a porous membrane placed before the electrode and Zhang and Lee,[185] when they observed the current being much lower when a polymer sheet was placed perpendicular to the electric field than when it was parallel. We also placed a non-conducting substrate between the working and depositing electrodes and noticed the formation of a thin dense deposit despite the lack of an electrical contact between the substrate and the applied field. The amount of deposit was related to the applied voltage, deposition time and substrate porosity, as shown in Figure 60.

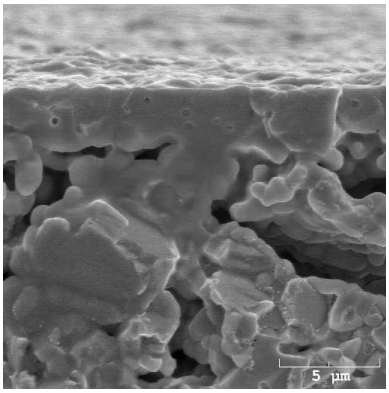

Figure 60. SEM cross-sectional image of deposition on a 300µm non-conductive substrates placed perpendicular to the applied field, but not physically connected to the circuit. The substrate had 64.2% open porosity and deposition was performed for 3 minutes in a 50V/cm applied field.

For further proof that a conductive substrate is not necessary, we deposited YSZ on NiO-YSZ substrates pre-fired at 1000ºC and 1100ºC using applied voltages from 25-150V and a 3min deposition time. The next series of figures corroborate the observations of Sarkar and Nicholson,[184] who saw a dense deposit form on a solvent permeable layer. The schematic in Figure 61 shows the setup for the series of deposition experiments.

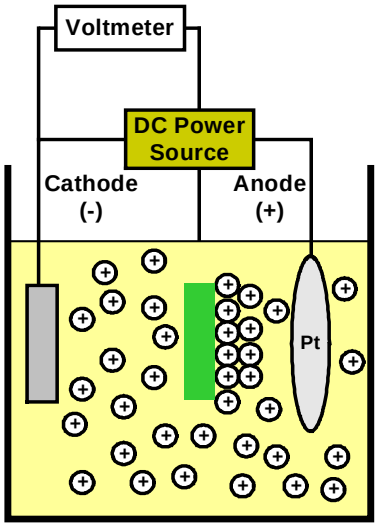

Figure 61. Schematic of deposition setup with substrates placed in between, but not touching the electrodes.

For the first experiment 50V was applied for 1 min between two Pt electrodes of 2cm spacing (E=25V/cm) with a carbon disk (the same porous carbon disks used for PEM gas diffusion membranes) placed between, but not touching either electrode. The current measured on the constant voltage source dropped from 0.74 to 0.69mA during the 1min deposition period indicating that not only was charge being transferred, but particles were being deposited as well. SEM images of the deposit after sintering at 1400ºC in air for 2hrs are shown in Figure 62.

(a) 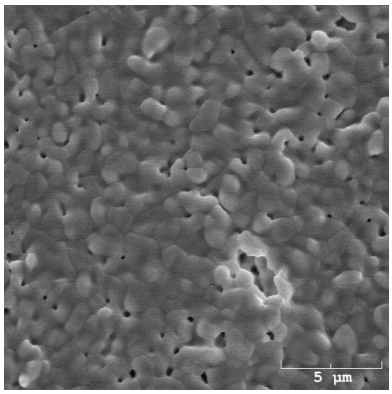

(b) 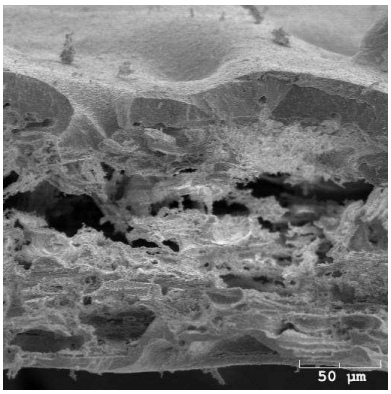

Figure 62. YSZ deposit on porous carbon substrate (a) surface and (b) cross-section. The applied voltage was 50V for 1min at an electrode spacing of 2cm, with the substrate placed in between.

A porous carbon substrate was used first because it is a conductive substrate and therefore should allow for some charge transfer and deposition. As can be seen in Figure 62(b), particles deposited occurred on both sides of the porous carbon substrate. The reason that deposit formed on both sides is that the conductive substrate allows for charge conduction across it, thus attracting particles to both sides. Particles shouldn't deposit on both sides of a non-conductive substrate due to the highly insulating behavior. To test this theory, 50V were then applied for 1min across a NiO-YSZ substrate pre-fired at 1000ºC placed between, but not touching, the two Pt electrodes of 2cm spacing (E=25V/cm). The current dropped from 0.32 to 0.29mA during deposition. Shown in Figure 63, are the surface and cross-sectional images of the deposit on the substrate.

(a) 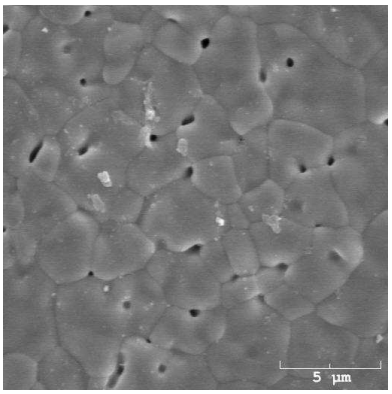

(b) 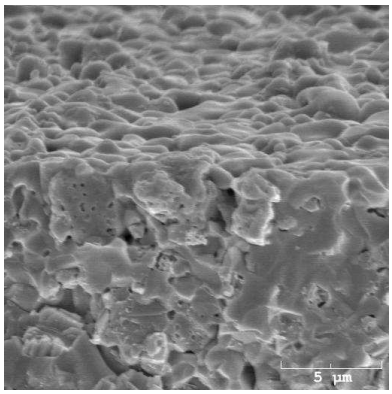

Figure 63. SEM (a) surface and (b) cross-sectional images of YSZ deposit on NiO-YSZ substrate pre-fired at 1000ºC. Deposition occurred at 50V for 1min.

Deposition only occurred on one side of the substrate, as was predicted, indicating that charge wasn't transferred through the substrate, only the pores. Nonetheless, particles were deposited on a non-conductive substrate placed between, but not touching the two EPD electrodes. Another interesting note was that a residual voltage remained on the non-conducting substrate after the voltage was removed from the system as shown in Figure 64.

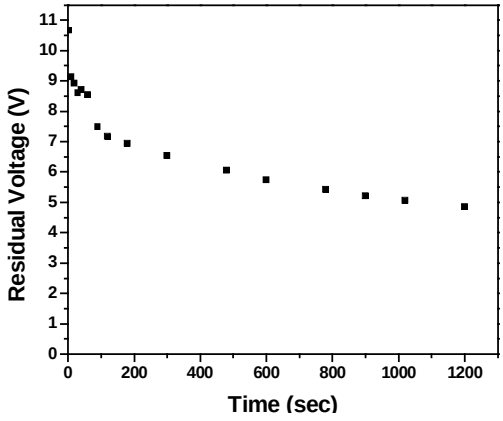

Figure 64. Discharge transient of residual voltage present at non-conductive substrate after removal of applied voltage.

This phenomenon was not observed when the conductive carbon substrate was used, indicating that polarization occurs on substrates placed in the electric field, but not touching either electrode. Figure 65 shows the deposit when the NiO-YSZ substrate is pre-fired at 1100ºC instead of 1000ºC, as was shown in Figure 63. The same deposition conditions of 50V for 1min were used between the two Pt electrodes of 2cm spacing (E=25V/cm). During deposition the measured current dropped from 0.32 to 0.28mA.

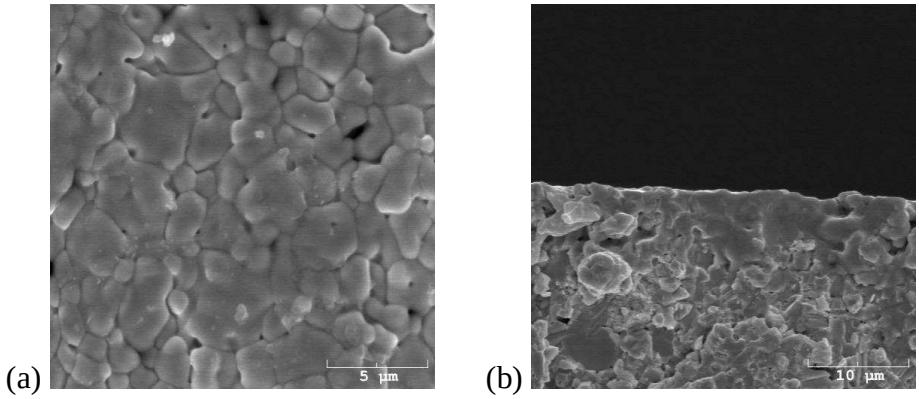

Figure 65. SEM (a) surface and (b) cross-sectional images of YSZ deposit on NiO-YSZ substrate pre-fired at 1100ºC. Deposition occurred at 50V for 1min.

Increasing the deposition voltage to 100V and holding the deposit time to 1 min on the same NiO-YSZ substrate pre-fired at 1100ºC resulted in the deposit shown in Figure 66. The current dropped from 0.47 to 0.40mA during the deposition process.

(a) 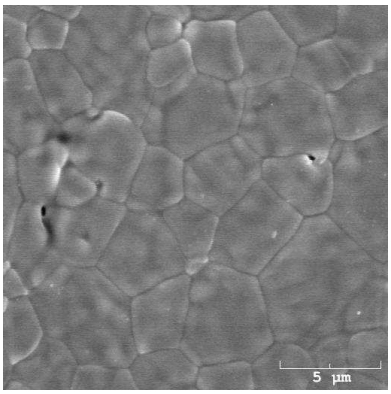

(b) 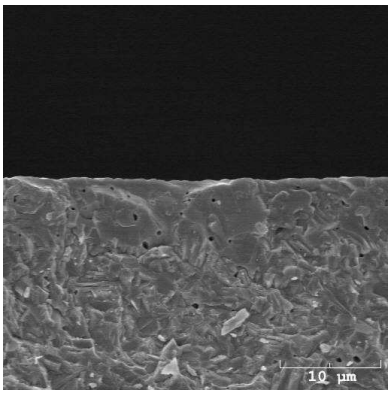

Figure 66. SEM (a) surface and (b) cross-sectional images of YSZ deposit on NiO-YSZ substrate pre-fired at 1100ºC. Deposition occurred at 100V for 1min.

In an attempt to improve deposition, a NiO-YSZ slurry similar to Table 21 was made, except that 15-wt% of carbon black was added to increase porosity. 100V was applied for 1min across the NiO-YSZ substrate, which was pre-fired at 1100ºC, and the resultant deposit is shown in Figure 67. Current dropped from 0.82 to 0.73mA during deposition. The higher initial current shows the effect of increasing the amount of open porosity in the substrate.

(a) 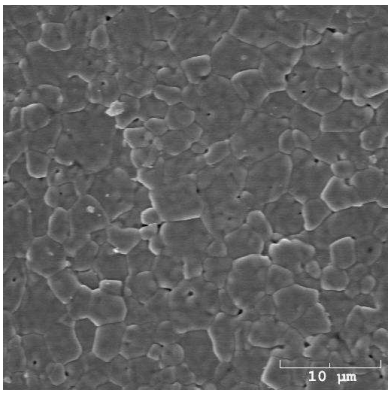

(b) 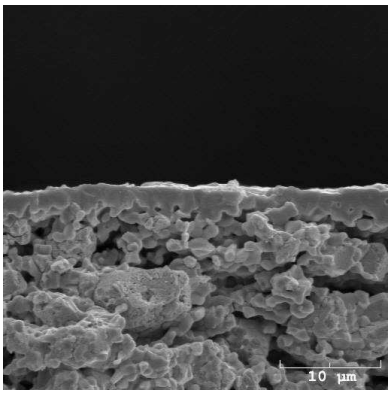

Figure 67. SEM (a) surface and (b) cross-sectional images of YSZ deposit on NiO-YSZ substrate pre-fired at 1100ºC. The substrate had increased porosity due to the addition of 15wt% carbon. Deposition was performed at 100V for 1min.

In all cases, deposition occurred on a substrate not connected to the electrical circuit while current continued to flow. Our explanation is that the charge is initially carried by the particle/solvent lyosphere, until the point where the movement of the particle is blocked (i.e. deposition), as shown in Figure 58. As the particle stops migrating, the charge carried by the particle is then transferred to some charge carriers in the liquid, which will eventually give up the charge at the working electrode and complete the circuit. As the charges leave the particle surface, the lyosphere becomes thin enough for coagulation to take place, as proposed by Sarkar and Nicholson.[145] A conductive substrate allows for a more facile charge transfer, resulting in an efficient system and a greater amount of deposit as compared to that on a non-conducting substrate.

Charge transfer may not be the sole deposition mechanism, but we speculate it's dominant during the majority of the deposition time-scale. It is plausible that as the deposition conditions and especially the time scale changes, the deposition mechanism also changes. Other competing mechanisms, such as momentum or velocity induced deposition, van der Waals attraction due to lyosphere distortion (without charge transfer), pH induced flocculation and charge neutralization have all shown to be possible under certain conditions and time-scales. For instance, at short time scales, particles in a dilute suspension could deposit from either velocity-induced methods or charge neutralization.[133,143] As the time scale increases, charge neutralization is no longer valid and since the particle velocity decreases as a function of deposition time, the particle accumulation mechanism becomes less likely as well.

Though the exact mechanism of EPD within this system is still unknown, a few generalities about the process have been determined. When the voltage is first applied (time zero), the system acts as a two dielectrics placed between two parallel-plate electrodes. After time zero, there is a transitional period where transport competes with dielectric displacement. During this period before steady-state flux density is reached,

the current or transport is influenced by the open porosity within the substrate, making substrate porosity the critical factor controlling the mass deposited. Reasonably, the increased current observed when a substrate of identical thickness (and material) but higher open porosity is used, could be the result of more solvent being able to conduct through the substrate. Therefore the effective conductivity through the substrate becomes higher due to a greater volume fraction of it being occupied by solvent. A lower limit to the amount of porosity within the substrate appears to follow percolation theory, as useable deposits don't appear to form on substrates with less than about 30% open porosity. Once steady state is reached, which according to Figure 49(a) occurs near 130 seconds, the flux density across each cell constituent is equivalent, the current and voltage become constant and the deposition occurs at a much lower and effectively constant rate. Figure 56 also reveals that once this steady state point is reached, the deposit density is reduced, as less deposit mass equates to a higher deposit thickness.

In order for a mechanism to hold true, it must work universally for all substrates. To test this theory, we fabricated porous YSZ substrates and porous $Fe_{50.1}Ni_{44.5}Cr_{5.4}O_x$ substrates to determine whether similar deposition would occur on these as well. Porous YSZ substrates are used as scaffolds for cathode and anode fabrication by infiltration methods and are typically fabricated by tape casting with pore forming agents. Electrolyte layers are usually cast simultaneously with the porous scaffold, which saves time and sintering steps, but doesn't allow for thin electrolyte formation. As seen in Figure 68, thin electrolytes could be deposited on porous YSZ substrates, thus proving the mechanism.

(a) 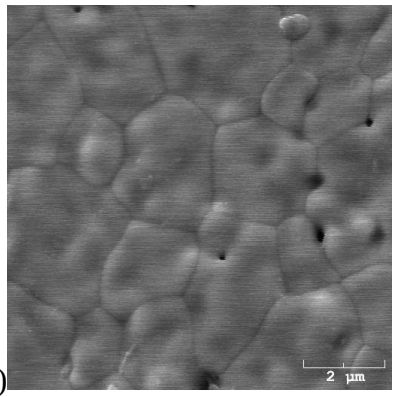

(b) 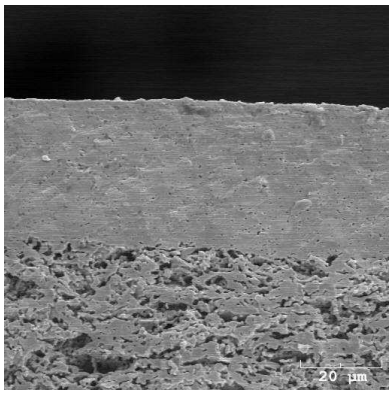

Figure 68. SEM (a) surface and (b) cross-sectional images of 40µm YSZ layer deposited on porous YSZ substrate at 175V for 3 min.

Lower voltages, such as 50V, were sufficient to form thin deposits, however the deposits weren't as dense and uniform as the ones formed at 175V, as shown in Figure 69.

(a) 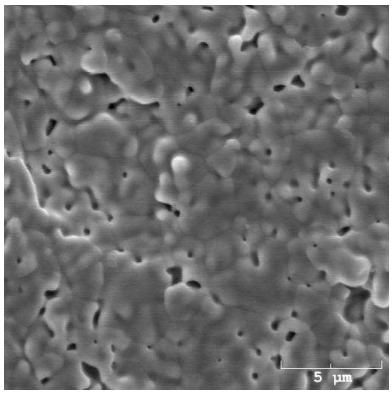

(b) 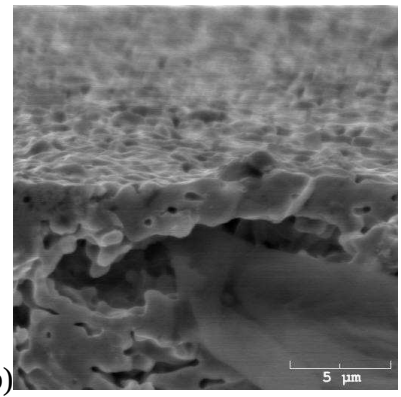

Figure 69. SEM images of (a) surface and (b) cross-section of a 3µm YSZ layer deposited on a porous YSZ substrate at 50V for 1min.

Deposition on porous YSZ substrates necessitates a higher voltage than does the NiO-YSZ composite substrates for two reasons: YSZ is more insulating than the NiO-YSZ composite, and the average pore size in the YSZ substrate was slightly less than that in the NiO-YSZ substrate. The combined effects of the insulating and dielectric properties of YSZ causes a lower effective applied voltage across the system, leading to a lower

force for deposition (gradient in voltage drop across suspension), and thus less deposit. The reduced gradient in the voltage drop also affects the uniformity and density of the deposit as the particles can't orient and transport in a proper manner for formation of a consistent layer. Deposits were also able to form on the porous $Fe_{50.1}Ni_{44.5}Cr_{5.4}O_x$ interconnect precursor (oxide form of the interconnect), as shown in Figure 70.

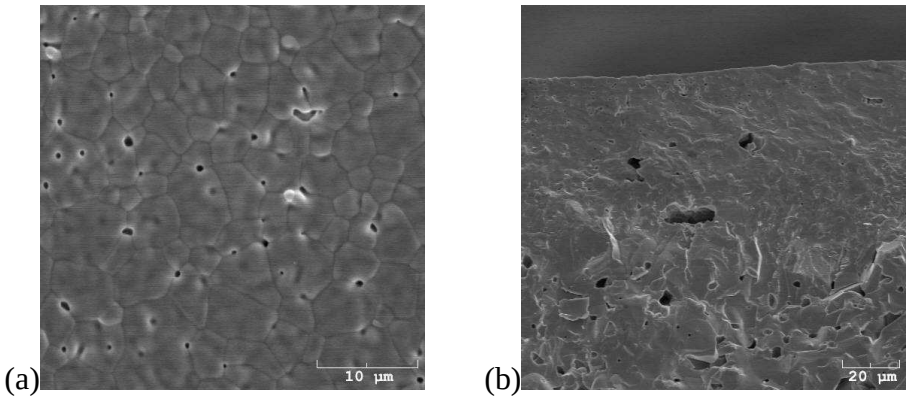

Figure 70. SEM images of (a) surface and (b) cross-section of 20µm YSZ deposit on Fe50Ni45Cr5Ox porous interconnect precursor at 200V for 3min.

In this manner, the process of EPD on porous non-conductive substrates could be used to fabricate interconnect supported SOFCs.

4.6 Optimization of Deposit

Once the fundamentals and mechanism of deposition were determined and we discovered that optimal deposition does not occur after 3min, we focused on improving the deposit such that we could achieve higher power density. The keys to improving power density were to keep the deposit thickness at roughly the 5µm seen in Figure 31(b), while improving the open circuit voltage to over 1V. Based on previous reports and our own validation of those reports, we decided to add 0.2g/L of iodine to the YSZ-acetylacetone suspension in order to improve the zeta-potential to >40mV, as seen in Figure 26. A zeta-potential above 40mV ensures a sticking factor, *f*, of unity, or rather

that all particles encountering the substrate are deposited onto it. A sticking factor of unity improves the deposition density and therefore we should achieve a higher packing of particles at the same deposition thickness. We determined that the open circuit voltage was below 1V due to poor deposition at the edge of the substrate and leaks in the sealant. In order to increase the open circuit voltage to above 1V, we repeated the deposition process twice. First the YSZ-acetylacetone suspension was ultrasonicated for 20min with the addition of 0.2g/L of I_2, followed by deposition at 50V for 1min. The substrate was then removed from the suspension and the suspension was ultrasonicated again for 5min. A second deposition at 50V for 1min was then performed, at which point the substrate was removed from the Teflon apparatus and dried overnight, followed by sintering in air to 1400ºC for 5 hrs at a ramp rate of 3ºC/min. The cathode was then applied by brush painting, followed by sintering in air at 1200ºC for 2hrs at a ramp rate of 3ºC/min. The cathode slurry wasn't prepared from conventional powders however. New powder was prepared by the glycine-nitrate process where nitrate salt precursors of the desired molar ratio are added to distilled water, at a concentration of 0.05M, along with glycine at a molar ratio of $2NO_3$:1glycine. The solution is then set on a hot plate and heated until combustion to produce very fine powders in the size range of 30-200nm. Those powders were then mixed in a 50:50 ratio with YSZ and added to binder and solvent to produce a higher performing cathode. The performance of the optimized electrolyte deposit with the higher performing cathode is shown in Figure 71.

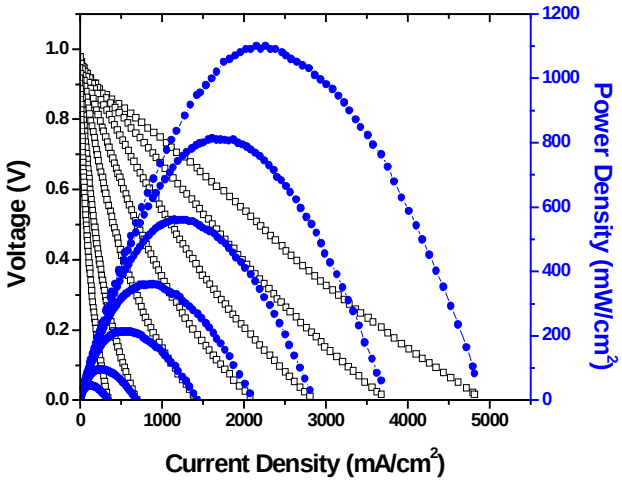

Figure 71. Performance of SOFC using optimized deposition parameters (0.2g/L I_2 in suspension, 300µm NiO-YSZ substrate, 50V applied for 1min - repeated twice).

The impedance spectra as a function of temperature are shown in Figure 72.

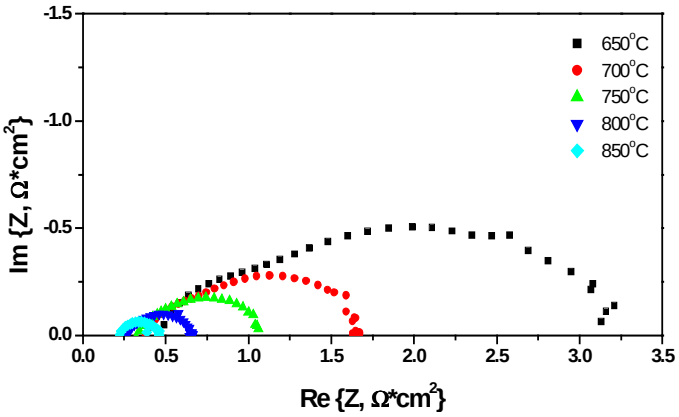

Figure 72. Impedance spectra of SOFC fabricated by EPD using optimized parameters.

4.7 Modeling of Deposition

The first model of EPD was developed by Hamaker based on his work in conjunction with Verway.[133,134] The model was based on their assumption that the deposition mechanism was akin to particle settling and accumulation, however it proved to be applicable despite their error in mechanism. After long deposit times, the deposit

weight or yield tends to deviate from the model for dilute suspensions because the concentration is no longer constant. For more concentrated suspensions, many repetitions of deposition need to be performed before deviation from the model occurs. The model has been improved over the years to account for changes in particle concentration, effective field, deposit and suspension resistance, constant voltage and constant current systems.[145,176,231,232,233]

4.7.1 Empirical Model

As was previously mentioned, Hamaker developed the first empirical model of EPD.[133] His model was based on the applied field, E, electrophoretic mobility of the suspended particles, μ, particle concentration, c_o, substrate or deposit area, A, deposit time, t, and another factor called the sticking factor, f.

Equation 22
$$Y = fEA\mu c_o t$$

the deposit yield can be differentiated with respect to the deposition time

Equation 23
$$\frac{dw}{dt} = w_o k e^{-kt}$$

to determine the average rate of deposition, $w_{(t)}$.

Equation 24
$$w(t) = w_o(1-e^{-kt})$$

where the kinetic factor, k, represents

Equation 25
$$k = \frac{Af\mu}{V}$$

The sticking factor, f, represents the percentage of particles that stick on the substrate after encountering it. In general, when the zeta potential is greater than 40mV, the value of the sticking factor is considered to be unity. The electrophoretic mobility is a measured property, often approximated by the Smoluchowski equation.

Equation 26
$$\mu = \frac{\varepsilon\varepsilon_o\zeta}{\eta}$$

Where ε is the dielectric constant of the suspension, ε_o is the dielectric constant of a vacuum, ζ is the zeta-potential of the particle and η represents the suspension viscosity. Many modifications of Hamaker's equation have been made to account for changes in particle concentration, effective electric field and the formation of a resistive deposit layer during deposition.[145,176] Sarkar and Nicholson identified differences in the kinetics of deposition from constant voltage and constant current sources, as shown in Figure 73.

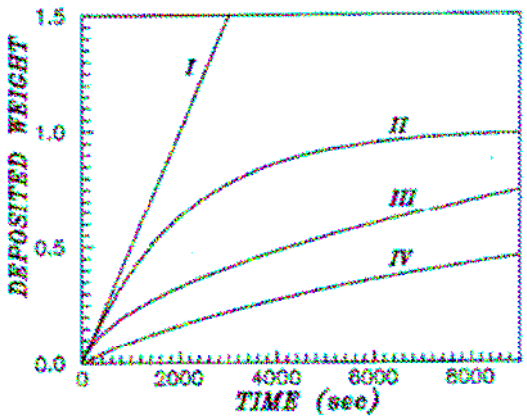

Figure 73. Schematic of four different deposition conditions. I – constant current/constant concentration, II – constant current/variable concentration, III – constant voltage/constant concentration and IV – constant voltage/variable concentration. [145]

They then developed general equations for constant voltage and constant current deposition and then an even more general equation, which is applicable to both systems.[145]

Equation 27

$$R'w(t) + (R'w_o + L)\ln\left(\frac{w_o - w(t)}{w_o}\right) + k'V_{app}t = 0$$

where

Equation 28

$$R' = \frac{(R_r - 1)}{\rho S}, \quad V_{app} = E(t)(L + w(t)R'), \quad k' = k\frac{I(t)}{I_{initial}}$$

When R_r=1, R'=0 and there is no difference between constant current and constant voltage deposition. Therefore Equation 27 is a universal equation for determining the deposit weight as a function of time. As can be seen in Equation 28, the kinetic factor, k', is time-independent, which means it has a variable value under constant voltage conditions and a constant value under constant current conditions. Will et al. developed an empirical equation, based on Hamaker's equation, that accounts for changing concentration and effective electric field during constant voltage deposition. Their equation can be used to determine the deposit weight,

Equation 29

$$m(t) = -\frac{d_o}{2\left(\frac{\frac{\varepsilon_D}{\varepsilon_s}-1}{\rho_D A}\right)} + \sqrt{\left(\frac{d_o^2}{4\left(\frac{\frac{\varepsilon_D}{\varepsilon_s}-1}{\rho_D A}\right)^2}\right) + \left(\frac{fA\mu c_o E}{\left(\frac{\frac{\varepsilon_D}{\varepsilon_s}-1}{A}\right)}\right)t}$$

thickness

Equation 30

$$d(t) = -\frac{d_o}{2\left(\frac{\varepsilon_D}{\varepsilon_s}-1\right)} + \sqrt{\left(\frac{d_o^2}{4\left(\frac{\varepsilon_D}{\varepsilon_s}-1\right)^2}\right) + \left(\frac{fA\mu c_o E}{\left(\frac{\varepsilon_D}{\varepsilon_s}-1\right)\rho_D}\right)t}$$

or the current transient during the deposition process.[176]

Equation 31

$$\int_o^t I\,dt = Q(t) = \rho_Q a_s m(t) = -\frac{a_s \rho_Q d_0}{2\left(\frac{\varepsilon_D}{\varepsilon_s} - 1\right)} + a_s \rho_Q \sqrt{\left(\frac{d_o^2}{4\left(\frac{\frac{\varepsilon_D}{\varepsilon_s} - 1}{\rho_D A}\right)^2}\right) + \left(\frac{fA\mu c_o E}{\left(\frac{\frac{\varepsilon_D}{\varepsilon_s} - 1}{A}\right)}\right)} t$$

As can be seen in Figure 74, Will's current transient model follows their experimental transients very closely.

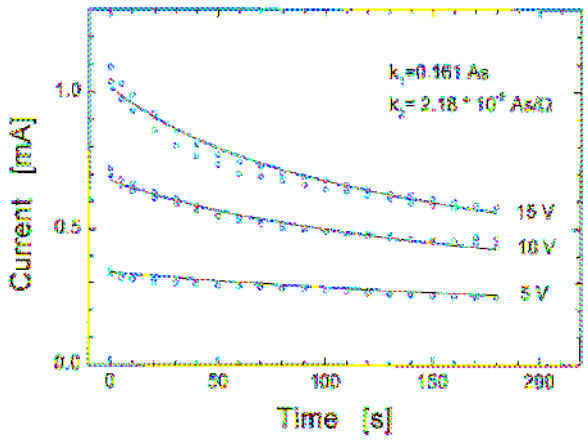

Figure 74. Comparison between experimental current transients and those from the empirical model of Will et al.

Taking their model at face value, we applied our empirical values to it to see how well the model compared to our experimental transients shown in Figure 55. Our fundamental parameters within the suspension were as follows: particle concentration, c_o=10kg/m^3, sticking factor, f=1, particle surface area, S=12.25m^2, surface charge density, a_s=0.076C/m^2, electrode distance, d_o=0.01m, dielectric constant of deposit, ε_D=31.4, dielectric constant of suspension, ε_s=21.9, substrate area, A=1.31*10^{-4}m^2, electrophoretic

mobility, μ=5.10*10^{-11}m^2/Vs and deposit density, $\rho_{D=}$3.3*10^{-9}kg/m^3. The empirical values of k_1 and k_2 were 0.0107As and 4.055*10^{-7}As/Ω, respectively as compared to Will's values of 0.161As and 2.18As/Ω. The result of applying Will's model to our experimental data is shown in Figure 75.

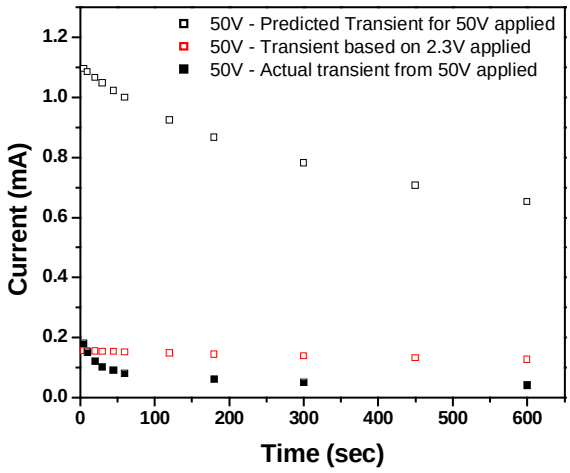

Figure 75. Comparison of our experimental current transient to that predicted by Will's model.

As can be seen, the experimental transient (■) and the predicted transient (□) are both very far apart as well as different in shape. The difference in the experimental and predicted values is due to the presence of the insulating substrate. Based on a physical approach, the effective applied voltage is 2.3V as given by:

Equation 32

$$V_{effective} = \frac{V_{applied}}{\varepsilon_{system}} = \frac{50V}{21.7} = 2.3V$$

For comparison, an applied voltage of 2.3V was input to Will's model and is also shown as the open red squares in Figure 75. It's now obvious that the effective applied voltage across the system is 2.3V, due to the presence of the dielectric deposition substrate. The model still doesn't follow the shape of the experimental current transient, however, as the predicted values follow a slight linear drop as a function of time, whereas the experimental values show a sharp initial drop followed by a gradual decline. The initial

drop is the result of hypothesized to be polarization within the dielectric substrate. Therefore Will's model has to be modified to account for the polarization resistance at short deposition times, where flux density is constant. At longer deposition times, where the current density is constant, the model and the experimental results appear to follow the same trend and thus modification shouldn't be necessary. Since Will et al. used a conductive substrate, they didn't have to account for polarization at the electrodes as we have to. We determined that, from an empirical perspective, the best way to account for the initial polarization drop was to use Sarkar and Nicholson's approach and use a time-independent kinetic parameter. The universal kinetic parameter is variable with time and normalized to the change in current. Figure 76 shows the change in current and the time-independent kinetic parameter with time.

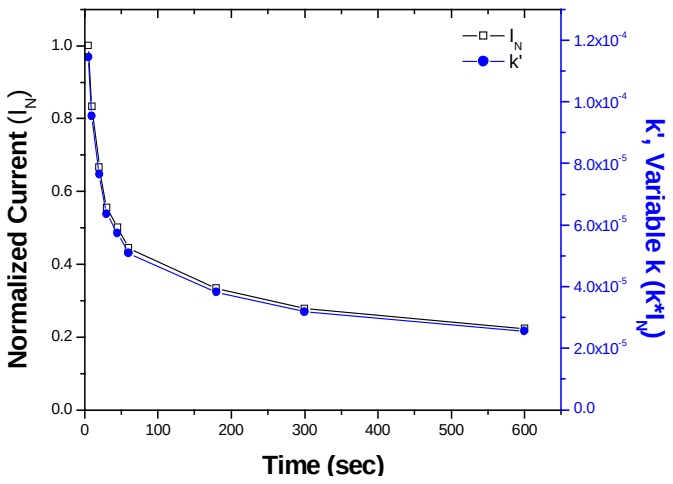

Figure 76. Change in time-independent kinetic parameter, based on the normalized current, with time.

Applying the variable kinetic parameter to Will's model results in an empirical current transient that closely follows the experimental results. The result of combining Equation 27, Equation 28, Equation 31 and Equation 32 is an empirical model that accounts for variable deposition kinetics as shown in Figure 77.

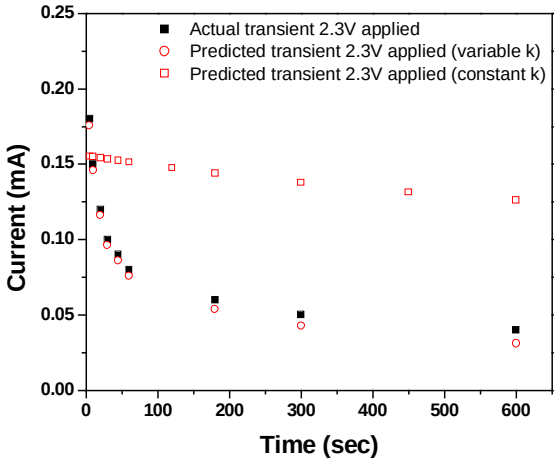

Figure 77. Comparison of experimental current transient with that from a modified version of Will's empirical model.

Further, the amount of weight deposited as a function of time can also be modeled using the same though process as outline above. Using a combination of the equations developed by Will and Sarkar and Nicholson, a variable kinetic parameter model proved to mirror the experimental data very closely, whereas the constant kinetic parameter model wasn't effective. These results are shown in Figure 78.

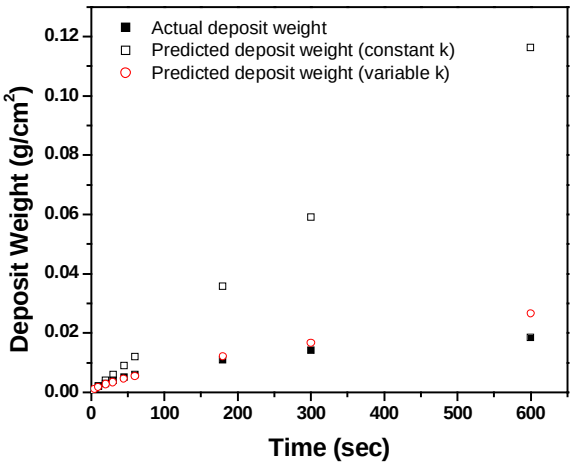

Figure 78. Comparison of the experimental deposit weight with that from empirical models based on constant and variable kinetic parameters.

As has been shown, combining the empirical model of Will (Equation 31) with a variable kinetic parameter, $i_{efficiency}$, to account for current (and thus deposition rate) decrease during constant voltage deposition, which is similar to that developed by Sarkar and Nicholson (Equation 28)

Equation 33

$$i_{efficiency} = \frac{I(t)}{I_{initial}}$$

and adding a term, $V_{effecive}$, to account for the effective voltage through a dielectric (Equation 32) was sufficient to model our constant voltage deposition on porous non-conducting substrates.

Equation 34

$$\int_o^t Idt = Q(t) = i_{eff}\rho_Q a_s m(t) = i_{eff} a_s \rho_Q \left(-\frac{d_0}{2\left(\frac{\varepsilon_D}{\varepsilon_s}-1\right)} + \sqrt{\left(\frac{d_o^2}{4\left(\frac{\frac{\varepsilon_D}{\varepsilon_s}-1}{\rho_D A}\right)^2}\right) + \left(\frac{fA\mu c_o V_{eff} d_o}{\left(\frac{\frac{\varepsilon_D}{\varepsilon_s}-1}{A}\right)}\right)} t \right)$$

Equation 34 accurately predicted the current transients and time dependent deposit weight for deposition times as long as 600sec.

4.7.2 Physical Model

Previously we reported the fundamentals of EPD on non-conductive substrates and compared them with that on conductive substrates. Two factors were determined to influence the amount of deposit on non-conducting substrates, the amount of porosity within the substrate and the thickness of that substrate. These two factors hold when a single substrate type is being used, but when different substrates are used, the dielectric constant must also be considered. When a metallic substrate is used, the conductivity of that substrate is not limiting to the deposition process, as there are readily available

electrons. Non-conductive substrates in a solvent act as two dielectrics sandwiched between parallel plate electrodes and therefore the deposition process is limited by the dielectric constant and thickness of the deposition substrate. Ohmic losses across the substrate represent the greatest losses in a system when a non-conductive substrate is used, as opposed to a system with a conductive substrate, which has the majority of its losses occur across the suspension. The presence of a non-conductive substrate also leads to significant polarization resistance at the cathode interface, which isn't observed in systems with conducting substrates.

A physical model was developed by Gonzalez-Cuenca et al., which is based on one-dimensional deposit growth under constant voltage conditions in a stirred suspension.[232] Two layers, the growing deposit and the suspension are considered in the model, which incorporates mass balance and no concentration gradients. They accounted for the electrostatics by starting with Maxwell's equations confined to Coulomb's Law and assumed that no charge is present at the cast-suspension boundary and that the permittivity of the cast and suspension is independent of position. These assumptions lead to the Poisson equation, which further simplified to the Laplace equation. Experimental values from Zhang et al. were used to evaluate the model's accuracy in predicting data.[234]

There are some assumptions that Gonzalez-Cuenca et al. used in their model that we don't agree with, specifically how they deal with the particle, cast and suspension permittivities and their lack of accounting for the change in dielectric constant of the suspension and cast as a function of deposition time. Contrary to Sareni[235] and González-Cuena.[232], J. Will et al. made the assumption that the dielectric constant of the deposit is greater than that of the suspension ($\varepsilon_D > \varepsilon_s$). Sareni[236] and González-Cuena.[232] assumed that the dielectric constant followed the Clausius-Mosotti approach (the suspension is considered as a periodic composite). The Clausius-Mosotti approachtreats the effective permittivity of the composite using the volume fraction, Φ_i, and relative permittivity, ε_i,

of the respective phases, but doesn't take into account the increased interface of the formed deposit.

Equation 35

$$\varepsilon = \varepsilon_s \frac{\varepsilon_p + 2\varepsilon_s + 2\phi_p(\varepsilon_p - \varepsilon_s)}{\varepsilon_p + 2\varepsilon_s - \phi_p(\varepsilon_p - \varepsilon_s)}$$

The solvent, *s*, is considered the host or matrix and the particle, p, is considered the filler material in this approach to determining the effective dielectric constant. The equation is restricted to a volume fraction of particle/filler less then 0.45 ($\Phi_p < 0.45$). Based on this approach, the dielectric constant of the YSZ deposit formed by J. Will would be ~9.7, which is significantly lower than the dielectric constant of the ethanol medium, 24.3. This calculation assumes that the polyethylenimine (PEI) dispersant has a negligible effect on the effective dielectric constant, since its volume fraction is only 0.1% of the entire suspension. Our own analysis on the dielectric constant of a wet deposit will be shown later.

Since our EPD system appears to follow Gaussian physics, we decided to develop our own physical model that added interfacial polarization into the equation by modeling the entire system similar to a Maxwell-Wagner two layer condenser. We modified the Maxwell-Wagner equation to include three layers: the substrate, the growing cast and the suspension, as shown in Figure 79.

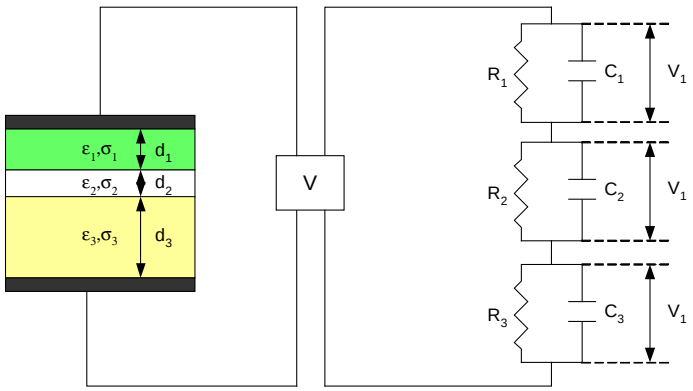

Figure 79. Schematic and equivalent circuit for modified Maxwell-Wagner two-layer condenser.

Solving the electrical circuit we determine that:

Equation 36

$$V_T = V_1 + V_2 + V_3$$
$$I_T = I_1 = I_2 = I_3 = C_i \frac{dV_i}{dt} + \frac{V_i}{R_i}$$

The boundary conditions are that initially the field distribution must follow the electrostatic requirement of constant flux density ($D_1=D_2=D_3$) and at steady state the field distribution must obey the condition of current continuity ($J_1=J_2=J_3$). Using these conditions, a transient linking initial and final stages can be derived. In order to determine the three independent V_i components of the current, I_i, three independent equations were determined, as shown.

Equation 37

$$(1) \quad C_1 dV_1 + \frac{V_1}{R_1} = C_2 dV_2 + \frac{V_2}{R_2}$$
$$(2) \quad C_2 dV_2 + \frac{V_2}{R_2} = C_3 dV_3 + \frac{V_3}{R_3}$$
$$(3) \quad V = V_1 + V_2 + V_3$$

These equations were independently solved by hand and through Mathematica v5.2, resulting in the same voltage derivative, V_i, equations.

Equation 38

$$V_1 = \left(\frac{1}{R_1+R_2+R_3}\right)\left(-VR_1 + R_1R_2C_1\frac{dV_1}{dt} + R_1R_3C_1\frac{dV_1}{dt} - R_1R_2C_2\frac{dV_2}{dt} - R_1R_3C_3\frac{dV_3}{dt}\right)$$
$$V_2 = \left(\frac{1}{R_1+R_2+R_3}\right)\left(-VR_2 + R_1R_2C_1\frac{dV_1}{dt} + R_1R_2C_2\frac{dV_2}{dt} - R_2R_3C_2\frac{dV_2}{dt} - R_2R_3C_3\frac{dV_3}{dt}\right)$$
$$V_3 = \left(\frac{1}{R_1+R_2+R_3}\right)\left(-VR_3 + R_1R_3C_1\frac{dV_1}{dt} + R_2R_3C_2\frac{dV_2}{dt} - R_1R_3C_3\frac{dV_3}{dt} - R_2R_3C_3\frac{dV_3}{dt}\right)$$

Since we're dealing with ordinary 1st order differential equations (Bernoulli Equations),[237] we can solve them by finding a general solution by separating the variables of the homogeneous equation when it's in the form of

Equation 39

$$y' + p(x)y = r(x)$$

Integrating by an integrating factor, *F(x)*

Equation 40

$$F(x) = e^{\int p dx}$$

results in a general solution of

Equation 41

$$y = e^{-\int p dx} \int r e^{\int p dx} dx + c$$

The value of *p*, in the integrating factor is represented by:

Equation 42

$$\frac{(R_1 + R_2 + R_3)}{R_1 R_2 R_3 (C_1 C_2 + C_1 C_3 + C_2 C_3)}$$

Rearranging Equation 38 into a form similar to Equation 39 and multiplying by the integrating factor resulted in Equation 41, which was simplified to the component V_i terms.

Equation 43

$$V_1 = V_{app}\left(\frac{R_1}{R_1 + R_2 + R_3}\right)\left\{1 - \left(1 - \frac{C_2 R_2 + C_3 R_3}{\tau}\right)e^{-t/\tau}\right\}$$

$$V_2 = V_{app}\left(\frac{R_2}{R_1 + R_2 + R_3}\right)\left\{1 - \left(1 - \frac{C_1 R_1 + C_3 R_3}{\tau}\right)e^{-t/\tau}\right\}$$

$$V_3 = V_{app}\left(\frac{R_3}{R_1 + R_2 + R_3}\right)\left\{1 - \left(1 - \frac{C_1 R_1 + C_2 R_2}{\tau}\right)e^{-t/\tau}\right\}$$

Where the time constant, τ, is defined as

Equation 44

$$\tau = \frac{(C_1 C_2 + C_1 C_3 + C_2 C_3)(R_1 R_2 R_3)}{(R_1 + R_2 + R_3)}$$

The values of V_1, V_2 and V_3 could then be fed into Equation 36 along with values of the differential dV_i terms. The dV_i terms were determined by solving Equation 36 for dV_i, similar to what was done for V_i. Since each of the constituent variables (C_i and R_i) are time-dependent, empirical expressions governing their behavior were generated from experimental results. To determine the time-dependent behavior of the capacitance, the dielectric constant of the deposit and the suspension were measured as a function of time using a Solartron 1255 Frequency Response Analyzer and a 1296 Dielectric Interface. The increase in dielectric constant of the deposit is shown in Table 23.

Table 23. Time-dependent dielectric constant of deposit layer. 'Smushed' represents the dielectric response when the two electrodes were smushed together with the deposit between.

Time (sec)	Dielectric Constant
0	21.69
30	24.49
60	24.64
180	25.11
300	25.60
600	25.67
1200	26.50
Smushed	31.17

As can be seen, the dielectric constant of the deposit increases with time. After the time-dependent experiments were concluded, the deposit was 'smushed' between the two electrodes and a final measurement taken. The resulting dielectric constant of the wet deposit was 31.17, quite close to literature values of the dielectric constant of YSZ, and proof that the dielectric constant of a wet deposit is greater than that of the suspension, as proposed by Will et al. This also indicates that the Clausius-Mosotti approach doesn't yield a valid representation of the dielectric constant of a wet deposit layer since the composite model doesn't account for the increased interface formed during the deposition process. Other experiments to determine changes in suspension conductivity and deposit growth rates were also conducted. All the constituents were assumed time-dependent except for those associated with the substrate, layer 1, which were assumed static, the values of which are shown.

Equation 45

$$C_1 = 7.25 * 10^{-11} F$$
$$R_1 = 232336 \Omega$$
$$d_1 = 300 * 10^{-6} m$$

The empirical expressions generated for each constituent variable of layers 2 (deposit) and 3 (suspension) are given.

Equation 46

$$C_2 = \frac{\varepsilon_{r2}\varepsilon_o A}{d_2} \quad where \quad \varepsilon_{r2} = 21.7 + 0.7Ln(t)$$
$$R_2 = (200334Ln(t) - 146768) - R_2 - R_3$$
$$d_2 = 4.23 * 10^{-8}(t)$$
$$C_3 = \frac{\varepsilon_{r3}\varepsilon_o A}{d_2} \quad where \quad \varepsilon_{r3} = 27 - 0.7Ln(t)$$
$$R_3 = 1230Ln(t) + 45442$$
$$d_3 = 0.0097 - 4.23 * 10^{-8}(t)$$

These experimental values and equations were plugged directly to Equation 43 resulting in a plot of the predicted voltage transients, which is given in Figure 81.

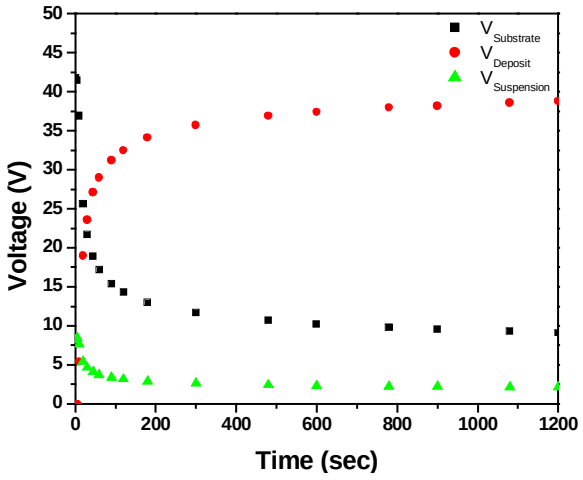

Figure 80. Plot of voltage transients calculated from Equation 43.

The values of V_1, V_2 and V_3 were then input into Equation 36, along with the derivative, dV_i, values, which obeyed the following relation.

Equation 47

$$dV_1 = -\frac{C_2R_2R_3V_1 + C_3R_2R_3V_1 - C_3R_1R_3V_2 - C_2R_1R_2V_3}{R_1R_2R_3(C_1C_2 + C_2C_3 + C_1C_3)}$$
$$dV_2 = -\frac{-C_3R_2R_3V_1 + C_1R_1R_3V_2 - C_3R_1R_3V_2 - C_1R_1R_2V_3}{R_1R_2R_3(C_1C_2 + C_2C_3 + C_1C_3)}$$
$$dV_3 = -\frac{-C_2R_2R_3V_1 + C_1R_1R_3V_2 - C_1R_1R_2V_3 - C_2R_1R_2V_3}{R_1R_2R_3(C_1C_2 + C_2C_3 + C_1C_3)}$$

The final result of this model is a current transient, shown in Figure 81, which follows very closely with the experimental values.

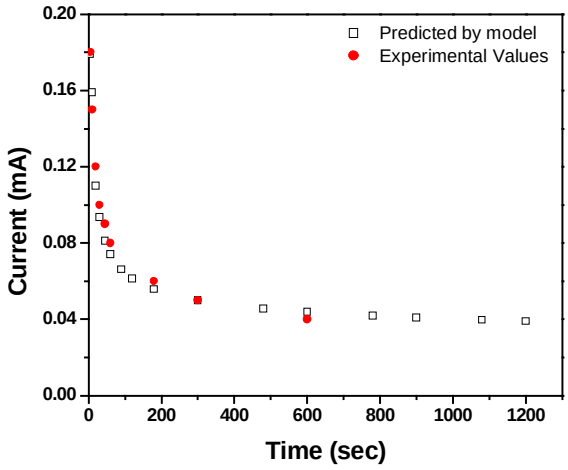

Figure 81. Plot of current transients from physical model compared to those from experiments. Note the agreement between the model and experimental data.

As is evident, the physical model accurately depicted the initial current drop due to polarization within the system. Given the agreement between the model and the experimental data, Equation 43 can be used to model constant voltage EPD on non-conducting substrates. In fact, non-conducting substrates are just one case for which this model can be used. The model itself is a very general case and can be easily modified for constant voltage EPD on conducting or non-conducting substrate use.

4.8 Conclusions

The longstanding assumption that EPD requires a conductive substrate is not necessarily true. A method for performing electrophoretic deposition on non-conducting substrates has been developed through the use of porous substrates. In essence deposition on a non-conductive substrate is akin to deposition on a conductive substrate that already has a non-conductive layer deposited on it. In practice, only the electrodes (working and counter) need to be conductive, so as to achieve a uniform driving force for deposition, be it through constant voltage or constant current. From a fundamentals/mechanistic

standpoint, EPD on non-conductive substrates follows most of the same trends as on conductive substrates. The deposit mass per unit area follows a linear trend with the amount of charge passed for all time-scales and a linear trend with voltage for deposition times less than 3 minutes. The amount of deposit increases with the substrate porosity and at the same level of porosity; increased substrate thickness decreases the amount of deposit.

EPD on porous non-conducting NiO-YSZ substrates was analyzed statistically through an inscribed central composite statistical design. YSZ deposit thickness, power density and ASR were influenced the greatest by the level of substrate firing temperature due to the resultant substrate porosity. Power density and ASR were also strongly influenced by the voltage quadratic term. Low levels of substrate firing temperature (1100°C), when combined with low levels of voltage (50V) and time (1min) lead to a 6μm film with high power density (628mW/cm^2) and low interfacial resistance (0.21Ωcm^2). Substrate firing temperature and/or voltage increases generally decreased deposit density and power density while increasing ASR. The time factor had its most significant influence on the deposit thickness and therefore also the power density, but wasn't found to affect ASR. A final experiment, generated by the model, validated the legitimacy of the model to predict experimental results.

The electrophoretic deposition of YSZ on a non-conducting and porous NiO-YSZ anode substrate has been demonstrated. We believe that this approach of using porous substrates for electrophoretic deposition on non-conducting substrates can be extended for both thin and thick film deposition on a variety of other non-conducting substrates as well. The success of electrophoretic deposition of YSZ on NiO-YSZ substrates is significant since it enables deposition of thin SOFC electrolytes at low cost.. The SOFC constructed on such bi-layers exhibited a power density of 1.2W/cm^2 at 850^{o}C and an

OCV of 1.01V. The feasibility of electrophoretic deposition on non-conducting substrates also opens up its use in other applications such as membranes supported on porous substrates for gas separation, sensors and other electrochemical devices.

Empirical and physical-based models were developed to model the experimental current transients and deposit weights as a function of deposition time. The empirical model combined two previous works with a factor to account for the non-conductive substrate. As was determined in the literature, an empirically based time-independent kinetic parameter was successful in modeling constant voltage EPD. A physical based model was developed, which was essentially an extension of the Maxwell-Wagner two-layer condenser. The model was able to account for polarization losses at the dielectric-electrode interface, the dynamic growth of a porous dielectric layer and time dependent physical properties (resistance and capacitance) within the suspension and deposit layers. This model can now be used as a very general case of a physical model for EPD regardless of deposition on a conductive or non-conductive substrate.

These results show that this technique is farther reaching than just for fabrication of dense electrolytes for SOFCs. Many applications would like use porous oxide substrates as the building block for device fabrication, but can't because of the difficulty in depositing a dense uniform layer over top of it. Other more common deposition techniques such as DC and RF sputtering, PVD, EVD and CVD struggle to form thin dense films on porous substrates. Therefore this breakthrough deposition technique opens the door for the deposition of thin dense layers on any porous non-conducting substrate, regardless of substrate or particle type.

V. HERMETIC SOLID OXIDE FUEL CELLS WITHOUT SEALANT

5.1 Literature Review

An SOFC at its simplest level is four independent materials sandwiched together to carry out an electrochemical reaction. These materials range from highly conducting metals to highly insulating ceramics, have drastically different lattice constants, thermal, electrical and mechanical properties, phase stabilities and ion activities. The majority of current research has been aimed at improving or altering these materials so that they interact more amicably during operation. Another avenue of research has been to develop intermediary materials with properties in between those of the two fuel cell components. These materials are sandwiched between the original fuel cell components to reduce unwanted reactivity. Despite improving the properties, adding new materials to the SOFC increases its complexity as well as the number of total interfaces. Increasing the number of materials causes the SOFC to operate in a much more interfacial dependent mode since for every added material there are up to two added interfaces, as shown in Figure 82.

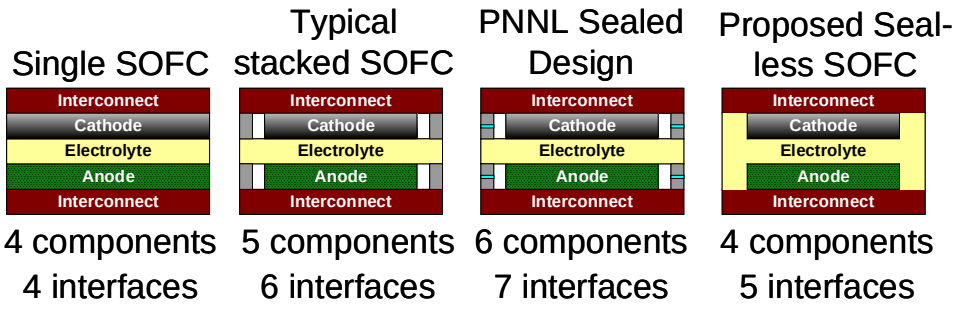

Figure 82. Evolution of SOFC design showing the introduction of multiple interfaces through external sealants, buffer layers and extraneous materials.

Interfacial dependence means that the charge carrying species now has to travel across more interfaces than actual bulk materials causing the interfacial properties to control the SOFC characteristics. At a critical complexity point, the bulk materials no longer control the operating mechanisms and their properties become insignificant compared to those of the interfaces themselves. SOFC performance therefore is no longer a function of the materials chosen, but the interfacial reaction layers formed between them.

When any two materials are joined together, a hybrid region develops between them. The thickness of that region is function of the degree of interaction between those materials. Therefore highly active materials or ions will readily give up their position in one material and cross the interface to react with another. As this occurs a new phase may develop, which may not be beneficial to the interface. Since phase stability controls a number of important characteristics such as interactions with neighboring materials, atmospheric interactions, ion affinity and activity, kinetics of reaction and potential changes in the physical properties, minimizing the amount of interaction is crucial. Depending on the interface, SOFC components desire both highly mixed and highly inert interfaces. The cathode-electrolyte interface performs best when the interface is mixed or gradual. The interconnect-electrode interface performs best when the interface is inert, or rather that no ions diffuse in either direction. Development of efficient interfaces between SOFC components is therefore essential for high power density and the stability of those interfaces will determine the lifetime, cyclability, and overall success of SOFCs as commercial energy conversion devices.

One of the major problems facing the advancement of solid oxide fuel cell (SOFC) technology is sealing between cells in a stack.[99,100] Typical glass and ceramic seals can form reactive phases,[101-103] leak[104] and/or degrade[101,102] over time, decreasing SOFC performance. While recent work addressing the issue of SOFC sealant materials shows progress, various problems still remain.[99,100] Hard seals such as those achieved using glass sealant materials are rigid and readily prevent gas mixing, but degrade over

time due to atmospheric conditions.[101-103, 111] Glass seals also have difficulty relaxing to the thermal stresses of cycling and often crack the materials in which they are in contact. Soft or compressive sealant materials such as various mica compositions and ceramic fiber seals have also been examined.[105] These materials tend to have higher leakage rates than the rigid glass materials, but show better thermal cycling characteristics. Presently there is no universal sealing method and research to improve stack sealing has centered on glass, ceramic and glass-ceramic hybrid materials.[238] Hybrid sealant materials developed at PNNL have achieved leakage rates as low as 0.01sccm/cm at 800°C for polycrystalline muscovite and phlogopite mica layers under $6.89*10^5$-$2.76*10^6$ Pa (100-400psi) compressive stresses.[239] Hybrid sealants using single crystal muscovite mica show leakage rates two orders of magnitude lower at compressive stresses of $1.72*10^5$-$6.89*10^5$ Pa (25-100psi), which are some of the lowest reported in literature, as shown in Table 24.[239,240,241,242]

Table 24. Literature values of leakage rate for SOFC sealants.

		Normalized* Leakage Rates (sccm/cm)					
Temp (ºC)	Compressive	Muscovite Single Crystal		Muscovite Paper		Phlogopite Paper	
	Stress (psi)	Plain	Hybrid	Plain	Hybrid	Plain	Hybrid
800	25	-	0.000359	-	-	-	-
800	50	-	0.000243	-	-	-	-
800	100	0.65	0.000155*	5.77	0.0126	8.85	0.0108
800	200	-	-	-	0.0122	-	0.0105
800	300	0.42	-	2.84	0.0115	2.97	0.0103
800	400	-	-	-	0.0107	-	0.0098
800	500	0.28	-	1.92	-	1.68	-

A typical glass seal is $5x10^{-5}$ sccm/cm @ 800ºC

5.2 Hermetic Seal

A unique SOFC design has been developed aimed at reducing system complexity by decreasing the number of components and interfaces. The design forms an inherent solid-state seal between interconnect and electrolyte through expansion of the electrolyte

layer beyond the anode chamber and down to interconnect. This exploits the requirements of the separator and sealant because both need to be dense, gas impermeable, non-reactive/chemically compatible with surrounding components and atmospheres as well as unaffected by the operating temperature. Since the primary SOFC components need to have similar CTE, the sealing capability of this interface will be determined by its ability to block gas transport and shouldn't be confounded by thermal issues. A schematic of the proposed hermetic design was shown in Figure 21 and a modified version is shown again here.

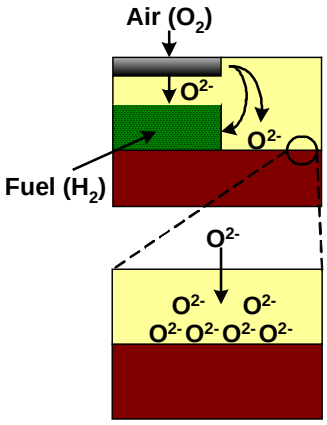

Figure 83. Proposed hermetic SOFC design showing the blocking electrode function of the YSZ|$FeNiCr_5$ interface.

5.2.1 Blocking Electrode

To evaluate the sealing capability of the proposed hermetic SOFC structure, the interfacial characteristics of each component in contact with the interconnect were examined. Symmetric cells of anode-interconnect and electrolyte-interconnect were fabricated in order to isolate the desired interface. The electrolyte-interconnect interface was prepared with two different geometries in order to analyze gas transport characteristics both across and along the interface. The two interfacial geometries,

longitudinal and lateral, differed with respect to how the electrolyte and interconnect were positioned, as shown in Figure 84.

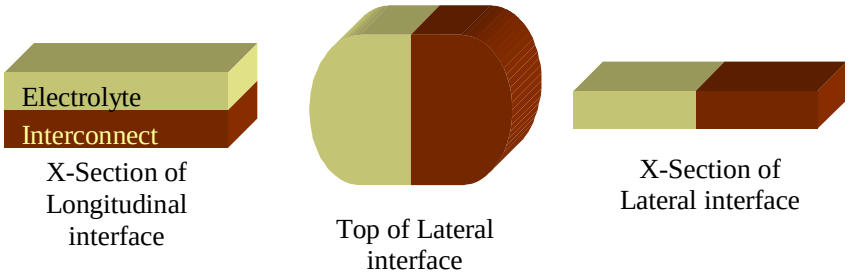

Figure 84. Schematics of longitudinal and lateral interfaces, which represent the critical interface in the hermetic design.

Symmetric cells were fabricated by lamination of individual component tapes, overcasting (longitudinal interface), and co-casting (lateral interface). Iron oxide (Fe_2O_3, >99.5%), nickel oxide (NiO, 97%) and chromium oxide (Cr_2O_3, 99%) powders were purchased from Fisher Scientific as the starting materials for the interconnect slurry. YSZ powder (8 mol%, Daiichi Corporation) with a median particle size of 0.26μm was used for the electrolyte slurry. The as-received NiO particle size (d<10μm) was initially too large to remain suspended and therefore was ball milled until it had a particle size of less than 3μm, as shown in Figure 24. The Fe_2O_3 and Cr_2O_3 powders were used as received and had particle sizes of less than five microns. Stoichiometric mixtures of the interconnect powders were prepared in order to achieve a final composition of $Fe_{47.5}Ni_{47.5}Cr_5$ ($FeNiCr_5$). This composition was chosen based on the recommendation of Church who studied the physical properties of various SOFC interconnect alloys from room temperature to 750°C and compared them to YSZ (CTE=$10.5*10^{-6}$ K^{-1}).[97] The interconnect slurry was prepared using 21% solids by volume, 60% by volume of solvent (an even mixture of ethanol and xylenes) and 21% dispersant (Z-3 Menhaden fish oil) with respect to solids content. The remainder of the slurry was organic binder

(polyvinyl butyral, B-98) and plasticizer (UCON polyalkylene glycol and S-160 butyl benzyl phthalate) with ratios of 3.8:1 and 2.5:1 to the solids content respectively. The exact formula for the interconnect slurry is shown in Table 25.

Table 25. Slurry formula for tape cast interconnect.

Component	Purpose	Weight (%)	Weight (g)	Volume (%)	Volume (cm^3)
Fe_2O_3	powder	50.1	20.04	11.8	3.82
NiO	powder	44.5	17.8	8.27	2.67
Cr_2O_3	powder	5.4	2.16	1.28	0.414
Ethanol	solvent	12.5	7.69	29.75	9.61
Xylenes	solvent	12.5	7.69	29.75	9.61
Menhaden Fish Oil	dispersant	2.5	1.54	4.67	1.54
Polyalkylene Glycol	plasticizer (type I)	3	1.85	5.73	1.85
Butyl Benzyl Phthalate	plasticizer (type II)	1.5	0.923	2.86	0.923
Polyvinyl Butyral	binder	3	1.85	5.73	1.85

The YSZ slurry was prepared using lower solids content (17.6% by volume) because the median particle size was considerably smaller, 64% by volume of solvent and 21% dispersant with respect to solids content. The same binder and plasticizer organics were added to the slurries in ratios of 3.7:1 and 3:1 of solids content respectively. The exact YSZ electrolyte formula is given in Table 26.

Table 26. Slurry formula for tape cast YSZ electrolyte.

Component	Purpose	Weight (%)	Weight (g)	Volume (%)	Volume (cm^3)
YSZ	powder	60	50	17.61	8.33
Ethanol	solvent	14.5	12.08	32.92	15.58
Xylenes	solvent	14.5	12.08	30.90	14.62
Menhaden Fish Oil	dispersant	3	2.49	5.26	2.49
Polyalkylene Glycol	plasticizer (type I)	2.625	2.187	4.62	2.187
Butyl Benzyl Phthalate	plasticizer (type II)	1.625	1.354	2.86	1.354
Polyvinyl Butyral	binder	3.75	3.12	6.59	3.12

All tape cast slurries were prepared using a two-stage milling process. The initial slurry contained only powder, solvent and dispersant and was ball-milled for four hours prior to addition of the other constituents. Ball-milling was then resumed for another 24 hours

before casting the slurries at a blade height of 150μm on a Mistler TTC-1200 tabletop caster, as shown in Figure 85.[117]

Figure 85. R.E. Mistler TTC-1200 table top caster.

Lamination of individual tapes was used to fabricate symmetric cells between the anode, electrolyte and interconnect materials. The longitudinal geometry was prepared by casting the electrolyte slurry overtop of the interconnect (overcastting) and then laminating two bi-layers together into a symmetric cell. Co-casting or the simultaneous (side-by-side) casting of two slurries and was used to fabricate the lateral interface geometry. The cast tapes were allowed to dry overnight before 1.9cm circular samples were punched, laminated together in a uniaxial press and sintered at 1300°C in 4%H_2 (balance Argon) for five hours, a schedule determined by dilatometry. A semi-constrained sintering technique, using 11.5cm x 11.5cm alumina firing plates and ceramic spacers of known thickness, was employed to ensure that the resulting samples would not warp during sintering. Though there is some debate as to whether the Cr_2O_3 can be fully reduced, Cochran et al., determined that mixing of the component powders in the oxide phase helps to ensure full reduction.[243] Figure 86 shows an XRD pattern of the interconnect after sintering.

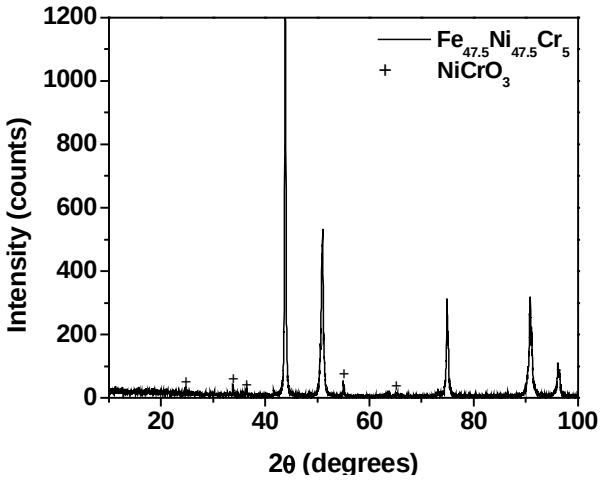

Figure 86. XRD pattern of reduced $Fe_{47.5}Ni_{47.5}Cr_5$ interconnect after sintering at 1300°C in 4%H_2 for 4hrs.

After sintering, silver electrodes were attached to the symmetric cell samples for testing in reducing (H_2 + 3%H_20), oxidizing (air) and SOFC operating environments. Interfacial properties of the symmetric cells were studied by electrochemical impedance spectroscopy (EIS) as a function of temperature and direct current (DC) bias. Samples were ramped to 550°C in each atmosphere and held for 30 minutes before testing. Impedance measurements were conducted in 50°C increments from 550°C to 750°C under open circuit (DC=0V) and DC bias conditions (DC=0.1, 0.3 and 0.5V) with 20-minute dwell times before each measurement. The frequency was swept from 1MHz to 20mHz with an AC perturbation of 20mV. The above experiments were also repeated for a bulk interconnect pellet of the same composition ($Fe_{47.5}Ni_{47.5}Cr_5$). This allowed the ohmic contribution of the interconnect to be subtracted from that of the electrolyte in the overall impedance spectra.

The first interfacial geometry, the longitudinal interface, sandwiches the electrolyte in between two interconnect layers in a symmetric cell structure. The longitudinal interface was prepared in order to determine the interfacial characteristics of gas species moving between interconnect and electrolyte layers. Ideally a dense interface

forms between the electrolyte and interconnect, which blocks gas transport. Impedance spectroscopy was used to measure the interfacial characteristics as a function of temperature and DC bias, as described above. If gaseous species are being blocked at the electrolyte-interconnect interface, mass transport limitation will result in an increase in impedance with applied DC bias. If gas species are not blocked, impedance will decrease with DC bias. Schematics of impedance spectra under mass transport and charge transport control are shown in Figure 87(a-b).

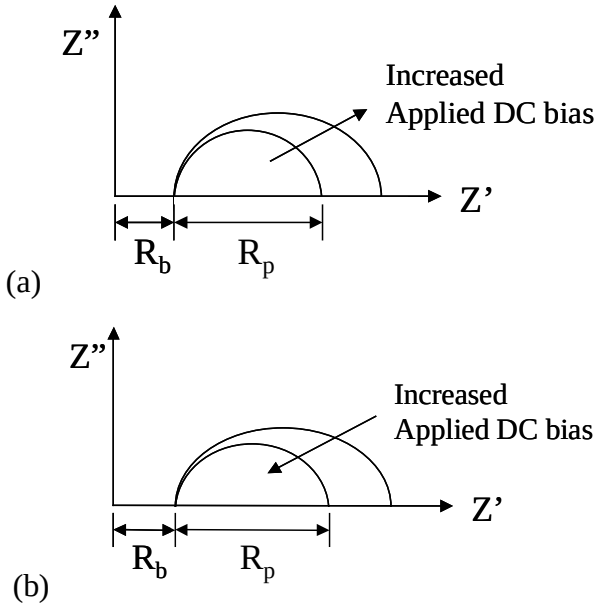

Figure 87. Schematics of impedance spectra under (a) mass transfer and (b) charge transfer control when a DC bias is imposed.

Blocking gas transport within the cell will also lead to a build up of ions at the interface causing a residual voltage to be retained within the cell even after removal of the applied bias. The ability of the cell to relax or dissipate this charge (relaxation time constant) should be proportional to the porosity of the interface. Initially symmetric cell samples were prepared by laminating individual layers of interconnect and electrolyte tape

together in the uniaxial press. Impedance characterization of the laminated symmetric cell is shown in Figure 88.

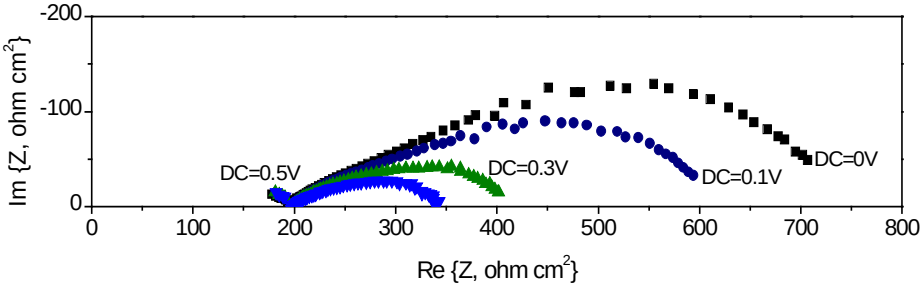

Figure 88. Impedance spectra of $FeNiCr_5$|YSZ|$FeNiCr_5$ laminated symmetric cell at 650°C in air as a function of DC bias.

The impedance of the symmetric cell formed by lamination decreased with increased applied DC bias as discussed previously.[244] The decrease in impedance with DC bias was due to the formation of bulk and interfacial porosity during testing. This can be seen in the SEM images, shown in Figure 89(a-c), of the electrolyte-interconnect interface, interconnect surface and interconnect bulk before and after testing.

(a) 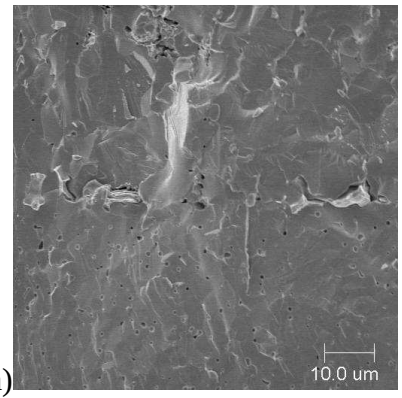

(b) 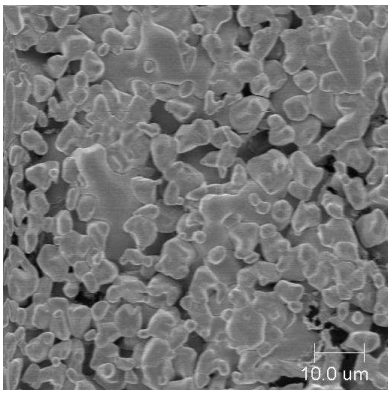

(c) 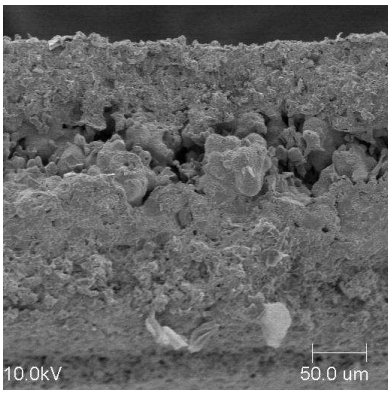

Figure 89. SEM images of (a) $FeNiCr_5$|YSZ electrolyte interface before testing, (b) $FeNiCr_5$ surface after testing and (c) $FeNiCr_5$ bulk after testing.

Based on the isothermal impedance trend as a function of DC bias it was determined that the sharp interface resulting from lamination of individual electrolyte and interconnect component tapes could not form an interface that blocked gas transport. The after-testing SEM images of the interconnect also showed that increased density was necessary. In order to achieve an interface that effectively blocked oxygen transport a fabrication method that allowed a more intimate mixture of the interconnect and electrolyte was required. Intermixing of the two layers was accomplished by overcasting of the electrolyte and interconnect tapes. Instead of casting each layer individually and uniaxially laminating them together, the layers were cast on top of each other while in the green state. The result is shown in Figure 90(a-b), which reveals a large region of intermixing between the YSZ electrolyte and the $FeNiCr_5$ interconnect as well as elimination of interfacial porosity. Another improvement was the surface of the $FeNiCr_5$ material, which shows a dense surface as opposed to the porous surface shown previously in Figure 88(b).

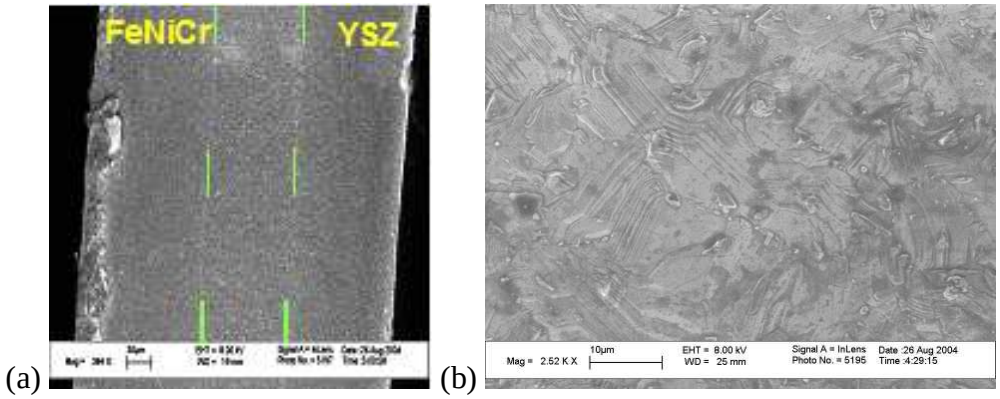

Figure 90. SEM images of (a) $FeNiCr_5$|YSZ interface by overcastting after testing and (b) dense $FeNiCr_5$ surface after testing.

Overcasting fabrication resulted in an intermixed region over 50µm thick between interconnect and electrolyte layers. Energy dispersive x-ray analysis (EDS) of the intermixed region revealed that it was in fact an intermixture of interconnect and electrolyte materials. The EDS spectrum of the intermixed region is shown in Figure 91.

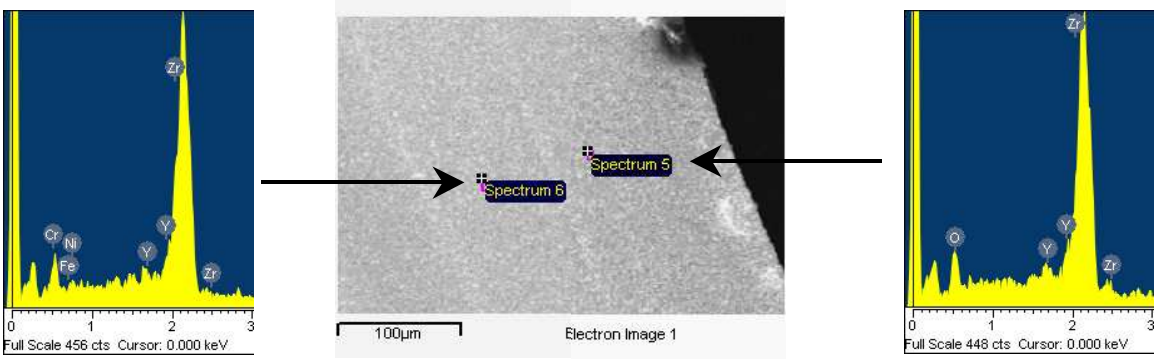

Figure 91. EDS spectrum of the $FeNiCr_5$|YSZ intermixed region after testing.

XRD of the YSZ|$FeNiCr_5$ cross-section didn't reveal any secondary phases present in the system, only the YSZ, $FeNiCr_5$, and a $NiCrO_3$-like oxidation phase of the interconnect, which was present previous to testing (see Figure 86), as shown in Figure 92.

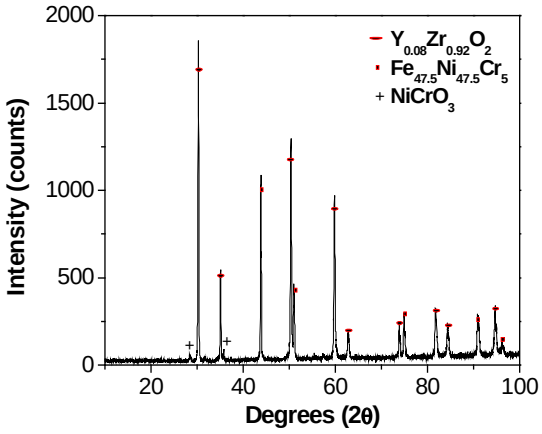

Figure 92. XRD pattern of YSZ|FeNiCr$_5$ cross-section after testing.

Electrochemical impedance spectroscopy analysis of the overcast structure in air revealed that the interface formed by overcasting prohibited gas transport. The interfacial resistance decreased as a function of temperature in an air atmosphere when not under polarization. Isothermally however, the interfacial impedance increased as a function of DC bias, as seen in Figure 93, indicating that oxygen ions were blocked at the interface.

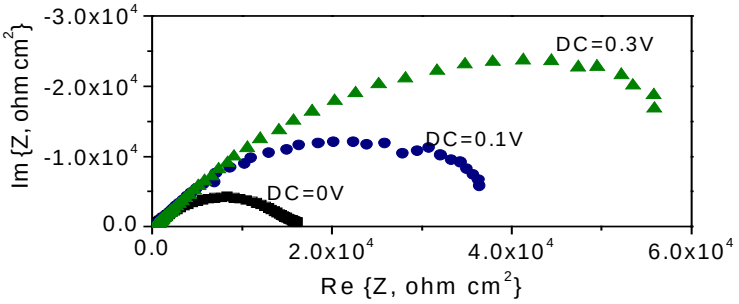

Figure 93. Impedance of FeNiCr$_5$|YSZ|FeNiCr$_5$ overcast symmetric cell interface at 650°C as a function of DC bias.

After the applied DC bias was removed from the cell, a significant amount of residual voltage remained at the interface. The remnant voltage was a function of both the applied bias and the temperature at which the measurement was taken. At its peak, a residual voltage of 0.498V remained at the interface after removal of 0.5V-applied bias at 750°C. Attempts to dissipate the residual charge by shorting the lead wires or just allowing the cell to relax had a negligible effect, implying that the interface formed by overcastting blocks ion transport and stores the charge at the interface. Since the measured relaxation time is slow, on the order of a capacitor, the interface must be dense. These were all desired characteristics for the proposed hermetic SOFC. A plot of the residual voltage at the interface and corresponding relaxation time constant as a function of temperature is shown in Figure 94.

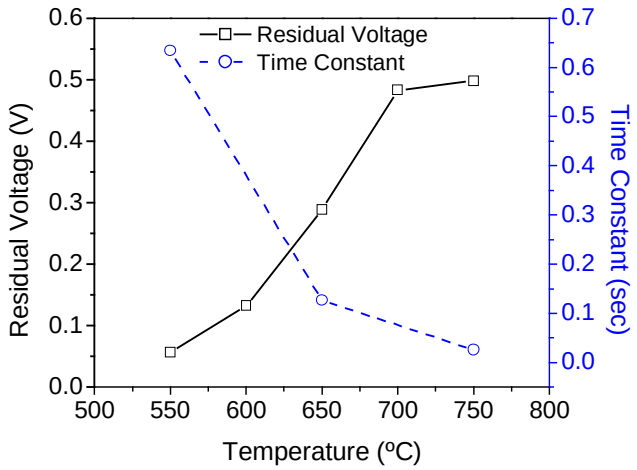

Figure 94. Residual voltage and relaxation time constant at metal-ceramic interface as a function of temperature.

When the atmosphere was changed to humidified (3 vol. % H_2O) hydrogen, the impedance also decreased as a function of temperature. The desired isothermal impedance trend under DC bias was for the impedance to decrease, which is opposite the trend for the air atmosphere. The proposed structure has one point where the

electrolyte/interconnect interface comes in contact with a reducing atmosphere, as seen in Figure 21 and Figure 83, corresponding to a line in three dimensions. Since the electrolyte and interconnect materials are not proton conductors, hydrogen should remain only in the anode chamber during SOFC operation. A decreasing trend in impedance with DC bias corresponds to oxygen ions being pumped into the anode chamber, from within the electrolyte, at a faster rate than under open circuit conditions. These oxygen ions are able to enter the anode both at the top as well as the sides due to the unique higher surface area interface created with the proposed geometry. Therefore the decreasing trend in impedance is acceptable and is shown in Figure 95.

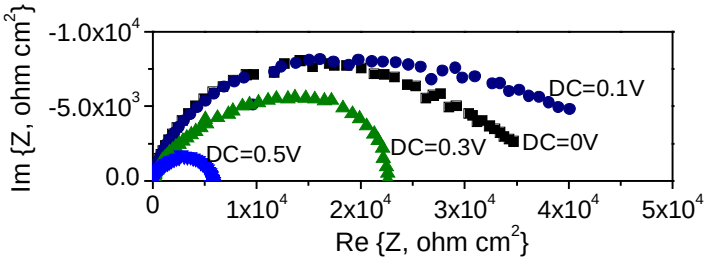

Figure 95. Impedance spectra of $FeNiCr_5$|YSZ|$FeNiCr_5$ as a function of DC bias in humidified hydrogen at 650°C.

Oxidation resistance of the interconnect alloy within the symmetric cell was not explicitly measured; however the physical properties and oxidation resistance of this alloy were previously quantified by Church.[52,97] Church measured the CTE of the alloy from room temperature to 750°C and found that it be $9.17*10^{-6}$ K^{-1}, which closely mirrored that of YSZ at temperatures above 400°C. The alloy was also subjected to oxidizing atmosphere at 700°C for 23 hours without significant observation of oxidation, dusting or spalling. The alloy was observed to remain conductive after all symmetric cell measurements up to 750°C in air and SEM did not reveal any evidence of surface microstructural changes due to oxidation. Switching from an air atmosphere to a hydrogen-containing atmosphere did not appear to affect the sample macrostructure (flatness, shape) or microstructure

(cracking due to oxidation-reduction cycling), which also indicates that the interconnect alloy must have entered the hydrogen atmosphere with negligible oxidation. Symmetric cells involving the anode (Ni-YSZ) and interconnect were also characterized by impedance spectroscopy. Since the anode and interconnect components would be in contact within the proposed hermetic structure as with any SOFC, the interfacial characteristics needed to be determined. The only atmosphere in which the symmetric cell was tested was humidified hydrogen as that is the only environment this interface will encounter in a SOFC. As would be expected for a cell with a continuous metallic phase, the bulk impedance increased steadily with temperature. Shown in Figure 96 is the total conductivity as a function of temperature of the interconnect-anode symmetric cell, as determined from impedance spectroscopy.

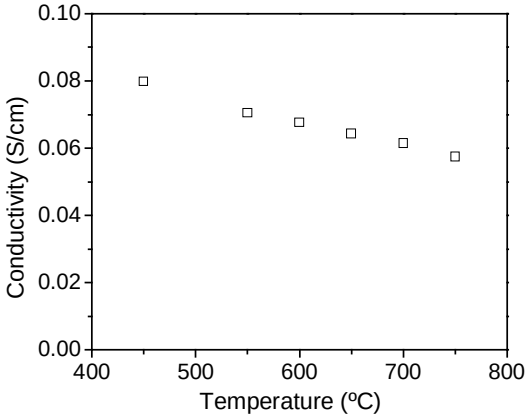

Figure 96. Conductivity of Ni-YSZ|$FeNiCr_5$|Ni-YSZ symmetric cell in humidified hydrogen.

After the success of the YSZ|$FeNiCr_5$ system in making a blocking electrode, the same series of fabrication steps and experiments were performed on the GDC|$FeNiCr_5$ system. Commercial powders of gadolinia-doped ceria (GDC, Rhodia) were obtained and dispersed in organic-based slurries. Ceramic tapes of GDC electrolyte, and the oxide form of FeNiCr stainless steel, as discussed earlier and shown in Table 25, were prepared by tape casting. The appropriate powders were suspended using Menhaden Fish Oil

(dispersant) polyvinyl butyral (binder), polyethylene glycol (type I plasticizer) and butyl benzyl phthalate (type II plasticizer). The slurries were prepared in a two-stage process and ball-milled as discussed previously. The formula for the GDC slurry is shown in Table 1.

Table 27. Slurry formula for tape cast GDC electrolyte.

Component	Purpose	Weight (%)	Weight (g)	Volume (%)	Volume (cm^3)
GDC	powder	60	50	17.60	8.33
Ethanol	solvent	14.5	12.08	32.92	15.58
Xylenes	solvent	14.5	12.08	30.90	14.62
Menhaden Fish Oil	dispersant	3	2.49	5.26	2.49
Polyalkylene Glycol	plasticizer (type I)	2.5	2.08	4.40	2.08
Butyl Benzyl Phthalate	plasticizer (type II)	2	1.29	2.73	1.29
Polyvinyl Butyral	binder	3.5	2.93	6.19	2.93

The green tape was cut into 1.9cm discs and laminated into symmetric cells using a Carver uniaxial press. Symmetric cells of interconnect/electrolyte/interconnect, and interconnect/interconnect were prepared and sintered at 1300°C for four hours in 4% H_2. Semi-Constrained sintering techniques were used in order to minimize warpage while still allowing the tape to sinter without cracking. Platinum electrodes were applied to the cells and electrochemical impedance spectroscopy measurements were conducted from 450°C-750°C in both air and humidified H_2. DC polarization of 0.1V, 0.3V and 0.5V was also applied at 550°C, 650°C and 750°C. The frequency was swept from 200KHz to 20mHz with a 20mV AC perturbation in all experiments. Impedance measurements were taken without applied potential as temperature increased, and with applied potential during temperature decrease. Measurements using no applied potential were also repeated as temperature decreased in order to observe any post applied potential changes in the interfacial properties.

As expected, the impedance decreased as a function of temperature in both air and humidified hydrogen atmospheres. The area specific impedance trends are shown in Figure 97(a-b).

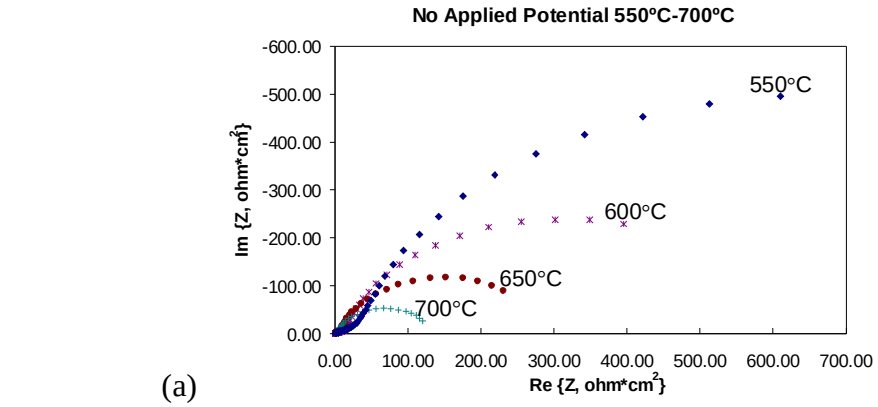

(a)

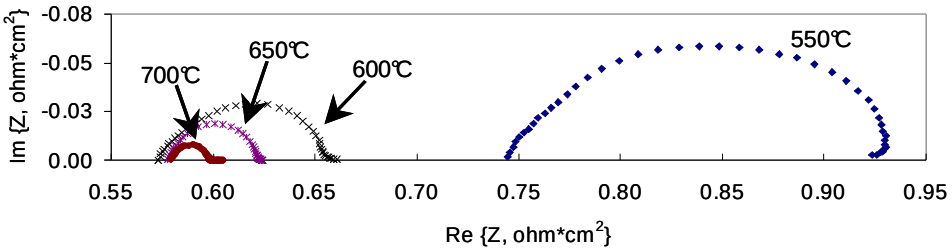

(b)

Figure 97. Area specific impedance spectra of GDC|$FeNiCr_5$|GDC symmetric cell tested in (a) air and (b) 4% H_2 from 550°C to 700°C.

The bulk resistance of the symmetric cell is composed of a single layer of electrolyte and two layers of interconnect. Thus for accuracy, the impedance measurements were corrected for the bulk resistance of the interconnect in both atmospheres values. As a side note, Figure 97(b) shows a drastic decrease in bulk impedance between 550ºC and 600ºC. The drop corresponds to the dramatic increase in the electronic transference number of GDC, especially under a reducing atmosphere, around 600ºC. As was mentioned in *section 2.1.1*, this is the issue with using GDC as an intermediate to high temperature electrolyte. As the electronic contribution to conductivity becomes large enough, electrons leak across the cell and reduce the OCV or even cause shorting. The bulk resistance values for the interconnect in air and humidified hydrogen are shown below in Figure 98.

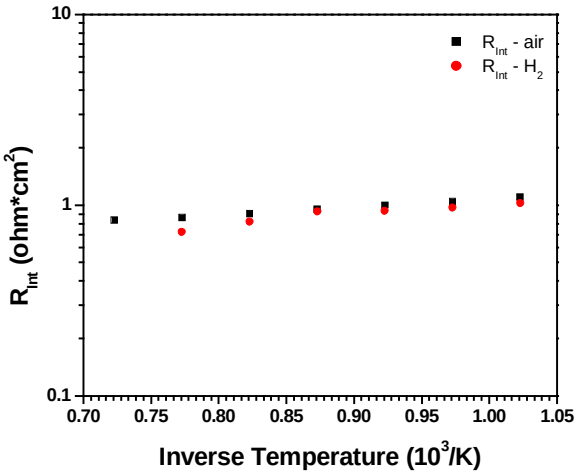

Figure 98. Plot of the log of bulk area-specific resistance versus inverse temperature for the $FeNiCr_5$ interconnect.

To summarize the previous plots, a single graph was made depicting the area specific bulk and polarization resistance values, compensated for lead wire and interconnect bulk resistance, as a function of inverse temperature. This is shown below as Figure 99.

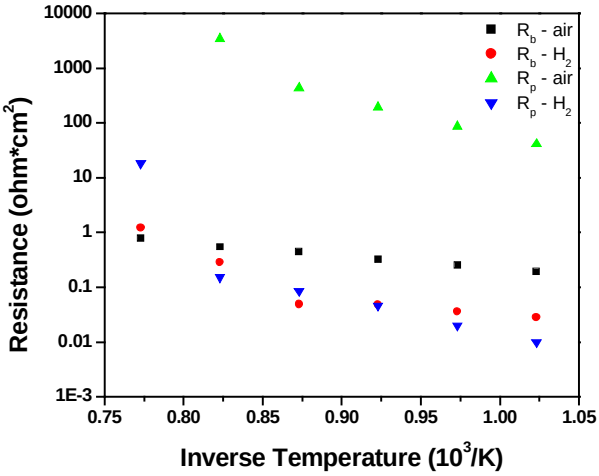

Figure 99. Plot of the log of area-specific polarization resistance versus inverse temperature for the interconnect/electrolyte/interconnect symmetric cell in air and humidified hydrogen atmospheres.

The temperature dependence trends for the symmetric cell without DC polarization showed a decreasing intercept and decreased interfacial resistance as shown in Figure

97(b). As temperature increases the bulk conductivity of the GDC layer should increase and thus the intercept should decrease. Another reason the bulk intercept decreases is that the electronic transference number of GDC increases dramatically within the intermediate temperature range. Therefore it was expected that the bulk resistance decrease greatly above 550°C. The polarization resistance should decease with temperature as well because the mass transfer limitations decrease. Since the interfacial resistance decreased with applied DC polarization, as seen in Figure 100, oxygen is able to permeate through the interconnect and reach the electrolyte.

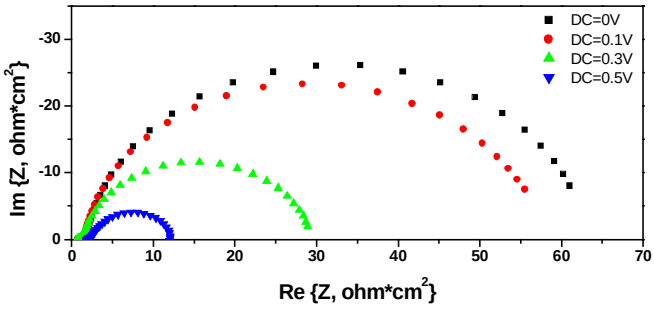

Figure 100. Area specific impedance spectra of symmetric cell tested at 750°C in air with applied DC bias from 0V-0.5V.

Despite the interfacial impedance being high, this data indicates that either the density of the interconnect was not high enough and therefore the interface between the two layers had less of a blocking effect at higher applied potentials or a reactionary layer formed between the GDC and $FeNiCr_5$ layers. To fabricate a complete hermetic seal, the blocking characteristics need to be improved. SEM imaging after testing revealed a porous interfacial layer between the electrolyte and a dense electrolyte surface, as shown in Figure 101(a-b).

(a) 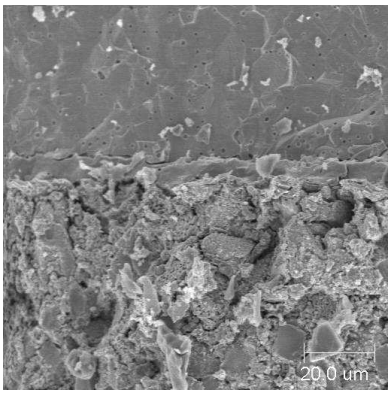

(b) 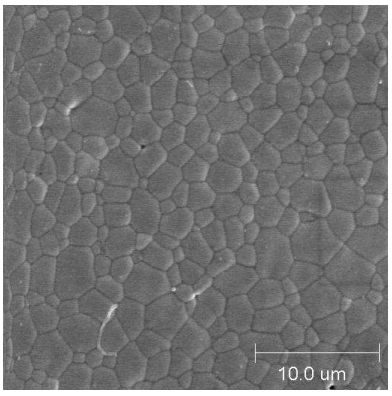

Figure 101. (a) GDC/Interconnect laminate without completely dense interface. (b) Surface image of dense GDC electrolyte.

This indicates that oxygen is more easily transported across the interface as DC bias is increased. Therefore the porous layer allowed oxygen to transfer across the interface from the electrolyte into the interconnect. Application of a DC bias only promoted this transport to occur at a higher rate, thus reducing the impedance further from the open circuit state. Traditional planar SOFCs typically use the interconnect as both a current collector and as a vehicle for gas flow channels. The interconnect used in this experiment would serve well for that application as it has a random connected surface porosity that allows gas to travel easily. For the type of seal-less SOFC attempting to be fabricated in this experiment, the surface porosity is not desired.

Tested and untested GDC|$FeNiCr_5$ samples were then cross-sectioned and viewed using a Hitachi S-800 SEM and LEO 1530 SEM to determine polarization effects on the interface. Surface images were also taken of untested samples to observe the apparent porosity, grain size and grain size distribution. EDS dot mapping was also done for tested and untested samples in order to determine the amount, if any, of ion movement across the interface as well as the effect of DC polarization on the elemental activity and distributions. The EDS dot map of the cross-section is shown in Figure 102.

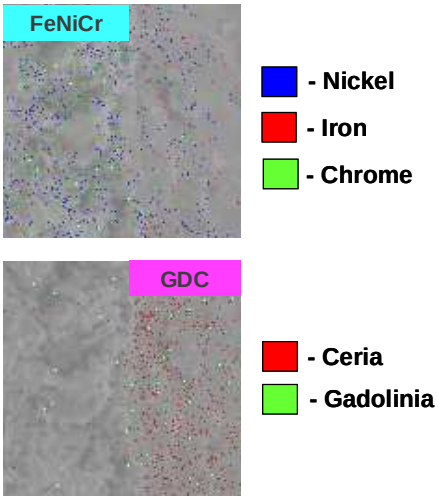

Figure 102. EDS dot map of the GDC|FeNiCr$_5$ cross-section after testing.

As is obvious, the Fe, Ni and Cr elements have crossed the interface into the GDC layer, which would cause a change in both the GDC properties and unit cell volume. After repeated efforts, it was determined that the GDC|FeNiCr$_5$ system wasn't suitable for use in the hermetic design. The leading reason for this determination were the degree of ion movement between the two components, which inevitably would result in degraded performance, and can't be prevented without the use of a buffer layer. Since the use of added layers, such as buffer layers, to improve performance by hindering reactions was against the principle of the hermetic design (which was developed to simplify SOFCs by reducing the number of components), further work on this system was not considered.

5.2.2 Leakage Rate

The electrolyte-interconnect lateral geometry samples, shown in Figure 84, were sealed to an alumina tube using ceramic cement (Autostic) to determine the leakage rate. The alumina tube setup was mounted in a vertical furnace (ATS clamshell) and manifolded with an inlet gas line flowing compressed argon through an Omega rotameter. An exit line fed the effluent gas to a mass spectrometer (Hiden Analytical HPR20). The setup for this experiment is shown in Figure 103.

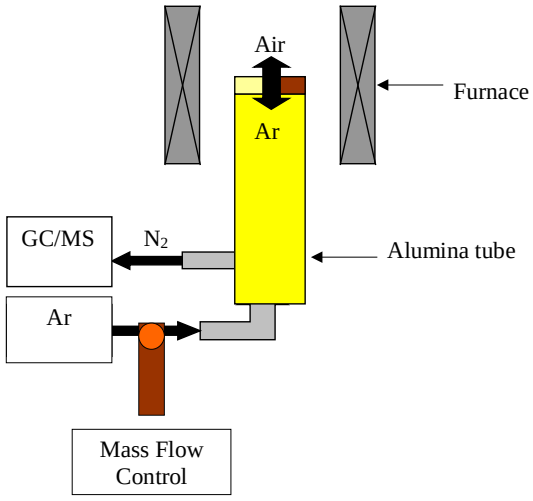

Figure 103. Experimental setup for lateral interface leakage rate testing.

The furnace was ramped to 550°C and held for 20 minutes prior to leakage rate measurement. Argon flow was set to 75sccm and the system was held for 10 minutes to allow for purging of residual water from the gas lines. The partial pressure of oxygen, due to impurity within the argon gas cylinder and gas lines, was also measured to ensure correct determination of oxygen due to seal leakage. Profile scans were taken using the residual gas analyzer with three iterations from 1amu to 80amu at 100 samples per atomic mass unit (amu). A Faraday detector collected the signal and the data was reported as pressure intensity versus amu. The leakage rate was determined based on the pressure intensity peak ratios for the detected gases and the assumption of the ideal gas law. Sealing a dense YSZ pellet with the Autostic cement and testing it under identical conditions also determined a baseline leakage rate of the entire setup. This allowed any leakage from the circumference of the pellet-alumina tube interface to be quantified. The longitudinal geometry samples characterized the gas transport properties across the interface, but not laterally along the interface. Oxygen ions were blocked at the hermetic interface and hydrogen ions kept in the anode chamber, however gas transport from outside the cell into the anode chamber wasn't determined. Testing the leakage rate of

the hermetic structure required preparation of a different interfacial geometry. The type of interface formed within the symmetric cell didn't allow for easy cross-sectional manifolding and therefore co-casting method was employed. With this technique the YSZ and interconnect slurries were co-cast into a single tape. After sintering, SEM imaging and EDS dot mapping were conducted on a single layer cross-section, which are shown in Figure 104(a-b).

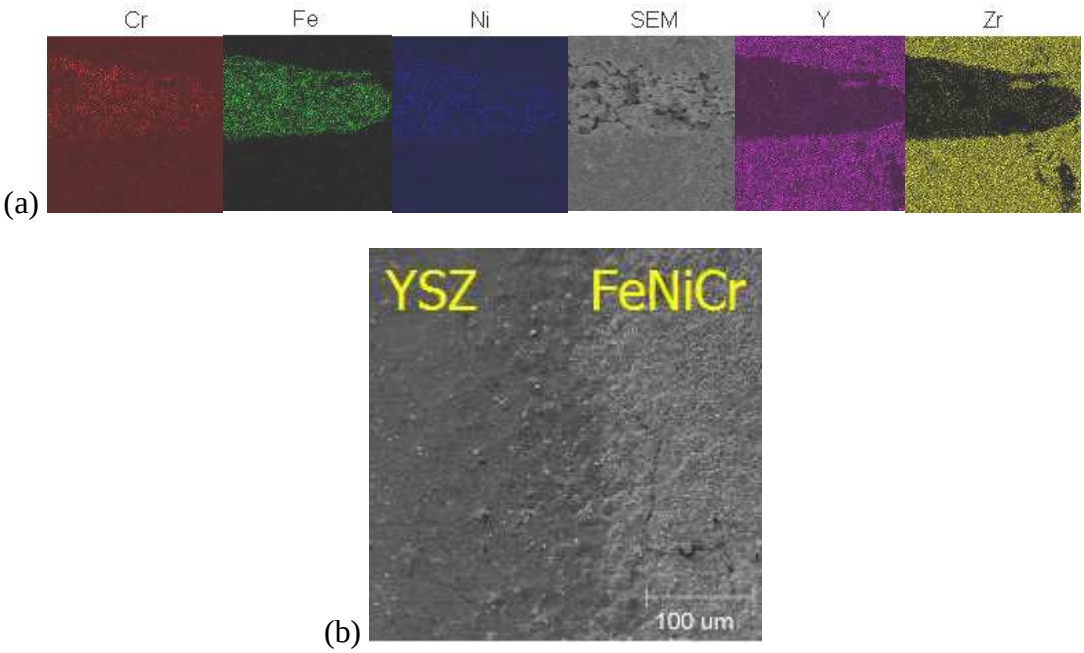

Figure 104. (a) SEM and EDS dot map of a single YSZ|$FeNiCr_5$ co-cast layer cross-section and (b) SEM of $FeNiCr_5$|YSZ surface interface.

The interface was not vertical as might be imagined when viewing the top surface, but rather has a more tortuous shape. The formation of a non-linear interface was due to the different shear rate or rheological characteristics of the two slurries. Though both slurries exhibit shear-thinning behavior, they don't have the same shear rate values and thus cast differently. Since the interconnect slurry was less viscous at the shear rate of casting, it cast in a higher surface area geometry than the more viscous YSZ slurry. Three of these

layers were aligned, laminated together and sintered to form a cell for leakage rate testing.

The leakage rate of the hermetic SOFC interface was determined using mass spectrometry (as shown in Figure 103). Lateral Interface leakage rates were determined by flowing argon gas through the inlet line and allowing the other side to be exposed to air. The effluent gas was fed to a mass spectrometer for composition determination. Primarily the effluent was probed for the presence of air species (primarily N_2 and O_2), which would correlate to leakage through the interface. The amount of oxygen species present within the argon gas cylinder was stated by Air Products to be less than 0.0005%. Due to the inevitable presence of water and trace gas species within the gas lines, the partial pressure of oxygen was measured at the gas outlet in order to be certain the quantified oxygen due to leakage wasn't being diluted with species from the gas lines. The partial pressure of oxygen was determined to be $1.31*10^{-2}$ Pa, which is about 0.0005% of the argon stream. Figure 105(a-b) shows the mass spectrum for the first scan at 750°C. The top spectrum is the full scale output from the first scan and the bottom spectrum shows a zoomed-in version highlighting the smaller intensity peaks.

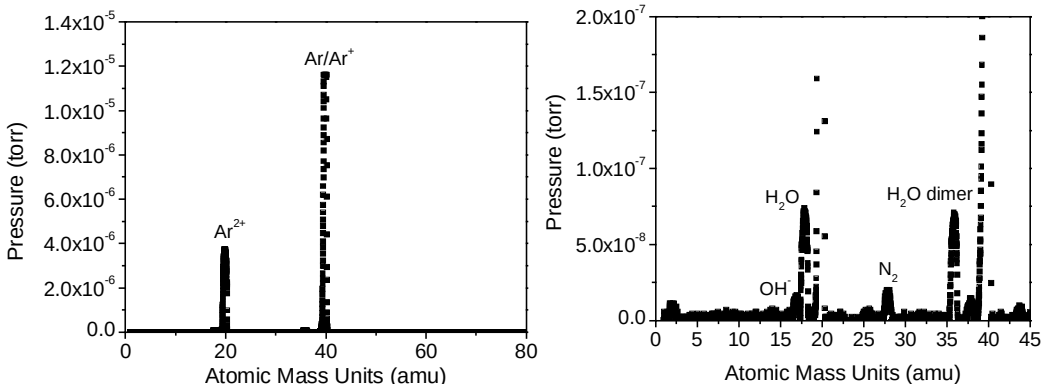

Figure 105. Mass spectrum from leakage rate testing at 750°C. (a) full spectrum from 1-100amu and (b) spectrum from 1-45amu.

Assuming the ideal gas law, the peak intensity ratios were used along with the argon flow rate to determine the leakage rate through the YSZ|$FeNiCr_5$ interface. The resulting

leakage rate as a function of temperature is shown in Table 28 and the corresponding trend plotted in Figure 106.

Table 28. Leakage rate data as a function of temperature.

Temperature (ºC)	N_2/O_2 ratio	Actual Leakage Rate (sccm)
550	3.696	0.139
600	3.964	0.133
650	3.615	0.092
700	3.545	0.081
750	3.674	0.027

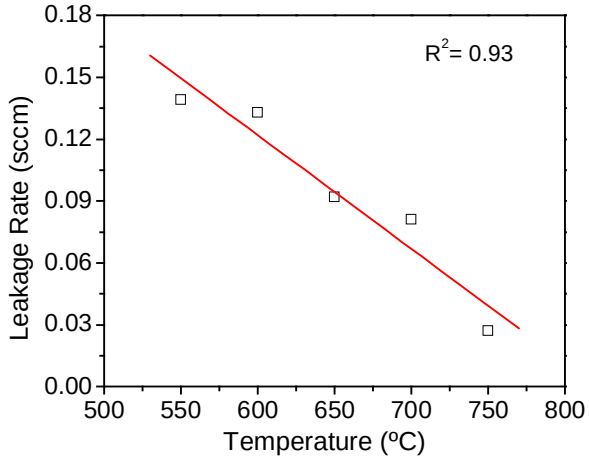

Figure 106. Plot of leakage rate as a function of temperature.

The leakage rate as shown in Figure 106, decreases linearly with increased temperature. The reduction in leakage rate was initially believed to be due to interconnect oxidation and removal of oxygen species from the effluent. This was not the case however, as the nitrogen to oxygen ratio in the effluent remained consistent with that of air and did not show a trend with temperature. The leakage rate decrease is therefore believed to simply be a thermal effect due to increased energy, lattice vibrations and collisions between gas molecules. This increases the tortuosity of the gas molecule path and reduces the leakage rate.

The sample was also held at 750°C for 2 hrs, with measurements every thirty minutes, in order to determine whether the leakage rate changed as a function of time. The leakage rate as a function of time for an isothermal soak at 750°C is shown in Figure 107 and Table 29.

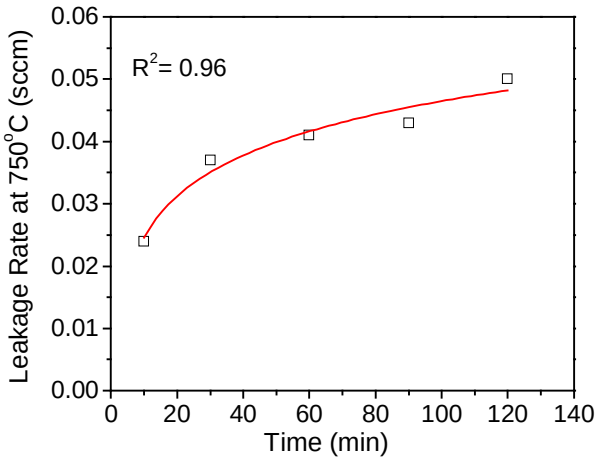

Figure 107. Plot of leakage rate as a function of time for isothermal soak at 750°C.

Table 29. Leakage rate data as a function of time for isothermal soak at 750°C.

Time at 750ºC (min)	N_2/O_2 ratio	Leakage Rate (sccm)
10	3.674	0.024
30	3.351	0.037
60	3.209	0.041
90	3.424	0.043
120	3.290	0.050

Figure 107 exhibits a logarithmic trend in leakage rate with time and appears to approach an asymptotic value. Since energy is no longer being increased, the gas transport along the interface can reach steady state, thus establishing equilibrium between the partial pressures of the gas species. This could reasonably be considered the steady state leakage rate for the hermetic seal at an operating temperature of 750°C, given a stationary application.

After testing, the sample was cross-sectioned and again SEM and EDS dot mapping were performed, as seen below in Figure 108.

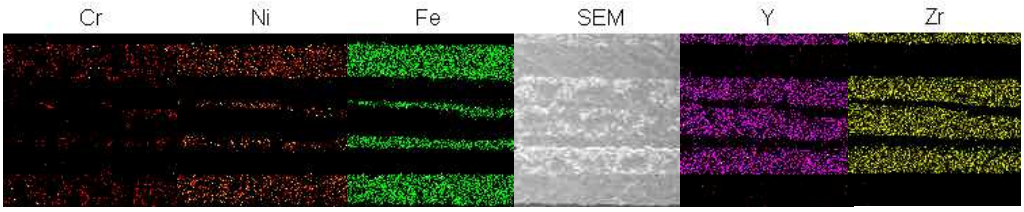

Figure 108 SEM with EDS dot map of $FeNiCr_5$|YSZ sample used for leakage rate testing.

Since three individual co-cast layers were laminated together to form a single cell, as previously discussed, there is a repeating pattern of Figure 104(a) within the tested cell. This cross-section corresponds to the schematic shown in Figure 109, where the dotted line corresponds to the region being shown in the SEM and EDS dot map and the solid lines represent the individual layers.

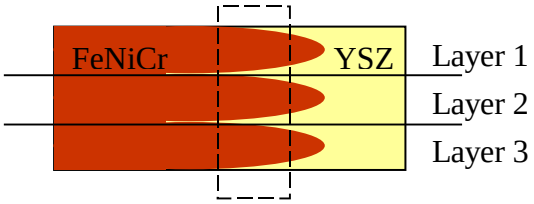

Figure 109. Schematic of $FeNiCr_5$|YSZ lateral interface cross-section showing three laminated co-cast layers.

5.3 Fabrication of Full Cell

Ceramic processing techniques such as tape casting and electrophoretic deposition are suitable low-cost methods of producing uniform thin oxide layers. Electrolyte- and anode-supported SOFC components are readily fabricated using these methods. Though both techniques allow for thin oxide layers, tape casting is more of a substrate producing technology while EPD is more of a thin-film and coating technology. Combination of

these two techniques through lamination of individual tapes as well as EPD on bisque-sintered substrates allows for co-firing, a reduction in the number of sintering steps and moreover a reduction in cost.[245] This fabrication method is common to planar SOFCs as electrolyte-supported SOFCs typically use tape casting for electrolyte and often anode fabrication. Anode-supported SOFCs however typically use tape cast anode materials and rely on other methods such as EPD for the subsequent layers.

Tape casting was chosen to be the basis for fabrication of hermetic SOFCs without sealant because it is a robust technique often used to make thin substrates of dense bulk materials and thus lends itself well to component manufacture for planar SOFCs. The scalability and long standing success of the tape casting process makes it a legitimate technique for low cost manufacturing of many SOFC components such as electrolyte membranes, anode materials, interconnect layers and laminates.[117] The tape casting method has already been used to fabricate SOFC components such as YSZ and GDC electrolytes, Ni-YSZ and Ni-GDC cermet anodes and $FeNiCr_5$ interconnect compositions, as shown in Figure 110.

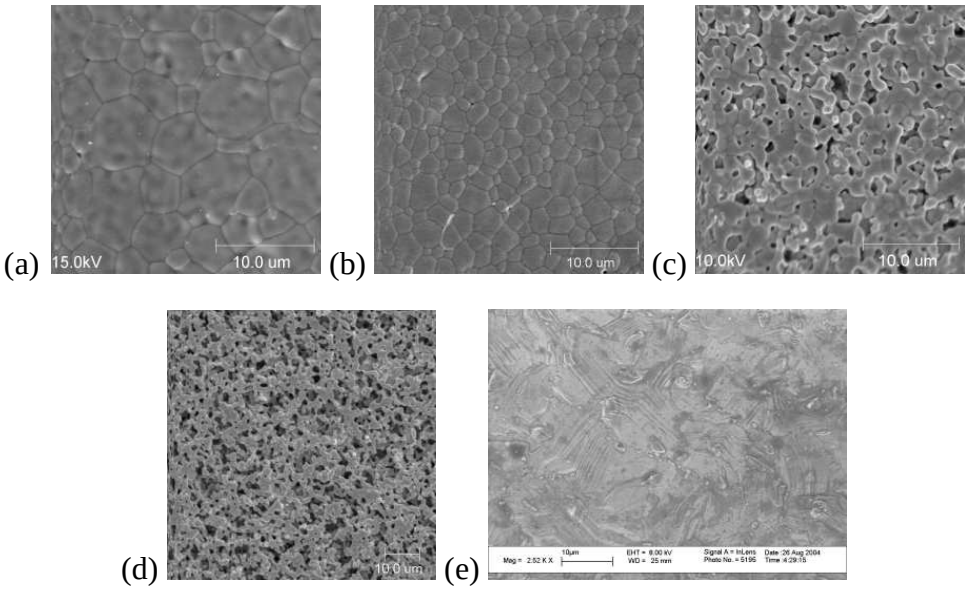

Figure 110. SOFC components fabricated by tape casting: (a) YSZ electrolyte, (b) GDC electrolyte, (c) Ni-YSZ anode, (d) Ni-GDC anode and (e) $Fe_{47.5}Ni_{47.5}Cr_5$ interconnect.

Hermetic SOFCs were first fabricated by laminating electrolyte, anode and interconnect tapes together in the proper design, as shown in Figure 21. A sintering profile for multi-layer ceramics was previously determined using dilatometry by Cochran, Lee and Church, who were sintering extruded hybrid honeycomb SOFCs in both oxidizing and reducing atmospheres.[52] Since a dilatometer wasn't available for direct determination of dimensional and density change of our tapes during the sintering profile, we chose to determine dimensional change at each segment of the profile. We segmented the known sintering profile into separate steps and measured the dimensional change at each step. The sintering profile for these hermetic and bipolar SOFCs fabricated by lamination is shown in Figure 111.

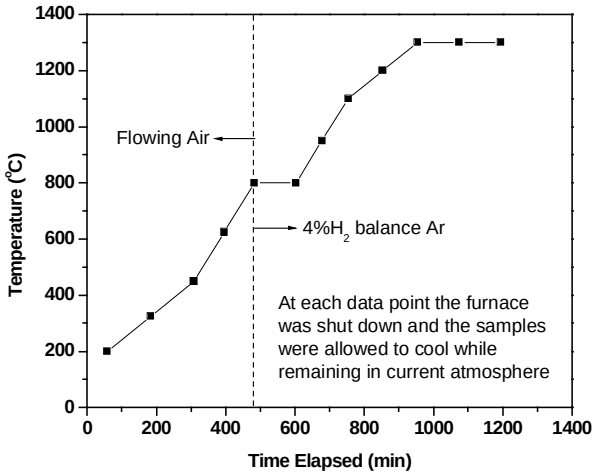

Figure 111. Sintering profile with explicit points corresponding to dimensional measurements.

The change in relative density at each explicit point in Figure 111 is shown in Figure 112.

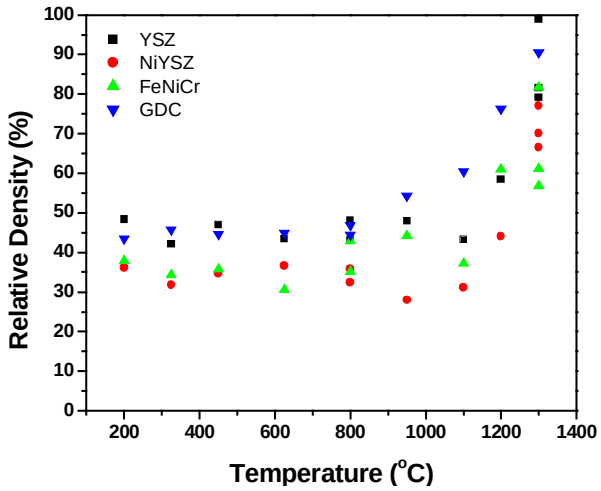

Figure 112. Change in relative density of different tapes during the sintering profile.

Our first hermetic SOFC consisted of an interconnect, porous YSZ scaffold (in place of the anode) and a dense YSZ electrolyte. After sintering, the cell remained flat, the electrolyte was dense and the interconnect and YSZ scaffold remained porous, as shown in Figure 113(a-b).

(a) 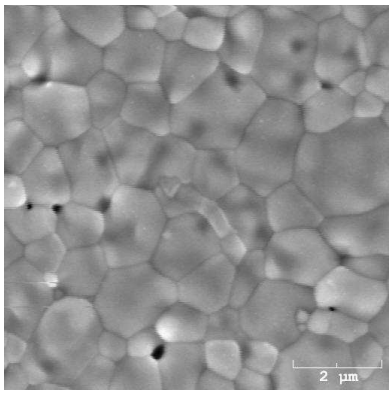

(b) 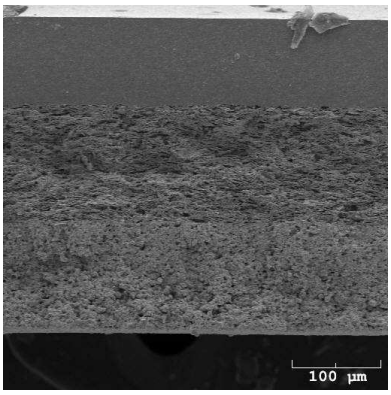

Figure 113. Hermetic SOFC fabricated by tape casting and lamination with YSZ scaffold in place of anode. (a) Dense electrolyte and (b) cross-section of cell showing YSZ electrolyte|YSZ scaffold|FeNiCr$_5$ interconnect, respectively from top to bottom.

The edge of the cell, shown in Figure 114, proves that the hermetic structure can be fabricated by lamination with a clean YSZ|FeNiCr$_5$ interface.

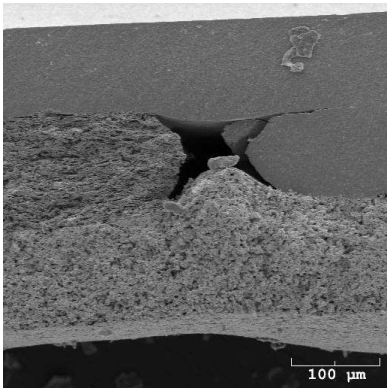

Figure 114. Edge of Hermetic SOFC fabricated by tape casting and lamination with YSZ scaffold in place of anode. The far left of the image shows the YSZ electrolyte|YSZ scaffold|$FeNiCr_5$ interconnect, respectively from top to bottom and the far right shows the hermetic YSZ|$FeNiCr_5$ interface.

After anode and interconnect slurry compositions, which produced tapes of similar shrinkage characteristics to YSZ, were determined, the YSZ scaffold was replaced with NiO-YSZ in order to fabricate a full cell. The results of lamination and sintering of these three layers proved even better than those with the YSZ scaffold, as shown in Figure 115.

(a) 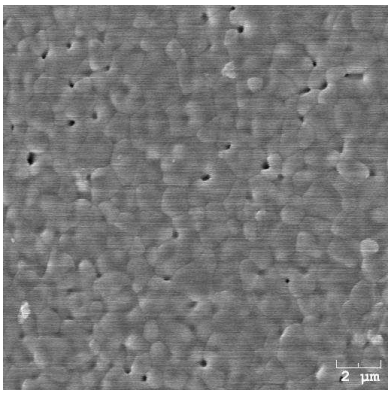

(b) 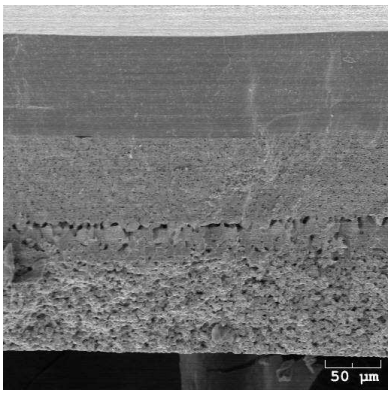

Figure 115. Hermetic SOFC with NiO-YSZ anode instead of porous YSZ scaffold. (a) Dense electrolyte and (b) YSZ electrolyte|NiO-YSZ|$FeNiCr_5$ interconnect, respectively from top to bottom.

The critical interface of the hermetic cell is shown in Figure 116.

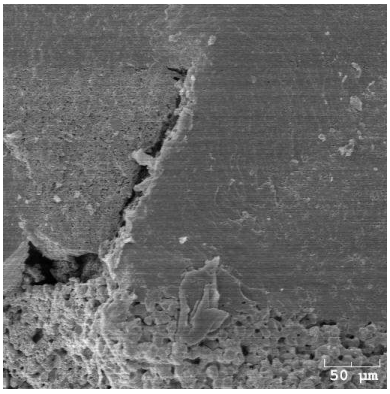

Figure 116. Edge of hermetic SOFC showing the porous NiO-YSZ anode chamber on the left and the critical YSZ|FeNiCr5 inteface on the right.

Notice that the NiO-YSZ layer has a much cleaner appearance (Figure 116) next to the hermetic interface than does the porous YSZ scaffold (Figure 114). Performance of this cell was only moderate as the hermetic SOFC had a sub-standard OCV (0.6V) resulting in a power density of only 75mW/cm^2 at 750ºC, as shown in Figure 117.

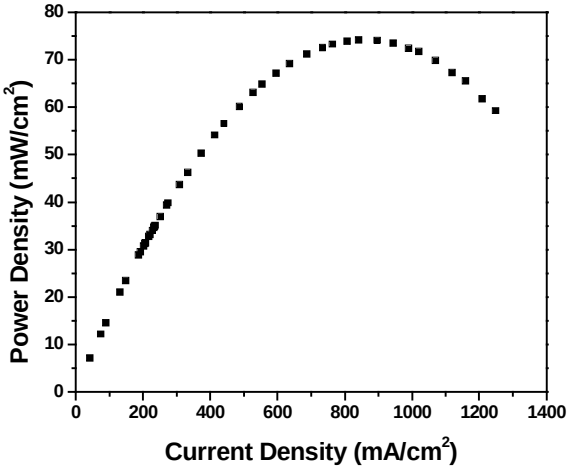

Figure 117. Performance of hermetic SOFC at 750ºC.

Interestingly however, the current density was quite high, which indicates that performance would improve greatly if the OCV can be increased to above 1V, as it should be. Therefore the hermetic SOFC fabricated by tape casting shows promise for being one of the first sealless planar designs.

Another form of the hermetic SOFC design was fabricated by a combination of EPD and tape casting. EPD was used to deposit thin anode and electrolyte layers on an interconnect support, to fabricate metal-supported hermetic SOFCs. Initial work in the area of metal-supported SOFCs utilized expensive thin film deposition methods.[246,247,248,249] Later, Carter et al.[250] and Villarreal et al.[251] fabricated metal-supported SOFCs using less expensive colloidal techniques. Matus et al. measured the rapid thermal cyclability of a porous Fe30Cr-Aluminum Titanate cermet metal-supported SOFC, which demonstrated very little performance loss after 50 cycles from 475K to 1075K at 50K/min.[252]

Electrophoretic deposition experiments were carried out on porous $Fe_{50.1}Ni_{44.5}Cr_{5.4}O_x$, fabricated by tape casting (see Table 25) substrates under constant voltage conditions. Suspensions of YSZ and NiO-YSZ were prepared using YSZ powder (8 mol%, Tosoh) and NiO powder (97%, d<10μm) purchased from Fisher Scientific. The NiO powder was too large for uniform dispersion and therefore was roll-milled in ethanol and 6mm YSZ media for 240 hours (see Figure 24). The mean particle size after milling reduced from less than 10μm to about 2μm. The milled NiO powder was mixed in a 1:1 ratio with NiO powder prepared by the glycine nitrate process. Both the YSZ and NiO-YSZ powders were dried for 48 hours at 100°C before being suspended in acetylacetone (Acac) solvent at a concentration of 10g/L (1.75g in 175mL). The suspensions were ultrasonicated for 20 minutes prior to deposition and for 5 minutes in between depositions, with each suspension being replenished every 5 depositions. The deposition apparatus was shown in Figure 28.

Deposition of the NiO-YSZ was performed at 300V for 2 minutes followed by 100V for 1 minute, resulting in 25mg of deposit. After deposition, a doctor blade was used to scrape away anode deposit from the outer thirds of the substrate leaving a strip of NiO-YSZ along the center. The exposed interconnect surface was quickly cleaned using a cotton swab soaked with acetyleacetone and then placed into the YSZ suspension for electrolyte deposition. YSZ was deposited at 50V for 3minutes resulting in 15mg deposit, which was sufficient for full surface coverage of both the anode deposit and exposed interconnect substrate. After sintering at 1300°C for 5hrs in 4% H_2 (balance Ar), the resulting YSZ surface was dense and the desired hermetic structure was achieved as seen in Figure 118.

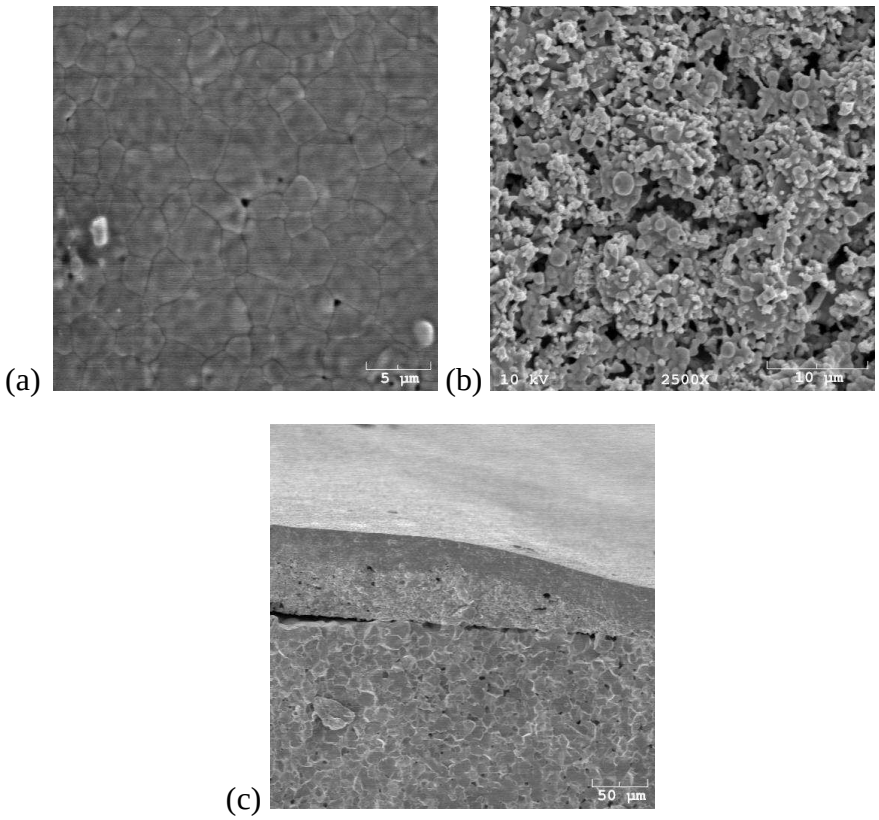

Figure 118. Hermetic SOFC fabricated by EPD on porous $Fe_{50.1}Ni_{44.5}Cr_{5.4}O_x$ interconnect support (a) dense electrolyte surface, (b) porous anode surface and (c) cross-section of cell showing electrolyte overlapping anode chamber and forming hermetic interface.

As can be seen in Figure 118(c), the electrolyte thickness was only 25μm over the anode, while being as thick as 40μm over the interconnect. A $La_{0.6}Sr_{0.4}Co_{0.8}Fe_{0.2}O_3$ cathode was then applied to the cell by brush-painting and sintered at 900°C for 2hrs. The open circuit voltage of the hermetic SOFC fabricated by EPD was 0.998 at 750ºC, which was considerably higher than the SOFC fabricated by tape casting. Unfortunately, however the OCV quickly dropped resulting in negligible performance. A more serious inquiry into metal-supported SOFCs fabricated by this process should result in positive results, given the microstructures deposited, their thickness and the initial OCV of the cell.

The low OCV encountered in the hermetic SOFC fabricated by tape casting was hypothesized to be due to interconnect oxidation causing porosity and loss of electrical contact. Once method of ensuring that interconnect oxidation in planar SOFCs is never an issue is to copy the structure of the tubular design and put two planar SOFCs in parallel. This form of planar cell is termed a 'bipolar' cell. Bipolar SOFCs have had little research conducted on them mainly due to the increased complexity of the electrical circuitry as compared to the planar or cell-in-series designs. The bipolar design does have some advantages however. Since the two SOFCs in parallel share a common interconnect, the interconnect is never exposed to an oxidizing atmosphere. Not only does this eliminate dual atmosphere effects such as redox instability and thermal expansion, but also the problems associated with chromium deposition and poisoning at the cathode as well as increased cathode polarization resistance due to the formation of an oxide scale. Essentially the bipolar design is void of two of the major obstacles inhibiting SOFC research: (1) chromium poisoning and (2) polarization losses during current collection at the cathode. We have fabricated bipolar cells consisting of YSZ (8 mol% Y_2O_3) electrolyte, Ni-YSZ anode and $Fe_{47.5}Ni_{47.5}Cr_5$ interconnect by tape casting and lamination. After stacking and laminating either monolithic or bi-layer tapes together, a single fire step is all that is needed to fabricate the symmetric interconnect-anode-

electrolyte portion of the bipolar cell. Shown in Figure 119 are the cross-sections of (a) the center and (b) the edge of a bipolar cell (without cathode) after sintering at 1300°C for 4 hours in 4%H_2/Ar.

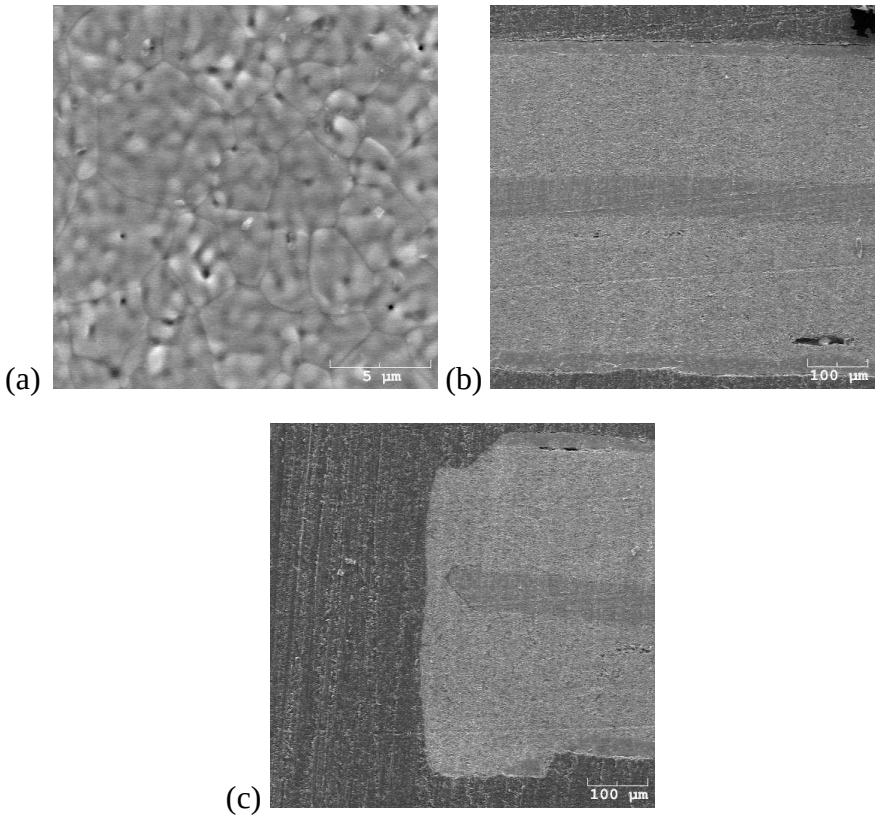

Figure 119. (a) Surface image of dense electrolyte and Cross-sectional images of (b) center and (c) edge of bipolar SOFC fabricated by tape casting and lamination.

The bipolar SOFC shown in Figure 119 was fabricated with a porous YSZ scaffold in place of the anode, similar to how initial hermetic SOFCs were fabricated. Similarly, once anode tapes of similar shrinkage (to the electrolyte) were determined, the porous YSZ scaffold was replaced with NiO-YSZ layers, as shown in Figure 120.

(a) 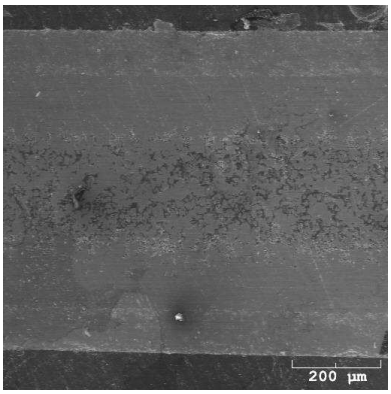

(b) 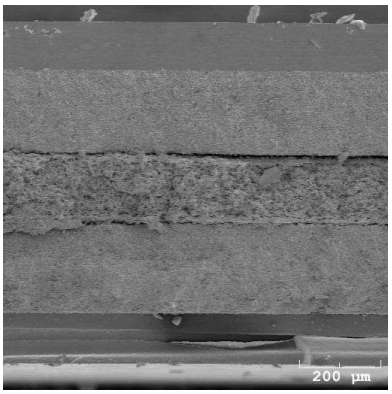

Figure 120. (a) Polished and (b) fracture SEM cross-sections of bipolar SOFC with NiO-YSZ anode fabricated by tape casting.

The SOFC component layers have also been fabricated with various thicknesses (i.e. electrolyte from 35-200µm, anode from 100-500µm…etc) without detriment to shrinkage during sintering. Also the anode has been separated into a more porous fuel flow field layer near the interconnect and a slightly more dense active layer near the electrolyte. The interconnect has been prepared as both a dense and porous layer, though in the bipolar design the degree of interconnect density isn't of consequence. Since the bipolar cell was sintered in a reducing atmosphere, there are severe limitations on how the cathode can bonded to the cell. There are various techniques to apply $La_{0.85}Sr_{0.15}MnO_{3-\delta}$ (LSM) cathodes to the bipolar cells including pulse laser deposition (PLD) and combustion chemical vapor deposition (CCVD). Recent work has also shown that after PLD of LSM, the perovskites phase can be formed with a temperature of only 550°C, can easily be achieved *in situ*.[253]

5.4 Conclusions

Fabrication and characterization of an YSZ|$FeNiCr_5$ interface fabricated by overcastting has shown the ability to block gas transport. Impedance spectroscopy of this interface revealed that as DC bias was increased from 0 to 0.3V, the resistance to gas transport increased, indicating mass transport limitation and the ability of this interface to

be used as a seal for SOFCs. Another indication of the quality of the seal was the accumulation of 0.498V charge at the $FeNiCr_5$|YSZ interface and the presence of a large relaxation time constant. Symmetric cells of Ni-YSZ and $FeNiCr_5$ yielded the expected trend of low impedance values and therefore won't cause a detriment to the proposed hermetic structure. When the electrolyte layer was switched from YSZ to GDC, similar trends were not seen. The electronic transference number of GDC was too high and activation control was observed in all impedance spectra. Material interactions were also observed between GDC and the $FeNiCr_5$ interconnect, indicating that the two would not be able to form an adequate hermetic seal for planar SOFCs. Leakage rate testing of the YSZ|$FeNiCr_5$ hermetic interface showed a decreasing trend in leakage rate with temperature. The leakage rate of the YSZ|$FeNiCr_5$ interface at 750°C was 0.027sccm, which is comparable to the hybrid seal developed at PNNL using polycrystalline mica and glass, which had a leakage rate of 0.01sccm at 800°C with $1.72*10^5$ Pa compressive stress. Isothermal leakage rates as a function of time did show an increasing logarithmic trend, however the leakage rate appeared to approach an asymptotic value of 0.05sccm after two hours.

Hermetic SOFCs were fabricated by two methods: (1) tape casting and lamination and (2) EPD on tape cast substrates. The hermetic SOFCs fabricated by tape casting and lamination remained flat after sintering and showed an OCV of 0.6V at 750ºC. The low voltage resulted in weak performance as the power density was only 75mW/cm^2 at 750ºC. The low OCV was hypothesized to be due to oxidation of the interconnect due to a leak in the fuel line. The fuel leak and oxidation lead to lower OCV from gas mixing and also weaker electrical contact. The current density of the hermetic SOFC was quite high however, indicating that the design and fabrication method show promise and potential for achieving higher power densities in the future. The second hermetic SOFC, fabricated by EPD on porous interconnect supports, showed great initial promise as its OCV was 0.998V at 750ºC. Unfortunately, this SOFC also had issues with gas leakage

and the OCV soon dropped resulting in negligible performance. Hermetic SOFCs fabricated using this method, however might show even greater potential than those fabricated by tape casting due to the ability to fabricate thin anode and electrolyte layers of controlled thickness and microstructure.

VI. SILVER-BASED INTERCONNECT MATERIALS

6.1 Literature Review

Silver is a noble metal most often used for current collecting and cathode materials in SOFCs. These applications came about due to its stability in oxidizing atmospheres as shown by the Ellingham diagram.[21] Interest has been shown in adopting the inert properties of silver for interconnect purposes. However since silver has been well documented as a selective conductor of oxygen, its use may cause oxygen to leak into the anode chamber the results of which would be oxidation of the metal in the anode cermet and reduced Nernst potential. Many studies have been conducted on the oxygen permeation rate through silver membranes starting with Dushman, Whetten and Young, Coles, Burroughs and Beavis.[196-200] Until now the primary focus was using silver membranes to admit high purity oxygen gas into vacuum systems, separation of O_2 from CO_2 and understanding the catalytic behavior in the epoxidation of ethylene and partial oxidation of methanol to formaldehyde. Dushman's original experiments on oxygen permeability were run from 450°C to 630°C. He observed a constant relationship between permeation rate and temperature as would be expected by diffusion theory. Whetten and Young found that high purity oxygen was found to permeate through silver at a rate such that a pressure of 2mmHg was built up from $2*10^{-10}$ mmHg in a 1000cc vessel in 1hr at 700°C. Their mass spectra also contained a peak at 34amu only when the partial pressure of oxygen was high. They concluded that this peak was the result of combined O^{16} and O^{18} to form an $(O^{16}O^{18})^{+}$ ion. Coles determined oxygen permeability equations as a function of temperature and pressure. Isothermal oxygen permeability (Q) was found proportional to the square root of the pressure difference across the silver barrier for pressures near and above 1atm.

Equation 48 $$Q \alpha P^{0.46}$$

The temperature dependence of oxygen permeability however differed from Dushman's results as Coles found a change in slope occurring at 630°C, as shown in Figure 121.

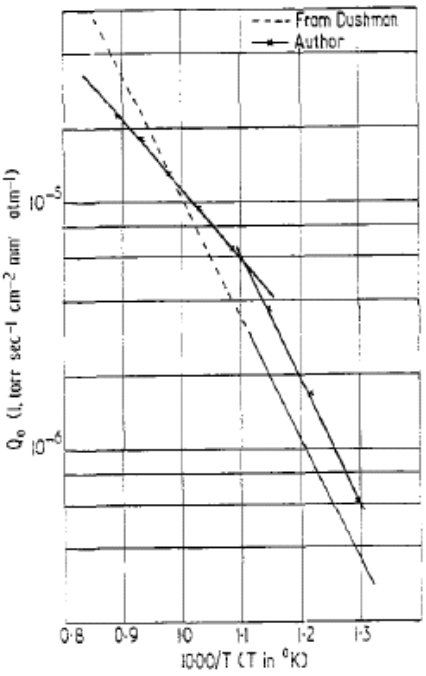

Figure 121. Oxygen permeability data of Coles and Dushman as a function of temperature.[196,198]

Since Coles performed his measurements from 500°C to 850°C he was able to notice the slope change and Dushman was not. Coles determined that the permeability of oxygen t follows one of two equations:

Equation 49

$$\log Q_0 = 0.3244 - \frac{5035}{T} (T < 630^{\circ C})$$

$$\log Q_0 = -2.108 - \frac{2841}{T} (T > 630^{\circ C})$$

The effect causing the change in temperature dependent slope and why it occurs at 630°C was not determined, however it is not due to a structural change. However, it was postulated that the discontinuity was due to oxygen entering the lattice. The lifetime of the silver barrier was also observed as a function of temperature and oxygen pressure. There was indication that the silver barrier becomes porous after 325.1torr of oxygen

throughput at 630°C and 750°C. At 900°C the barrier failed after 10 minutes and only 80.1torr oxygen throughput. This indicates that the barrier failure is temperature dependent and there was also indication that the porosity was between grain boundaries. Burroughs also conducted mass spectrometry measurements as a function of temperature from 500°C to 700°C.[199] He determined that carbon oxides such as carbon dioxide and carbon monoxide evolved within the silver during initial oxygen leakage. The presence of the carbon was believed to be the result of the filament heater coiled around the silver tube. His analysis also resulted in a peak at 34amu at high oxygen partial pressure, though he believed it was due to the creation of H_2O_2. Beavis also determined the presence of carbon oxides during initial silver emissions, but found further contaminant gases of hydrogen sulfide and sulfur dioxide.[200] Only after conditioning of the membrane for one hour was high purity oxygen obtained. The relative peak amplitudes as a function of time was plotted and shown, where the oxygen peak takes over an hour to reach its maximum value. He also concluded that the peak at 34amu was due to an $(O^{16}O^{18})^+$ ion based on a comparison of the peak height ratios to the natural isotopic abundance of oxygen. Based on the high temperature data from Bazan[254], Beavis determined a diffusion coefficient of $4*10^{-6}$ cm^2s^{-1} at 550°C. Using the data of Dushman and Lafferty,[255] the diffusion coefficient would be $1*10^{-6}$ cm^2s^{-1} at 550°C.

Outlaw et al. studied the permeability and diffusivity characteristics of oxygen through silver in a number of publications.[201-204] Though left unpublished, oxygen permeation through silver (100), (110) and (111) single crystals as well as transport mechanism were said to be determined. This research formed the basis for their future work regarding oxygen separation, permeation, flux and rate-limiting steps. Outlaw's work in 1990 determined that though the permeability through each silver crystal facet may be equivalent, the diffusivities are drastically different. Since the oxygen was found to reside primarily at the octahedral site in the lattice, the solubility (S) should be the same at all facets. Therefore the permeability (K) varies only with the diffusivity (D):

Equation 50 $$K = DS$$

The rate-determining step was theorized to be dissociation of the molecular oxygen into atomic oxygen. To prove this, they conducted experiments where the surface was allowed to dissociate molecular oxygen and where the surface only interacted with atomic oxygen. Glow discharge experiments, where a DC field (E/n ~ 10^{-14} V cm^{-2}) was applied to the gas (0.5 torr O_2) upstream of the silver surface, allowed the surface to interact with atomic oxygen. Since CO_2 would also be present in the gas stream, they determined the dissociative energy for separating one oxygen atom from CO_2 compared to O_2, and found that they were 128kcal mol^{-1} and 118kcal mol^{-1} respectively. The dissociation reaction is due to electron impact and not electron attachment as shown:[256,257]

Reaction 21 $$CO_2 + e^- \rightarrow \left[CO_2^{*^3}\Pi\right] \rightarrow CO + O + e^-$$

where the $^3\Pi$ is the first excited state. This indicated that the source of monotomic oxygen formation before interaction was being interaction with the silver surface would be difficult to determine. When atomic oxygen interacted with the silver surface, it lead to a much higher oxygen flux ($2.83*10^{14} cm^{-2}s^{-1}$) through the membrane as compared to when molecular oxygen ($4.4*10^{13}$ $cm^{-2}s^{-1}$). This gave considerable relevance to the theory that molecular dissociation was the rate-limiting step.[201]

A non-destructive depth profile of oxygen-exposed silver using Angle resolved Auger electron spectroscopy (ARAES) and ion scattering spectroscopy (ISS) revealed interesting results as to where the oxygen resides.[202] Due to the low sticking coefficients of oxygen on silver facets, the interaction above 20°C is quite weak. The sticking coefficients are shown in Table 30.[258]

Table 30. Sticking coefficients of oxygen on different silver facets.

Ag Crystal Facet	Sticking Coefficient
{110}	$1*10^{-3}$
{001}	$1*10^{-5}$
{111}	$1*10^{-6}$

The ISS technique probed the outermost layer of the silver fact, while the ARAES technique could probe from 2-20 atomic layers of silver. Since these techniques are so surface sensitive, contamination is of great importance to accurately determining the oxygen profile. The results are shown in Figure 122 and are consistent with the models proposed by Kuk and Feldman on (110)[259] and Ning et al on (111) surfaces.[260]

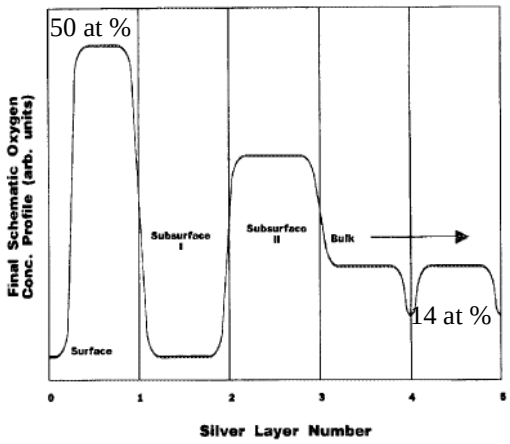

Figure 122. Preferential concentration of oxygen in the silver {110} sublattice. [202]

These model-validated results indicate that there are subsurface oxygen concentrated and deficient regions within the first few atomic layers of silver. The atomic oxygen appears to preferentially reside between the second and third sub-layers of silver. This forms a deficient layer just below the silver surface. The models and results also indicate that the layers where oxygen is residing correspond to lattice contraction and expansion, relative to the bulk, between the first two and second two sub-layers respectively. The overall impact of these results is that oxygen doesn't reside at the surface, but rather sits

preferentially at subsurface layers leading to lattice distortion. It was thought that this was why the oxygen sticking coefficient was so low at the silver surfaces.

Comparison of oxygen transport through Ag (110), Ag (polycrystals) and Ag_2Zr from 400°C-800°C revealed substantial deviation from diffusion-controlled transport. Below 630°C the diffusivity activation barrier increases over 4 kcal mol^{-1}, while above 630°C the barrier reduces to the bulk level of 11 kcal mol^{-1} consistent with zero concentration at the vacuum interface. The permeation rates of oxygen through these materials are relatively the same over the entire temperature range studied as shown in Figure 123, with Ag_2Zr being slightly higher.[203]

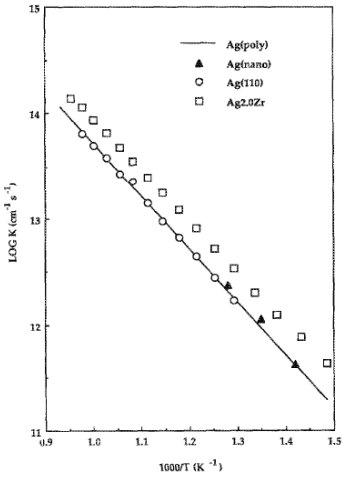

Figure 123. Oxygen permeability as a function of temperature for different silver samples, as measured by Outlaw.

Using the mathematics of diffusion from Crank,[261] the permeability of oxygen in Ag (110), Ag (polycrystal) and Ag (nanocrystal) are represented by:

Equation 51
$$K = 5.2\times10^{18}\ \exp\left(\frac{-22860}{RT}\right)\ \text{cm}^{-1}\text{s}^{-1}$$

While for Ag_2Zr, the permeability is represented by:

Equation 52
$$K = 4.9\times10^{18}\ \exp\left(\frac{-21800}{RT}\right)\ \text{cm}^{-1}\text{s}^{-1}$$

The addition of Zr to the Ag lattice increased the permeability by a factor of two because of decreased grain size and increased defect density. The diffusivities of the silver samples however were different, as shown in Figure 124.

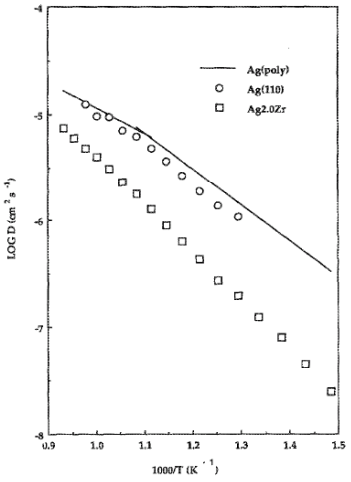

Figure 124. Oxygen diffusivity as a function of temperature as determined by Outlaw et al.

The Ag (110) sample had two distinct linear regions, as shown previously, which are described by the following equations:

Equation 53
$$D_{110} = 1.55\times10^{-1}\exp\left(\frac{-18500}{RT}\right)\ \mathrm{cm^2 s^{-1}}$$

for 500°C<T<630°C, and

Equation 54
$$D_{110} = 1.55\times10^{-2}\exp\left(\frac{-14500}{RT}\right)\ \mathrm{cm^2 s^{-1}}$$

for 630°C<T<800°C. The Ag (polycrystal) had diffusivity equations, respectively, of:

Equation 55
$$D_{poly} = 3.2\times10^{-2}\exp\left(\frac{-15330}{RT}\right)\ \mathrm{cm^2 s^{-1}}$$

for 500°C<T<630°C, and

Equation 56
$$D_{poly} = 2.96\times10^{-3}\exp\left(\frac{-11050}{RT}\right)\ \mathrm{cm^2 s^{-1}}$$

for 630°C<T<800°C. As discussed previously, the break in the linearity of the diffusivity curve was presumed the result of oxygen trapping by defects at the subsurface layers. Above 630°C, the Ag (110) and Ag (polycrystal) samples exhibit similar diffusivities with activation energies only 3.5 kcal mol^{-1} different. Below 630°C, the diffusivities begin to separate due to a greater difference in activation energy. The Ag_2Zr sample didn't exhibit the same break in the diffusivity response with temperature. The diffusivity is actually quite different due to an activation energy (22.0kcal/mol) twice that of Ag (polycrystal). The break in linearity also diminished greatly and was pushed to a higher temperature (725°C) due to the addition of Zr. Ag_2Zr has a substantially increased sticking coefficient due to the segregated Zr surface layer (56nm), which allow for a much higher surface oxygen concentration. However, during oxygen permeation, the Zr layer becomes Zr_xO_y (near ZrO_2) and considerably reduces the diffusivity. The effect of oxygen solubility on Zr was studied by comparing permeation of oxygen through Ag_2Zr and $Ag_{0.05}Zr$.[204] The results of this study showed that the permeability was virtually identical in both systems and therefore not solubility controlled. Therefore the enhanced transport was deemed a sensitive function of the surface. Work on hydrogen permeation through a Cu-Zr alloy by Mitchell et al.[262] also showed a reduced magnitude and increased activation energy of the diffusivity. Another consideration for the change in diffusivity with temperature is that the vapor pressure of silver is quite high ($4.4*10^{-5}$ torr at 800°C) leading to a large surface defect density. This defect density may be similar to a disordered surface, which could indicate that the oxygen dissolution in the bulk may be the rate-limiting step.

Wu et al.'s work on extraction of O_2 from CO_2 lead to the determination of the sticking coefficient of atomic and molecular oxygen on silver as a function of temperature.[204] This was reported as a ratio of the sticking coefficient of atomic oxygen to molecular oxygen as shown in Figure 125.

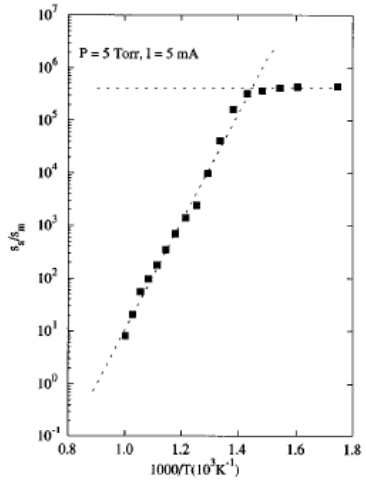

Figure 125. Ratio of the sticking coefficient of atomic oxygen to molecular oxygen.

Comparison of this data with that of Campbell showed that the sticking coefficient of atomic oxygen on Ag(111) and Ag (001) is considerably higher than that of molecular oxygen, 0.4 versus 10^{-6} at 217°C and 1 versus 10^{-5} at 25°C, respectively. The result is important in that it shows the exponential decrease in the sticking coefficient with temperature and the significantly higher ability for atomic oxygen to adsorb on silver compared to molecular oxygen.

6.2 Pure Silver Interconnects

Recently, the use of silver as an SOFC interconnect has been examined. Singh measured the structural degradation of silver when exposed to SOFC dual atmosphere conditions, revealing the formation of significant porosity at the grain boundaries.[263] The porosity was attributed to the thermodynamic formation of steam within the lattice. Meulenberg tested silver as a contact element for bipolar interconnects, and the results were promising with no degradation in interfacial resistance over 554hrs operation.[264] Silver evaporative loss rates of 0.094μg/cm^2/hr at 690°C and 1.29μg/cm^2 /hr at 790°C in air and 0.161μg/cm^2/hr at 800°C in humidified 4% hydrogen of were determined using 3L/min flow rates and exposure times of up to 1065hrs. Barnett also determined

evaporative loss rates of silver of 0.05um/yr, 0.3um/yr and 2um/yr at 700°C, 750°C, and 800°C respectively.[265] Though seemingly very different, when converted to units of μm/s, Barnett's evaporative rates are only about an order of magnitude less than those of Meulenberg. Both sets of values are a couple orders of magnitude greater than the calculated loss rates based on the $4*10^{-5}$torr vapor pressure of silver at 800°C measured by Outlaw.[203] These results are summarized in Table 31.

Table 31. Summary of literature data on evaporative loss of silver at high temperature.[201,264,265]

S. Barnett		
Temperature (^oC)	Evaporative Loss Rate (um/yr)	Evaporative Loss Rate (um/s)
700	0.05	$1.58*10^{-9}$
750	0.3	$9.51*10^{-9}$
800	2	$6.34*10^{-8}$

W.A. Meulenberg		
Temperature (^oC)	Evaporative Loss Rate ($ug/cm^2/hr$)	Evaporative Loss Rate (um/s)
690	0.094	$2.49*10^{-8}$
790	1.29	$3.41*10^{-7}$

R.A. Outlaw		
Temperature (^oC)	Evaporative Loss Rate (torr)	Evaporative Loss Rate (um/s)
800	$4*10^{-5}$	$7.12*10^{-10}$
800	$5*10^{-5}$	$7.97*10^{-10}$

The objectives of this study were to: (1) compare experimental data on oxygen permeation through polycrystalline silver with literature values, (2) calculate the equivalent leaking current density due to oxygen permeation under fuel cell conditions, (3) calculate silver loss rates and quantify silver degradation in static and dual atmosphere environments and (4) determine the amount of nickel oxidation within the anode which occurs due to oxygen permeation through the silver interconnect. These experiments will serve to evaluate the effectiveness of silver as an interconnect for intermediate temperature SOFCs.

6.2.1 Oxygen Permeability and Diffusivity

In an actual fuel cell operating environment there is no appreciable overall pressure difference between components of the cell, but instead it's the partial pressure difference between species that is the driving force for gaseous permeation. Therefore rather than use an ultra-high vacuum system to measure the permeation rate of oxygen, which uses an overall pressure difference across each side of the membrane as the driving force, we chose to seal the silver membrane in a dual atmosphere environment, similar to an actual fuel cell interconnect, and monitor the effluent with a mass spectrometer. Using this setup, shown in Figure 103, we experimentally measured the oxygen permeability and diffusivity through polycrystalline silver as a function of temperature in order to evaluate its potential as an SOFC interconnect. We then validated these results by calculating the activation energies and intrinsic values of the permeation and diffusion processes using density functional theory.

Silver foil samples (Alfa Aesar, 99.9%) were stamped and mounted to an alumina tube using both ceramic (Autostic ceramic cement) and metallic (Heraeus, silver conductor paste) sealants. The setup was mounted in a vertical clam-shell furnace (Applied Test Systems) and heated to 800°C. After flowing argon gas at 75sccm for 20 minutes, in an effort to blow-off residual water adsorbed within system, the effluent line was attached to a mass spectrometer (Hiden Analytical HPR20). The effluent line was also split to allow excess effluent to flow into a beaker containing water, as recommended by Hiden Analytical. The mass spectrometer scanned the effluent gas from 1-50 amu at a resolution of 100 samples per amu, in order to detect oxygen and oxygen containing species. The driving force for oxygen permeation through the silver membrane was the chemical potential difference between the ambient atmosphere in the furnace and the inert atmosphere provided by argon gas flowing into the alumina tube. This setup is very similar to those often used in gas separation experiments, except a mass spectrometer was used instead of a gas chromatograph. The oxygen partial pressure

within the inert gas chamber was measured to be $9.77*10^{-5}$torr before testing. Checking the oxygen partial pressure served to ensure that the oxygen partial pressure was similar to the measurement pressure of the UHV systems found in literature.

Three repetitions of oxygen permeation experiments were conducted from 800°C-450°C in 50°C increments with argon flow set at 75sccm. The flow rate was controlled by a rotometer (Omega), which was calibrated to argon gas. Effluent gas collected by the mass spectrometer was heated to a temperature above 160°C to prevent condensation and possible recombination of gaseous species. The cold cathode gauge pressure in the ultra-high vacuum (UHV) housing of the mass spectrometer was monitored throughout the experiments to remain at a constant $3*10^{-6}$torr.

The permeation rate of oxygen through polycrystalline silver was measured using mass spectrometry. Using the relative pressure intensity of each detected species and the known amount of argon gas flowing through the system, the volume of each species was determined. The permeation rate of oxygen through polycrystalline silver was measured using mass spectrometry. Using the normalized pressure intensity of each detected species along with the known amount of argon gas flowing through the system, the quantity of each species was determined. The mathematics of Crank describes how the permeation rate and diffusivity through a planar membrane are determined.[261] According to Fick's 2nd Law, the change in concentration with time is equal to the diffusional flux of species as shown.

Equation 57

$$\frac{\partial C}{\partial t}(x,t) = D\left(\frac{\partial^2 C(x,t)}{\partial x^2}\right)$$

Based on the set of boundary conditions given

Equation 58

$$C(x,t=0) = g(x)$$
$$C(x=0,t) = SP_0^{1/2} = C_1$$
$$C(x=d,t) = SP_d^{1/2} = C_2$$

and assuming Sievert's Law applies

Equation 59

$$J(x=d, t\to\infty)=\frac{DSP_0^{1/2}}{d}=\frac{KP_o^{1/2}}{d}=J_{ss}$$

The steady state flux can be determined as

Equation 60

$$J_{ss}=\frac{P_{ss}f}{AkT}$$

Knowing the linear relation between the diffusion coefficient and permeation rate

Equation 61

$$K=DS$$

allows the permeation rate ($cm^{-2}s^{-1}$) to be determined by:

Equation 62

$$K=\frac{P_{ss}fd}{P_0^{1/2}AkT}$$

where P_{ss} is the downstream steady state pressure, P_o is the upstream oxygen partial pressure, f is the conductance, d is the thickness, A is the area, k_B is Boltzmann's constant and T is temperature. Figure 126 shows the agreement between our experimental data for permeation and that of literature.

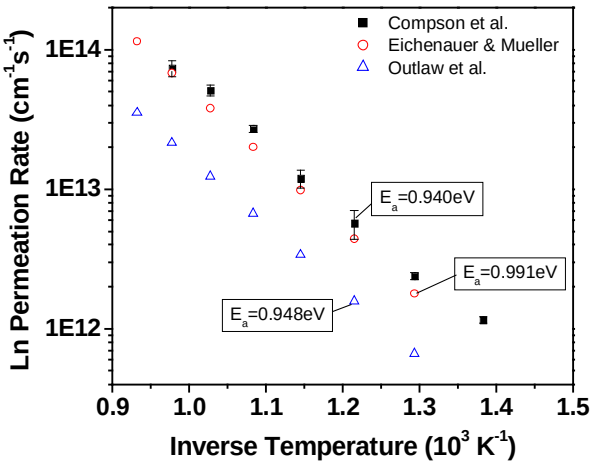

Figure 126. Arrhenius plot of measured permeation rate of oxygen through polycrystalline silver. The filled symbols are the authors measured values and the open symbols are literature values.

Our measured activation energies of 0.940eV for permeation is similar to the reported values of 0.948eV and 0.991eV by Outlaw and Eichenauer & Mueller, respectively,

through polycrystalline silver.[201,266,267] Outlaw determined a relation between the permeability, *K*, and diffusivity, *D*, which depends only on the solubility, *S*, of oxygen on each crystal facet. Equation 61 was used to calculate the effective diffusivity of oxygen through our system, which is shown in Figure 127.

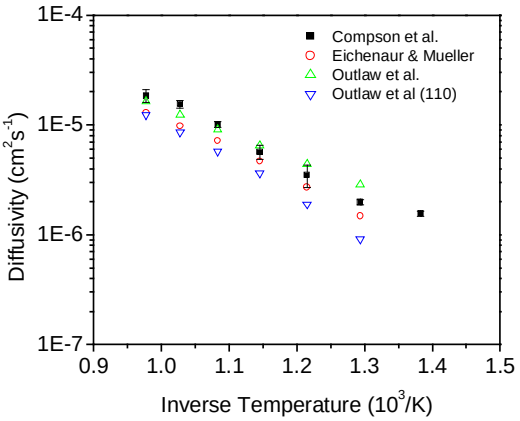

Figure 127. Arrhenius plot of measured diffusivity of oxygen through polycrystalline silver. The filled symbols are the authors measured values and the open symbols are literature values.

The measured activation energies for diffusion were 0.66eV (450ºC<T<630ºC) and 0.58eV (630ºC<T<800ºC), which were also near the 0.66eV (T<630ºC) and 0.48eV (T>630ºC) observed by Outlaw.[266,267] The pre-exponential value for permeation was $3*10^{18}cm^{-1}s^{-1}$ and for diffusion was $0.0407cm^2/s$ (450ºC<T<630ºC) and $0.0159cm^2/s$ (630ºC<T<800ºC). These are close to Outlaw's pre-exponential values of $5.2*10^{18}cm^{-1}s^{-1}$ for permeation and $0.032cm^2/s$ (450ºC<T<630ºC) and $0.00296cm^2/s$ (630ºC<T<800ºC) for diffusion.[204]

Slight differences between the measured values and those reported in the literature were attributed to a difference in grain size between the silver samples, as suggested by Outlaw. The average grain size (mean intercept grain size) of the silver foil used in these experiments was 80.60±2.36μm, as determined by stereological techniques, which is considerably smaller than the 1mm grain sizes used by previous authors.[268] The

presence of smaller sized grains leads to a larger grain boundary area and the possibility for greater amounts of defects and creation of pores between grains. The grain boundary area per unit volume was measured as $0.0124 \pm 0.0036 \mu m^{-1}$, again by stereological techniques. Significant grain growth was also encountered, which could lead to the formation of further defects and thus increase the oxygen permeation rate. Grain growth is confirmed in the SEM images before and after testing, as shown in Figure 128(a-b).

(a) 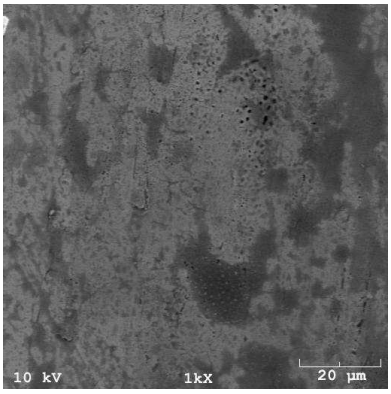

(b) 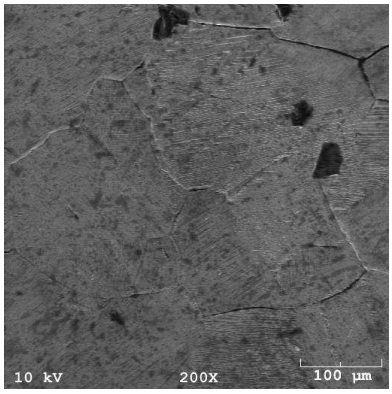

Figure 128. SEM images of silver foil (a) before testing and (b) after testing.

The diffusion of monatomic oxygen species through the silver lattice results in an effective leaking current through the interconnect. This current opposes that of the operating fuel cell and therefore is essentially a counter-current causing reduction in cell potential and fuel utilization through oxidation of the metallic phase of the anode. The leaking current density was calculated from the flux (see Equation 60), which was determined from the relation:

Equation 63

$$J_{O_2} = \frac{P_{O_2} f}{A k_B T}$$

where J_{O_2} is the steady state oxygen flux, P_{O_2} is the downstream pressure, f is the conductance, A is the area of the silver membrane, k_B is Boltzmann's constant and T is the temperature. The oxygen flux and leaking current density are shown in Table 32.

Table 32. Effective oxygen flux and oxygen leaking current density through a 50μm silver foil.

Temperature (K)	Flux ($cm^{-2}s^{-1}$)	Current Density ($mAcm^{-2}$)
723	$3.546*10^{11}$	$2.273*10^{-4}$
773	$7.330*10^{11}$	$4.699*10^{-4}$
823	$1.648*10^{12}$	$1.056*10^{-3}$
873	$3.906*10^{12}$	$2.504*10^{-3}$
923	$8.333*10^{12}$	$5.342*10^{-3}$
973	$1.569*10^{13}$	$1.006*10^{-2}$
1023	$2.271*10^{13}$	$1.456*10^{-2}$

Based upon the collected data, the leaking current density is 0.0053±0.0003mA/cm^2 and 0.015±0.003mA/cm^2 at 650°C and 750°C, respectively, which should have negligible effects on fuel cell performance. These results are similar to those calculated from the oxygen flux data of Wu,[204] 0.00417mA/cm^2, and Outlaw,[201] 0.00288mA/cm^2, at 650°C. However, these results are lower than the 0.967mA/cm^2 at 750°C calculated using the data of Park,[268] who measured the oxygen flux through a silver membrane using an electrochemical cell. Figure 129 shows an Arrhenius plot of the leaking current density as a function of temperature for the empirical oxygen flux results.

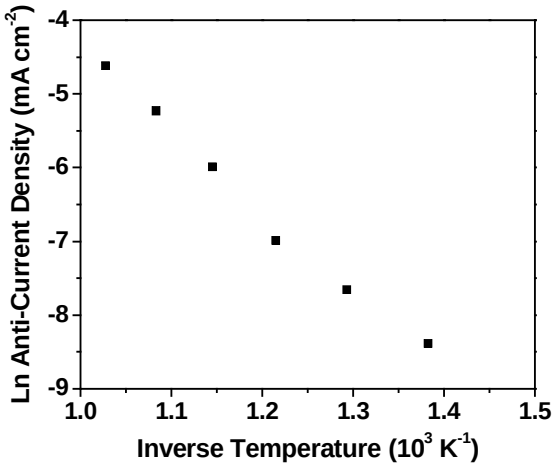

Figure 129. Natural log of current density as a function of inverse temperature for oxygen permeating through silver.

6.2.2 Mechanism of Oxygen Diffusion

Modeling of the surface interactions taking place between oxygen molecules and silver revealed preferential orientation and planar sticking coefficients. Though there are three possible types of adsorption (surface potential energy wells) for oxygen on silver surfaces, dissociative chemisorption is dominant above 150K. The other two forms of adsorption are molecular physisorbtion and molecular chemisorption, which are stable below 40K and 150K respectively. Outka et al. used NEXAFS at temperatures around 100K to observe oxygen chemisorbed on Ag(110) and determined that oxygen orients parallel to the surface (Θ=90°) along the $[1\bar{1}0]$ azimuth.[269] The O-O bond length also increased from 1.207Å to 1.47Å when chemi-adsorbed to Ag exhibiting a σ^* resonance and resembling a single-bonded peroxo species. This is in contrast to the results obtained by Bange, using ESDIAD, who determined the O-O bond has a component along the [001] azimuth.[270] Gravil et al. used spin density functional theory to calculate binding energies and bond lengths due to chemisorption for different directions and bonding sites as shown in Table 33.[271]

Table 33. Binding energis and bond lengths of O_2 chemisorption on Ag.

Site	Axis	Energy (eV) fixed	Energy (eV) relaxed	Distance (Å) O—O	Distance (Å) O_2-Ag	Spin
ffh	⟨001⟩	0.50	0.55	1.45	1.20	0.12
ffh	$\langle 1\bar{1}0\rangle$	0.42	0.51	1.48	0.96	0.25
lb	⟨001⟩	0.37	···	1.32	2.07	1.23
lb	$\langle 1\bar{1}0\rangle$	0.04	0.10	1.48	0.94	0.10
ffh	⟨001⟩	0.23	···	1.28	2.19	1.41
ffh	$\langle 1\bar{1}0\rangle$	0.10	···	1.28	2.19	1.60
lb	⟨001⟩	0.33	···	1.30	2.19	1.36
lb	$\langle 1\bar{1}0\rangle$	0.02	···	1.28	2.19	1.62

This data was based on calculated values of 5.5eV, 1.24Å, and 0.18eV for the binding energy, bond length and vibrational quantum of an oxygen molecule. The experimental values were 5.2eV, 1.21Å and 0.19eV respectively. A six layer silver slab with a 3x2

surface cell separated by a six layer vacuum gap composed the supercell geometry. Oxygen molecules were introduced to both sides of the slab and all atoms were allowed to relax such that the residual force on any one atom did not exceed 0.1eV $Å^{-1}$. The binding energy and bond length were calculated as a function of the oxygen molecule height above the silver surface as shown in Figure 130.

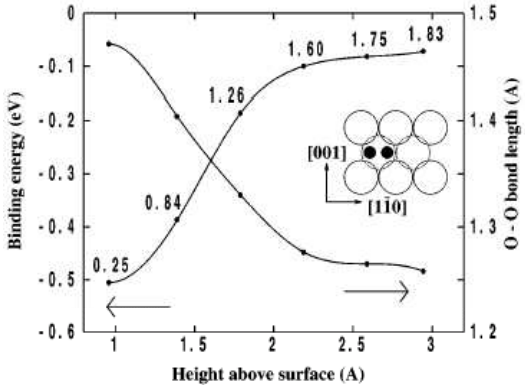

Figure 130. Binding energy and bond lengths of O_2 on Ag, as calculated by DFT.

An important determination from this work was that as oxygen dissociatively chemisorbes to the silver surface, the silver atoms in the plane of the surface relax towards the oxygen atom by 0.12Å along the [001] and 0.03Å along the [1$\bar{1}$0]. The four atoms in the surface plane also relax outwards by 0.07Å while the sub-surface silver atom directly below the chemisorbed oxygen relaxes inwards by 0.23Å. This represents a drastic relaxation of the surface for chemisorbtion at the four-fold site as compared to relatively negligible relaxation for chemisorbtion at the long bridge of short bridge sites. Each of these site possibilities is shown in Figure 131, for the 3x2 supercell.

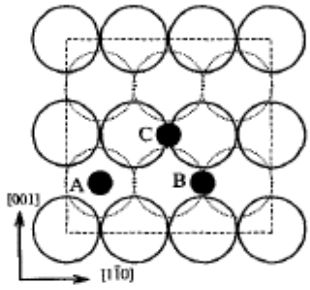

Figure 131. The surface adsorption sites for O_2 on Ag(110).

During chemisorbtion there is also considerable lengthening of the oxygen-oxygen bond length from the gas phase value of 1.24Å to 1.47 ± 0.01Å depending on the adsorption site. It was also important to note that in contrast to the oxygen molecule, the chemisorbed state was not spin polarized, which agrees with experiment.[272,273] Vattuone et al determined that the energy barrier to oxygen dissociation at silver surfaces above 150K was 0.7 ± 0.3eV.[274] He also determined that the sticking coefficient of molecular and dissociated oxygen was azimuthally anisotropic and has non-normal energy scaling with surface corrugation. R. Franchy et al.,[275] studied the negative ion resonances of O_2 on Ag and concluded via molecular beam studies that O_2-Ag interaction was strongly face dependent and was characterized by the dependence of the sticking coefficient on angle of incidence and energy of the gas phase molecules. Much of Franchy's results were in good agreement with those previously published on Ag(110), Ag(111) and Ag(001).[276,277,278,279,280,281,282,283,284,285]

Even though numerous theoretical studies on oxygen-silver interactions have been reported, to the best our knowledge, no theoretical interpretation for diffusion coefficients of oxygen through a silver bulk phase using periodic density functional theory (DFT) methods is available in the literature.[271,286,287] It should be noted that the computational work in this section was performed by Dr. Yongman Choi as a validation method for the experimental work already discussed.[288] Rather than reproduce the complete work of

someone else, I will merely summarize the necessary parts as they apply to validation of the experimental results. All quantum chemical calculations were carried out using the VASP (Vienna *ab initio* simulation package) software[289,290] with the projector augmented wave method (PAW).[291] The spin polarization method was applied because an oxygen species is spin-polarized triple in its ground state. Generalized gradient approximation (GGA) using the Perdew-Wang (PW91) functional[292] was utilized to describe the exchange and correlation energies and Vanderbilt ultrasoft pseudopotentials[293] was used. The Brillouin zone was sampled at (3×3×3) **k**-points with the Monkhorst-Pack method[294] and a 400eV cut-off energy was applied. As shown in Figure 132(a-b), a six-layer Ag(110) surface model was constructed to examine O-Ag interactions and O diffusion into its bulk phase since the solubility and transport of oxygen species is further through (110) than (111) and (100).[295]

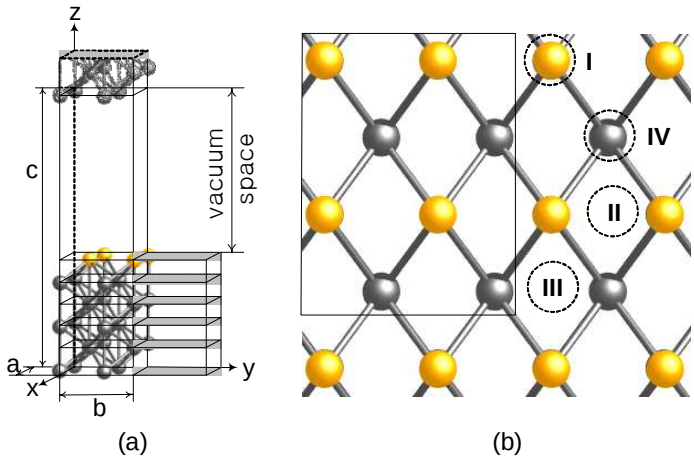

Figure 132. (a) Illustration of a slab model for Ag(110). (b) Four adsorption sites for O-Ag(110) interactions: I**,** II**,** III **and** IV **denote to atop, long bridge, short bridge, and four-fold hollow sites. A rectangle represents the top view of a supercell used in this study.**

Each layer of the surface model has four atoms and each slab was separated by a vacuum spacing greater than ~25 Å to ensure no interactions between slabs. All the calculations were carried out by fixing the bottom layer and the Ag atoms on the unrelaxed layer was

set to estimated bulk parameters. In this study, the relative energy is described by $\Delta E = -(E[slab + adsorbate] - E[slab] - E[O])$, where E[slab + adsorbate], E[slab], E[O] denote the calculated electronic energies of adsorbed species on the surface model, a clean surface, and triplet O. In order to examine O diffusion pathways on the Ag(110) surface and in the bulk phase, we applied the nudged elastic band (NEB) method.[296]

Our predicted lattice constant of 4.11 Å is in line with experimental[297] and theoretical[271,286,298,299] values (4.09 Å and 4.05-4.19 Å, respectively). As aforementioned, quantum chemical calculations were carried out to map out diffusion pathways of O on Ag(110) and incorporation through bulk diffusion into Ag. As illustrated in Figure 132(b), four active sites were examined, including "atop," "short bridge," "long bridge," and "four-fold hollow," corresponding to **I**, **II**, **III**, and **IV**, respectively. We found a slight surface reconstruction by the atomic oxygen adsorption. Table 34 compiles the adsorption energies and the distances between the adsorbed oxygen and the Ag(110) surface.

Table 34. Relative Energies and the Shortest Distance between Adsorbed O and the Surface of Intermediates from O-Ag(110) Interactions.

active site	relative energy (eV)	$d_{O\text{-surface}}$ (Å)
atop	2.41	1.796
short bridge	3.56	1.197
long bridge	3.77	0.303
four-fold hollow	3.94	0.528

The adsorption energy of 3.94eV at the hollow site is stronger than those of atop, short bridge, and long bridge sites with adsorption energies of 2.41, 3.56, and 3.77eV, respectively. Our predicted adsorption energies are qualitatively in good agreement with an available theoretical study by Gravil and coworkers.[287] Therefore O on Ag(110) preferentially adsorb on the four-fold hollow site. The bond distances of the adsorbed

oxygen species on the surface are 1.796, 1.197, 0.303, and 0.528 Å for the four sites (see Table 34). Furthermore, to interpret O diffusion into the bulk phase, we optimized stable intermediates at octahedral sites. Figure 133(a-b) schematically illustrates energetically favorable intermediates on the surface and in the bulk phase (**A** and **B** and **C**, **D**, and **E**, respectively).

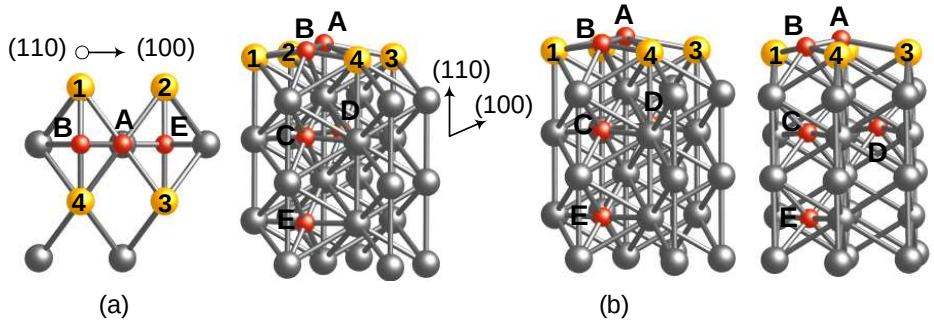

Figure 133. Oxygen adsorption on Ag(110) at the four-fold hollowsite, surface diffusion to the long bridge site, and diffusion to the bulk. (a) A top view and (b) side vies at different angles.

A and **B** denote adsorbed oxygen species at hollow and long bridge sites, respectively, whereas **C**, **D**, and **E** correspond to stable intermediates optimized at octahedral sites on the third and fifth layer based on Ag(110). Figure 134 illustrates schematic potential energy profiles for the diffusion process using the NEB calculations.[296]

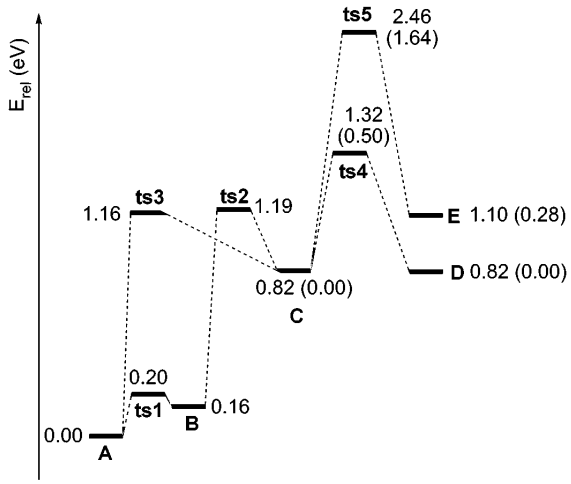

Figure 134. Schematic energy profiles for diffusion processes of O through Ag at the GGA-PAW level of theory.

An adsorbed oxygen species on the hollow site can diffuse to the long bridge site with a 0.16eV endothermicity by overcoming a 0.20eV barrier at **ts1** through the surface. The oxygen species on the long bridge site can further diffuse into the Ag bulk phase - at the octahedral site **C** after overcoming a 1.03eV at **ts2**. In addition to the pathway, **C** can also be formed directly via **ts3** with a barrier of 1.16eV. The barriers forming a stable intermediate at the octahedral site **C** is slightly higher than that reported by Sun and coworkers (0.92eV) due to the different surface models. In addition to the initial O incorporation into the subsurface, we examined O diffusion in the bulk (see Figure 134). As illustrated in Figure 133(b), the diffusion process can occur via two further pathways from **C** to **D** and **E**. Judging from the different barrier heights of 0.50 to 1.6 eV to **D** and **E** sites, respectively, the diffusion process in the bulk phase may preferentially take place through octahedral **C** to **D** sites in the [100] direction rather than the [110] direction. Davidson and coworkers experimentally probed the locations of subsurface oxygen species within the silver lattice using angle-resolved auger electron spectroscopy (ARAES) and ion scattering spectroscopy (ISS).[202] They determined that oxygen species concentrate at the surface adsorption sites, and between the second and third atomic

layers. In between the concentrated oxygen layers is a region of oxygen depletion and after the third atomic layer the oxygen concentration stabilized to a bulk state within the silver lattice. It could be related to the stable structures at **C** and **D** on the second and fourth layers, respectively, in the [100] direction. As well known, the diffusion process can be described by the hopping mechanism - once incorporated into the lattice, it hops from an interstitial site to a more stable position through a transition state.[300,301]

Based on the *ab initio* results of predicted reaction barriers, vibrational frequencies of a reactant and a transition state, and the lattice constant of Ag, we interpreted the experimental diffusivity. According to Wert and Zener,[302] the diffusion coefficients for interstitial atomic oxygen species can be predicted using transition state theory (TST)[303] according to

Equation 64
$$D = D_o \exp(-E_o / k_B T)$$

where E_o, k_B, and T denote an estimated reaction barrier in electron volts (eV) at 0 K, Boltzmann's constant, and temperature in K. Also, pre-exponential factor D_o can be described by

Equation 65
$$D_o = n\alpha a^2 \left(\prod_{j=1}^{3N} \nu_j / \prod_{j=1}^{3N-1} \nu_j^{\dagger} \right)$$

where n and α denote that "the number of nearest neighbor interstitial positions" and "a coefficient related to the location of the interstitial positions" according to Wert and Zener,[37] respectively. a, ν, and $\nu^{\dagger}$ are the lattice constant of Ag and vibrational frequencies of initial and transition states, respectively.[301] Table 35 compiles parameters used for the prediction of diffusion coefficients of O through Ag (110).

Table 35. Parameters used for Diffusion coefficient predictions

n [a]	α [a]	a (Å)[b]	ν (cm^{-1})[c]	$\nu^{\dagger}$ (cm^{-1})[c]
12	1/12	4.110	412, 371, 296	496, 108, *i*33

[a] From ref. 37.
[b] This work.
[c] Vibrational frequencies for **C** and **ts4**, respectively. *i* denotes an imaginary frequency.

Figure 135 shows the comparison of the experimental data with our prediction. To reproduce the experimental results, it is reasonable to lower the reaction barrier from 0.50 to 0.66eV.

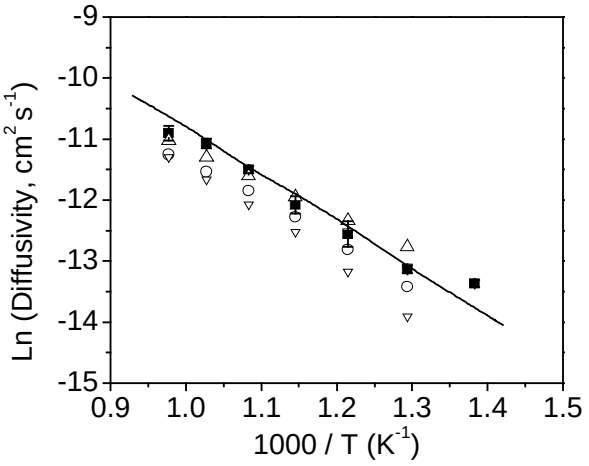

Figure 135. Arrhenius plot of oxygen diffusivity through silver. The filled symbols are measured values in this work and the open symbols are literature data. The solid line corresponds to the predicted results.

6.2.3 Silver Degradation

Theoretical mass loss rates of silver were calculated first assuming a bulk silver sample in an oxidizing atmosphere and then the same sample in a vacuum atmosphere. Using these values, an upper and lower limit of mass loss due to sublimation can be determined. Based on a derivation of the Clausius-Clapeyron equation, a material that is outgassing or losing mass at a constant rate (i.e. evaporation or sublimation from a bulk material), the amount of mass loss for silver should be as follows[304]

Equation 66

$$\frac{\partial m}{\partial t} = W$$

where the mass loss per unit area per unit time ,*W*, is represented as

Equation 67

$$W = 0.0583(P_v)\left(\frac{M}{T}\right)^{1/2} f\left(\frac{g}{cm^2 s}\right)$$

The mass loss rate is dependent on the vapor pressure, P_v (torr), molecular mass, M, temperature, T (K), and the sticking coefficient, f. For silver, the vapor pressure as a function of temperature can be calculated based on the following equations and empirical values.

Equation 68

$$\log P_v = A - \frac{B}{T} - C\log T \text{ (torr)}$$

where A = 11.85, B = 14270 and T is the temperature in K. Figure 136 shows the Arrhenius relation between the vapor pressure of silver and temperature assuming a sticking coefficient of unity.

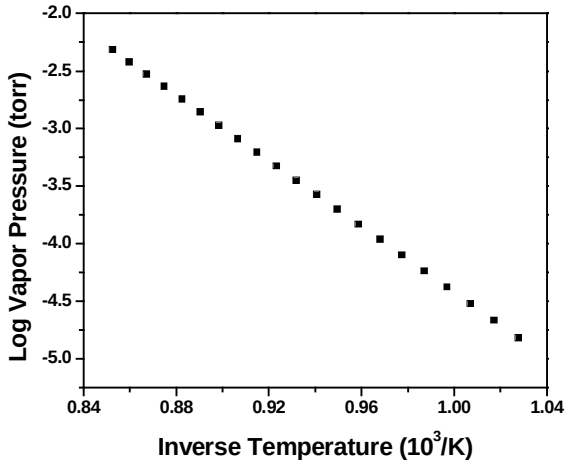

Figure 136. Arrhenius plot of vapor pressure of silver as a function of temperature.

The mass loss per unit area and time can then be calculated by the following.

Equation 69

$$\log W = A'' - \frac{B}{T} - C''\log T$$

Where *A"* and *C"* are represented by

Equation 70

$$A'' = A + \log(0.0583) + 0.5\log M$$
$$C' = 0.5 + \log C$$

The mass loss rate per unit area and time is not only dependent on the conditions such as temperature, but also on the sticking coefficient, *f*. The sticking coefficient, as used in these equations, is the inverse of the sticking probability. Sticking probability, *S* is defined as the probability that a molecule will adsorb onto a surface upon collision. It is also known as the rate of molecular adsorption divided by the collision frequency as shown.

Equation 71

$$S = \frac{R_{ads}}{J_s}$$

The surface collision frequency can be calculated based on the ideal gas law using the following formula:

Equation 72

$$J_s = n * \left[\frac{k_b T}{2\pi m} \right]^{1/2}$$

where n^* is the number of adsorbate molecules per unit volume in gas phase as determined by the pressure (torr), T is the temperature (K), k_B is Boltzmann's constant and m is the mass of the adsorbate (g). The collision frequency is also given by another formula also based on the ideal gas law.

Equation 73

$$z = 2\sqrt{\pi}\left(\frac{N}{V}\right)^2 \sigma^2 \sqrt{\frac{RT}{M}}$$

where z is the collision frequency (collisions/sec), N is Avagadro's number (molecules/mol) adjusted to temp and pressure, V is the Volume (m^3), σ is the diameter of the gas molecule (m), R is the universal gas constant (0.0000821 m^3*atm/K*mol), T is the temperature (K) and M is the molecular mass (Kg/mol).

As the sticking coefficient increases, so does the mass loss rate, *W*, as shown in Figure 137.

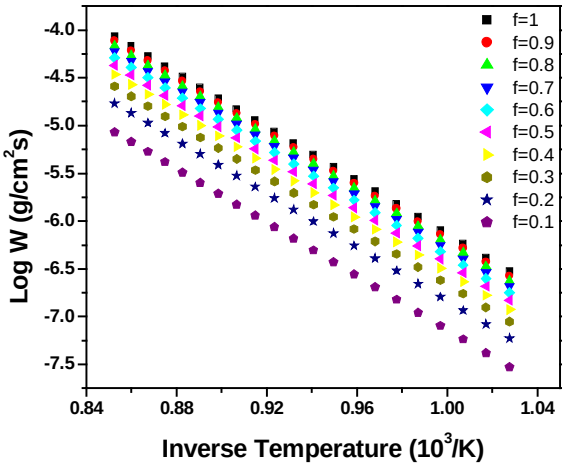

Figure 137. Arrhenius plot of the mass loss rate per unit area and time (g/cm^2/s) as a function of sticking coefficient.

After dividing the mass loss rate, *W*, by the density of silver (10.5 g/cm^3), the loss rate in units of cm/s can be determined, as shown in Figure 138.

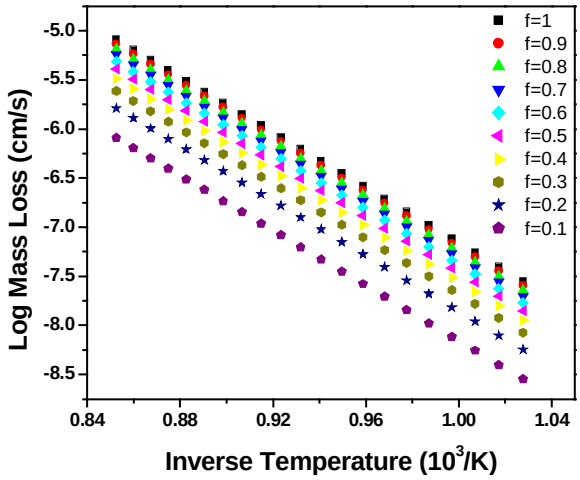

Figure 138. Arrhenius plot of loss rate per unit time (cm/s) as a function of sticking coefficient.

Otherwise the mass loss rate, *W*, can be used to calculate the loss rate (cm/s) based on the actual geometry of the specific sample being measured.

Calculation of the sublimation rate in a vacuum leads to an estimate of the upper limit for the rate of material loss of silver from a foil at high temperature.[305] The following assumptions have been made: (1) a thin boundary layer surrounding the foil is at the equilibrium sublimation vapor pressure, P_c, for a given temperature, T. The actual non-equilibrium pressure will be lower; (2) All atoms within the boundary layer travel at the same speed, the mean thermal velocity V, determined from the simplified kinetic theory of dilute gases;[306]

Equation 74
$$V = \sqrt{\left(\frac{8kT}{m\pi}\right)}$$

and (3) No atoms leaving the boundary layer return to the surface. This means that the sticking factor (sticking coefficient) of the silver atoms is unity and that the mean free path for all temperatures and pressures exceeds the size of the boundary layer.

For a particular temperature of interest, 750°C (1023k), the upper limit or overestimate of the sublimation rate is determined as follows. The flux of silver atoms out of the boundary layer occurs in all directions; since only atoms leaving perpendicular to the boundary are of interest, the mass flux away from the surface will be divided in half. The mean thermal velocity of the silver atoms at 750°C is:

Equation 75
$$V = \sqrt{\left(\frac{(8)(1.38*10^{-23}\,J/k)(1023k)}{(107.87g/mol)(1.67*10^{-27}\,g/atom)(\pi)}\right)} = 446.74m/s$$

The vapor density within the boundary layer, due to sublimation of silver atoms from the surface, at 750°C is given by:

Equation 76
$$\rho_{Ag} = \frac{P_c m T^o}{P^o \overline{V^o} T} = \frac{(0.0106Pa)(107.87g/mol)(293k)}{(1.013*10^5\,Pa)(22.4L/mol)(1023k)} = 1.467*10^{-10}\,g/cm^3$$

Where P^o is the equilibrium vapor pressure at room temperature (101325Pa), V^o is the molar volume of an ideal gas at room temperature (22.4L mol^{-1}), and T^o is the equilibrium reference temperature (293k). Because only half of the atoms move away from the surface, as mentioned earlier, the mass flux away from the surface is:

Equation 77
$$\phi = \frac{V\rho_{Ag}}{2} = \frac{(44674cm/s)(1.467*10^{-10}\,g/cm^3)}{2} = 3.26*10^{-6}\,g/cm^2/s$$

Therefore the mass loss rate is $3.26*10^{-6}$g/cm^2/s at 750°C. Using the theoretical density of silver (10.5g/cm^3), the geometric loss rate of silver is calculated to be $3.11*10^{-7}$cm/s or $3.11*10^{-3}$μm/s. Keep in mind that these numbers are upper limits and represent overestimates of the silver loss rate due to sublimation in a vacuum at 750°C. Boundary conditions and assumptions were made that inflate the loss rate beyond the non-equilibrium or actual rate. These results were compared to Table 31 and showed agreement with the equilibrium vapor pressure of silver as well as the mass loss rate, *W*, at SOFC operating temperatures.

Experimental measurements were then carried out to determine the actual affects of SOFC operating conditions on mass loss and degradation of silver. Static isothermal and dual atmosphere exposure experiments were carried out on a 50μm silver foil used in the permeation experiments to examine grain growth and possible grain boundary degradation. First, a silver foil was exposed to a uniform air atmosphere at 750°C for 24 and 72hrs. The results, shown in Figure 139(a-b), correspond with the aforementioned grain growth on the silver surface.

(a) 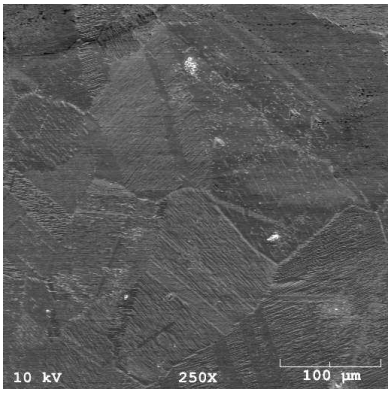

(b) 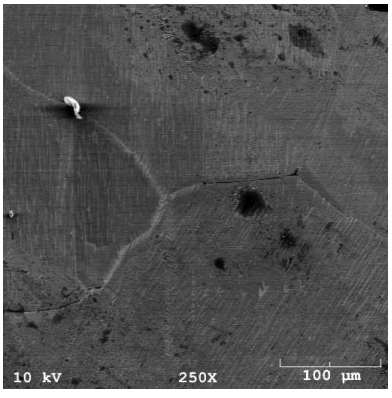

Figure 139. SEM images of the surface of a 50μm dense silver foil after exposure to air at 750°C for (a) 24hrs and (b) 72hrs.

After 24 and 72hrs of exposure, the average grain size was calculated to be 133.69±10.02μm and 197.63±24.09μm, respectively. These corresponded with grain boundary surface area per unit volume values of $0.0075\pm0.0006\mu m^{-1}$ and $0.0051\pm0.0006\mu m^{-1}$ after 24 and 72hrs, respectively. No grain boundary degradation was found to occur on the silver foil samples, however significant faceting was observed on the surface. Faceting of the grains was likely caused by the sublimation, surface diffusion and re-deposition of silver atoms at high temperature. Coles,[198] Singh,[263] Meulenberg[264] and Outlaw[267] also reported significant grain growth and faceting after exposure to oxygen containing atmospheres at high temperature. A second foil sample was sealed to an alumina tube and exposed to a dual (air/H_2+H_2O) atmosphere at 750°C for 24hrs. The silver surface was exposed to air within the furnace, while humidified hydrogen was fed to the surface. After 24hrs exposure, the sample was cooled and each surface was characterized**.** As is clearly visible in Figure 140(a-b), silver degrades much faster when the dual atmosphere contains hydrogen rather than inert argon.

(a) 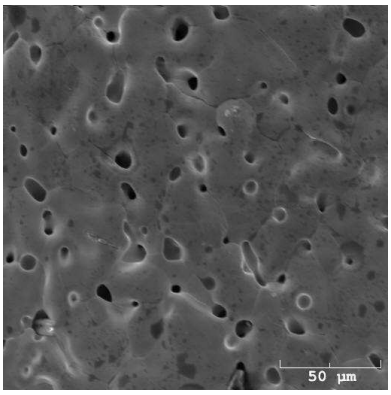

(b) 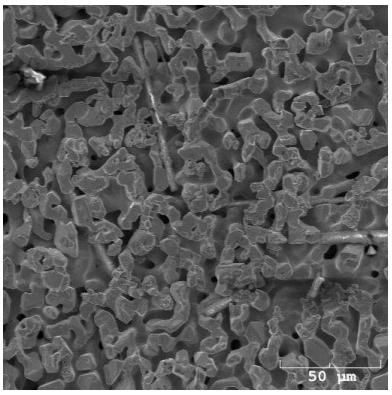

Figure 140. SEM images of silver foil under dual atmosphere for 24hrs. (a) Surface of silver foil exposed to air and (b) surface of silver foil exposed to humidified hydrogen.

The surface exposed to hydrogen experienced more degradation than the surface exposed to air, indicating that pores begin to form on the fuel-rich side. Similar to Singh, we attributed the cause of rapid degradation on the fuel-rich side has to the formation of steam within the silver.[263]

The oxidation front, the amount of nickel oxidation within the SOFC anode due to oxygen permeation through silver, was measured as a function of time and silver layer thickness. Silver layers were DC sputtered onto porous Ni-YSZ cermet anodes and further annealed at 200°C for 2hrs. Static oxidation experiments were performed at 750°C for 3 and 8hrs under SOFC operating conditions in order to determine the amount, if any, of nickel oxidation. At a given operating temperature, equilibrium should be reached between the humidified reducing atmosphere, oxygen flux through silver and nickel oxidation within the anode. Optical micrographs showed obvious oxidation in the sample sputtered for 60 minutes at 70 watts, resulting in a silver layer thickness of 4.7μm. After exposure to SOFC conditions for 3hrs, an 8μm oxidation front formed, which spread to about 30μm after 8hrs. Figure 141(a-d) shows the optical and SEM cross-sectional images of the oxidation front for both exposure times.

(a) 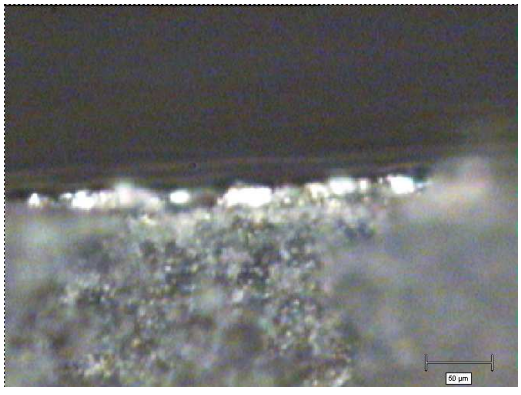 (b) 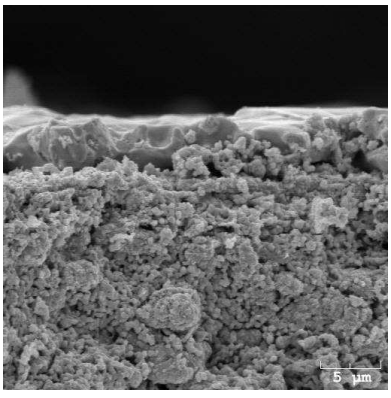

(c) 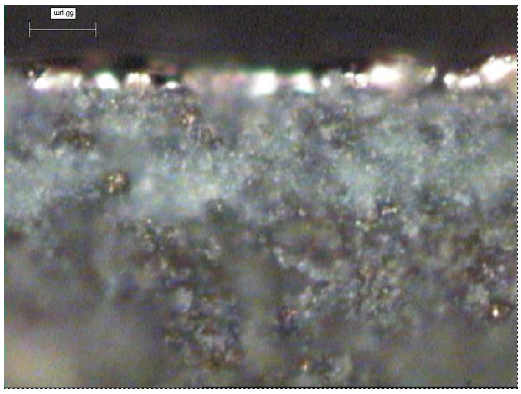 (d) 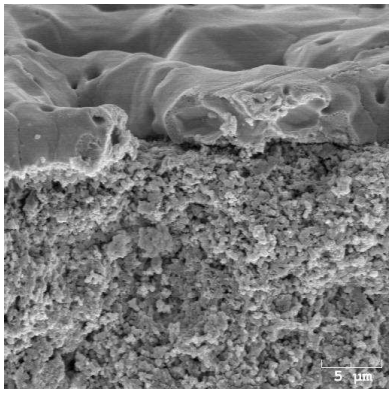

Figure 141. (a) Optical and (b) SEM cross-sectional images of sample with 4.7µm thick silver layer after 3hrs exposure. (c) Optical and (d) SEM cross-sectional images of sample with 4.7µm thick silver layer after 8hrs exposure.

The presence of NiO due to oxidation was confirmed using Raman spectroscopy as shown in Figure 142.

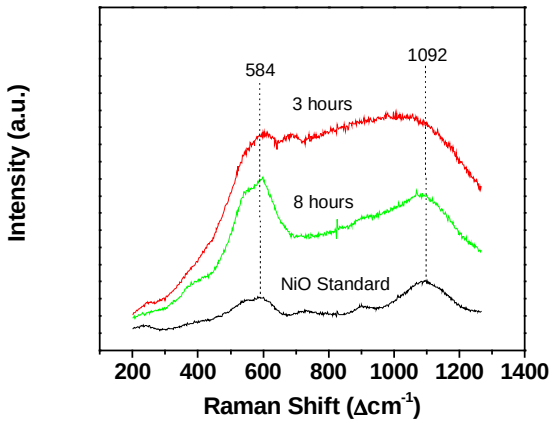

Figure 142. Raman spectrum of sample with 4.7µm thick silver layer after (a) 3hrs and (b) 8hrs exposure.

Connectivity between the silver layer and the anode was lost in both samples indicating that either all the nickel within the oxidation front had oxidized or at least enough to stop percolation of the metallic phase. Increasing the sputtering time to 120 minutes at 70

watts increased the deposited silver layer to 6.6µm. Oxidation of this sample was not noticeable after 3 hours exposure, however an oxidation front of 18µm was observed after 8 hours exposure, as shown in Figure 143(a-d).

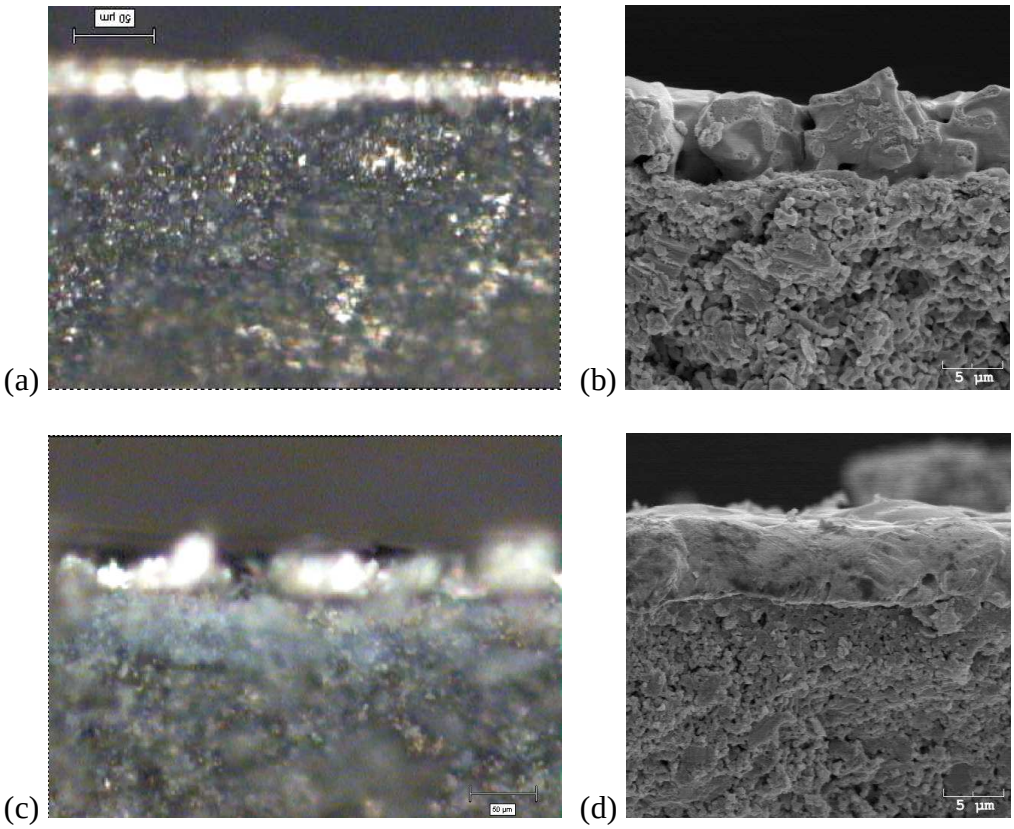

Figure 143. (a) Optical and (b) SEM cross-sectional images of sample with 6.6µm thick silver layer after 3hrs exposure. (c) Optical and (d) SEM cross-sectional images of sample with 6.6µm thick silver layer after 8hrs exposure.

This was again confirmed using Raman spectroscopy as shown in Figure 144.

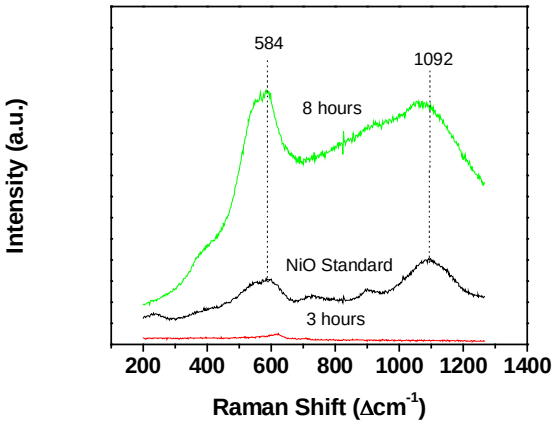

Figure 144. Raman spectrum of sample with 6.6µm thick silver layer after (a) 3hrs and (b) 8hrs exposure.

Both samples remained connective after testing, which means that even though an oxidation front is present after 8 hours, there wasn't complete nickel oxidation within the front. A silver layer of 11.9µm was obtained through 180 minutes of sputtering at 70 watts. Exposure to SOFC operating conditions for 3 and 8hrs didn't reveal evidence of nickel oxidation, as seen in Figure 145(a-d).

(a) 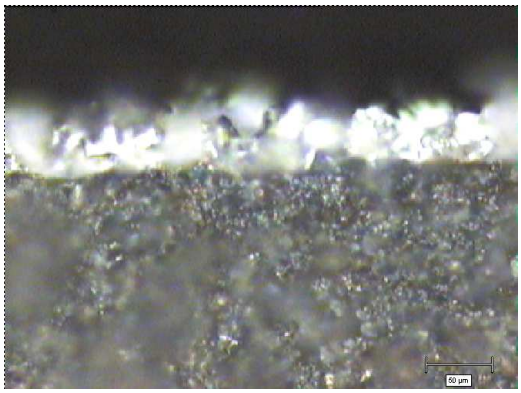 (b) 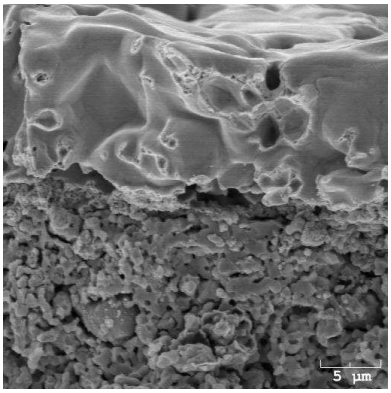

(c) 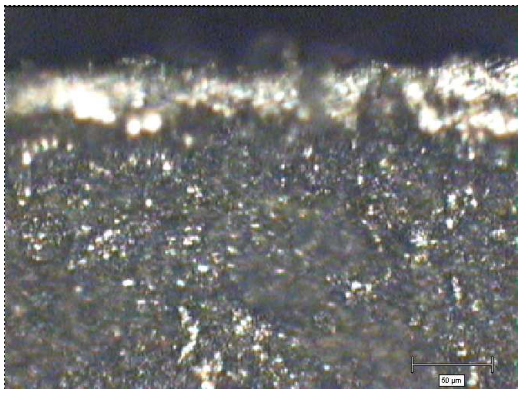 (d) 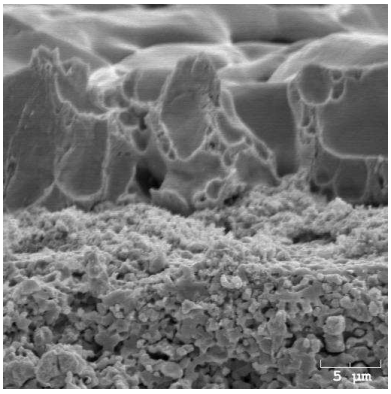

Figure 145. (a) Optical and (b) SEM cross-sectional images of sample with 11.9µm thick silver layer after 3hrs exposure. (c) Optical and (d) SEM cross-sectional images of sample with 11.9µm thick silver layer after 8hrs exposure.

Thus either nickel oxidation didn't occur or was on a length scale that couldn't be detected within the $1um^2$ resolution of the Raman microscope. The Raman spectra in Figure 146(a-b) confirm the lack of nickel oxide within the samples.

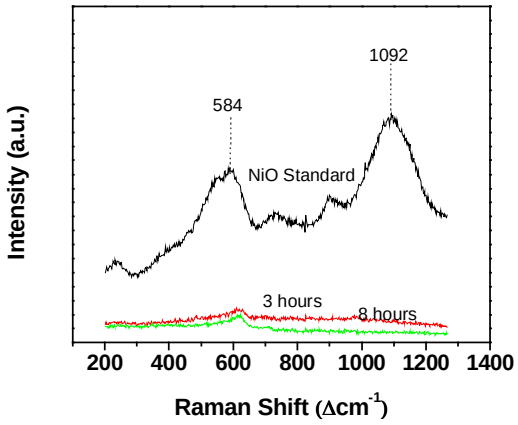

Figure 146. Raman spectrum of sample with 11.9µm thick silver layer after (a) 3hrs and (b) 8hrs exposure.

Connectivity between the silver layer and the anode was also retained within the samples.

Backscatter SEM imaging and EDS analysis were also completed on each sample cross-section. Compared to the optical images, the backscatter SEM images failed to improve the contrast between the nickel and nickel oxide phases and therefore weren't provided. In addition to Raman measurements, qualitative Ni and NiO phase analysis was also performed using EDS. NiO was observed in the same samples as previously mentioned, while no significant oxygen was detected in the sample with the 11.9μm thick silver layer. These results are identical to those achieved using Raman spectroscopy and therefore also weren't provided.

Comparison of the measured oxidation front thickness to that predicted from the oxygen flux data resulted in some discrepancies. The theoretical oxidation front after 8 hrs exposure should be 0.3μm, based on the known oxygen flux through a dense silver foil at 750°C, the volume fraction of nickel within anode and the anode geometry. Increased nickel oxidation could result from the presence of porosity however, since there is a finite sputtered thickness necessary to achieve a continuous silver layer over the porous anode. The surface of the 4.7μm silver layer is not entirely continuous, as seen in Figure 147(a-c), and therefore nickel oxidation occurs readily due to porosity, not permeation.

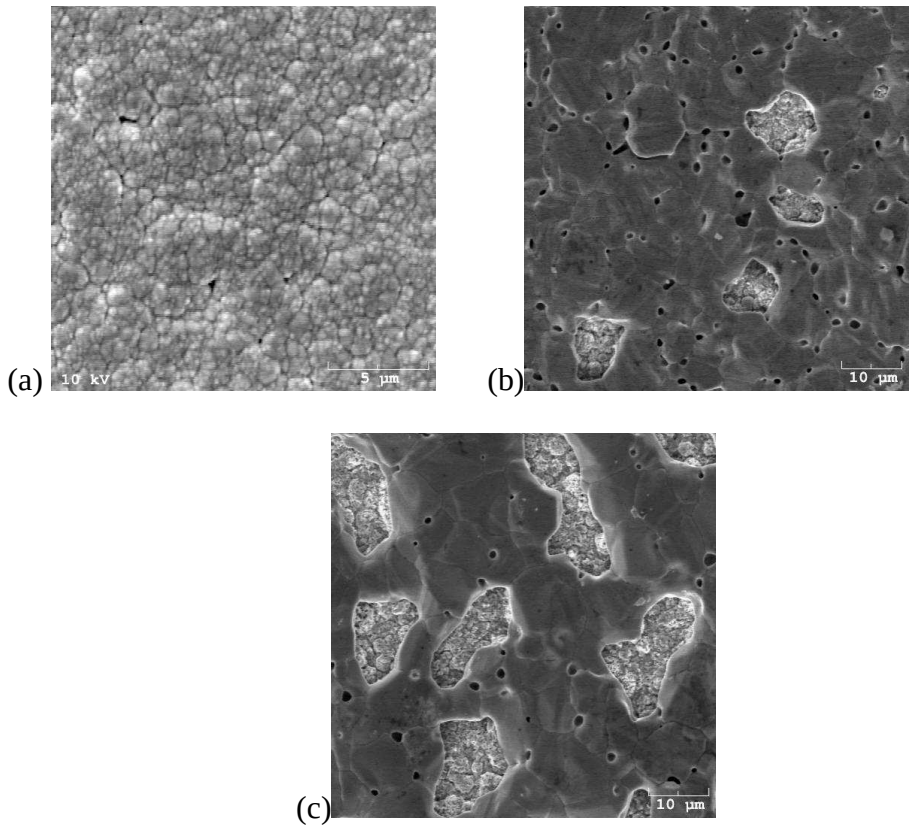

Figure 147. SEM image of the surface of the 4.7µm silver layer (a) after deposition, (b) after 3hrs exposure and (c) after 8hrs exposure.

The surface discontinuity increased as a function of dwell time, eventually exposing and subsequently oxidizing some of the Ni-YSZ anode. The oxidation front is much more suppressed when the silver layer thickness increases to 6.6µm due to increased silver layer continuity. However after 8hrs exposure to SOFC operating conditions, an oxidation front begins to grow due to grain boundary degradation of the silver layer. As previously mentioned, silver tends to degrade at the grain boundaries under SOFC operating conditions, resulting in clustering of silver grains with large pores in between. This is apparent in Figure 148(a-c), where the surface of the 6.6µm silver layer is imaged after initial deposition, 3 and 8hr exposure times.

(a) 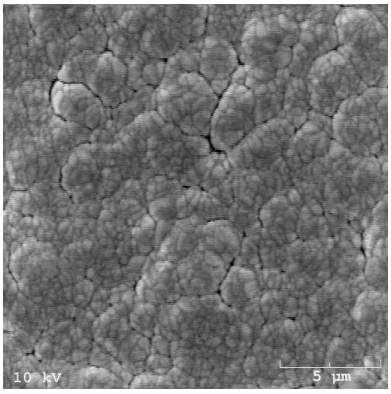

(b) 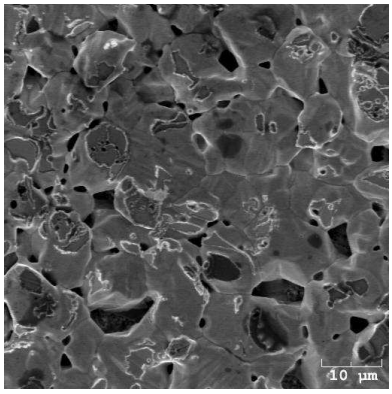

(c) 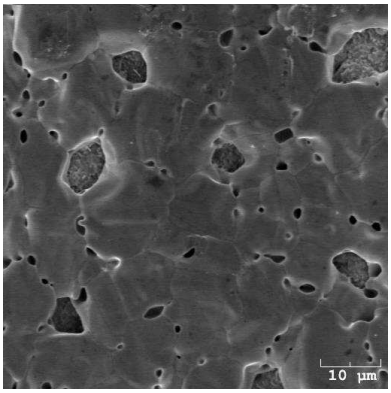

Figure 148. SEM images of the surface of the 6.6µm silver layer (a) after deposition, (b) after 3hrs exposure and (c) after 8hrs exposure.

The increasing surface porosity due to grain boundary degradation caused the dramatic increase in the oxidation front observed between Figure 143(a) and 121(c). It's also apparent from Figure 149(a-c) that the surface of the 11.9µm thick silver layer remains continuous enough to prevent nickel oxidation within the anode even after 8hrs exposure.

(a) 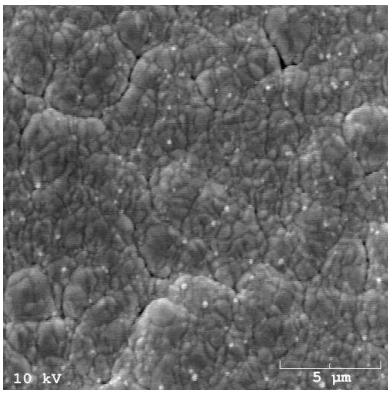

(b) 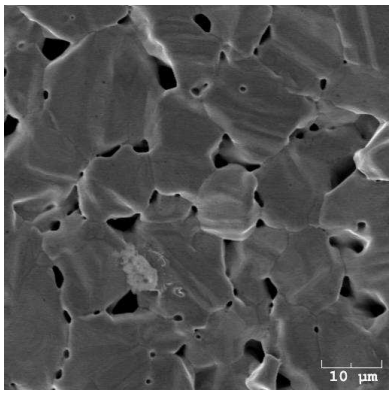

(c) 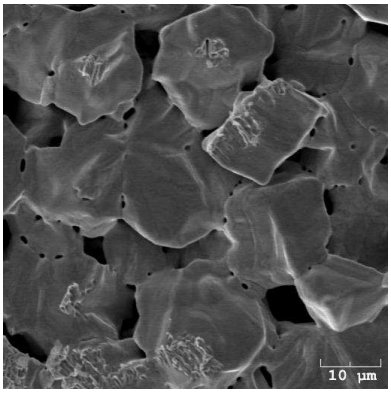

Figure 149. SEM image of the surface of the 11.9µm silver layer after (a) after deposition, (b) after 3 hours exposure and (c) after 8 hours exposure.

Table 36 displays the amount of surface porosity in each sputtered silver layer as a function of exposure time.

Table 36. Volume fraction porosity within the silver surface for the as-deposited, 3hr and 8hr exposure samples.

Silver Layer Thickness (um)	Testing Conditions	Volume Fraction Porosity	Uncertainty
4.7 um	As-deposited	0.0144	0.0013
	3 hour exposure	0.1536	0.0046
	8 hour exposure	0.2704	0.0051
6.6 um	As-deposited	0.0104	0.0011
	3 hour exposure	0.1248	0.0029
	8 hour exposure	0.1656	0.0036
11.9 um	As-deposited	0.0072	0.0009
	3 hour exposure	0.0920	0.0034
	8 hour exposure	0.1072	0.0029

These results do not suggest long-term oxidation prevention, but represent a thickness where anode oxidation was inhibited within the testing timeframe and conditions. The surface degradation rate or silver loss can be roughly estimated using Figure 147(a-c). Though not all the silver is lost to sublimation (vapor phase and diffusional transport probably accounts for the majority of silver movement) a rough estimate of the silver degradation rate can be calculated from our results. The sample

with an initial 4.7μm silver layer degraded to such a point that after 8hrs some portions of the silver were completely removed, which would indicate a minimum degradation rate of $1.6*10^{-4}$μm/s. Theoretical mass loss rates of silver, due to sublimation, were then calculated in order to compare with the estimated experimental degradation rate. The theoretical mass loss rate of silver at 750ºC (due to sublimation) is in the range of $1.4*10^{-3}$ (f = 1) to $1.4*10^{-4}$cm/s (f = 0.1), based on Figure 137. In reality, the sticking factor is probably minimal, since vapor phase and diffusional transport of silver are probably more dominant mechanisms of silver movement that is sublimation. The rough estimate of $1.6*10^{-4}$μm/s falls within the calculated range and in fact is quite close to the sticking factor of 0.1, which is what we predicted. Since an approximate sticking factor is now known, we can estimate the degradation rate of a silver interconnect under SOFC operating conditions over a wide temperature range, as shown in Figure 150.

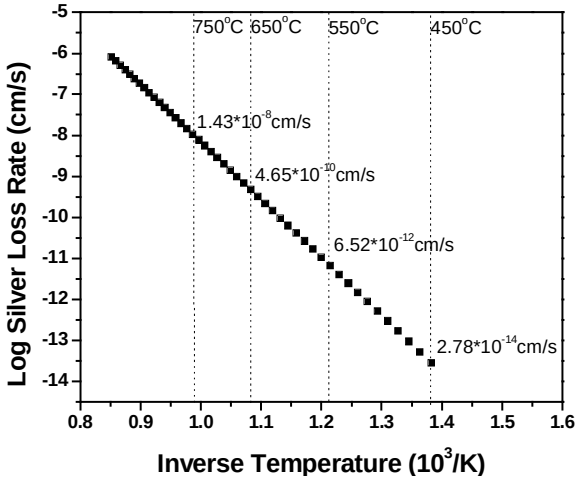

Figure 150. Calculated loss rates of silver from 450-900ºC based on a sticking factor, *f*, of 0.1. This sticking factor best fit the estimated silver degradation rate of $1.6*10^{-4}$μm/s from our experiments.

Though the estimated experimental degradation rate of calculated loss rate of silver represent values too high for realistic use of silver as an SOFC interconnect at 750ºC, the calculated loss rates at temperatures less than 650ºC do not. As seen in Figure

150, the calculated loss rate of silver decreases by two orders of magnitude for every 100ºC reduction in operating temperature. These significant decreases in silver loss rate, when considered with its negligible leaking current density, make silver a viable interconnect material for SOFC applications at temperatures less than 650ºC.

6.3 Conclusions

The inert properties of silver over a wide temperature range make it a strong candidate for an intermediate temperature solid oxide fuel cell (SOFC) interconnect. Silver however, is known to be a selective conductor of H_2 and O_2, which could potentially lead to cell degradation through fuel mixing. Oxygen permeability and diffusivity were determined to follow an Arrhenius relation with activation energies of 0.94eV and 0.59eV, respectively, which are comparable to literature values. Despite oxygen permeation rates increasing with temperature, the effective leaking current density generated at high temperatures remained negligible, indicating that there wouldn't be any appreciable effect on cell performance.

Periodic DFT calculations were used to validate the experimental activation energies and pre-exponential values as well as determine the transport path of oxygen from a surface adsorbate through to bulk diffusion. A least-squared analysis of the experimental permeation rates and diffusion coefficients in the temperature ranges of 723 – 1073 K give in the expressions of $K = 3.0\times10^{18} \exp(-0.94/k_BT)$ cm^{-1} s^{-1} and $D = 4.1\times10^{-2} \exp(-0.66/k_BT)$ cm^2 s^{-1}, respectively. The diffusivity coefficients predicted by transition state theory are in good agreement with the experimental data after slightly adjusting the calculated barrier heights at the GGA-PAW level of theory. The experimental and computational approaches will be applied to examine oxygen conduction mechanisms for noble metals used in high temperature electrochemical applications. Based on our

experimental and computational results for oxygen transport, silver's known inert properties in oxidizing and reducing environments and the effective leaking current density, silver should be considered a candidate material for intermediate temperature SOFC interconnects.

Similar to what has been reported in the literature, porosity forms at the grain boundaries of silver when exposed to a H_2/O_2 dual atmosphere at high temperature. A silver layer of about 12μm, deposited on a Ni-YSZ anode by DC sputtering, was sufficient to prevent a quantifiable oxidation front after 8 hours exposure to SOFC operating conditions at 750ºC. Nevertheless significant surface porosity was still observed within the silver layer. A silver degradation rate of $1.6*10^{-4}$μm/s was estimated based on the results and compared to thermodynamic predictions of the silver evaporative loss rate. Based on the agreement between these values, we extrapolated the effective degradation rate of silver to an operating temperature range of 450-900ºC. Considering the effective leaking current density through silver and estimated degradation rate, silver appears to be suitable for use as an SOFC interconnect at operating temperatures less than 650ºC. While silver would theoretically make a viable interconnect for intermediate temperature SOFCs, the grain boundary degradation appears too severe for successful application.

VII. CONCLUDING REMARKS

The aforementioned works related to investigating particular engineering obstacles in fabricating reliable SOFCs for stack development were the direct result of sustained collaboration with fellow researchers, particularly Dr. William Rauch and Dr. Laxmidhar Besra and consistent support from my advisor, Dr. Meilin Liu. Our work has addressed specific engineering-based hurdles such as economical and reproducible fabrication of thin film electrolytes, the design and fabrication of a stackable SOFC, eliminating the need for external sealant materials and potential replacement interconnect materials for intermediate temperature SOFCs. The ideas behind these works were born as sketches on a whiteboard that grew into functional devices after careful planning and considerable lab effort. I was fortunate enough to have been given the necessary latitude to investigate these ideas, formulate the processing routes and see them to fruition and for that opportunity I am entirely grateful to my advisor.

Electrophoretic deposition is fast and cost-effective method of depositing thin films of ceramics. Deposits were purported to form only on conductive substrates and therefore early work on SOFC applications focused on cathode supports. As interest in this method grew, researchers tried to deposit thin electrolyte layers on anode supports, which were already in the reduced (Ni-YSZ) state. Dr. Besra and I took fabrication of SOFCs by EPD even further when we proposed that this process could be done on non-conducting substrates provided that those substrates were sufficiently porous. Eventually we proved our contention and developed a method for depositing thin electrolyte layers on porous anode substrates. This work simplifies processing of anode-supported SOFCs, while also maintaining a sufficient power density. Optimized parameters resulted in the deposition of a 5μm electrolyte, which after coating with an LSM:YSZ composite cathode provided 1.1W/cm^2 at 850ºC. These results have greater implications than

merely SOFCs, as they set the groundwork for coating any porous ceramic with a layer of dense material. The ability to deposit ceramic material on porous non-conducting substrates could apply to oxygen or hydrogen separation membranes, sensors, thermal or environmental barrier coatings and much more.

Tubular and segmented-cell-in-series SOFC designs may not provide the power density of planar designs, but have the advantage of creating and maintaining an integrated hermetic seal within the structure. Planar designs have suffered from the lack of a proven external sealant, which has resulted in material instability, reactivity and gas leakage. Dr. William Rauch and I therefore proposed a new planar SOFC design, which forms a hermetic seal without the necessity of an external sealant. By incorporating aspects of tubular and segmented-cell-in-series designs, we've been able to fabricate and successfully test a completely hermetic SOFC. The hermetic design contains a critical interface between the interconnect and electrolyte, which when formed correctly acts as a blocking electrode under DC bias conditions. The interface also has a leakage rate on the same order as current compressive mica-based external seals, 10^{-2} sccm at 750ºC. The proposed hermetic or sealless design was fabricated by tape casting lamination as well as electrophoretic deposition and attained open circuit potentials of 0.7V and 0.99V, respectively. The tape cast cell then achieved 76mW/cm^2 at 750ºC using a porous silver cathode. It is important to note that the tape cast cells were fabricated in a single firing step while the EPD cells only required two firing steps. The importance or implication of this work is that external sealants aren't necessary for fabricating a stackable cell. Eliminating the need for external sealants greatly improves SOFC reliability because it removes a very reactive and unstable interface. Increased efforts to fabricate and optimize SOFCs of this hermetic design should only increase their stability and potential lifetime.

Another very reactive interface and perhaps the most detrimental interface to SOFC performance is the cathode-metal interconnect interface. Chromium poisoning of

cathode materials represents a significant hurdle that interlayers don't appear able to solve. A potential interconnect candidate for intermediate temperature SOFCs is a Silver-YSZ composite. Silver is thermodynamically inert to oxidation at intermediate operating temperatures and though it's known to be a selective conductor of oxygen and hydrogen, there is potential to suppress that conduction through tortuous paths within a composite structure. In order to evaluate silver's effectiveness and durability as an SOFC interconnect in a dual atmosphere environment, we measured the rate of oxygen permeation and diffusion through polycrystalline silver foils. The activation energies of these processes were compared with literature reports and then validated using quantum chemical calculations. An effective leaking current density was then determined as a function of temperature, which essentially represents the amount of current that would be lost if silver was used solely as the interconnect material. At 750ºC, silver was shown to only leak 0.967mA/cm^2 of oxygen through to the anode chamber, which is negligible compared to the current density during SOFC operation. Next we observed silver's durability and performance under dual atmosphere conditions. Silver was used as a standalone interconnect in order to evaluate its upper threshold for degradation. Significant silver grain boundary degradation and anode (Ni) oxidation was observed after only 8hrs exposure to SOFC operating conditions at 750ºC. Raman spectroscopy was used to verify the presence of NiO on the anode side of the interconnect. Based on the amount of silver degradation and the time-scale of the experiments, we calculated an experimental degradation rate. This rate corresponded to a theoretical mass loss rate of $1.6*10^{-4}$μm/s, calculated using kinetic gas theory and a transpiration rate, *f*, of 0.1.

Based on the works we have completed, we have come to the following general conclusions.

- A novel approach to depositing thin film layers on porous non-conducting ceramics has been developed, characterized and modeled. This method,

when applied to SOFC fabrication proved to significantly simplify and expedite the processing of anode-supported SOFCs.

- Planar SOFCs can be designed such that external sealants are not necessary. The proposed hermetic design achieved an OCV of up to 0.99V and a power density of 75mW/cm^2. These structures were easily stacked and co-fired for a cost-effective approach to fabricating stackable SOFCS.
- Silver-based interconnect materials were inert in oxidizing environments, but degraded quickly under dual atmosphere conditions at high temperatures (T~750ºC). Based on our experimental and calculated degradation rates, Silver may not be suitable for SOFC operating temperatures greater than 650ºC.

REFERENCES

[1] N.Q. Minh and T .Takahashi, Science and Technology of Ceramic Fuel Cells. Elsevier Science B.V., Amsterdam, The Netherlands, 1995.

[2] N.Q. Minh, "Ceramic Fuel Cells," *J. Am .Cer. Soc.*, **76**[3], 563-588 (1993).

[3] W.R. Grove, "Gas Voltaic Battery," *Philos. Mag.*, **14**, 127-130 (1839).

[4] L. Mond and C. Langer, "A New Form of Gas Battery," *Proceedings of the Royal Society of London*, **46**, 296-304 (1889).

[5] F.W. Ostwald, "Die wissenschaftliche Elektrochemie der Gegenwart ind die technishe der Zukunft (The Scientific Electrochemistry of the Present and the Technology of the Future)," *Z. Elektrochem.*, **1**, 122-125 (1894).

[6] W. Nernst, "Über Die Elektrolytische Leitung Fester Korper Bei Sehr Hohen Temperaturen (On the Electrolytic Conduction of Solid Bodies at Very High Temperatures)," *Z. Elektrochem.*, **6,** 41-43 (1899).

[7] W. Schottky, "Über stromliefernde Prozesse em Konzentrationsgefälle fester Elektrolyte (On Current Supplying Processes from Concentration Gradients of Solid Electrolytes)," *Wiss. Veröff. Siemens Werken*, **14**[2], 1-19 (1935).

[8] E. Baur and H. Preis, "Über Brennstoff-Ketten mit Festleitern (Fuel Cells with Solid Conductors)," *Z. Elektrochem.*, **43**, 727-732 (1937).

[9] A.B. Stambouli and E. Traversa, "Fuel Cells, An Alternative Energy Source," *Ren. and Sus. Energy Rev.*, **6**, 297-306 (2002); A.B. Stambouli and E. Traversa, "Solid Oxide Fuel Cells: A Review of and Environmentally Clean and Efficient Source of Energy," *Ren. and Sus. Energy Rev.*, **6**, 433-455 (2002).

[10] R.J. Bratton and P. Singh, "Review of Tubular Solid Oxide Fuel Cell Developments," *Cer. Trans.*, **65,** 239-262 (1996).

[11] H.-H. Möbius, "On the History of Solid Electrolyte Fuel Cells," *J. Solid State Electrochem.*, **1**, 2-16 (1997).

[12] M.L. Perry and T. Fuller, "A Historical Perspective of Fuel Cell Technology in the 20th Century," *J. Electrochem. Soc.*, **149**[7], S59-S67 (2002).

[13] M. Cifrain and K. Kordesch, Handbook of Fuel Cells – Fundamentals, Technology and Applications. John Wiley & Sons Ltd., New York, NY, pp.267 (2003).

[14] K. Kordesch, J. Gsellmann and B. Kraetschner, "AFC Performance," in *Proceedings of Power Sources*, J. Thompson (ed.) Academic Press, **9**, pp.379 (1983).

[15] C. Rayment and S. Sherwin, Introduction to Fuel Cell Technology, Report to Dept. of Aerospace and Mech. Eng., Univ. of Notre Dame, May 3, 2003.

[16] J. Laramie and A. Dicks, Fuel Cell Systems Explained. John Wiley & Sons Ltd., Chichester, England, 2000.

[17] EG&G Services, Fuel Cell Handbook. Parsons, Inc., Morgantown, WV, 2000.

[18] A.J. Bard and L.R. Faulkner, Electrochemical Methods: Fundamentals and Applications 2nd Ed. John Wiley & Sons, Inc., New York, NY, 2001

[19] D.C. Harris, Quantitative Chemical Analysis, 5th Ed. W.H. Freeman and Company, New York, NY, 1999.

[20] R.T. DeHoff, Thermodynamics in Materials Science. McGraw-Hill Inc., New York, NY, 1993.

[21] C.H.P. Lupis, Chemical Thermodynamics of Materials. Prentice Hall Publishing, New York, NY, 1993.

[22] P. Singh and N.Q. Minh, "Solid Oxide Fuel Cells: Technology Status," *Int. J. App. Cer. Tech.*, **1**[1], 5-15 (2004).

[23] S.J. Skinner and J.A. Kilner, "Oxygen Ion Conductors," *Materials Today*, **6**[3], 30-37 (2003).

[24] Solid Oxide Fuel Cells Schematic. 14 December 2006. < http://www.seca.doe.gov/fuelcellani.html>

[25] S.D. Park, M.J. Vohs, R.J. Gorte, "Direct Oxidation of Hydrocarbons in a Solid Oxide Fuel Cell," *Nature*, **404**, 265-267 (2000).

[26] O. Costa-Nunes, J.M. Vohs and R.J. Gorte, "A Study of Direct Conversion SOFC with *n*-Butane at Higher Fuel Utilization," *J. Electrochem. Soc.*, **150**[7], A858-A863 (2003).

[27] B.C.H. Steele, "Running on Natural Gas," *Nature*, **400**, 619-621 (1999).

[28] H. Kim, S. Park, J.M. Vohs and R.J. Gorte, "Direct Oxidation of Liquid Fuels in a Solid Oxide Fuel Cell," *J. Electrochem. Soc.*, **148**[7], A693-A695 (2001).

[29] G.J. Saunders, J. Preece and K. Kendall, "Formulating Liquid Hydrocarbon Fuels for SOFCs," *J of Power Sources*, **131**, 23-26 (2004).

[30] Z.F. Zhou, C. Gallo, M.B. Pague, H. Schobert and S.N. Lvov, "Direct Oxidation of Jet Fuels and Pennsylvania Crude Oil in a Solid Oxide Fuel Cell," *J. of Power Sources*, **133**, 181-187 (2004).

[31] L. Aguilar, S. Zha, Z. Cheng, J. Winnick and M. Liu, "A Solid Oxide Fuel Cell Running on Hydrogen Sulfide and Sulfur-Containing Fuels," *J. of Power Sources*, **135**, 17-24 (2004).

[32] J. Liu, B.D. Madsen, Z.Q. Ji and S.A. Barnett, "A Fuel-Flexible Ceramic-Based Anode for Solid Oxide Fuel Cells," *Electrochem. and Solid State Letts.*, **5**, A122-A124 (2002).

[33] L. Aguilar, S. Zha, S. Li, J. Winnick and M. Liu, "Sulfur-Tolerant Materials for the Hydrogen Sulfide SOFC," *Electrochem. and Solid State Letts.*, **7**[10], A324-A326 (2004).

[34] H. He, R.J. Gorte and J.M. Vohs, "Highly Sulfur Tolerant Cu-Ceria Anodes for SOFCs," *Electrochem. and Solid State Letts.*, **8**[6], A279-A280 (2005).

[35] Z. Cheng, S. Zha and M. Liu, "Stability of Materials as Candidates for Sulfur-Resistant Anodes of Solid Oxide Fuel Cells," *J. Electrochem Soc.*, **153**[7], A1302-A1309 (2006).

[36] D.W. Dees, U. Balachandran, S.E. Dorris, J.J. Heiberger, C.C. Mcpheeters and J.J. Picciolo, in *Proceedings of the First International Symposium on Solid Oxide Fuel Cells*, Electochemical Society, Pennington, N.J. pp.317, 1989.

[37] T.H. Etsell and S.N. Flengas, "Overpotential Behavior of Stabilized Zirconia Solid Electrolyte Fuel Cells," *J. Electrochem. Soc.*, **118**, 1890-1900 (1971).

[38] H. Binder, A. Köhling, H. Krupp, K. Richter and G .Sandstede, "Elektrochemische Oxydation Von Kolhen-Wasserstoffen In Einer Festelektrolyt-Brennstoffzelle Bei Temperaturen Von 900-1000ºC (Electrochemical oxidation of coal gas in a solid electrolyte gas cell at temperatures of 900-1000ºC)," *Electrochim. Acta*, **8**[10], 781-793 (1963).

[39] A.L. Lee, Internal Reforming Development for Solid Oxide Fuel Cells, Report No. DOE/MC/22045-2, U.S. Dept. of Energy, Washington, D.C., 1987.

[40] A.L. Lee, R.F. Zabranksy and W.J. Huber, "Internal Reforming Development for Solid Oxide Fuel Cells," *Ind. Eng. Chem. Res.*, **29**, 766-773 (1990).

[41] W.Z. Zhu and S.C. Deevi, "Development of Interconnect Materials for Solid Oxide Fuel Cells," *Mat. Sci and Eng. A*, **348**[1-2], 227-243 (2003).

[42] J.W. Fergus, "Metallic Interconnects for Solid Oxide Fuel Cells," *Mat. Sci and Eng. A*, **397**[1-2], 271-283 (2005).

[43] J.W. Fergus, "Lanthanum Chromite-Based Materials for Solid Oxide Fuel Cells Interconnects," *Solid State Ionics*, **171**[1-2], 1-15 (2004).

[44] C.E. Hatchwell, N.M. Sammes, G.A. Tompsett and I.W.M Brown, "Chemical Compatibility of Chromium-based Interconnect Related Materials with Doped Cerium Oxide Electrolyte," *J. of the Eur. Cer. Soc.*, **19**, 1697-1703 (1999).

[45] S.P. Jiang, J.P. Zhang and X.G. Zheng, "A Comparative Investigation of Chromium Deposition at Air Electrodes of Solid Oxide Fuel Cells," *J. of the Eur. Cer. Soc.*, **22**[3], 361-373 (2002).

[46] Z. Zeng and K. Natesan, "Corrosion of Metallic Interconnects for SOFC in Fuel Gases," *Solid State Ionics*, **167**[1-2], 9-16(2004).

[47] L. Jian, J. Huezo and D.G. Ivey, "Carburisation of Interconnect Materials in Solid Oxide Fuel Cells," *J. of Power Sources*, **123**[2], 151-162 (2003).

[48] Z. Yang. K.D. Meinhardt and J. Stevenson, "Chemical Compatibility of Barium-Calcium-Aluminosilicate-Based Sealing Glasses with the Ferritic Stainless Steel Interconnect in SOFCs," *J. of The Electrochem. Soc.*, **150**[8] A1095-A1101 (2003).

[49] V.A.C Haanapel, V. Shemet, I.C. Vinke and W.J. Quadakkers, " A Novel Method to Evaluate the Suitability of Glass Sealant- Alloy Combinations under SOFC Stack Conditions," *J. of Power Sources*, **141**, 102-107 (2005).

[50] N. Lahl, D. Bahadur, K. Singh, L. Singheiser and K. Hilpert, "Chemical Interactions Between Aluminosilicate Base Sealants and the Components on the Anode Side of Solid Oxide Fuel Cells," *J. of the Electrochem Soc.*, **149**[5], A607-A614 (2002).

[51] P. Batfalsky, V.A.C Haanapel, J. Malzbender, N.H. Menzler, V. Shemet, I.C. Vinke and R.W. Steinbrech, "Chemical Interactions Between Glass-Ceramic Sealants and Interconnect Steels in SOFC Stacks," *J. of Power Sources*, **155**[2], 128-137 (2006).

[52] B. Church, T.H. Sanders Jr, R.F. Speyer and J.K. Cochran, "Interconnect Thermal Expansion Matching to Solid Oxide Fuel Cells," *J. of Mat. Sci.*, **40**, 4893-4898 (2005).

[53] C.D. Zuo and M. Liu, "Novel BZCY Electrolyte for Low-Temperature SOFCs," *Adv. Mat.*, in press.

[54] H.S. Isaacs, Zirconia Fuel Cells and Electrolyzers: The Science and Technology of Zirconia. A.H. Heuer and L.W. Dobbs eds., American Ceramic Society, 1981.

[55] J.D. Cawley, "Overview of Zirconia with Respect to Gas Turbine Applications," *NASA Technical Paper 2286* (1984).

[56] J. LeFevre, "Some Structural Modifications in Fluorite Type Phases in Systems Based on Zirconia and Hafnium Oxide," *Ann. Chim. (Paris)*, **8**[1-2], 117-149 (1963).

[57] H.G. Scott, "Phase Relationships in the Zirconia-Yttria System," *J. Mat. Sci.*, **10**, 1527-1535 (1975).

[58] M.B. Trigg and E.R. McCartney, "Comparison of the Reactions Systems ZrO2-Si3N4 and TiO2-Si_3N_4 Structural Ceramics," *J. Am. Cer. Soc.*, **64**, C151-C152 (1981).

[59] V.S. Stubican, R.C. Hink and S.P. Ray, "Phase Equilibria and Ordering in the System ZrO_2-Y_2O_3," *J. Am. Cer. Soc.*, **61**[1-2], 17-21 (1978).

[60] F.A. Kroger and H.J. Vink, "Relations Between the Concentrations of Imperfections in Crystalline Solids, *Solid State Phys.*, **3**, 307-435 (1956).

[61] T. Ishihara, T. Shibayama, S. Ishikawa, K. Hosoi, H. Nishiguchi and Y. Takita, "Novel Fast Ion Conductor and Application for the Electrolyte of Solid Oxide Fuel Cell," *J. Eur. Cer. Soc.*, **24**, 1329-1335 (2004).

[62] R. Maenner, E. Ivers-Tiffée, W. Wersing, W. Kleinlein, in *Proceedings of the 2nd European Ceramics Society Conference*, G. Zeigler and H. Hausner eds., Deutsche Keramische Gesellschaft, pp. 2085 (1991).

[63] F. Tietz, G. Stochniol and A. Naoumidis, in *Proceedings of the 5th European Conference on Advanced Ceramics, Processes and Applications*, L.A.J.L. Sarton and H.B. Zeedijk, Nertherlands Society for Materials Science, **2**, 271, 1997.

[64] Y. Mizutani, M. Tamura, M. Kawai and O. Yamamoto, "Development of High Performance Electrolyte in SOFC," *Solid State Ionics*, **72**[2], 271-275 (1994).

[65] F. Tietz, "Innovative Materials in Advanced Energy Technologies," in *Proceedings of the 9th CIMTEC – World Ceramic Congress and Forum on New Materials*, P. Vincenzini ed., Techna Publishers S.R.L., Faenza, Italy, **24**, 61, 1999.

[66] I. Yasuda and M. Hishinuma, in *Proceedings of the 64th Annual Electrochemical Society of Japan*, Extended Abstracts, Yokohoma, Japan, The Electrochemical Society of Japan, pp. 63, 1997

[67] F. Tietz, "Thermal Expansion of SOFC Materials," *Ionics*, **5** 129-139 (1999).

[68] E. Lara-Curzio and M. Radovic, "Reliability and Durability of Materials and Components for Solid Oxide Fuel Cells," *DOE SECA Annual Report*, ORNL group, 2003.

[69] J.B. Wang, J.-C. Jiang and T.-J. Huang, "Study of Ni-Samaria-doped Ceria Anode for Direct Oxidation of Methane in Solid Oxide Fuel Cells," *J. of Power Sources*, **122**[2], 122-131 (2003).

[70] C. Xia and M. Liu, "Microstructures. Conductivities and Electrochemical Properties of $Ce_{0.9}Gd_{0.1}O_2$ and GDC-Ni Anodes for Low-Temperature SOFCs," *Solid State Ionics*, **152-153**, 423-430 (2002).

[71] S. Zha, W. Rauch and M. Liu, "Ni-$Ce_{0.9}Gd_{0.1}O_{1.95}$ Anode for GDC Electrolyte-Based Low-Temperature SOFCs," *Solid State Ionics*, **166**, 241-250 (2004).

[72] S.-I. Lee, K. Ahn, J.M. Vohs and R.J. Gorte, "Cu-Co Bimetallic Anodes for Direct Utilization of Methane in SOFCs," *Electrchem. And Solid State Lett.*, **8**[1], A48-A51 (2005).

[73] S.-I. Lee, J.M. Vohs and R.J. Gorte, "A Study of SOFC Anodes Based on Cu-Ni and Cu-Co Bimetallics in CeO_2-YSZ," *J. Electrochem. Soc.*, **151**[9], A1319-A1323, (2004).

[74] S. Mcintosh, J.M. Vohs and R.J. Gorte, "Effect of Precious-Metal Dopants on SOFC Anodes for Direct Utilization of Hydrocarbons," *Electrochem and Solid State Lett.*, **6**[11] A240-A243 (2003).

[75] Y.M. Choi, C. Compson, M.C. Lin and M. Liu, "Ab Initio Analysis of Sulfur Tolerance of Ni, Cu and Ni-Cu Alloys for Solid Oxide Fuel Cells," *J. Alloys and Comp.*, **427**, 25-29 (2007).

[76] A. Atkinson, S. Barnett, R.J. Gorte, J.T.S Irvine, A.J. McEvoy, M. Mogensen, S. Singhal, and J. Vohs, "Advanced Anodes for High-Temperature Fuel Cells," *Nature*, **3**, 17-27 (2004).

[77] W.Z. Zhu and S.C. Deevi, "A Review on the Status of Anode Materials for Solid Oxide Fuel Cells," *Mat. Sci & Eng .A*, **362**, 228-239 (2003).

[78] C.H. Bartholomew, P.K. Agrawal and J.R. Kratzer, "Sulfur Poisoning of Metals," *Adv. in Cat.*, **31**, 135-173 (1982).

[79] R.W. Revie, Uhlig's Corrosion Handbook 2nd Ed. John Wiley & Sons, Inc., New York, NY, 2000.

[80] Y.M. Choi, C. Compson, M.C. Lin and M. Liu, "A Mechanistic Study of H_2S Decomposition on Ni- and Cu-Based Anode Surfaces in a Solid Oxide Fuel Cell," *Chem. Phys. Lett.*, **421**, 179-183 (2006).

[81] E. Koep, D. Mebane, R. Das, C. Compson and M. Liu, "Characteristic Thickness of a Dense La0.8Sr0.2MnO3 Electrode," *Electrochem. and Solid State Lett.*, **8**[11], A592-A595 (2005).

[82] E. Koep, A Quantitative Determination of Electrode Kinetics using Micropatterned Electrodes. *PhD Thesis*, School of Materials Science and Engineering, Georgia Institute of Technology, May 2006. Available at < http://etd.gatech.edu/theses/available/etd-04032006-224453/>.

[83] E. Koep, C. Compson, M. Zhou and M. Liu, "A Photolithographic Process for Investigation of Electrode Reaction Sites in Solid Oxide Fuel Cells," *Solid State Ionics*, **176**, 1-8 (2005).

[84] M. Gödickemeier, K. Sasaki, L.J. Gaukler and I. Reiss, "Perovskite Cathodes for Solid Oxide Fuel Cells Based on Ceria Electrolytes," *Solid State Ionics*, **86-88**[2], 691-701 (1996).

[85] S. Srilomsak, D.P. Schilling and H.U. Anderson, "Thermal Expansion Studies on Cathode and Interconnect Oxides," in *Proceedings of the First International Symposium on Solid Oxide Fuel Cells*, S.C .Singhal ed. The Electrochemical Society, Pennington, NJ, pp.129-140 (1989).

[86] E. Ivers-Tiff6e, W. Wersing, M. Schieβl, H. Greiner, "Ceramic and Metallic Components for a Planar SOFC,"*Ber. Bunsenges. Phys. Chem.*, 94, 978 (1990).

[87] A. Hammouche, E. Siebert, A. Hammou, "Crystallographic, Thermal and Electrochemical Properties of the System $La_{1-x}Sr_xMnO_3$ for High Temperature Solid Oxide Fuel Cells," *Mater. Res.Bull.*, **24**, 367 (1989).

[88] H. U. Anderson, "Review of P-Type Doped Perovskite Materials for SOFC and other Applications," *Solid State Ionics*, **52**, 33 (1992).

[89] R. Chiba, T. Ishii, in *Proc. 4th Int. Symp. Solid Oxide Fuel Cells (SOFC-IV)*, eds. M. Dokiya, O.Yamamoto, H. Tagawa, S. C. Singhal, The Electrochemical Society, Pennington, NJ, 1995, p. 482.

[90] G. Ch. Kostogloudis, N. Vasilakos, Ch. Ftikos, "Elastic Properties of Ceramic Oxides used in Solid Oxide Fuel Cells (SOFC)," *J. Eur. Cer. Soc.*, **17**[12], 1523-1532 (1997).

[91] G. Ch. Kostogloudis, Ch. Ftikos, "Characterization of $Nd_{1-x}Sr_xMnO_{3+/-\delta}$ SOFC Cathode Materials," *J. Eur. Cer. Soc.*, **19**[4], 497-505 (1999).

[92] M. B. Phillipps, N. M. Sammes, O. Yamamoto, "$Gd_{1-x}A_xCo_{1-y}Mn_yO_3$ (A identical with Sr, Ca) as a Cathode for the SOFC," *Solid State Ionics*, **123**[1], 131-138 (1999).

[93] G. Ch. Kostogloudis, N. Vasilakos, Ch. Ftikos, "Crystal Structure, Thermal and Electrical Properties of $Pr_{1-x}Sr_xCoO_{3-\delta}$ (x=0, 0.15, 0.3, 0.4, 0.5) Perovskite Oxides," *Solid State Ionics*, **106**[3], 207-218 (1998).

[94] H. Tu and U. Stimming, "Advances, Aging Mechanisms and Lifetime in Solid Oxide Fuel Cells," *J. of Power Sources*, **127**, 284-293 (2004).

[95] K. Huang, P.Y. Hou and J.B. Goodenough, "Reduced Area Specific Resistance for Iron-Based Metallic Interconnects by Surface Oxide Coatings," *Mat. Res. Bull.*, **36**, 81-95 (2001).

[96] Y. Matsuzaki and I. Yasuda, "Electrochemical Properties of a SOFC Cathode in Contact with a Chromium-Containing Alloy Separator," *Solid State Ionics*, **132**, 271-278 (2000).

[97] B. Church, Fabrication and Characterization of Solid Oxide Fuel Cell Interconnect Alloys. *PhD Thesis*, School of Materials Science and Engineering, Georgia Institute of Technology, May 2006. Available at < http://etd.gatech.edu/theses>.

[98] K. Choy, W. Bai, S. Charojrochkul and B.C.H. Steele, "The Development of Intermediate Temperature Solid Oxide Fuel Cells for the Next Millennium," *J. of Power Sources*, **71** 361-369 (1998).

[99] K.S. Weil, C.A. Coyle, J.S. Hardy, J,Y. Kim and G.-G. Huang "Alternative Planar SOFC Sealing Concepts," *Fuel Cells Bulletin,* May 2004.

[100] Y.-K. Lee and J.-W. Park, "Reactions of (La,Ca)CrO_3 Sealants with Yittria-Stabilized Zirconia-(LaCa)CrO_3 Planar Solid Oxide Fuel Cell (SOFC) Stacks," *Mat. Chem. and Phys.*, **45,** 97-102 (1996).

[101] Z. Yang, J.W. Stevenson, K.D. Meinhardt, "Chemical Interactions of Barium-Calcium Aluminosilicate-based Sealing Glasses with Oxidation Resistant Alloys," *Solid State Ionics*, **160**, 213-225 (2003).

[102] S.-B. Sohn, S.-Y. Choi, G.-H. Kim, H.-S. Song and G.-D. Kim "Stable Sealing Glass for Solid Oxide Fuel Cells," *J. of Non-Crystalline Solids,* **297,** 103-112 (2002).

[103] R. Zheng, S.R. Wang, H.W. Nie and T.-L. Wen "SiO_2-CaO-B_2O_3-Al_2O_3 Ceramic Glaze as Sealant for Planar ITSOFC," *J. of Power Sources,* **128,** 165-172 (2004).

[104] Y.-S. Chou and J.W. Stevenson, "Thermal Cycling and Degradation Mechanisms of Compressive Mica-Based Seals for Solid Oxide Fuel Cells," *J. of Power Sources,* **112,** 376-383 (2002).

[105] S. Taniguchi, Kadowaki, T. Yasuo, Y. Akiyama, Y, Miyake and K. Nishio, "Improvement of Thermal Cycle Characteristics of a Planar-Type Solid Oxide Fuel Cell by Using Ceramic Fiber as Sealing Material," *J. of Power Sources*, **90,** 163-169 (2000).

[106] S. P. Simner and J.W. Stevenson, "Compressive Mica Seals for SOFC Applications," *J. Power Sources*, **102**, 310-316 (2001).

[107] J. M. Ralphz, A. C. Schoeler, M. Krumpelt, "Materials for Lower Temperature Solid Oxide Fuel Cells," *J. of Mat. Sci.* **36**, 1161-1172 (2001).

[108] K. Eichler, G. Solow, P. Otschik and W. Schaffrath, "BAS (BaO-Al_2O_3-SiO_2) Glasses for High Temperature Applications," *J. Eur. Cer. Soc.*, **19**, 1101-1104 (1999).

[109] T.-L. Wen *, D. Wang, H.Y. Tu, M. Chen, Z. Lu, Z. Zhang, H. Nie, W. Huang, "Materials Research for Planar SOFC Stack," *Solid State Ionics,* **152– 153**, 399-404 (2002).

[110] T. I. Khan, A. Al-Badri, *J. of Mat. Sci.*, "Reactive Brazing of Ceria to an ODS Ferritic Stainless Steel," **38**, 2483-2488 (2003).

[111] N. Lahl, K. Singh, L. SIingheiser, K. Hilpert, "Chemical Interactions Between Aluminosilicate Base Sealants and the Components of the Anode Side of Solid Oxide Fuel Cells," *J. of Mat. Sci.*, **35**, 3089-3096 (2000).

[112] W.J. Dollard, "Solid Oxide Fuel Cell Development at Westinghouse," *J. of Power Sources*, **37,** 133-139 (1992).

[113] B. Godfrey, K. Föger, R. Gillespie, R. Bolden and S.P.S. Badwal "Planar Solid Oxide Fuel Cells: The Australian Experience and Outlook," *J. of Power Sources*, **86**[1-2], 68-73 (2000).

[114] K. Föger, B. Godfrey and T. Pham "Development of 25kW Fuel Cell System," *Fuel Cells Bulletin*, **No. 5**, 9-11 (1999).

[115] S.P.S. Badwal and K. Foger, "Solid Oxide Electrolyte Fuel Cell Review," *Cer. Int.*, **22** 257-265 (1996).

[116] F. Tietz, H.-P. Buchkremer and D. Stöver, "Components Manufacturing for Solid Oxide Fuel Cells," *Solid State Ionics*, **152-153**, 378-381 (2002).

[117] R.E. Mistler and E.R. Twiname, Tape Casting: Theory and Practice. The American Ceramic Society, Westerville, OH, 2000.

[118] D.J. Shanefield, Organic Additives and Ceramic Processing. Kluwer Academic Publishers, Boston, MA, 1995.

[119] G. Howatt, R.G. Breckenridge and J.M. Brownlow, "Fabrication of Thin Ceramic Sheets for Capacitors," J. Am. Cer. Soc., **30**[8], 237-242 (1947).

[120] G.N. Howatt, "Method of Producing High-Dielectric High Insulation Ceramic Plates," U.S. Patent 2.582,993.

[121] J.L. Park, "Manufacture of Ceramics," U.S. Patent 2,966,719.

[122] H. Stetson and B. Schwartz, "Laminates, New Approach to Ceramic Metal Manufacture: Part 1: Basic Process," *Am. Cer. Soc. Bull.*, **40**[9] 584- (1961).

[123] H.W. Stetson, "Method of Making Multilayer Circuits," U.S. Patent 3,189,978.

[124] W.J. Gyurk, "Methods for Manufacturing Multilayered Monolithic Ceramic Bodies," U.S. Patent 3,192,086.

[125] B. Schwartz and D.L. Wilcox, "Laminated Ceramics," in Proceedings of the Electronic Components Conference, pp.17-26, 1967.

[126] R.E. Mistler, D.J. Shanefield and R.B. Runk, "Tape Casting of Ceramics," in Ceramic Fabrication Before Firing. G.Y. Onoda and L.L. Hench eds., John Wiley & Sons, New York, NY, 1978.

[127] H. Ohrui, T. Matsushima and T. Hirai, "Performance of Solid Oxide Fuel Cell Fabricated by Co-firing," *J. Power Sources*, **71**, 185-189 (1998).

[128] W. Schafer, A. Koch, U. Herold-Schmidt and D. Stolten, "Materials, Interfaces and Production Techniques for Planar Solid Oxide Fuel Cells," *Solid State Ionics*, **86-88**, 1235-1239 (1996).

[129] Z. Liu, G. Roman, J. Kidwell and T. Cable, "Development of Advanced Planar Solid Oxide Fuel Cells with High Strength," *Ceramic Engineering and Science Proceedings*, **25**[3], 239-244 (2004)

[130] G. Martinelli, M.C. Carotta, M. Ferroni, Y. Sadaoka and E. Traversa, "Screen-Printed Perovskite-Type Thick Films as Gas Sensors for Environmental Monitoring," *Sensors and Actuators B*, **55**, 99-110 (1999).

[131] P.V. Dollen and S.A. Barnett, "A Study of Screen-Printed Yittria-Stabilized Zirconia Layers for Solid Oxide Fuel Cells," *J. Am. Cer. Soc.*, **88**[12], 3361-3368 (2005).

[132] D. Rotureau, J.-P. Viricelle, C. Pijolat, M. Caillol and M. Pijolat, "Development of a Planar SOFC Device using Screen-Printing Technology," *J. Eur. Cer. Soc.*, **25**, 2633-2636 (2005).

[133] H.C. Hamaker, "Formation of a Deposit by Electrophoresis," *Trans. Farad. Soc.*, **36**, 279-287 (1940).

[134] H.C. Hamaker and E.J.W. Verway, "The Role of the Forces Between the Particles in Electrodeposition and Other Phenonmenon," *Trans. Farad. Soc.*, **36**, 180-185 (1940).

[135] De Bozes, M., *Phil. Trans.*, **43**, 419 (1745).

[136] F.F. Reuss, "Charge-Induced Flow," In *Proceedings of the Imperial Society of Naturalists of Moscow*, **3**, 327-344 (1809).

[137] W. Pickard, "Remarks on the Theory of Electrophoretic Deposition," *J. Electrochem. Soc.*, **115**, 105C-108C (1968).

[138] H. Koelmans and J. Th. G. Overbeek, "Stability and Electrophoretic Deposition of Suspensions in Non-Aqueous Media," *Disc. Farad. Soc.*, **18**, 52-63 (1954).

[139] H. Koelmans, "Suspensions in Non-Aqueous Media," *Philips Res. Rep.*, **10**, 161-193 (1955).

[140] D.R. Brown and F.W. Salt, "The Mechanism of Electrophoretic Deposition" *J. App. Chem.*, **15**, 40-48 (1968).

[141] M. Shimbo, K. Tanzawa, M. Miyakawa and T. Emoto, "Electrophoretic Deposition of Glass Powder for Passivation of High-Voltage Transistors," *J. Electrochem. Soc.*, **132**, 393-398 (1985).

[142] E. Sluzky and K. Hesse, "Electrophoretic Preparation of Phosphor Screens," *J. Electrochem. Soc.*, **136**, 2724-2727 (1989).

[143] F. Grillon, D. Fayuelle, and M. Jeandin, "Quantitative Image Analysis of Electrophoretic Coating," *J. Mat. Sci. Lett.*, **11**, 272-275 (1992).

[144] J. Mizuguchi, K. Sumi, and T. Muchi, "A Highly Stable Nonaqueous Suspension for Electrophoretic Deposition of Powdered Substances," *J. Electrochem. Soc.*, **130**, 1819-1825 (1983).

[145] P. Sarkar and P.S. Nicholson, "Electrophoretic Deposition (EPD): Mechanisms, Kinetics and Applications to Ceramics," *J. of Am. Cer. Soc.*, **79** 1987-2002 (1996).

[146] O.O. Van der Biest and L.J. Vandeperre, "Electrophoretic Deposition of Materials," *Annu. Rev. Mater. Sci.*, **29**, 327-352 (1999).

[147] D. De and P.S. Nicholson, "Role of Ionic Depletion in Deposition during Electrophoretic Deposition," *J. Am. Cer. Soc.*, **82**, 3031-3036 (1999).

[148] Y. Fukuda, N. Nagarajan, W. Mekky, Y. Bao, H.-S. Kim and P.S. Nicholson, "Electrophoretic Deposition – Mechanisms, Myths and Materials," *J. Mater. Sci.*, **39**, 787-801 (2004).

[149] F. Bouyer, and A. Foissy, "Electrophoretic Deposition of Silicon Carbide," *J. Am Cer. Soc.*, **82**, 2001-2010 (1999).

[150] G. Anné, K. Vanmeensel, O.O. Van der Biest, J. Vleugels, "Influence of the Suspension Composition on the Electric Field and Deposition Rate During Electrophoretic Deposition," *Colloids and Surfaces A: Physiochem. Eng. Aspects*, **245**, 35-39 (2004).

[151] G. Anné, B. Neirinck, K. Vanmeensel, O.O. Van der Biest, and J. Vleugels, "Origin of the Potential Drop over the Deposit During Electrophoretic Deposition," *J. Am. Cer. Soc.*, **89**, 823-828 (2006).

[152] H. Negishi, K. Yamaji, T. Imura, D. Kitamoto, T. Ikegami, and H. Yanagishita, "Electrophoretic Deposition Mechanism of YSZ/n-Propanol Suspension," *J. Electrochem. Soc.*, **152**, J16-J22 (2005).

[153] M. Wei, A.J. Ruys, B.K. Milthorpe, C.C. Sorrell, J.H. Evans, "Electrophoretic Deposition of Hydroxyapatite Coatings on Metal Substrate: A Nano-Particulate Dual Coating Approach," *J. Sol-gel Sci. & Tech.*, **21**, 39-48 (2001).

[154] T.M. Sridhar and U. K. Mudali, "Development of Bioactive Hydroxyapatite Coatings on Type 316L Stainless Steel by Electrophoretic Deposition for Orthopaedic Applications," *Trans. Indian Inst. Metals*, **56** (3), 221-230 (2003).

[155] J.-H. Yum, S.-Y. Seo, S. Lee, Y.-E. Sung, "$Y_3Al_5O_{12}$:$Ce_{0.05}$ Phosphor Coating on Gallium Nitride for White Light Emitting Diodes," *J. Electrochem. Soc.*, **150**, 2, H47-H52 (2003).

[156] M.J. Shane, J.B. Talbot, B.G. Kinney, E. Sluzky and H.R. Hesse, "Electrophoretic Deposition of Phophors II: Deposition Experiments and Analysis," *J. Colloid and Interface Sci.*, **165**, 334-340 (1994).

[157] M.J. Shane, J.B. Talbot, R.G. Schreiber, C.L. Ross, E. Sluzky and K.R. Hesse, 'Electrophoretic Deposition of Phophors I: Conductivity and Zeta Potential Measurements," *J. Colloid and Interface Sci.*, **165**, 325-333 (1994).

[158] K. Hayashi, and N. Furuya, "Preparation of Gas Diffusion Electrodes by Electrophoretic Deposition," *J. Electrochem. Soc.*, **151** (3), A354-A357 (2004).

[159] J.Y.Choudhury, K.N. Rai and H.S.Ray, "Electrophoretic Deposition of Ceramic Compounds on Metal and Graphite Substrates," *Trans. Ind. Inst. Metals*, **31**(6), 1978, pp.468-469.

[160] K. Yamashita, E. Yonehara, X.Ding, M. Nagai, T. Umegaki and M. Matsuda, "Electrophoretic Coating of Multilayered Apatite Composite on Alumina Ceramics," pp.46-53, in HA coating on alumina ceramics, John Wiley and sons, Inc. 1998.

[161] S.J. Limmer and G. Cao, "Sol-gel Electrophoretic Deposition for the Growth of Oxide Nanorods," *Adv. Mater.*, **15** (5), 427-431 (2003).

[162] C. Du, D. Heldbrant, N. Pan, " Preparation and Preliminary Property Study of Carbon Nanotubes Films by Electrophoretic Deposition," *Mater. Lett.*, **57**, 434-438 (2002).

[163] S. Put, J. Vleugels, G. Anne, O. Van der Biest, "Functionally Graded Ceramic and Ceramic-Metal Composites Shaped by Electrophoretic Deposition," *Colloids and Surfaces A: Physicochemical and Engineering Aspects*, **222**, 223-232 (2003).

[164] P. Sarkar, S. Datta and P.S. Nicholson, "Functionally Graded Ceramic/Ceramic and Metal/Ceramic Composites by Electrophoretic Deposition," *Composites Part B*, **28B**, 49-56 (1997).

[165] B. Ferrari, A.J. Sanchez-Herencia and R. Moreno, "Electrophoretic Forming of Al_2O_3/ Y-TZP Layered Ceramics form Aqueous Suspension.," *Mater. Res. Bull.*, **33** (3), 487-499 (1998).

[166] S.K. F. Yau and C.C. Sorrel, "High-J_c $(Bi,Pb)_2Sr_2Ca_2CuO_{10+x}$ Tapes Fabricated by Electrophoretic Deposition," *Physica C*, **282-287**, 2563-2564 (1997).

[167] J. Van Tasses and C.A. Randall, "Electrophoretic Deposition and Sintering of Thin/Thick PZT Film," *J. Eur. Ceram. Soc.*, **19**, 955-958 (1999).

[168] K. Hasegawa, S. Kunugi, M. Tatsumisago and T. Minami, "Preparation of Thick Films by Electrophoretic Deposition using Modified Silica Particles Derived by Sol-Gel Method," *J. Sol-gel Sci. & Tech.*, **15**, 243-249 (1999).

[169] W. Shan, Y. Zhang, W. Yang, C. Ke, Z. Gao, Y. Ke, Y. Tang, "Electrophoretic Deposition of Nano-Size Zeolites in Non-Aqueous Medium and its Application in Fabricating Thin Zeolite Membranes," *Microporous and Mesoporous Materials*, **69**, 35-42 (2004).

[170] T. Klemensø, C. Chung, P.H. Larsen, and M. Mogensen, "The Mechanism Behind Redox Instability of Anodes in High Temperature SOFCs," *J. Electrochem. Soc.*, **152**, A2186-A2192 (2005).

[171] T. Ishihara, K. Shimose, T. Shiomitsu, and Y. Takita, "Electrophoretic deposition of Y_2O_3–stabilized ZrO_2 on the porous $La_{0.8}Sr_{0.2}MnO_3$ cathode substrate for SOFC," In *Proceedings of the Fourth International Symposium on Solid Oxide Fuel Cells*, eds. M. Dokiya, O. Yamamoto, H. Tagawa and S.C. Singhal, The Electrochemical Society, pp. 334-343, 1995.

[172] T. Ishihara, K. Shimose, T. Kudo, H. Nishiguchi, T. Akbay, and Y. Takita, "Preparation of Yttria-stabilised Zirconia Thin Films on Strontium–doped

$LaMnO_3$ Cathode Substrate via Electrophoretic Deposition for Solid Oxide Fuel Cells," *J. Am. Cer. Soc.*, **83**, 1921-1927 (2000).

[173] R.N. Basu, C.A. Randall, and M.J. Mayo, "Development of Zirconia Electrolyte Films on Porous Lanthanum Manganite Cathodes by Electrophoretic Deposition," In *Proceedings of Materials Research Society: New Materials for batteries and Fuel cells*, San Francisco, USA, vol. 575, pp.303-308, 2000.

[174] Z. Peng, and M. Liu, "Preparation of Dense Platinum-Yttria Stabilized Zirconia and Yttria Stabilized Zirconia Films on Porous $La_{0.9}Sr_{0.1}MnO_3$ (LSM) Substrates," *J. Am. Cer. Soc.*,**84**, 283-288 (2001).

[175] F. Chen and M. Liu, "Preparation of Yttria Stabilized Zirconia (YSZ) Films on $La_{0.9}Sr_{0.1}MnO_3$ (LSM) and LSM-YSZ Substrates Using an Electrophoretic Deposition (EPD) Process," *J. Eur. Cer. Soc.*, **21**, 127-134 (2001).

[176] J. Will, M. Hruschka, L. Gubler, and L.J. Gauckler, "Electrophoretic Deposition of Zirconia on Porous Anodic Substrates," *J. of Am. Cer. Soc.*, **84**, 328-332 (2001).

[177] I. Zhitomirsky, and A. Petric, "Electrophoretic Deposition of Ceramic Materials for Fuel Cell Applications," *J. Eur. Cer. Soc.*, **20**, 2055-2061 (2000).

[178] K. Kobayashi, I. Takahashi, M. Shiono and M. Dokiya, "Supported $Zr(Sc)O_2$ SOFCs for Reduced Temperature Prepared by Electrophoretic Deposition," *Solid State Ionics*, **152-153**, 591-596 (2002).

[179] K. Yamaji, H. Kishimoto, Y. Xiong, T. Horita, N. Sakai, and H. Yokokawa, "Performance of Anode-Supported SOFCs Fabricated with EPD Techniques," *Solid State Ionics*, **175**, 165-169 (2004).

[180] T. Ishihara, K. Sato, Y. Mizuhara, and Y. Takita, "Preparation of Yttria-Stabilized Zirconia Films for Solid Oxide Fuel Cells by Electrophoretic Deposition Method," *Chem. Lett.*, 943-46 (1992).

[181] M. Matsuda, T. Hosomi, K. Murata, T. Fukui, and M. Miyake, "Direct EPD of YSZ Electrolyte Film onto Porous NiO-YSZ Composite Substrate for Reduced-Temperature Operating Anode-Supported SOFC," *Electrochem. and Solid State Lett.*, **8**, A8-A11 (2005).

[182] T. Ishihara, K. Sato, and Y. Takita, "Electrophoretic Deposition of Y_2O_3 Stabilised ZrO_2 Electrolyte Films in Solid Oxide Fuel Cells," *J. Am. Cer. Soc.*, **79**, 913-919 (1996).

[183] L. Besra, C. Compson, and M. Liu, "Electrophoretic Deposition on Porous Tapecast Substrates," *J. Am. Cer. Soc.*, **89**[10], 3003-3009 (2006).

[184] P. Sarkar, O. Prakash, G. Wang, and P.S. Nicholson, "Micro-Laminate Ceramic/Ceramic Composites (YSZ/Al2O3) by Electrophoretic Deposition," *Cer. Eng. Sci. Proc.*, **15**, 1019-1027 (1994).

[185] J. Zhang, and B.I. Lee, "Electrophoretic Deposition and Characterization of Micrometer-Scale $BaTiO_3$ Based X7R Dielectric Thick Films," *J. Am. Cer. Soc.*, **83**, 2417-2422 (2000).

[186] F.J. Gardner, M.J. Day, N.P. Brandon, M.N. Pashley and M. Cassidy, "SOFC Technology Development at Rolls Royce," *J. of Power Sources*, **86**[1-2], 122-129 (2000).

[187] S. Singhal, "Recent Progress in Tubular Solid Oxide Fuel Cell Technology," in *Proceedings of the 1998 International Gas Research Conference*, Madison, WI, USA, Omnipress, pp. 422, 1998.

[188] R.S.R Gorla, "Probabilistic Analysis of a Solid Oxide Fuel Cell Based Hybrid Gas Turbine System," Applied Energy, **78**, 63-74 (2004).

[189] SOFC Gas Turbine Hybrid. 12 December 2006 <http://www.powergeneration.siemens.com/en/fuelcells/hybrid/index.cfm>

[190] T. Hosomi, M. Matsuda and M. Miyake, "Electrophoretic Deposition for Fabrication of YSZ Electrolyte Film on Non-Conducting Porous NiO-YSZ Composite Substrate for Intermediate Temperature SOFC," *J. Eur. Cer. Soc.*, In Press.

[191] J. Malzbender, E .Wessel, R.W. Steinbrech, "Reduction and Re-oxidation of Anodes for Solid Oxide Fuel Cells," *Solid State Ionics*, **176**[29-30], 2201-2203 (2005).

[192] J. Malzbender, E .Wessel, R.W. Steinbrech and L. Singheiser, "Reduction and Re-oxidation of Anodes for Solid Oxide Fuel Cells," *Ceramic Engineering and Science Proceedings*, **25**[3], 387- 392 (2004).

[193] C. Xia and M. Liu "Low-Temperature SOFCs Based on $Gd_{0.1}Ce_{0.9}O_{1.95}$ Fabricated by Dry Pressing," *Solid State Ionics*, **144**[3-4], 249-255 (2001).

[194] B. Rauch, C. Compson and M. Liu, Invention Disclosure on Hermetic SOFCs without Sealant, submitted April 2004, provisional filing November 2005.

[195] M. Ziomek-Moroz, B.S. Covino Jr., G.R. Holcomb, S.D. Cramer, S.A. Matthes, S.J. Bullard, J.S. Dunning, D.E. Alman, R. Wilson, and Prabhakar Singh, "," *Proceedings of the 17th Annual Conference on Fossil Energy Materials*, NETL, Morgantown, WV, 2003.

[196] S. Dushman, Scientific Foundations of Vacuum Technique, John Wiley & Sons Inc., NY, 1949.

[197] N.R. Whetten & J.R. Young, "Use of A Silver Tube to Admit Oxygen to a Vacuum System," *Rev. of Sci. Inst.*, **30**[6], 472-473 (1959).

[198] R.E. Coles, "The Permeability of Oxygen to Silver," *J. App. Phys.*, **14**, 342-344 (1963).

[199] E.G. Burroughs, "Mass Spectrographic Analysis of Silver Membrane Oxygen Leak," *Rev. of Sci. Inst.*, **40,** 33-35 (1969).

[200] L.C. Beavis, "Oxygen Permeation Through Silver," *Rev. of Sci. Inst.*, **43**, 122-127 (1971).

[201] R.A. Outlaw, "O_2 and CO_2 Glow-Discharge-Assisted Oxygen Transport Through Ag," *J. of App. Phys.*, **68[**3], 1002-1004 (1990).

[202] M. Davidson, G.B. Hoflund and R.A. Outlaw, "Nondestructive Depth Profile Study of Oxygen-Exposed Large-Grain Using Angle Resolved Auger Electron Spectroscopy and Ion Scattering Spectroscopy," *J. of Vac. Sci. Tech. A*, **9**, 1344-1350 (1991).

[203] R.A. Outlaw, D. Wu, M.R. Davidson and Gar B. Hoflund, "Study of the Oxygen Transport Through Ag (110), Ag (poly), and Ag 2.0 Zr," *J. of Vac. Sci. Tech. A*, **10**, 1497-1502 (1992).

[204] D. Wu, R.A. Outlaw and R.L. Ash, "Glow-Discharge Enhanced Permeation of Oxygen Through Silver," *J. of App. Phys.*, **74**, 4990-4994 (1993).

[205] J. Van Herle and A.J. McEvoy, "Oxygen Diffusion Through Silver Cathodes for Solid Oxide Fuel Cells," *J. Phys. Chem. Solids*, **55**, 339-347 (1994).

[206] I. Kontoulis and B.C.H. Steele, "Determination of Oxygen Diffusion in Solid Ag by an Electrochemical Technique," *Solid State Ionics*, **47**, 317-324 (1991).

[207] J.Will, A. Mitterdorfer, C. Kleinlogel, d. Perednis, L.J. Gauckler, "Fabrication of thin electrolytes for second generation solid oxide fuel cells," *Solid State Ionics*, **131**, 79-96 (2000).

[208] X. Chen, N. Wu, A. Ignatiev, "Thin Film Oxide Fuel Cell and Method for Forming," US Patent No. 6,645,656 B1, Nov.11, 2003.

[209] U.B. Pal and S.C. Singhal, "Electrochemical Vapour Deposition of Yttria Stabilized Zirconia Films," *J. Electrochem. Soc.*, **137**, 2937-2941 (1990).

[210] M. Inaba, A. Mineshinge and T. Maeda, "Growth Rate of Yttria Stabilized Zirconia Thin Films Formed by Electrochemical Vapour Deposition using NiO as an Oxygen Source- II Effect of the Porosity of NiO Substrate," *Solid State Ionics*, **104**[3-4], 303-310 (1997).

[211] Z. Xu, J. Shankar, and S. Yarmolenko, "Yttria-Stabilised Zirconia Coatings Produced using Combustion Chemical Vapour Deposition," *Surface and Coatings Technology*, **177**, 52-59 (2004).

[212] Z. Ogumi, Y. Uchimoto, Y. Tsuji and Z. Takehara, "Electrodeposition of Thin Yttria-Stabilized Zirconia Layers using Glow-Discharge Plasma," *J. Appl. Phys.*, **72**, 1577-1582 (1992).

[213] T. Hosomi, M. Matsuda and M. Miyake, "Electrophoretic Deposition for Fabrication of YSZ Electrolyte Film on Non-Conducting Porous NiO-YSZ Composite Substrate for Intermediate Temperature SOFC," *J. Eur. Cer. Soc.*, In Press.

[214] M. S. J. Gani, "Electrophoretic Deposition - A Review," *Ind. Ceram.*, **14**, 163–174 (1994).

[215] A. R. Boccaccini and C. B. Ponton, "Processing Ceramic-Matrix Composites Using Electrophoretic Deposition," *J. of Materials*, **47**[10], 34–37 (1995).

[216] L. Besra, C. Compson and M. Liu, "Electrophoretic Deposition of YSZ Particles on Non-Conducting Porous NiO-YSZ Substrates for Solid Oxide Fuel Cell Applications," *Journal of the American Ceramic Society*, **89**[10], 3003-3009 (2006).

[217] C. Compson, L. Besra and M. Liu, "Electrophoretic Deposition on Porous Non-Conductors," *NASA TECH BRIEFS*, LEW-18009-1, In Press.

[218] C. Compson, L. Besra and M. Liu, "Fundamentals of Electrophoretic Deposition on Non-Conducting Substrates," *J. Eur. Cer. Soc.*, Submitted.

[219] C. Compson, L. Besra, D. Earl and M. Liu, "Modeling Electrophoretic Deposition on Porous Non-Conducting Substrates using Design of Experiments," *Journal of the American Ceramic Society*, **89**[9], 2787-2795 (2006).

[220] T. Mathews. N. Rabu, J.R. Sellar and B.C. Muddle, "Fabrication of La_{1-x} Sr_x Ga_{1-y} Mg_y $O_{3-(x+y)/2}$ Thin Films by Electrophoretic Deposition and its Conductivity Measurement," *Solid state Ionics*, 128, 111-115 (2000).

[221] L. Vandeperre, C.Zhao and O. Van der Biest, "Correlation Between Surface Charge of a Powder in Water and Electrophoretic Deposition from Non-Aqueous Media," Novel chemistry and Processing of ceramics- In *Proceedings of the Novel Chemistry/Processing session of the Sixth conference and Exhibition of the European Ceramic Society*, J. Binner ed., Brighton, UK, June 20-24, 1999, Published by IOM Communications Ltd, London, 2000, pp.69-74.

[222] M. Zarbov, I. Schuster and L. Gal-Or, "Methodology for Selection of Charging Agents for Electrophoretic Deposition of Ceramic Particles," *J. Mat. Sci.*, **39**, 813-817 (2004).

[223] S. Okumura, T. Tsukamoto and N. Koura, "Fabrication of Ferroelectric BaTiO3 Films by Electrophoretic Deposition," *Jpn. J, App Phys.*, **32**, 4182-4185 (1993).

[224] D.C. Montgomery, Design and Analysis of Experiments 5th Ed., John Wiley & Sons, New York, 2001.

[225] R. Verseput, "Digging into DOE," *Quality Digest*, **21**(6) (2001).

[226] R.H. Myers and D.C. Montgomery, Response Surface Methodology, John Wiley & Sons, New York, 1995.

[227] ASTM Standard C 20, Standard test method for apparent porosity, water absorption, apparent specific gravity and bulk density of burned refractory brick and shapes by boiling water.

[228] L. Besra, C. Compson and M. Liu, "Electrophoretic Deposition on Non-Conducting Substrates: The case of YSZ film on NiO-YSZ composite substrates for solid oxide fuel cell application," *Solid State Ionics*, submitted.

[229] L. Besra, and M. Liu, "A review on fundamentals and applications of electrophoretic deposition (EPD)," *Progress in Materials Science*, **52**, 1-61 (2007).

[230] Y. Fukada, N. Nagarajan, W.Mekky, Y. Bao, H.S. Kim and P.S. Nicholson. "Electrophoretic Deposition – Mechanisms, Myths and Materials," *J. of Mat. Sci.*, **39**, 787-801 (2004).

[231] P.M. Biesheuvel and H. Verweij, "Theory of Cast Formation in Electrophoretic Deposition," *J. Am. Cer. Soc.*, **82**[6], 1451-1455 (1999).

[232] M. Gonzáles-Cuenca, P.M. Biesheuvel and H. Verweij, "Modeling Constant Voltage Electrophoretic Deposition from a Stirred Suspension," *AIChE Journal*, **46**[3], 626-631 (2000).

[233] G. Anné, K. Vanmeensel, J. Vleugels and O. Van der Biest, "A Mathematical Description of the Kinetics of the Electrophoretic Deposition Process for Al_2O_3-Based Suspensions," *J. Am. Cer. Soc.*, **88**[8], 2036-2039 (2005).

[234] Z .Zhang, Y. Huang and Z. Jiang, "Electrophoretic Deposition Forming of SiZ-TZP Composites in a Nonaqueous Sol Media," *J. Am. Cer. Soc.*, **77**, 1946-1949 (1994).

[235] B. Sareni, L. Krähenbühl, A. Beroual and C. Brosseau, "Effective Dielectric Constant of Periodic Composite Materials," *J. App. Phys.*, **80**[3], 1688-1696 (1996).

[236] B. Sareni, L. Krähenbühl, A. Beroual and C. Brosseau, "Effective Dielectric Constant of Periodic Composite Materials," *J. App. Phys.*, **80**[3], 1688-1696 (1996).

[237] E. Kreyszig, Advanced Engineering Mathematices, 8th Ed. John Wiley & Sons, Inc., New York, NY, 1999.

[238] K.S. Weil, J.Y. Kim and J.S. Hardy, "Reactive Air Brazing: A Novel Method of Sealing SOFCs and Other Solid State Electrochemical Devices," *Electrochem. and Solid State Lett.*, **8**[2] A133- (2005).

[239] Y.-S. Chou, J.W. Stevenson, L.A. Chick, "Ultra-low Leak Rate of Hybrid Compressive Mica Seals for Solid Oxide Fuel Cells," *J. of Power Sources*, **112** 130-136 (2002).

[240] Y.-S. Chou and J.W. Stevenson, "Mid-term Stability of Novel Mica-based Compressive for Solid Oxide Fuel Cells," *J. Power Souces*, **115**[2], 274-278 (2003).

[241] Y.-S. Chou and J.W. Stevenson, "Phlogopite Mica-based Compressive Seals for Solid Oxide Fuel Cells: Effect of Mica Thickness," *J. Power Sources*, **124**[2], 473-478 (2003).

[242] Y.-S. Chou and J.W. Stevenson, "Long-term Thermal Cycling of Phlogopite Mica-based Compressive Seals for Solid Oxide Fuel Cells," *J. Power Sources*, **140**[2], 340-345 (2005).

[243] J.K. Cochran, J.K. Lee and T. Sanders, "Metallic Articles Formed by Reduction of Non-Metallic Articles and Method of Producing Metallic Articles," U.S. Patent 6,582,651.

[244] C. Compson and M. Liu, "Impedance Spectroscopy Characterization of Hermetically Sealed SOFCs" in *Membranes and Separators for Fuel Cells,* P. Arora et al (Eds.), Electrochemistry Society Proceedings, PV 2004-XX, The Electrochemical Society, Pennington, NJ, 2004, forthcoming.

[245] H. Ohrui, T. Matsushima and T. Hirai, "Performance of Solid Oxide Fuel Cell Fabricated by Co-firing," *J. Power Sources*, **71**, 185-189 (1998).

[246] T. Okuo, S. Nagata, Y. Kaga, Y. Kasuga, A. Momma, K. Tksukamoto and F. Uchiyama, in *First European Solid Oxide Fuel Cell Forum Proceedings*, Baden, Switzerland, Vol.2 p. 909 (1994).

[247] P. Fragnaud, P. Charpentier, D.M. Schleich and C. Lunot C, in *Proceedings of the Second International Symposium on New Materials For Fuel Cell and Modern Battery Systems II*, P. 119, Montreal, Canada (1997).

[248] G. Schiller, R. Henne, M. Lang, R. Rockdaschel and S. Schaper, in *Fourth European Solid Oxide Fuel Cell Proceedings*, Oberrohrdorf, Switzerland, Vol. 1, p 37 (2000).

[249] T. Kato, S. Wang, A. Negishi, S. Nagata and K. Nozaki, in *Fourth European Solid Oxide Fuel Cell Proceedings*, Oberrohrdorf, Switzerland, Vol. 2, p 553 (2000).

[250] J. Carter, J. Ralph, J. Bae, T. Cruse, C. Rossignol, M. Krumpelt and R. Kumar, in *Fuel Cell 2002 Abstracts*, Palm Springs, CA, p. 874 (2002).

[251] I. Villarreal, C. Jacobson, A. Leming, Y. Matus, S. Visco and L. De Jonghe, "Metal-Supported Solid Oxide Fuel Cells," *Electrochem. and Solid State Lett.*, **6**[9], A178-A179 (2003).

[252] Y. Matus, L.C. De Jonghe, C.P. Jacobson and S.J. Visco, "Rapid Thermal Cycling of Metal-Supported Solid Oxide Fuel Cell Membranes," *Solid State Ionics*, **176**, 443-449 (2005).

[253] E. Koep, C. Jin, M. Haluska, R. Das, R. Narayan, K. Sandhage, R. Snyder, and M. Liu, "Microstructure and electrochemical properties of cathode materials for SOFCs prepared via pulsed laser deposition," *J. Power Sources*, **161**[1] 250-255 (2006).

[254] J.C. Bazan, "A Stationary Electrochemical Method of Measuring the Diffusion Coefficient of Oxygen in Metals," *Electrochim Acta*, **13**, 1883-1885 (1968).

[255] Dushman and Lafferty, Scientific foundations of Vacuum Technique 2nd Ed., John Wiley & Sons, NY, 1962.

[256] K.K. Corvin and S.J.B. Corrigan, "Dissociation of Carbon Dioxide in the Positive Column of a Glow Discharge," *J. Chem. Phys.*, **50**, 2570-2574 (1969).

[257] M.J. Barton and A. Von Engel, "Electric Dissociation of CO_2," *Phys. Lett. A*, **32**, 173-174 (1970).

[258] C.T. Campbell, "Atomic and Molecular Oxygen Adsorption on Ag(111)," *Surf. Sci.*, **157**, 43-60 (1985).

[259] Y. Kuk and L.C. Feldman, "Oscillitory Relaxtion of the Ag(110) Surface," *Phys. Rev. B*, **30**[10], 5811-5816 (1984).

[260] N.Ning, Y. Qingliang and Y. Yiying, "Multilayer Relaxation at the Surface of FCC Metals: Cu, Ag, Au, Ni, Pd, Pt, Al," *Surf. Sci.*, **206**[1-2], L857-L863 (1988).

[261] J. Crank, The Mathematics of Diffusion 1st Ed., Oxford Univ. Press, 1956.

[262] D.J. Mitchell, J.M. Harris, R.C. Patrick, E.P. Boespflug and L.C .Beavis, "Deuterium Permeation Through Copper with Trapping Impurities," *J. App. Phys.*, **53**, 970-978 (1982).

[263] P. Singh, Z. Yang, V. Viswanathan and J.W. Stevenson, "Observations on the Structural Degradation of Silver During Simultaneous Exposure to Oxidizing and Reducing Environments," *J. of Mat. Eng. And Per.*, **13**, 287-294 (2004).

[264] W.A. Meulenberg, O. Teller, U. Flesch, H.P. Buchkremer and D. Stover, "Improved Contacting by the use of Silver in Solid Oxide Fuel Cells up to an Operating Temperature of 800ºC," *J. Mater. Sci.*, **36**, 3189-3195 (2001).

[265] S.Barnett, "A New Solid Oxide Fuel Cell Design Based on Thin Film Electrolytes," *Energy*, **15**, 1-9 (1990).

[266] W. Eichenauer and G. Mueller, "Diffusion and Solubility of Oxygen in Silver," *Z Metallk*, **53**, 321-325 (1962).

[267] R.A. Outlaw, S.N. Sankaran, G.B. Hoflund and M.R. Davidson, "Oxygen Transport Through High-Purity Large-Grain Ag," *J. Mater. Res.*, **3**, 1378-1383 (1988).

[268] J.-H. Park, "Measuring Oxygen Diffusivity and Solubility in Solid Silver with a Gas-Tight Electrochemical Cell," *Mat. Lett.*, **9**, 313-316 (1990).

[269] D.A. Outka, J. Stöhr and W. Jark "Orientation and Bond Length of Molecular Oxygen on Ag(110) and Pt(111): A Near-edge Xray Absorption Fine-Structure Study," *Phys Rev. B*, **35[**8], 4119-4122 (1987).

[270] K. Bange, T.E. Madey and J.K. Sass, "The Adsorption of Oxygen on Ag(110): A New View of Structure and Bonding," *Chem. Phys. Lett.*, **113**, 56- (1985).

[271] P.A. Gravil and D.M. Bird, "Adsorption and Dissociation of O_2 on Ag(110)," *Phys. Rev. Lett.*, **77**[18], 3933-3936 (1996).

[272] W. Wurth, J. Stöhr, P. Feulner, X. Pan, K. R. Bauchspiess, Y. Baba, E. Hudel, G. Rocker, and D. Menzel, "Bonding, Structure, and Magnetism of Physisorbed and Chemisorbed O_2 on Pt(111)," *Phys. Rev. Lett.*, **65**, 2426-2429 (1990).

[273] M. Zomack, "An Electron Spin Resonance Study of Adsorbed Gases in Ultrahigh Vacuum," *PhD Thesis*, Freie Universitat Berlin (1987).

[274] L. Vattuone, M. Rocca and U. Valbusa, "Anharmonic Shift in the Stretching Frequency of O_2 Chemisorbed on Ag (110)," *Surf. Sci.*, **314**, L904- (1994).

[275] R. Franchy, F. Bartolucci, F. Bautier de Mongeot, F. Cemic, M. Rocca, U. Valbusa, L. Vattuone, S. Lacombe, K. Jacobi, K.B.K. Tang, R.E. Palmer, J. Villette, D. Teillet-Billy and J.P. Guayacq, "Negative Ion Resonances of O_2 adsorbed on Ag Surfaces," *J. Phys.: Condens. Matter,*, **12**, R53-R82 (2000).

[276] H.A. Engelhardt and D. Menzel, "Adsorption of Oxygen On Silver Single Crystal Surfaces," *Surf. Sci.*, **57**, 591-618 (1976).

[277] C.T. Campbell, "An XPS Study of Molecularly Chemisorbed Oxygen on Ag(111)," *Surf. Sci.*, **173**, L641-L646 (1986).

[278] M.E.M. Spruit and A.W. Kleyn, "Dissociative Adsorption of O_2 on Ag(111)," *Chem. Phys. Lett.*, **159**, 342-348 (1989).

[279] A. Raukema and A.W. Kleyn, "Transient Trapping Desorption of Molecules at Surfaces," *Phys. Rev. Lett.*, **74**, 4333-4336 (1995).

[280] F. Bautier de Mongeot, U. Valbusa and M. Rocca, "Oxygen Adsorption on Ag(111)," *Surf. Sci.*, **339**, 291-296 (1995).

[281] E.L. Garfunkel et al., "The Coadsoroption of Sodium and Oxygen on Ag(100): An XPS, UPS and HREELS Study," *Surf. Sci,*, **164**, 511-525 (1985).

[282] C.S. Ares Fang, *Surf. Sci.*, "Surface Structural Transition of Adsorption of Oxygen on Ag(100)," **235**, L291-L294 (1990).

[283] M. Rocca, P. Traversaro and U. Valbusa "Initial Sticking Coefficient of O_2 on Ag(001)," *J. Elec. Spectrosc. Rel. Phen.*, **54-55**, 131 (1990).

[284] J. Torras, J.M. Ricart, F. Illas and J. Rubio, "Bonding of Atomic Oxygen to Cu(100) and Ag(100) Surfaces: A Theoretical Comparitive Study," *Surf. Sci.*, **297**, 57-65 (1993).

[285] F. Bautier de Mongeot, M. Rocca and U. Valbusa, "Energy and Angle Dependence of the Initial Sticking Coefficient of O_2 on Ag(001)," *Surf. Sci.*, **363**, 68-72 (1996).

[286] Q. Sun, Y. Wang, K. Fan, and J. Deng, J., "Ab initio pseudopotential study of dehydrogenation of methanol on oxygen modified Ag(110) surface," *Surf. Sci.*, **459**[1-2], 213-222 (2000).

[287] P.A. Gravil, J.A. White and D.M Bird, "Chemisorption of O_2 on Ag(110)," *Surf. Sci.*, **352-354**, 248-252 (1996).

[288] C. Compson, Y.M. Choi and M. Liu, "An Experimental and Computational Study on Oxygen Diffusion Through Silver," *J. Phys. Chem. A*, Submitted.

[289] G. Kresse and J. Furthmüller, "Efficient Iterative Schemes for *ab initio* Total-Energy Calculations Using a Plane-Wave Basis Set," *Phys. Rev. B*, **54**, 11169-11186 (1996).

[290] G. Kresse and J. Hafner, "*Ab initio* Molecular Dynamics for Liquid Metals," *Phys. Rev. B*, **47**, 558-561 (1993).

[291] P. Blochl, "Projector Augmented-Wave Method," *Phys. Rev. B*, **50**, 17953-17979 (1994).

[292] J.P. Perdew, K. Burke, and M. Ernzerhof, "Generalized Gradient Approximation Made Simple, " *Phys. Rev. Lett.*, **77**, 3865-3868 (1996).

[293] D. Vanderbilt, "Soft Self-Consistent Pseudopotentials in a Generalized Eigenvalue Formalism," *Phys. Rev. B*, **41**, 7892-7895 (1990).

[294] H.J. Monkhorst and J.D. Pack, "Special Points for Brillouin Zone Integrations," *Phys. Rev. B*, **13**, 5188-5192 (1976).

[295] A.J. Nagy, G. Mestl, D. Herein, G. Weinberg, E. Kitzelmann and F. Schlogl, "The Correlation of Subsurface Oxygen Diffusion withVariations of Silver Morphology in the Silver-Oxygen System," *J. Catal.*, **182**[2], 417-429 (1999).

[296] G. Henkelman and H. Jönsson, "Improved Tangent Estimate in the Nudged Elastic Band Method for Finding Minimum Energy Paths and Saddle Points," *J. Chem. Phys.*, **113**, 9978-9985 (2000).

[297] G. Bracco, M. Canepa, P. Cantini, F. Fossa, L. Mattera, S. Terreni, and D. Truffelli, "Impact Collision Ion Scattering Study of Ag (110)," *Surf. Sci.*, **270**, 61-67 (1992).

[298] W.-X. Li, C. Stampfl, and M. Scheffler, "Subsurface Oxygen and Surface Oxide Formation at Ag(111): A Density Functional Theory Investigation," *Phys. Rev. B*, **67**, 045408 (2003).

[299] Y. Xu, J. Greeley and M. Mavrikakis, "Effect of Subsurface Oxygen on the Reactivity of the Ag (111) Surface," *J. Am. Chem. Soc.*, **127**, 12823-12827 (2005).

[300] P. Kamakoti, and D.S. Sholl, "A Comparison of Hydrogen Diffusivities in Pd and CuPd Alloys using Density Functional Theory," *J. Membrane Sci.*, **225**, 145-154 (2003).

[301] D.E. Jiang, E.A. Carter, "Carbon Dissolution and Diffusion in Ferrite and Austenite from First Principles," *Phys. Rev. B*, **67**, 214103 (2003).

[302] C. Wert, and C. Zener, "Interstitial Atomic Diffusion Coefficients, " *Phys. Rev.*, **76**, 1169-1175 (1949).

[303] K.J. Laidler, Chemical Kinetics 3rd ed. Benjamin Cummings: Massachusetts, 1997.

[304] A. Roth, Vacuum Technology, North-Holland Publishing Co., NY, 1976.

[305] P. Thieberger, "Upper Limits for Sublimation Losses from Hot Carbon Targets in Vacuum and in Gasses," Brookhaven National Laboratory, Nov. 2000.

[306] J.O. Hirschfelder, C.F. Curtis and R.B. Bird, Molecular Theory of Gases and Liquids, John Wiley & Sons, NY, 1964.